



**HAL**  
open science

# Caractérisation 3D de l'hétérogénéité de la perméabilité à l'échelle de l'échantillon

Amir Soltani

► **To cite this version:**

Amir Soltani. Caractérisation 3D de l'hétérogénéité de la perméabilité à l'échelle de l'échantillon. Autre. Institut National Polytechnique de Lorraine, 2008. Français. NNT: 2008INPL049N . tel-01748692

**HAL Id: tel-01748692**

**<https://hal.univ-lorraine.fr/tel-01748692>**

Submitted on 29 Mar 2018

**HAL** is a multi-disciplinary open access archive for the deposit and dissemination of scientific research documents, whether they are published or not. The documents may come from teaching and research institutions in France or abroad, or from public or private research centers.

L'archive ouverte pluridisciplinaire **HAL**, est destinée au dépôt et à la diffusion de documents scientifiques de niveau recherche, publiés ou non, émanant des établissements d'enseignement et de recherche français ou étrangers, des laboratoires publics ou privés.



## AVERTISSEMENT

Ce document est le fruit d'un long travail approuvé par le jury de soutenance et mis à disposition de l'ensemble de la communauté universitaire élargie.

Il est soumis à la propriété intellectuelle de l'auteur. Ceci implique une obligation de citation et de référencement lors de l'utilisation de ce document.

D'autre part, toute contrefaçon, plagiat, reproduction illicite encourt une poursuite pénale.

Contact : [ddoc-theses-contact@univ-lorraine.fr](mailto:ddoc-theses-contact@univ-lorraine.fr)

## LIENS

Code de la Propriété Intellectuelle. articles L 122. 4

Code de la Propriété Intellectuelle. articles L 335.2- L 335.10

[http://www.cfcopies.com/V2/leg/leg\\_droi.php](http://www.cfcopies.com/V2/leg/leg_droi.php)

<http://www.culture.gouv.fr/culture/infos-pratiques/droits/protection.htm>

# THÈSE

DE L'INSTITUT NATIONAL POLYTECHNIQUE DE  
LORRAINE

ÉCOLE DOCTORALE ÉNERGIE MÉCANIQUE MATÉRIAUX

pour obtenir le titre de

**DOCTEUR DE L'INPL**

**Spécialité : Mécanique Energétique**

Présentée et soutenue par

Amir SOLTANI

**CARACTÉRISATION 3D DE L'HÉTÉROGÉNÉITÉ DE LA  
PERMÉABILITÉ À L'ÉCHELLE DE L'ÉCHANTILLON**

soutenue le 21 octobre 2008 devant le jury composé de :

Christian DAVID, professeur, université de Cergy-Pontoise

Fred DELAY, professeur, université de Poitiers

Mostafa FOURAR, professeur, INPL

Mickaele LE RAVALEC-DUPIN, ingénieur de recherche, IFP

Patrick EGERMANN, Chef du groupe R&D stockage, GDF Suez

Didier LASSEUX, chargé de recherche CNRS, ENSAM Bordeaux

Benoit NOETINGER, ingénieur de recherche, IFP

*Rapporteur*

*Rapporteur*

*Directeur*

*Co-Directeur*

*Examineur*

*Examineur*

*Invité*

# Table des matières

<b>Résumé</b>	<b>1</b>
<b>Remerciements</b>	<b>3</b>
<b>1 Introduction</b>	<b>4</b>
1.1 L'hétérogénéité à l'échelle de l'échantillon jusqu'à l'échelle du réservoir . . .	5
1.2 Hétérogénéité et données de gisement . . . . .	6
1.3 Hétérogénéité et modélisation numérique . . . . .	7
1.4 Hétérogénéité et géostatistique . . . . .	9
1.5 Objectifs de la thèse . . . . .	10
<b>2 Etat de l'art</b>	<b>12</b>
2.1 Caractérisation à l'échelle du réservoir . . . . .	12
2.2 Caractérisation à l'échelle de la carotte et du pore . . . . .	13
<b>3 Caractérisation unidimensionnelle de l'hétérogénéité de la perméabilité</b>	<b>18</b>
3.1 Introduction . . . . .	18
3.2 Description de la méthodologie . . . . .	18
3.3 Echantillons de roche et modèles numériques . . . . .	20
3.3.1 Echantillons de roche . . . . .	20
3.3.2 Modèles numériques . . . . .	20
3.4 Validation numérique . . . . .	21
3.4.1 Calcul des dérivées . . . . .	21
3.4.2 Déplacement immiscible . . . . .	22
3.4.3 Déplacement miscible . . . . .	22
3.5 Validation expérimentale . . . . .	22
3.6 Conclusion . . . . .	26
<b>4 Caractérisation tridimensionnelle de l'hétérogénéité de la perméabilité</b>	<b>27</b>
4.1 Introduction . . . . .	27
4.2 Paramétrage du modèle de perméabilité . . . . .	27

4.2.1	Définition de la fonction objectif . . . . .	28
4.3	Boucle de calage . . . . .	29
4.3.1	Optimisation simple . . . . .	29
4.3.2	Optimisation graduelle . . . . .	29
4.4	Validation numérique . . . . .	30
4.4.1	Modèles numériques . . . . .	30
4.4.2	Méthodologie . . . . .	31
4.4.3	Résultats des tests de validation . . . . .	31
4.5	Application aux expériences en laboratoire . . . . .	32
4.5.1	Résultats pour le composite 2 . . . . .	32
4.5.2	Résultats pour le grès SG20 . . . . .	32
4.6	Conclusion . . . . .	33
<b>Conclusions et perspectives</b>		<b>34</b>
<b>Annexe</b>		<b>38</b>
<b>1 Introduction</b>		<b>39</b>
1.1	Heterogeneity from the core to the entire reservoir . . . . .	40
1.2	Reservoir data and heterogeneity . . . . .	41
1.3	Numerical modeling and heterogeneity . . . . .	42
1.4	Geostatistics and heterogeneity . . . . .	45
1.5	Objectives of the study . . . . .	45
<b>2 Literature Review</b>		<b>48</b>
2.1	Field scale permeability characterization . . . . .	48
2.2	Core scale permeability characterization . . . . .	50
2.3	Concluding remarks . . . . .	55
<b>3 Core Analysis and Measurements</b>		<b>56</b>
3.1	Laboratory experiments . . . . .	56
3.1.1	Experimental devices and setup . . . . .	57
3.1.2	Experimental procedure . . . . .	60
3.2	Core description . . . . .	61
3.2.1	Natural core samples . . . . .	61
3.2.2	Numerical core samples . . . . .	67
3.3	Preliminary data analysis . . . . .	68
3.3.1	Petrophysical analysis . . . . .	68
3.3.2	Statistical analysis . . . . .	70
3.4	Chapter summary . . . . .	78

<b>4</b>	<b>One-Dimensional Permeability Characterization</b>	<b>79</b>
4.1	Description of the methodology . . . . .	79
4.2	Numerical validation . . . . .	81
4.2.1	Sensitivity analysis . . . . .	81
4.2.2	Numerical differentiation . . . . .	87
4.2.3	Numerical immiscible displacement . . . . .	89
4.2.4	Numerical miscible displacement . . . . .	92
4.3	Experimental validation . . . . .	94
4.3.1	Experimental results . . . . .	95
4.4	Concluding remarks . . . . .	102
<b>5</b>	<b>Three Dimensional Permeability Characterization: Theory</b>	<b>104</b>
5.1	Optimization problem . . . . .	104
5.1.1	Definition of the objective function . . . . .	105
5.2	Optimization methods . . . . .	107
5.3	Parametrization techniques . . . . .	108
5.3.1	Pilot point technique . . . . .	109
5.3.2	Gradual deformation method . . . . .	109
5.4	Optimization workflow . . . . .	111
5.4.1	Simple optimization . . . . .	112
5.4.2	Gradual optimization . . . . .	113
5.5	Concluding remarks . . . . .	115
<b>6</b>	<b>Three Dimensional Permeability Characterization: Dynamic Data</b>	<b>116</b>
6.1	Numerical models and the available data . . . . .	116
6.1.1	Numerical data analysis . . . . .	117
6.2	Laboratory experiments and the available data . . . . .	123
6.2.1	Laboratory data analysis and processing . . . . .	123
6.3	Concluding remarks . . . . .	139
<b>7</b>	<b>Three Dimensional Permeability Characterization: Application</b>	<b>140</b>
7.1	PumaFlow numerical simulator . . . . .	140
7.2	Numerical validation . . . . .	143
7.2.1	Model-3 . . . . .	144
7.2.2	Model-4 . . . . .	153
7.3	Experimental validation . . . . .	159
7.3.1	Composite 2 . . . . .	160
7.3.2	Sandstone SG20 . . . . .	166
7.4	Concluding remarks . . . . .	179
	<b>Conclusions and Perspectives</b>	<b>181</b>



# Table des figures

1.1	Heterogeneity from micro to gigascopic scales . . . . .	40
1.2	Computed porosity as a function of the volume considered for a numerical sandstone sample . . . . .	41
1.3	Schematic of vertical permeability variation in a reservoir . . . . .	44
3.1	The core-holder assembly . . . . .	57
3.2	The distribution plug with spiral pattern . . . . .	58
3.3	X-ray CT scanning and the resulting two-dimensional matrix of CT data . .	59
3.4	The experimental setup . . . . .	60
3.5	Thin sections of different core samples . . . . .	63
3.6	Tomography profiles computed for different core samples . . . . .	65
3.7	Cross sectional CT images of plug1-1 and plug1-2 used in composite 1 . . . .	65
3.8	Cross sectional CT images of plug1-3 and plug1-4 used in composite 1 . . . .	66
3.9	Cross sectional CT images of Fontainebleau plug used inside composite 2 . .	66
3.10	Cross sectional CT images of samples LJ001, K13 and SG20 . . . . .	67
3.11	The relative class frequencies of porosity data for composite 2, sample K13 and SG20 . . . . .	73
3.12	The experimental variograms of porosity data for composite 2 and sample SG20	76
3.13	The modeled variograms of porosity data for composite 2 and sample SG20 .	77
4.1	Schematic view of the pressure drop across the core sample . . . . .	80
4.2	The permeability field for the numerical model with $80 \times 35 \times 35$ grid cells .	84
4.3	Cumulative production and watercut against dimensionless time for the $80 \times 35 \times 35$ model . . . . .	84
4.4	The permeability field with $80 \times 107 \times 107$ grid cells . . . . .	85
4.5	Cumulative production and watercut against dimensionless time for the up-scaled model (for cells along axis $X$ ) . . . . .	86
4.6	Cumulative production and watercut against dimensionless time for the up-scaled model (for cells along axis $Y$ and $Z$ ) . . . . .	87
4.7	$\Delta p(t)$ and its time derivative fluctuations for a homogeneous model . . . . .	88
4.8	Filtering small scale $\Delta p(t)$ time derivative fluctuations . . . . .	89



4.9	Comparison of the processed permeabilities with the absolute ones for the homogeneous model . . . . .	89
4.10	The permeability field for the numerical Model-2 . . . . .	90
4.11	Numerical pressure drop data for Model-1 and Model-2 . . . . .	90
4.12	2D images of the 3D simulated concentration maps at different times for numerical Model-1 and Model-2 (immiscible displacement) . . . . .	91
4.13	Comparison of the processed numerical permeabilities with the absolute ones for Model-1 and Model-2 (immiscible displacement) . . . . .	92
4.14	Numerical pressure drops for Model-1 and Model-2 when performing miscible displacement . . . . .	93
4.15	Comparison of the processed numerical permeabilities with the absolute ones for Model-1 and Model-2 (miscible displacement) . . . . .	93
4.16	2D images of the 3D simulated concentration maps at different times for numerical Model-1 and Model-2 (miscible displacement) . . . . .	94
4.17	2D images of the 3D concentration maps at different times for composite 2 . . . . .	96
4.18	Comparison of the processed experimental permeabilities with absolute ones for composite 1 and composite 2 . . . . .	97
4.19	Inlet-outlet pressure drop data before and after scaling for composite 1 and 2 . . . . .	98
4.20	Comparison of the processed permeabilities with the absolute ones for two cut parts of the low permeability lavoux . . . . .	99
4.21	Inlet-outlet pressure drop data against injection time for sample LJ001 . . . . .	100
4.22	Comparison of processed permeabilities with the minipermeameter results for LJ001 . . . . .	100
4.23	The processed permeabilities for the coarse-grained sandstone K13 . . . . .	101
4.24	2D images of the 3D concentration maps for the coarse-grained sandstone K13 . . . . .	102
5.1	Schematic of realization chain during a gradual deformation based optimization . . . . .	111
5.2	CONDOR workflow used for a simple calibration of the 3D permeability field . . . . .	113
5.3	CONDOR workflow used for a gradual deformation based calibration of the 3D permeability field . . . . .	114
6.1	Cross sectional images of the 3D porosity map for Model-3 . . . . .	118
6.2	Cross sectional images of the 3D permeability map for Model-3 . . . . .	119
6.3	Reference inlet-outlet pressure drop data for numerical Model-3 . . . . .	119
6.4	Reference concentration maps for numerical Model-3 . . . . .	120
6.5	Cross sectional images of the 3D permeability map for Model-4 . . . . .	121
6.6	Reference inlet-outlet pressure drop data for numerical Model-4 . . . . .	122
6.7	Reference concentration maps for numerical Model-4 . . . . .	122
6.8	The inlet-outlet pressure drop data against injection time for composite 2 . . . . .	124
6.9	Schematic of the sample SG20 numerical model . . . . .	126
6.10	Original cross sectional images of the 3D porosity map for composite 2 . . . . .	127

6.11	Processed cross sectional images of the 3D porosity map for composite 2 . . .	128
6.12	The arithmetic average of composite 2 and SG20 porosity values per slice . .	129
6.13	Visualization of the CT noise . . . . .	129
6.14	Cross sectional images of the 3D porosity map for sample SG20 . . . . .	130
6.15	2D images of the 3D concentration maps obtained at successive times for composite 2 . . . . .	132
6.16	The frequency distribution of some concentration images for composite 2 . .	133
6.17	A 2D concentration image taken at a distance of 61.2 mm from the inlet face of composite 2. . . . .	133
6.18	Comparison of an original and processed concentration data for composite 2	134
6.19	2D images of the 3D concentration maps for sandstone SG20 taken at two successive times (normal injection) . . . . .	136
6.20	2D images of the 3D concentration maps for sandstone SG20 taken at two successive times (normal injection) . . . . .	137
6.21	2D images of the 3D concentration maps for sandstone SG20 taken at two successive times (inverse injection) . . . . .	137
6.22	2D images of the 3D concentration maps for sandstone SG20 taken at two successive times (inverse injection) . . . . .	138
6.23	2D images of the 3D concentration maps for sandstone SG20 taken at two successive times (inverse injection) . . . . .	139
7.1	The relative permeability data used in PumaFlow simulator . . . . .	142
7.2	Comparison of the reference and the simulated $\Delta p(t)$ for the primary optimization of Model-3 . . . . .	147
7.3	The evolution of different parameters for primary calibration of Model-3 . . .	147
7.4	The evolution of different parameters for second primary optimization of Model-3 . . . . .	149
7.5	Comparison of a the reference and simulated concentration maps for primary optimization of Model-3 . . . . .	150
7.6	Evolution of the objective function for Model-3 during the gradual deformation based optimization . . . . .	151
7.7	Comparison of the reference and simulated $\Delta p(t)$ for Model-3 after the gradual deformation based optimization . . . . .	152
7.8	Comparison of a the reference and simulated concentration maps for the gradual deformation based optimization of Model-3 . . . . .	152
7.9	The evolution of different parameters for Model-3 during the gradual deformation based optimization . . . . .	153
7.10	Comparison of the reference and the simulated $\Delta p(t)$ for the primary optimization of Model-4 . . . . .	154
7.11	Comparison of a the reference and the simulated concentration maps for the primary optimization of Model-4 . . . . .	156

7.12	Comparison of the reference and the simulated $\Delta p(t)$ for the gradual deformation based optimization of Model-4 . . . . .	156
7.13	Evolution of the objective function for the gradual deformation based optimization of Model-4 . . . . .	157
7.14	The evolution of different parameters for Model-4 during the gradual deformation based optimization . . . . .	158
7.15	Comparison of a the reference and the simulated concentration maps for the gradual deformation based optimization of Model-4 . . . . .	159
7.16	Comparison of the reference and the simulated $\Delta p(t)$ for the primary optimization of composite 2 . . . . .	161
7.17	The evolution of different parameters for composite 2 during the primary optimization . . . . .	162
7.18	Comparison of the reference and the simulated concentration maps for the primary optimization of composite 2 . . . . .	163
7.19	Evolution of the objective function for composite 2 during the gradual deformation based optimization . . . . .	164
7.20	Evolution of the different parameters for composite 2 during the gradual deformation based optimization . . . . .	165
7.21	Comparison of the reference and the simulated concentration maps for the gradual deformation based optimization of composite 2 . . . . .	165
7.22	Comparison of the reference and the simulated $\Delta p(t)$ for the primary optimization of SG20 (normal injection) . . . . .	167
7.23	Comparison of the reference and the simulated $\Delta p(t)$ for the primary optimization of SG20 (inverse injection) . . . . .	167
7.24	Comparison of the reference and the simulated concentration maps for the sample SG20 after the primary optimization (normal injection) . . . . .	168
7.25	Comparison of the reference and the simulated $\Delta p(t)$ for the gradual deformation based optimization of SG20 (normal injection) . . . . .	169
7.26	The evolution of the inversion parameters for the sample SG20 during the gradual deformation based optimization (normal injection) . . . . .	171
7.27	Comparison of the reference and the simulated concentration maps for the sample SG20 after the gradual deformation based optimization (normal injection) . . . . .	172
7.28	Comparison of the reference and the simulated concentration maps for the sample SG20 after the primary optimization (inverse injection) . . . . .	173
7.29	The evolution of the inversion parameters for the sample SG20 during the gradual deformation based optimization (inverse injection) . . . . .	174
7.30	Comparison of the reference and the simulated $\Delta p(t)$ for the gradual deformation based optimization of SG20 (inverse injection) . . . . .	175

7.31	Comparison of the reference and the simulated concentration maps for the sample SG20 after the gradual deformation based optimization (inverse injection) . . . . .	175
7.32	Comparison of the reference and the simulated concentration maps for the sample SG20 after introducing two pilot points (inverse injection) . . . . .	176
7.33	Comparison of the reference and the simulated concentration maps for the sample SG20 after using both the gradual deformation and the pilot point method (inverse injection) . . . . .	177
7.34	The evolution of the inversion parameters for the sample SG20 during the optimization with both the gradual deformation and the pilot point method (inverse injection) . . . . .	178

# Liste des tableaux

3.1	Petrophysical properties considered to generate the numerical core samples . . . . .	68
3.2	Petrophysical properties of the core samples studied in this work . . . . .	71
3.3	Petrophysical properties of the small plugs used to create composites 1 and 2 . . . . .	71
3.4	The mean and variance of porosity data . . . . .	73
3.5	The ranges related to modeled variograms . . . . .	75
4.1	Properties of the numerical model with $80 \times 35 \times 35$ grid cells . . . . .	83
4.2	Properties of the numerical model with $80 \times 107 \times 107$ grid cells . . . . .	85
6.1	The correlation coefficient values for different blocks in Model-3 . . . . .	118
6.2	Statistical properties of $b(\mathbf{x})$ for different blocks in Model-4 . . . . .	120
6.3	The correlation coefficient values for different blocks in Model-4 . . . . .	122
7.1	The initial inversion parameters for primary calibration of Model-3 . . . . .	145
7.2	Comparison of the $\sigma^2$ and the average permeability after primary calibration of Model-3 . . . . .	148
7.3	Comparison of the $\sigma^2$ and the average permeability after the gradual deformation based calibration of Model-3 . . . . .	153
7.4	Comparison of the $\sigma^2$ and the average permeability after the primary calibration of Model-4 . . . . .	155
7.5	Comparison of the parameters for Model-4 (block1-4) after the gradual deformation based optimization . . . . .	158

# Résumé

Les roches réservoir ont différentes propriétés, l'une des plus importantes étant la perméabilité. Les variations de perméabilités au sein des roches influencent très fortement la façon dont les fluides s'y écoulent. Une modélisation réaliste des milieux poreux doit rendre compte de ces variations de perméabilité. L'objet de cette thèse est de développer des méthodologies permettant d'identifier la distribution spatiale des valeurs de perméabilité dans des échantillons de roches.

Nous avons tout d'abord développé en laboratoire des expériences d'injection de fluide miscible très visqueux dans des échantillons initialement saturés par une saumure peu visqueuse. Pendant l'injection, l'évolution au cours du temps de la pression différentielle entre les deux faces de l'échantillon a été enregistrée par des capteurs de pression. En outre, des mesures scanner ont fourni une carte 3D de la porosité ainsi que des cartes 3D décrivant la distribution spatiale des concentrations dans l'échantillon à différents temps. Cette expérience a été répétée sur différents échantillons affichant des niveaux différents d'hétérogénéité.

Nous avons tout d'abord mis en place une méthode d'interprétation donnant directement le profil 1D de la perméabilité le long de la direction d'écoulement à partir de la pression différentielle mesurée au cours du temps. Cette méthode a été validée numériquement et expérimentalement.

Puis, afin d'affiner la description de l'agencement des valeurs de perméabilité dans l'échantillon, c'est à dire d'obtenir un modèle 3D de perméabilité représentatif de l'échantillon, nous avons développé une méthodologie itérative de calage des pressions et des concentrations. Cette méthode passe par deux étapes : une optimisation simple pour caler les pressions, ce qui permet de capturer l'hétérogénéité dans la direction de l'écoulement et une optimisation complexe pour caler les concentrations pour capturer l'hétérogénéité transverse dans la zone éclairée par le fluide injecté. Cette méthode a été validée à partir de tests numériques, ce qui a permis de contrôler le potentiel de reconstruction du modèle de perméabilité. Les deux cas considérés ont été positifs. Enfin, la méthode a été appliquée à deux des expériences d'injection de fluide visqueux que nous avons réalisées en laboratoire sur deux échantillons. Nous avons pu alors déterminer des modèles de perméabilité capables de reproduire assez

bien les données de pression et de concentration acquises pendant l'injection.

# Remerciements

J'ai passé trois agréables années à l'IFP dont je garderai un souvenir impérissable. J'ai rencontré des personnes exceptionnelles et j'ai collaboré avec de grands professionnels. Merci à l'équipe de pétrophysique et simulation numérique à l'IFP et à l'Institut Nationale Polytechnique de Lorraine. Je voudrais exprimer ma gratitude et mes sincères remerciements à Mickaele Le Ravalec et Moustafa Fourar pour avoir cru en mes capacités. Merci pour votre aide et votre gentillesse.

Je voudrais également remercier Élisabeth Rosenberg, Benoît Noetinger et Frédéric Roggero pour leurs précieux conseils et aussi les membres du jury pour avoir été présent le jour tant attendu de ma soutenance.

Je me suis fait des amis qui m'ont accompagné et qui ont su me distraire lorsque j'en avais besoin. Magnolia, Houkay, Salman, Alexandre, Thomas et Marius, je pense bien à vous.

Pour le temps que j'ai passé en laboratoire, je n'oublie évidemment pas les techniciens disponibles et bienveillants qui m'ont apporté leur aide. Merci à Corinne, Benoît, Dannilo et Hervé.

Dans notre département, j'ai travaillé avec des ingénieurs de mérite tels que Véronique, Yann et Lin.

Je suis également reconnaissant à notre chef de département, Patrick Lemonier, la directrice de R03, Olga Vizika, et les secrétaires pour leur efficacité.

Une pensée émue pour ma famille en Iran, toujours présente à mes côtés malgré la distance. J'admire leur patience, leur joie de vivre et leur foi en moi. Sans leurs encouragements, je ne serais sans doute pas la même personne. Je pense tout spécialement à Rokhsareh et Sina, mes tendres neveux qui ont vu le jour lorsque je faisais mes études en France.

Sans oublier ma femme, Lydie, pour m'avoir soutenu et avoir été une source d'inspiration au quotidien et ma belle famille pour m'avoir si bien accueilli au sein des leurs. L'amour est une force et je compte aller loin auprès de ceux que j'aime.



# Chapitre 1

## Introduction

Selon International Energy Outlook (IEO2007, mai 2007), la consommation mondiale de pétrole passera de 83 millions de barils par jour en 2004 à 118 millions en 2030. Si on continue d'utiliser les réserves d'hydrocarbure, alors l'industrie et l'académie des sciences auront à trouver de meilleurs moyens pour les produire. L'objectif principal de l'étude d'un gisement est de déterminer les conditions optimales nécessaires pour maximiser le taux de récupération des hydrocarbures avec un degré de certitude acceptable. Les ingénieurs de réservoir doivent décrire les diverses caractéristiques du gisement à partir des données disponibles. La modélisation numérique de réservoir est la technique la plus sophistiquée pour atteindre cet objectif. Les réservoirs sont modélisés selon un maillage 3D dans lequel les cellules sont remplies par des données pétrophysiques (par exemple, la porosité, la perméabilité ou d'autres propriétés de gisement). Les propriétés du gisement ont différentes influences et importances en fonction de leurs divers impacts sur l'écoulement des fluides. La perméabilité est l'une des propriétés les plus importantes du réservoir. Elle a une forte incidence sur l'écoulement du fluide en créant des barrières d'écoulement et des chemins préférentiels. Bien que depuis plus d'un siècle, les ingénieurs aient extrait du pétrole et du gaz des gisements, ils sont encore mal informés sur la distribution de la perméabilité (ou porosité) dans le gisement. Idéalement, si les réservoirs étaient homogènes, mesurer leurs propriétés dans n'importe quel endroit permettrait leur description complète. Malheureusement, les réservoirs sont hétérogènes. La formation des roches est le produit de divers phénomènes géologiques comme la sédimentation, l'évolution diagénétique et la déformation mécanique. Ces phénomènes géologiques peuvent se produire de façon séquentielle ou simultanée, ce qui rend la formation des roches complexe et non homogène. La connaissance relative à l'hétérogénéité des réservoirs est très incomplète en raison du peu de données disponibles. Cette connaissance est limitée à des données de puits et des études sismiques. Être conscient de l'influence de l'hétérogénéité des gisements sur l'écoulement des fluides et la production est crucial pour une bonne gestion des réservoirs. Différentes méthodes de caractérisation de gisement sont conçues pour intégrer les données disponibles dans le modèle numérique et réduire les incertitudes concernant la production à venir.

## 1.1 L'hétérogénéité à l'échelle de l'échantillon jusqu'à l'échelle du réservoir

L'hétérogénéité du réservoir peut être mesurée selon différentes échelles, depuis l'échelle du pore jusqu'à l'ensemble du réservoir. Bien que les propriétés de réservoir puissent varier sur différentes échelles, il est pratique de diviser l'hétérogénéité suivant quatre niveaux distincts [25] comme le montre la Figure 1.1 (voir annexe).

1. *Hétérogénéité microscopique.* Ce type d'hétérogénéité est évalué à un niveau microscopique. Il est aussi appelé hétérogénéité au niveau du pore. Il inclut les pores et la distribution des grains, les canaux microscopiques et la lithologie des roches.
2. *Hétérogénéité macroscopique.* L'hétérogénéité macroscopique est observée au niveau de l'échantillon. Elle agit sur la perméabilité et la porosité, les propriétés pétrophysiques telles que la perméabilité relative et la pression capillaire.
3. *Hétérogénéité mégascopique.* L'ordre de grandeur de ce type d'hétérogénéité est environ le même que celui d'une maille dans un simulateur de réservoir. Il fait quelques dizaines de mètres à la verticale comme à l'horizontale. Les propriétés mesurées à cette échelle incluent les données de diagraphie ainsi que les données sismiques et les essais de puits [31].
4. *Hétérogénéité gigascopique.* L'hétérogénéité gigascopique est mesurée à l'échelle du réservoir. Elle affecte les données mesurées à partir des tests de traceurs, des essais de puits et la localisation des failles.

Pour décrire l'hétérogénéité d'un réservoir, celle-ci doit être définie à la bonne échelle pour être représentative. Durant l'étude d'un réservoir, différentes mesures sont effectuées à divers niveaux. La perméabilité relative est mesurée à l'échelle de l'échantillon tandis que la perméabilité des essais de puits est calculée à l'échelle du réservoir. À l'échelle microscopique, un système poreux naturel est toujours hétérogène en raison de la variabilité spatiale des pores [18]. Par conséquent, les mesures d'une même propriété à cette échelle montrent des variations significatives. Par exemple, la porosité au niveau microscopique peut être égale à un dans le pore ou à zéro dans le grain. Lorsque la mesure est faite à grande échelle, les variations des propriétés observées à une échelle plus petite sont réduites parce qu'elle sont moyennées [31]. En d'autres termes, les variations d'une propriété mesurée diminuent en même temps que l'échelle augmente. Cette dépendance par rapport à l'échelle est appelée "effet de support". La Figure 1.2 (voir annexe) montre un exemple classique. La Figure 1.2(a) (voir annexe) montre une coupe transversale d'une roche de grès synthétique avec les dimensions  $3.8 \times 3.8 \times 1.0 \text{ cm}^3$ . Les variations de la porosité calculée diminuent tandis que le volume poreux augmente (Figure 1.2(b), voir annexe).

Un autre exemple concerne la perméabilité. La perméabilité d'un échantillon est mesurée sur un volume de  $0.00001 \text{ m}^3$ . D'autre part, la perméabilité déduite des essais de puits est obtenue sur un volume de  $10^4$  jusqu'à  $10^6 \text{ m}^3$ . Il y a au moins 10 ordres de grandeur entre

le volume sur lequel la perméabilité est mesurée à l'échelle de l'échantillon et celui des essais de puits. Cette différence doit être soigneusement examinée lors de la définition des valeurs des perméabilités dans les mailles numériques. Un bon ajustement de la perméabilité en respectant le volume des cellules est nécessaire avant que les valeurs des mailles numériques soient représentatives. Tout comme pour la perméabilité, l'effet de support influe également sur les valeurs de porosité déduites de mesures sur échantillon et diagraphies.

## 1.2 Hétérogénéité et données de gisement

Dans une étude de réservoir, deux types de données sont généralement disponibles : les “données statiques”, souvent collectées avant la production et les “données dynamiques”, acquises au cours de la production et qui changent avec le temps. Les données statiques mesurées à certains endroits fournissent directement des informations sur les propriétés pétrophysiques. Par conséquent, elles varient lorsque le lieu de mesure change. Selon le type de mesure, les données statiques sont affectées par les différentes échelles de l'hétérogénéité. Par exemple, la perméabilité ou la porosité peuvent être obtenues par les mesures faites en laboratoire sur des échantillons extraits d'un puits. Dans ce cas, les propriétés mesurées sont influencées par les hétérogénéités macroscopiques. La perméabilité et la porosité peuvent également être obtenues à partir des données de diagraphie le long d'un puits. Ici, la mesure de ces propriétés est affectée par l'hétérogénéité mégascopique. Les données sismiques mesurées avant la production ou pendant l'étude géologique peuvent être utilisées pour localiser les failles principales. Elles sont influencées par l'hétérogénéité gigascopique. Les données statiques telles que la porosité et la perméabilité présentent toujours des variations spatiales à l'échelle du réservoir. Des analyses statistiques sont effectuées pour décrire ces variations [35, 31]. Les techniques statistiques sont également utilisées pour modéliser les hétérogénéités à l'échelle du pore [50, 17, 2].

Les données dynamiques telles que la pression ou la production sont dépendantes du temps. Elles varient quand le fluide se déplace au moment de la production. Elles sont généralement mesurées dans les puits. Aujourd'hui, les données sismiques sont aussi utilisées pour mesurer les variations de la saturation des hydrocarbures au cours de la production. Selon le type d'écoulement dans le réservoir, les différentes hétérogénéités peuvent induire divers effets. Au moment de la récupération primaire, l'énergie naturelle du réservoir est utilisée. Lorsque l'énergie naturelle est épuisée, le réservoir peut-être être soumis à l'injection d'eau, de  $CO_2$  ou également à celles de surfactants ou polymères. D'après Kelkar et Perez [31], quand l'écoulement devient complexe, l'effet des hétérogénéités à petite échelle augmente. L'hétérogénéité gigascopique a un impact sur la performance globale du réservoir durant la récupération primaire. Lorsque le système d'écoulement se transforme en récupération secondaire, d'autres niveaux d'hétérogénéités peuvent affecter l'écoulement dans le milieu poreux. Les hétérogénéités mégascopique et macroscopique créent des chemins préférentiels. En conséquence, les fluides mouvants empruntent ces chemins, ce qui contribue à réduire

l'efficacité du balayage et la récupération des hydrocarbures. Au cours d'une récupération améliorée, même l'hétérogénéité microscopique peut avoir une incidence sur la production du réservoir. En raison de la complexité des systèmes d'écoulement à ce stade de la récupération, l'hétérogénéité microscopique peut avoir une influence sur la façon dont l'interface entre le fluide injecté et les hydrocarbures est formée et se déplace [31].

### 1.3 Hétérogénéité et modélisation numérique

Comme mentionné précédemment, la modélisation d'un réservoir est la technique la plus sophistiquée pour décrire les diverses propriétés du réservoir sur la base des données disponibles. Le but d'une simulation numérique de réservoir est de prévoir sa performance de la façon la plus précise possible. Les simulateurs commerciaux (ECLIPSE, PumaFlow, etc.) utilisent des schémas numériques afin de simuler l'écoulement des fluides à l'intérieur des réservoirs. Avec cette technique, le réservoir est discrétisé sur un nombre défini de mailles. Dans chaque maille, un bilan matière est obtenu sur la base de la loi de conservation de la masse, de la loi de Darcy [12] et des relations capillaires. Les équations 1.1 à 1.5 décrivent les écoulements polyphasiques dans une maille :

$$\nabla \cdot [\lambda_i(\nabla p_i - \gamma_i \nabla z)] = \frac{\partial}{\partial t} \left[ \frac{\phi S_i}{B_i} \right] + q_i \quad i = o, w \quad (1.1)$$

$$\begin{aligned} \nabla \cdot [R_s \lambda_o(\nabla p_o - \gamma_o \nabla z) + \lambda_g(\nabla p_g - \gamma_g \nabla z)] \\ = \frac{\partial}{\partial t} \left[ \phi \left( \frac{R_s}{B_o} S_o + \frac{S_g}{B_g} \right) \right] + R_s q_o + q_{fg} \end{aligned} \quad (1.2)$$

$$S_o + S_w + S_g = 1 \quad (1.3)$$

$$p_{cow} = p_o - p_w \quad (1.4)$$

$$p_{cog} = p_g - p_o \quad (1.5)$$

La transmissibilité  $\lambda_i$  est définie par  $\lambda_i = \frac{k_{ri}}{\mu_i B_i} k$ ,  $i = o, w, g$  et  $\gamma_i$  est défini par  $\gamma_i = \rho_i \mathbf{g}$ ,  $i = o, w, g$ . Dans cette équation,  $k$  est le tenseur de perméabilité absolue,  $k_{ri}$  est la perméabilité relative de la phase  $i$ ,  $\mu$  est la viscosité,  $\mathbf{g}$  est la gravité,  $\rho$  est la densité,  $z$  est l'axe vertical tourné vers le bas,  $p$  est la pression,  $B_i$  est le facteur de formation de la phase  $i$ ,  $\phi$  est la porosité,  $S$  est la saturation,  $R_s$  est le rapport de production gaz-huile,  $t$  est le temps,  $p_c$  est la pression capillaire et  $q$  est le débit.  $q_{fw}$  est le débit de gaz. Pour plus de détails concernant les techniques de simulation de réservoir, le lecteur est invité à se référer au livre de Aziz et Settari [1].

Comme on peut le constater dans les équations ci-dessus, il est nécessaire de connaître les caractéristiques des roches et des fluides pour simuler les écoulements polyphasiques dans

le réservoir. Les données caractérisant les roches sont directement liées à des techniques de caractérisation de réservoir. Elles incluent [18] :

- |                                  |                             |
|----------------------------------|-----------------------------|
| 1. La profondeur de gisement     | 2. L'épaisseur du gisement  |
| 3. La porosité                   | 4. La perméabilité          |
| 5. La pression capillaire        | 6. La perméabilité relative |
| 7. La saturation en hydrocarbure | 8. La compressibilité       |

Une valeur pour chacun de ces paramètres doit être attribuée à chaque maille du modèle. De toute évidence, avec un maillage fin, la simulation numérique est plus détaillée et plus longue (en termes de temps CPU). Pour réaliser des simulations d'écoulement rapidement, il faut réduire le nombre de mailles. D'une part, l'hétérogénéité du réservoir doit être représentée de façon aussi précise que possible, et d'autre part, le nombre de mailles doit être aussi réduit que possible. Décider de l'importance d'une contrainte par rapport à l'autre est un sujet important, mais qui ne sera pas traité dans cette étude.

Nous rappelons que la perméabilité est l'une des propriétés les plus importantes d'une roche réservoir. Son hétérogénéité peut créer des chemins préférentiels et des barrières qui affectent l'écoulement des hydrocarbures à l'échelle de l'échantillon comme à l'échelle du réservoir.

Les variations de perméabilité dans un gisement peuvent se manifester verticalement comme horizontalement. Une roche stratifiée est un bon exemple d'hétérogénéité du champ de la perméabilité dans le sens vertical. La Figure 1.3 (voir annexe) représente schématiquement un réservoir qui contient trois couches de différentes perméabilités. La quantité d'eau qui entre dans chaque couche est proportionnelle à la perméabilité de cette zone si l'eau injectée a la même mobilité ( $k_{rw}/\mu_w$ ) que l'huile déplacée [51]. Dans ces conditions, l'eau se déplace de préférence dans la couche la plus perméable, laissant derrière elle une énorme quantité d'huile dans les couches les moins perméables. À partir de calculs simples, on peut montrer qu'au moment de la percée de l'eau, environ 30% de l'huile a été produite.

Les variations microscopiques de perméabilité affectent le calcul de la perméabilité relative. Dans les techniques d'analyse d'échantillon (SCA), les perméabilités relatives sont définies dans le cadre d'un système d'équations décrivant l'écoulement immiscible dans les milieux poreux :

$$\vec{v}_i = -\frac{kk_{ri}}{\mu_i}(\nabla p_i - \rho_i \vec{g}) \quad (1.6)$$

$$\frac{\partial \phi \rho_i S_i}{\partial t} = -\nabla \cdot (\rho_i v_i) \quad (1.7)$$

$v_i$  est la vitesse de Darcy de la phase  $i$ . Les perméabilités relatives sont déterminées à partir d'expériences impliquant des déplacements immiscibles instables. Pour un système diphasique, l'échantillon est typiquement soumis à une injection d'eau. Les fluides en place sont soit de l'huile soit du gaz. Si l'on suppose que : 1) le milieu poreux est homogène, 2) l'écoulement est monophasique et incompressible, et 3) les forces capillaires et la gravité sont négligeables, ce système d'équations peut être explicitement résolu et les perméabilités

relatives directement calculées à partir des données de production et de pression [10]. Plusieurs auteurs ont convenu que les données obtenues à partir de l'analyse d'échantillons sont généralement influencées par les pressions capillaires et l'hétérogénéité, et donc, que les hypothèses ci-dessus sont fréquemment erronées [54, 65, 44, 22]. Estimer la perméabilité relative tout en considérant l'hétérogénéité à petite échelle peut avoir un impact immédiat sur la performance du gisement [65].

## 1.4 Hétérogénéité et géostatistique

L'un des principaux objectifs de la caractérisation du réservoir est de décrire sa géologie de façon réaliste. Il est clairement impossible d'obtenir une image détaillée du réservoir à partir d'un petit nombre de données de puits et de données sismiques. Les gisements sont hétérogènes en ce sens que, les perméabilités mesurées sur les échantillons extraits d'un puits peuvent varier. Ainsi, remplir un maillage numérique de réservoir avec la perméabilité et la porosité n'est pas une tâche facile en raison du peu de données disponibles. Aujourd'hui, une description stochastique du réservoir est préférée par les ingénieurs de réservoir et les géologues. Issues des techniques statistiques, différentes images du réservoir sont créées sur la base des informations obtenues à partir des puits. Plusieurs images (ou réalisations) du réservoir, contenant des millions de mailles, peuvent être générées en respectant les données statiques recueillies dans les puits et les études sismiques. Des détails sur les méthodes de génération de ces images peuvent être trouvés dans des monographies spécialisées [31, 35]. La géostatistique se sert du fait que, pour de nombreux phénomènes naturels, les valeurs pour une même variable en 2 points séparés par une petite distance sont similaires. Quand la distance entre ces variables augmente, la différence entre leurs valeurs s'accroît [31]. Compte tenu de ce fait, la géostatistique détecte la relation spatiale entre les données statiques. Comme ce nombre de données est insuffisant au sein du réservoir, la géostatistique est utilisée pour construire le modèle même dans les zones où on n'a aucune mesure. Dans ce cas, les techniques géostatistiques génèrent des images approximatives des réservoirs en respectant leurs modèles de variabilité. Ces modèles sont finement maillés. Comme la simulation numérique pour un modèle fin est coûteuse et longue, le nombre de mailles doit être réduit, d'où le recours à une étape de mise à l'échelle (upscaling) permettant de réduire le temps calcul. Une simulation numérique d'écoulement est effectuée sur le modèle préalablement mis à l'échelle et les données dynamiques mesurées sont comparées aux résultats de cette simulation. De toute évidence, les modèles géologiques doivent être modifiés afin de fournir des résultats dynamiques similaires à celui du réservoir. Cette procédure de modification connue sous le nom de "calage d'historique" implique des techniques d'optimisation.

## 1.5 Objectifs de la thèse

L'objet principal de cette thèse est d'améliorer l'interprétation des expériences de laboratoire menées sur des échantillons naturellement hétérogènes. Comme il a été indiqué précédemment, l'interprétation des mesures pétrophysiques telles que les perméabilités relatives s'appuie sur une hypothèse d'homogénéité qui n'est pas toujours fondée.

À l'échelle du réservoir, de nombreuses approches ont été développées dans le cadre du calage d'historique afin de caractériser l'hétérogénéité des champs de perméabilité. Elles font intervenir des techniques relevant de la géostatistique et de l'optimisation. L'objectif sera donc de tirer avantage de ces techniques pour caractériser l'hétérogénéité du champ de perméabilité à l'échelle de l'échantillon. Les sujets suivants sont pris en compte.

**Expériences en laboratoire.** Des expériences d'injection miscibles visqueuses sous scanner sont réalisées sur des échantillons ayant différents degrés d'hétérogénéité. L'analyse des données scanner fournit une carte 3D de la porosité et des cartes 3D de la concentration pour différents temps. En outre, l'évolution de la pression différentielle (entrée-sortie) est mesurée alors que le débit est constant. Ces données détaillées sont complétées par la panoplie standard des mesures de caractérisation réalisées en pétrophysique.

**Caractérisation 1D de la perméabilité à l'échelle échantillon.** Nous étudions l'évolution de la pression en fonction du temps. Un profil 1D de perméabilité absolue le long de l'échantillon est estimé en utilisant les données de pression différentielle mesurées au cours du test de déplacement miscible visqueux. On suppose que l'échantillon est constitué d'un nombre infini de tranches perpendiculaires à la direction d'écoulement. Ainsi, nous déterminons une valeur de perméabilité pour chaque section. Des expériences numériques comme des expériences en laboratoire sont effectuées pour valider la méthodologie. Des écoulements numériques sont effectués pour des modèles représentant des échantillons pour obtenir les données de pression différentielle. Ces modèles sont constitués de blocs de perméabilité différente. En outre, l'injection miscible visqueuse a été faite à débit imposé sur des échantillons très perméables et peu perméables. Des mesures de CT scan sont réalisées pour examiner la dispersion dans le milieu poreux et observer l'évolution de la position de l'interface entre les deux fluides en fonction du temps.

**Caractérisation 3D de la perméabilité à l'échelle de l'échantillon.** Enfin, nous nous concentrons sur la distribution 3D de la perméabilité dans les échantillons. Une modèle 3D est construit et des valeurs de porosité et perméabilité sont attribuées à chaque maille. Ces champs de porosité et de perméabilité sont hétérogènes à l'échelle de l'échantillon, mais homogène à l'échelle de la maille. Pour déterminer un modèle de perméabilité qui valide l'ensemble des données disponibles, on utilise une procédure d'optimisation. En substance, on génère un modèle de perméabilité initial qui accommode les données statiques. Puis, ce modèle est modifié successivement jusqu'à ce qu'il vérifie aussi les données dynamiques.

L'annexe jointe à ce document donne de plus amples détails sur les travaux développés au cours de cette thèse.



# Chapitre 2

## Etat de l'art

Les roches réservoir ont différentes propriétés, l'une des plus importantes étant la perméabilité. Les variations de perméabilité au sein des roches influencent très fortement la façon dont les fluides s'y écoulent. Une modélisation réaliste des milieux poreux doit rendre compte de ces variations de perméabilité. Pour ce faire, les hétérogénéités de perméabilité doivent être caractérisées à l'échelle du milieu poreux que l'on souhaite modéliser [50]. Ce chapitre rappelle différents travaux réalisés pour caractériser l'hétérogénéité de la répartition des perméabilités dans l'espace. Les méthodes présentées traitent de l'hétérogénéité suivant trois échelles fondamentales : l'échelle du pore, l'échelle de la carotte et l'échelle du réservoir. Le chapitre est organisé en deux sections : la première se concentre sur l'hétérogénéité à l'échelle du réservoir et la deuxième sur l'hétérogénéité à l'échelle du pore et de la carotte.

### 2.1 Caractérisation à l'échelle du réservoir

Une méthode classique de caractérisation de l'hétérogénéité de la perméabilité à l'échelle du réservoir a été introduite par Matthews et Russell [38]. Elle a ensuite été reprise et améliorée par Bourdet *et al.* [9]. Cette méthode, très utilisée pour l'analyse des essais de puits, permet d'estimer la perméabilité moyenne de la formation à l'échelle de la distance inter-puits. Elle repose sur l'inversion des données de pression mesurées au fond des puits, l'écoulement étant monophasique. Un essai de puits consiste à modifier le débit d'injection ou de production dans un puits et à suivre les variations de pression en résultant en fonction du temps. Ces variations et leurs dérivées par rapport au temps sont ensuite reportées sur un graphe log-log et comparées à des courbes de référence. Une courbe de référence correspond à une représentation analytique de la réponse en pression pour un puits et un réservoir donnés. La perméabilité moyenne de la formation est donnée par la courbe type qui reproduit le mieux l'évolution de la pression et de sa dérivée.

Feitosa *et al.* [20] ont introduit un nouvel algorithme de caractérisation qui donne la perméa-

bilité du réservoir en fonction de la distance par rapport au puits. Les données considérées sont à nouveau les variations de pression enregistrées pendant un essai de puits. Feitosa *et al.* [20] ont montré que si le profil de perméabilité ainsi obtenu est lisse, il peut être considéré comme précis. Lorsque le profil de perméabilité présente de brusques variations, il est considéré comme approché, bien que la tendance moyenne soit correcte.

Kaczmaryk et Delay [29] ont utilisé des tests d'interférence pour caractériser les propriétés hydrauliques d'un aquifère calcaire fracturé. Dans ce cas, l'aquifère est modélisé par un double milieu et une procédure d'inversion est mise en place pour caler les données mesurées par la réponse du modèle. Kaczmaryk et Delay [29] ont ainsi mis en évidence que la perméabilité de fracture est à peu près constante à l'échelle de l'aquifère (200 m). Ce résultat a été confirmé par Bernard *et al.* [6] à partir de tests d'interférence différents. La perméabilité de fracture s'homogénéise sur des distances de l'ordre de 100 – 200 m.

A ce jour, la plupart des techniques de caractérisation de la perméabilité à l'échelle du réservoir font appel à des méthodes d'optimisation. La perméabilité et la porosité dans le réservoir sont inconnues, sauf au niveau des puits. Des outils géostatistiques sont alors appliqués pour générer un modèle initial représentatif du réservoir. Ce premier modèle vérifie les données statiques, mais pas le comportement dynamique du réservoir. Les données statiques ne varient pas au cours du temps à cause des écoulements de fluide; il s'agit par exemple d'une mesure de perméabilité faite sur une carotte prélevée dans un puits. Au contraire, les données dynamiques évoluent tout au long de la vie du réservoir; il s'agit par exemple de débits d'huile mesurés dans un puits. Les écoulements de fluide sont ensuite simulés pour le modèle de réservoir initial. Si les réponses numériques ainsi obtenues diffèrent des données dynamiques collectées sur le terrain, un processus itératif de modification des paramètres du modèle de réservoir est mis en place jusqu'à ce qu'un calage acceptable soit atteint. La résolution de ce problème de calage fait intervenir des méthodes d'optimisation dont l'objectif est de minimiser la fonction mesurant l'écart entre les données dynamiques et les réponses numériques correspondantes. Les valeurs de perméabilité étant inconnues dans le réservoir, excepté dans les puits, le nombre de paramètres à gérer est très important : un modèle de réservoir peut contenir plusieurs millions de mailles, ce qui donne donc autant de paramètres. Cette difficulté a motivé le développement de techniques de paramétrage géostatistiques, notamment la méthode des points pilotes (Marsily [14]) ou la méthode de déformation graduelle (Hu [27]). Ces techniques permettent de modifier l'ensemble des propriétés pétrophysiques habillant le modèle de réservoir à partir d'un nombre limité de paramètres.

## 2.2 Caractérisation à l'échelle de la carotte et du pore

De nombreux travaux de recherche ont été entrepris dans le domaine de la modélisation des milieux poreux à l'échelle macroscopique. Ces modèles sont suffisamment simples pour

permettre des simulations d'écoulement en un temps acceptable, tout en intégrant les caractéristiques essentielles des milieux poreux [50, 5]. Des présentations détaillées des différents types de modèles (modèles périodiques, réseaux de Bethe, modèles de réseaux, modèles continus...) ont été faites, entre autres, par Sahimi [50] et Dullien [18].

On recourt aux modèles de réseaux pour prédire les écoulements de fluide dans l'espace poreux depuis de nombreuses années. Ces réseaux, souvent cubiques, sont formés par exemple d'un assemblage de tubes et de sphères. Les modèles de réseaux sont aujourd'hui beaucoup employés dans le domaine du pétrole pour faire le lien entre les écoulements macroscopiques et la physique des écoulements à l'échelle du pore. Ils permettent de mieux comprendre l'influence de l'hétérogénéité à l'échelle du pore sur la dispersion, les perméabilités relatives, les pressions capillaires (Laroche and Vizika [33], Dijeljic et Blunt [7], Blunt et King [8], Xu *et al.* [62])...

Les scanners fournissent des coupes 2D permettant de visualiser, avec une résolution de l'ordre de quelques microns, la topologie de l'espace poreux dans les échantillons de roche [17]. Plusieurs méthodes ont été proposées pour construire des images 3D de l'espace poreux à partir des images 2D obtenues sous scanner. Toutes ces méthodes utilisent les propriétés statistiques du milieu poreux déduites de l'analyse des images 2D disponibles. Bakke et Oren [2] ont eu recours à des méthodes stochastiques de simulation objet pour analyser la distribution des tailles de grains sur les coupes 2D. Ils ont ensuite modélisé des assemblage 3D de sphères dont les tailles respectaient la loi de distribution déterminée au préalable. En intégrant en outre différents schémas d'altération comme la cimentation ou le dépôt de particules argileuses, Bakke et Oren [2] ont obtenu une représentation plus réaliste des roches sédimentaires.

De même, Kameda [30] a sélectionné des échantillons de grès naturels et artificiels et collecté des images 2D à partir d'un scanner pour chacun des échantillons. Puis, il a généré des modèles 3D du milieu poreux à partir de techniques de simulation de type pixel. Kameda [30] a montré que les porosités et longueurs de corrélation déduites de l'analyse des images 2D doivent être prises en compte simultanément pour simuler un réseau 3D respectant la forme et la taille des pores et grains. L'écoulement des fluides a été simulé pour chacun des modèles, ce qui a conduit à l'estimation de leur perméabilité équivalente. La représentation des perméabilités en fonction de la porosité a alors permis de dégager une tendance utilisable pour déduire la perméabilité de la porosité.

Okabe et Blunt [45] ont procédé suivant un schéma analogue, mais ont préféré appliquer une méthode stochastique de simulation multi-points pour générer le modèle 3D. La statistique multi-point est apprise au préalable sur une image d'entraînement qui correspond ici aux coupes 2D collectées sous scanner. Okabe et Blunt [45] ont montré que ce type de modélisation rendait mieux compte de la connectivité des pores.

Le modélisation macroscopique des milieux poreux n'est pas l'unique méthode de caractérisation des milieux poreux. Il existe de nombreuses techniques utilisées en routine pour caractériser les échantillons de roche. L'amélioration de ces techniques a permis de mieux identifier les hétérogénéités à petite échelle et de mieux comprendre leur impact sur la production des hydrocarbures dans les réservoirs. Baraka-Lokmane *et al.* [3] ont utilisé par exemple les acquisitions scanner, la résonance magnétique (MRI), l'analyse de sections fines, etc, pour caractériser des échantillons de grès avec des tailles de grains, des porosités et des minéralogies différentes. Ils ont montré la cohérence de l'ensemble des mesures et souligné la valeur ajoutée de l'analyse de l'ensemble de ces mesures en termes de description des propriétés d'écoulement.

Louis *et al.* [37] ont examiné des sections fines issues d'un échantillon de grès des Vosges. Leur analyse a permis de déterminer la taille des grains et l'orientation des pores. L'anisotropie de l'espace poreux a ensuite été précisée par des mesures de susceptibilité magnétique (AMS). Louis *et al.* [37] disposaient aussi d'images scanner. La comparaison de ces différentes données leur a permis de distinguer deux zones dans l'échantillon : une zone peu compactée et une zone compactée de porosité deux fois moindre que celle de la zone peu compactée. Louis *et al.* [37] ont montré que les perméabilités de ces zones, déduites de l'équation de Kozeny-Carman, vérifiaient les mesures de perméabilité réalisées en laboratoire. Ces travaux ont mis en évidence le fait que les données microstructurales contribuent à une meilleure caractérisation des variations de perméabilité à l'échelle de l'échantillon. Cette conclusion a été confirmée par Ménendez *et al.* [39] qui ont analysé des milieux granulaires créés artificiellement.

Zweers *et al.* [65] ont mentionné que l'hétérogénéité à l'échelle de l'échantillon peut être ignorée si la taille des hétérogénéités dans le réservoir est soit beaucoup plus grande, soit beaucoup plus petite que l'échelle des échantillons de roche. Le problème de la prise en compte de l'hétérogénéité à l'échelle de l'échantillon devient fondamental lorsque les hétérogénéités dans le réservoir se manifestent à l'échelle de l'échantillon. Durant les dernières années, de nombreux travaux, à la fois théoriques et pratiques, ont été consacrés à l'identification de la distribution des perméabilités à l'intérieur d'un échantillon de roche. Withjack [60] a souligné très tôt l'intérêt potentiel des mesures scanner pour l'analyse de carottes. Withjack *et al.* [61] ont ensuite déterminé les champs de perméabilité à l'intérieur d'échantillons de roche à partir des cartes 3D de porosité mesurées par scanner. Pour ce faire, ils ont supposé que l'écoulement était associé à un faisceau de tubes de courant, les propriétés de ces tubes étant constantes tout le long des tubes. Ces auteurs ont pu alors montrer que les variations locales de perméabilité affectent fortement la dispersion et la forme du profil de saturation.

Plus récemment, Olivier *et al.* [46] ont employé une technique de corrélation analogue à celle de Withjack [60] et ont mis en évidence l'influence de l'hétérogénéité à petite échelle

sur les mesures de perméabilités relatives. Ils ont effectué des tests d'imbibition en régime permanents et transitoire sur des échantillons de carbonates vacuolaires. En utilisant les estimations de porosité déduites des mesures de scanner, ces auteurs ont construit des modèles 3D représentant la répartition des vacuoles et de la matrice dans les échantillons. Ils ont montré que les courbes de perméabilités relatives déduites de ces modèles avaient plus de sens que celles obtenues à partir du modèle homogène unidimensionnel, généralement employé. Olivier *et al.* [46] ont aussi mis en avant le bénéfice des techniques d'imagerie dans la compréhension des déplacements de fluide dans le milieu poreux à l'échelle du millimètre.

Hamon et Roy [26] listent différentes méthodes expérimentales utilisées pour caractériser l'hétérogénéité de la perméabilité à l'échelle de l'échantillon (par exemple, tests de traceurs, miniperméamètres, scanner). Ils ont montré que la plupart de ces méthodes contribuent effectivement à la caractérisation des hétérogénéités perpendiculaires à la direction d'écoulement. Ils ont en outre souligné que les écoulements en régime transitoire sont très sensibles aux hétérogénéités de perméabilité parallèle à la direction d'écoulement lorsque les forces capillaires sont négligeables.

Moctezuma *et al.* [41] ont déduit de mesures scanner une carte 3D de la porosité d'un échantillon. Ils ont aussi fait des tests de traceurs et déterminé des profils de dispersion. Après avoir défini un seuil de porosité, ces auteurs ont considéré que les valeurs de porosité supérieures à ce seuil correspondaient à des vacuoles de très forte perméabilité tandis que les valeurs inférieures étaient associées à une matrice de très faible perméabilité. Finalement, Moctezuma *et al.* [41] ont observé que les profils de dispersion pouvaient être reproduits numériquement en ajustant le rapport de la perméabilité des vacuoles sur la perméabilité de la matrice.

L'utilisation des tests de traceurs pour caractériser l'hétérogénéité des milieux poreux a aussi été prônée par Fourar [22] qui a proposé d'approcher le milieu hétérogène par un milieu équivalent stratifié. Le flux de traceurs dans un milieu stratifié peut se formuler analytiquement en fonction de la distance et du temps. La relation en résultant dépend d'un paramètre  $H$ , dit facteur d'hétérogénéité, qui quantifie le degré d'hétérogénéité du milieu stratifié. Fourar [22] a développé une relation empirique explicitant ce paramètre et montré qu'il décroît avec la distance mesurée à partir de la face d'injection dans l'échantillon.

Dauba *et al.* [13] ont montré que les échantillons présentant des hétérogénéités longitudinales peuvent se caractériser à l'aide de profils de concentration enregistrés sous scanner lors de d'expériences déplacement miscible. Ces auteurs ont ensuite modélisé les échantillons à partir d'un modèle avec deux zones de mobilité. Les contrastes des perméabilités et des fractions volumiques des deux zones ont été calés en exécutant des procédures de calage d'historique. Dauba *et al.* [13] ont conclu que leur modèle hétérogène rend mieux compte des perméabilités relatives que le modèle homogène unidimensionnel utilisé en général.

Une alternative pour établir des cartes 3D de la perméabilité dans les échantillons s'appuie sur l'analyse des temps d'arrivée mesurés pour un test de traceurs. Si la position du front est connue à différents temps, la méthode des temps d'arrivée fournit la répartition spatiale des perméabilités dans l'échantillon [61]. Cette méthode bénéficie du fait que l'inversion des données est directe et non itérative comme dans les processus de calage d'historique. Cette approche a été beaucoup appliquée par Zhan et Yortsos [63] qui ont mis sa validité en évidence dans le cas où les contrastes de perméabilité sont faibles à modérés et où le champ de perméabilité affiche une corrélation spatiale. On peut toutefois lui reprocher de n'avoir été validée que sur des cas synthétiques.

Watson *et al.* [59] ont développé une technique de détection d'hétérogénéité qui est basé sur un test de déplacement immiscible : la pression différentielle au travers de l'échantillon est enregistrée pendant l'expérience de déplacement immiscible. La pression capillaire, la compressibilité et la gravité sont négligées. Dans ces conditions, Watson *et al.* [59] ont montré que pour un débit constant, la pression différentielle est linéaire en fonction du temps pourvu que l'échantillon soit homogène. Ils ont aussi mentionné que le début de la zone où il y a rupture de l'homogénéité peut être identifiée. Ce test de détection a été validé à la fois par des expériences synthétiques et des expériences en laboratoire. Fincham et Gouth [21] ont utilisé la même technique pour mesurer les perméabilités relatives à l'huile dans des échantillons peu consolidés et saturés par une saumure de faible viscosité. Les changements de pente de la courbe donnant la pression différentielle permettent d'identifier différents domaines de perméabilité le long de la direction d'écoulement.

# Chapitre 3

## Caractérisation unidimensionnelle de l'hétérogénéité de la perméabilité

### 3.1 Introduction

Nous cherchons à ce stade à développer une approche physique pour estimer le profil de perméabilité dans l'échantillon, le long de la direction d'écoulement, sans passer par une méthode itérative de calage. La première section introduit la méthodologie proposée pour déterminer le profil de perméabilité. Les sections qui suivent sont consacrées à la validation de la méthode tant à partir d'expériences numériques que d'expériences menées en laboratoire.

### 3.2 Description de la méthodologie

La méthodologie présentée ci-dessous s'inspire des travaux de Fincham et Gouth [21] (voir chapitre précédent). Toutefois, nous nous concentrons ici sur la caractérisation des perméabilités absolues plutôt que des perméabilités relatives.

Nous considérons un échantillon initialement saturé par un fluide de faible viscosité dans lequel nous injectons un fluide de forte viscosité. Les deux fluides sont supposés incompressibles et la température uniforme et constante (*i.e.*, la porosité, les densités et viscosités sont constantes). Le fluide très visqueux est injecté à l'une des extrémités libres de l'échantillon ( $x = 0$ ) à débit constant. Le fluide produit est collecté à l'autre extrémité de l'échantillon ( $x = L$ ) à pression atmosphérique. La pression différentielle au travers de l'échantillon est enregistrée au cours du temps. Nous faisons les hypothèses suivantes.

1. Le déplacement de fluide est dominé par les forces visqueuses. Les fluides en présence sont miscibles : il n'y a pas d'effet de capillarité.
2. Le front est de type piston (à cause du rapport de viscosité élevé).
3. Les perméabilités absolues de l'échantillon pour le fluide injecté ou le fluide déplacé

sont identiques.

Pour un écoulement unidimensionnel d'une unique phase fluide dans le milieu poreux, la loi de Darcy [12] conduit à :

$$Q = -\frac{kAr}{\mu} \frac{dp}{dx} \quad (3.1)$$

où  $Q$  est le débit,  $Ar$  la surface d'une section de l'échantillon perpendiculaire à la direction d'écoulement,  $\mu$  la viscosité du fluide injecté,  $p$  la pression. L'écoulement se fait suivant l'axe  $X$ .  $k$  est la perméabilité absolue de l'échantillon. La loi de Darcy stipule que pour un échantillon de roche strictement homogène, la relation entre le débit et la pression différentielle est linéaire. La pente de cette droite donne la perméabilité  $k$ . Le déplacement visqueux considéré ici est transitoire, ce qui signifie que la pression différentielle au travers de l'échantillon est une fonction du temps. L'intégrale de l'équation ci-dessus par rapport à la position  $x$  s'écrit :

$$\Delta p(t) = \int_0^x \frac{-Q\mu}{Ark(x)} dx \quad (3.2)$$

Dans cette équation, la perméabilité  $k$  est la seule variable dépendant de la position  $x$ . Si on suppose que le déplacement est de type piston, alors la pression différentielle au travers de l'échantillon peut s'écrire comme la somme de deux termes : la chute de pression dans le fluide injecté (fluide très visqueux) et la chute de pression dans le fluide déplacé (fluide peu visqueux) :

$$\Delta p_{inlet-outlet} = \Delta p(t) = \Delta p_{inlet-front} + \Delta p_{front-outlet} \quad (3.3)$$

On réécrit alors l'équation 3.2, d'une part, pour le fluide injecté et d'autre part, pour le fluide déplacé. Puis, ces équations sont incorporées dans l'équation 3.3 :

$$\Delta p(t) = \int_0^{x_f} \frac{-Q\mu_{invading}}{Ark(x)} dx + \int_{x_f}^L \frac{-Q\mu_{defending}}{Ark(x)} dx \quad (3.4)$$

$x_f$  indique la position du front.  $\mu_{invading}$  et  $\mu_{defending}$  sont les viscosités des fluides injecté et déplacé, respectivement. La théorie de Buckley-Leverett [10] donne la relation suivante entre la position du front et le temps :

$$x_f = \frac{Q}{Ar\phi} t \quad (3.5)$$

$\phi$  est la porosité. Comme précisé plus haut, la perméabilité absolue est fonction de la position du front. Si on se réfère à l'équation 3.5, elle dépend aussi du temps. On dérive à présent l'équation 3.4 par rapport au temps :

$$\frac{\partial \Delta p(t)}{\partial t} = \frac{-Q}{Ar\phi} \left( \frac{Q\mu_{invading}}{Ark(x_f)} - \frac{Q\mu_{defending}}{Ark(x_f)} \right) \quad (3.6)$$



On obtient finalement l'expression suivante pour la perméabilité au niveau du front :

$$k(x_f) = k = \frac{Q^2(\mu_{invading} - \mu_{defending})}{-Ar^2\phi\frac{\partial\Delta p(t)}{\partial t}} \quad (3.7)$$

Cette relation permet d'estimer la perméabilité le long de l'échantillon traversé par le front. Comme la position du front est une fonction du temps, on peut relier la perméabilité au temps d'injection.

### 3.3 Echantillons de roche et modèles numériques

#### 3.3.1 Echantillons de roche

En laboratoire, il est commun de construire des échantillons de roches composites en mettant bout à bout de petits échantillons. De cette façon, on contrôle mieux les variations de perméabilité le long de l'échantillon et les limites entre les différentes zones de mobilité [26]. On peut accoler des échantillons de faible perméabilité à des échantillons de forte perméabilité, ce qui induit des contrastes de perméabilité très forts.

Pour cette étude, nous avons sélectionné :

- Deux échantillons composites élaborés chacun en accolant quatre échantillons de roche : composite 1 et composite 2 ;
- Trois échantillons hétérogènes, dont l'hétérogénéité s'exprime à une échelle supérieure à celle du pore : un échantillon de calcaire de faible perméabilité, un échantillon de calcaire très perméable qui a été altéré par acidification et un grès à gros grains, friable, contenant beaucoup de mica et d'argile. On notera que ce troisième échantillon est traversé en son milieu par une couche de nature non identifiée.

Les propriétés pétrophysiques de ces 5 échantillons sont listées dans le tableau 3.2 (voir annexe).

Pour construire les échantillons composites, nous avons considéré plusieurs échantillons de grès et calcaire, de diamètre 38 *mm* et de longueur variable allant jusque 80 *mm*. Nous avons conservé uniquement ceux qui étaient homogènes, c'est à dire ceux dont les profils d'adsorption déterminés sous scanner étaient plus ou moins constants suivant l'axe *X*. Huit échantillons ont finalement été retenus et ont été regroupés par quatre pour créer les deux échantillons composites. Les propriétés pétrophysiques de chacun de ces 8 petits échantillons sont reportées dans le tableau 3.3 (voir annexe).

#### 3.3.2 Modèles numériques

En parallèle, nous avons élaboré deux modèles numériques, c'est à dire des grilles 3D habillées en propriétés pétrophysiques (porosité et perméabilité), qui représentent les composites 1 et 2. Ces deux modèles sont référencés sous les noms modèle 1 et modèle 2. Ces

modèles contiennent chacun  $78 \times 40 \times 40$  mailles. Les dimensions de la grille sont précisées dans le tableau 4.1 (voir annexe). Les 4 petits échantillons formant les composites deviennent ici 4 blocs. Pour chaque bloc, on suppose la porosité constante et égale à la porosité mesurée sur les petits échantillons. Par contre, la perméabilité est supposée hétérogène et est générée aléatoirement à partir de l'algorithme FFTMA [34]. La longueur caractéristique de l'hétérogénéité étant inférieure à la taille du bloc, la perméabilité est statistiquement homogène ce qui permet l'émergence d'une perméabilité moyenne ou effective par bloc. La perméabilité moyenne des blocs correspond aux perméabilités effectives mesurées pour chacun des petits échantillons.

## 3.4 Validation numérique

Nous simulons ici des expériences d'écoulement sur les modèles numériques (modèle 1 et modèle 2). L'objectif est de valider numériquement la méthodologie proposée. Les simulations d'écoulement sont réalisées à l'aide du simulateur de lignes de courant 3DSL (StreamSim Technology, Inc.). Ce simulateur est très rapide comparé aux simulateurs de type différences finies et est moins pénalisé par la dispersion numérique [4].

On simule d'abord des déplacements immiscibles en ignorant la diffusion moléculaire et la saturation irréductible en eau. Ensuite, on simule des déplacement miscibles pour appréhender l'importance de la diffusion moléculaire et son impact sur la détermination du profil de perméabilité le long de l'échantillon. Les périodes d'injection varient entre 50 et 72 minutes, suivant les volumes poreux. Nous considérons des conditions reproduisant celles des expériences effectuées en laboratoire et choisissons des courbes de perméabilités relatives ( $k_r$ ) en croix de façon à obtenir un déplacement de type piston. Les conditions sont :

- Des  $k_r$  en croix avec des points limites valant 1 ( $k_{rw} = S_w$  et  $k_{ro} = 1 - S_w$  : on a donc  $k_{rw} + k_{ro} = 1$  pour toute valeur de  $S_w$ ) ;
- Un rapport de viscosité très favorable ;
- Pas de pression capillaire.

Les simulations d'écoulement fournissent en sortie l'évolution de la la pression différentielle en fonction du temps.

### 3.4.1 Calcul des dérivées

Pour estimer le profil de perméabilité, nous devons déterminer la dérivée par rapport au temps de la la pression différentielle (équation 3.7). Pour ce faire, nous procédons numériquement. Il apparaît alors que la dérivée présente beaucoup de petites fluctuations. Pour les éliminer ou au moins réduire leur impact sur nos calculs, nous augmentons l'intervalle de temps entre 2 points de  $\Delta p$ .

### 3.4.2 Déplacement immiscible

Le rapport de viscosité est fixé à 60. Les effets de la gravité sont ignorés et le nombre de temps pour lesquels on calcule  $\Delta p(t)$  est fixé à 200. La simulation montre qu'au cours de l'injection, le fluide injecté envahit les blocs l'un après l'autre. La réponse simulée pour la pression différentielle montre clairement l'existence de quatre blocs dans les modèles (Figure 4.11, voir annexe). L'application de la méthodologie proposée dans la section 3.2 permet ensuite d'obtenir le profil de perméabilité le long des modèles. Ces estimations sont comparées aux perméabilités moyennes des blocs sur la Figure 4.13 (voir annexe). Pour le modèle 1, l'accord entre les perméabilités estimées et les perméabilités moyennes des blocs est très bon. Pour le modèle 2, la perméabilité du troisième bloc est légèrement surestimée. Ce comportement est lié au fait que  $\Delta p(t)$  est inversement proportionnel à la perméabilité : les variations de  $\Delta p(t)$  sont moins sensibles aux fortes perméabilités.

### 3.4.3 Déplacement miscible

Nous simulons aussi des déplacements miscibles pour apprécier l'influence de la miscibilité sur la pression différentielle. Quand deux fluides miscibles sont mis en contact, ils sont initialement séparés par un front net. Au bout d'un certain temps, une zone de transition se développe à l'interface dans laquelle les fluides diffusent l'un dans l'autre [50]. Dans notre cas, la zone de transition se développe très lentement à cause du rapport élevé des viscosités. On suppose que 10% de la phase déplaçante diffuse dans la phase déplacée. La viscosité de la zone de transition est alors calculée à partir d'une loi de mélange en puissance  $\frac{1}{4}$  [4].

Une expérience de type miscible est simulée pour les deux modèles numériques avec les mêmes conditions d'écoulement que pour le cas immiscible. Les pression différentielle simulées (Figure 4.14, voir annexe) apparaissent plus lisses que dans le cas immiscible. Toutefois, le front reste raide (Figure 4.16, voir annexe) et l'effet de la miscibilité est négligeable (Figure 4.15, voir annexe). Le profil de perméabilité estimé sous-estime légèrement les perméabilités du modèle 1. La perméabilité du troisième bloc du modèle 2 est à nouveau surestimée. Globalement, l'accord entre les profils de perméabilité et les perméabilités moyennes des blocs est très correct.

## 3.5 Validation expérimentale

Le matériel expérimental permet de faire des expériences d'écoulement en régime permanent et transitoire sur des échantillons consolidés soumis à des conditions de pression et température ambiantes. Des capteurs permettent de mesurer la pression différentielle du temps. Des images sont acquises sous scanner à différents temps pour visualiser les déplacements de fluide.

Les deux échantillons composites et les trois échantillons hétérogènes (section 3.3.1) sont soumis à la procédure suivante.

1. Les propriétés physiques et pétrophysiques (longueur, diamètre, poids, porosité et perméabilité absolue) sont mesurées avant toute expérience.
2. Une expérience de déplacement visqueux miscible est réalisée et l'évolution de la pression différentielle au cours du temps est enregistrée. Si nécessaire, une seconde expérience de déplacement visqueux miscible est réalisée, mais en injectant cette fois le fluide très visqueux à l'autre extrémité de l'échantillon.
3. Des cartes 3D de concentration sont acquises à différents temps pour certains échantillons suivant la disponibilité du scanner.

### Echantillons composites

Les deux échantillons composites sont initialement saturés à température ambiante par une saumure contenant 30 g de NaCl par litre. La pression initiale est uniforme et supposée égale à  $10^5$  Pa. Les échantillons sont placés dans des gaines afin d'assurer un écoulement linéaire avec des conditions aux limites dites de type "perméamètre". Pour tout déplacement miscible stable, la convection devrait contrôler la dispersion. Des tests de traceurs sont souvent mis en oeuvre pour déterminer des débits d'injection appropriés. Cependant, Fourar *et al.* [23] ont montré que pour des échantillons hétérogènes, les profils de concentration ne dépendent pas des débits (la convection domine la dispersion) et la diffusion moléculaire peut être ignorée. Nous avons réalisé nos expériences avec des débits correspondant aux débits optimaux permis par les instruments de mesure (gaine et capteurs de pression). Le fluide injecté est une glycérine de viscosité 60 cp. Le débit d'injection est constant et vaut 15 cc/h. On enregistre l'évolution de la pression différentielle au travers de l'échantillon jusqu'à ce qu'elle se stabilise.

L'une des hypothèses de base de la méthodologie développée dans cette étude est que le front est de type piston pendant le déplacement des fluides. Pour vérifier la pertinence de cette hypothèse, des cartes 3D de concentration sont acquises sous scanner pour le composite 2 à différents temps. Ces mesures (Figure 4.17, voir annexe) confirment que le front est assez stable et que l'hypothèse relative à sa forme est raisonnable.

Les profils de perméabilité déduits des pressions enregistrées à l'aide de l'équation 3.7 sont comparés aux perméabilités des différents échantillons utilisés pour créer les composites sur la Figure 4.18 (voir annexe). L'accord n'est pas aussi bon que ce qui a été mis en évidence dans les tests de validation numériques. Toutefois, les profils de perméabilité estimés suivent les variations de perméabilité des petits échantillons mis bout à bout.

Les points suivants méritent d'être discutés.

1. Tout d'abord, on produit toujours de la saumure de faible viscosité après observation de la percée de la glycérine, ce qui entraîne une augmentation de  $\Delta p(t)$ . La courbe

$\Delta p(t)$  est donc remise à l'échelle pour préserver la cohérence vis à vis des perméabilités effectives mesurées pour les échantillons composites. Le temps d'injection n'affecte pas les perméabilités calculées, mais il doit aussi être cohérent au regard du temps de balayage théorique. L'équation 3.8 est utilisée pour corriger les données enregistrées.

$$\begin{aligned}\Delta p_{scaled} &= \Delta p_{recorded} \times \frac{\Delta p_{theoretical} (PVI = 1)}{\Delta p_{recorded} (PVI = 1)} \\ \Delta t_{scaled} &= \Delta t_{recorded} \times \frac{\Delta t_{theoretical} (PVI = 1)}{\Delta t_{recorded} (PVI = 1)}\end{aligned}\quad (3.8)$$

Les résultats de cette correction sont présentés sur la Figure 4.19 (voir annexe).

2. La dérivée par rapport au temps de  $\Delta p(t)$  est beaucoup plus bruitée que ce qui avait été observé pour les expériences numériques. La pression différentielle est mesurée toutes les 6 sec., ce qui génère plus de fluctuations sur les pressions. Ce phénomène est plus prononcé encore quand le fluide injecté atteint des zones très perméables. Les données de pression requièrent donc un traitement pour lisser les variations et éliminer le bruit.
3. Après le premier saut de pression, le fluide visqueux continue d'envahir l'échantillon et  $\Delta p(t)$  augmente progressivement jusqu'au temps de percée. Juste avant la percée,  $\Delta p(t)$  varie très lentement pendant une période dite de stabilisation. Les petites variations de  $\Delta p(t)$  à la fin de l'expérience explique pourquoi la méthode ne parvient pas à estimer la perméabilité près de la face par laquelle les fluides sont produits (Figure 4.18, voir annexe). Une expérience supplémentaire est donc réalisée : l'échantillon est retourné et le fluide visqueux est injecté au niveau de ce qui était initialement la face de production.
4. Les changements de perméabilité en passant d'un petit échantillon à un autre ne sont pas aussi raides que ceux mis en évidence pour les expériences numériques. La miscibilité des deux fluides entraîne la création entre les deux fluides d'une zone de transition dont la viscosité est inférieure à celle du fluide injecté. Cette zone atténue l'impact du contraste de perméabilité sur les variations de pression lorsque le front passe d'un petit échantillon à un autre.
5. En outre, la méthodologie que nous proposons permet de caractériser les variations de perméabilité le long de la direction d'écoulement. L'échantillon est comme découpé en tranches et les perméabilités calculées sont associées à chacune de ces tranches. Chaque tranche est supposée homogène. Or, les petits échantillons utilisés pour construire les composites ne sont pas parfaitement homogènes. La méthodologie développée ne permet pas de rendre compte de l'hétérogénéité dans les tranches perpendiculaires à la direction d'écoulement.

### Echantillon de calcaire de faible perméabilité

On considère à présent un échantillon de calcaire hétérogène de 7,7 cm de long et de 3,8 cm de diamètre. Sa perméabilité effective est de 4 mD. Le profil d'adsorption mesuré pour cet

échantillon montre deux régions distinctes (Figure 3.6, voir annexe). L'échantillon est saturé initialement par une saumure avec 30  $g/l$  de NaCl. Le fluide injecté est une glycérine de viscosité 60  $cp$ . Le débit d'injection est constant et vaut 6  $cc/h$ . Comme la perméabilité de l'échantillon est très faible, le débit ne peut pas excéder cette valeur à cause des limites d'utilisation des capteurs. Lorsque l'expérience de déplacement miscible est achevée, l'échantillon est coupé en deux en se référant à un changement brusque observé sur le profil d'adsorption CT. Nous mesurons alors la perméabilité effective de chacun des deux morceaux. Le profil de perméabilité déduit de la pression différentielle est comparé à ces mesures de perméabilité sur la Figure 4.20 (voir annexe). L'accord est relativement bon, sauf sur la fin du profil. Ce problème a déjà été mentionné plus haut.

### Echantillon de calcaire de forte perméabilité

Le deuxième échantillon de calcaire fait 6,2  $cm$  de long et 4,9  $cm$  de diamètre. Sa perméabilité effective est de 240  $mD$ . L'hétérogénéité de l'échantillon a été renforcée par une injection préliminaire de  $CO_2$  : elle se manifeste le long de la direction d'écoulement, mais aussi perpendiculairement.

Comme dans les expériences présentées plus haut, l'échantillon est saturé initialement par une saumure avec 30  $g/l$  de NaCl. Le fluide injecté est une glycérine de viscosité 60  $cp$ . Le débit d'injection est constant et vaut 85  $cc/h$ . L'échantillon étant très perméable, le fluide très visqueux est injecté dans les deux sens : tout d'abord, nous faisons une injection de la gauche vers la droite pour caractériser la perméabilité dans la première partie de l'échantillon, puis une injection de la droite vers la gauche pour caractériser la perméabilité dans l'autre partie. L'évolution des pression différentielle obtenues est représentées sur la Figure 4.21 (voir annexe). Dès que la perméabilité de l'échantillon est supérieure à 100  $mD$ , nous recommandons de procéder suivant deux injections, une injection normale et une injection inverse. Avec l'injection inverse, nous cherchons à nous affranchir du bruit qui perturbe la détermination des perméabilités d'autant plus que la perméabilité est forte et que le front a déjà traversé une bonne partie de l'échantillon. Pour confirmer ou infirmer les résultats déduits de notre technique d'interprétation, nous disposons aussi 32 minipermeamètres le long de l'échantillon, ce qui nous permet d'avoir des valeurs de perméabilité de surface sur 8 sections. Les résultats sont reportés sur la Figure 4.22 (voir annexe). Ils confirment le potentiel de la méthode d'interprétation proposée.

### Echantillon de grès à grains grossiers

Le dernier échantillon est un grès à grains grossiers, appelé K13. Sa perméabilité effective est de 170  $mD$ . Ses propriétés sont décrites dans le tableau 3.2 (voir annexe). L'échantillon est marqué par une couche de 1,5  $cm$  d'épaisseur, dont la nature n'est pas clairement identifiée. L'existence d'une hétérogénéité à petite échelle est mise en évidence par les mesures de scanner (Figure 3.6, voir annexe).

Un test de traceurs sous scanner est réalisé au préalable afin de mieux apprécier l'impact de l'hétérogénéité. L'échantillon est d'abord saturé par une saumure avec 30  $g/l$  de NaCl. Puis, une saumure à 30  $g/l$  de NaCl est injecté dans l'échantillon suivant un débit de 60  $cc/h$ . Les images scanner collectées montrent un front très dispersé (Figure 4.24, voir annexe). L'écoulement ne semble pas impacté par la présence d'une stratification ou d'une barrière, mais il apparaît que la partie inférieure de l'échantillon est plus perméable que la partie supérieure.

Après ce test préliminaire, nous reprenons la procédure classique. L'échantillon est d'abord saturé par une saumure avec 30  $g/l$  de NaCl. Puis, on injecte une glycérine de viscosité 200  $cp$ . Cette viscosité est choisie pour stabiliser autant que possible le déplacement du front. La glycérine est injectée avec un débit de 60  $cc/h$ . Pendant l'injection, on mesure la pression différentielle et on collecte quelques images 3D de concentration (Figure 4.24, voir annexe). En comparant ces cartes de concentration à celles acquises pendant le test de traceurs, on montre que la dispersion induite par la diffusion a été supprimée.

L'échantillon étant très perméable, nous effectuons une injection normale et une injection inverse. Le traitement des chutes de pression mesurées fournit un profil de perméabilité dont les valeurs oscillent entre 70 et 220  $mD$  (Figure 4.23, voir annexe). L'échantillon étant très friable, aucune autre mesure n'a pu être menée pour valider ces résultats.

## 3.6 Conclusion

Nous avons développé dans ce chapitre une méthodologie pour caractériser les variations de la perméabilité le long de la direction d'écoulement. La caractérisation est unidimensionnelle. La méthode repose sur l'injection d'un fluide miscible très visqueux dans un échantillon de roche initialement saturé par un fluide peu visqueux. On déduit le profil de perméabilité des variations de la pression différentielle.

La méthodologie proposée est validée à la fois par des expériences numériques et des expériences en laboratoire. Les profils estimés concordent avec les mesures faites par ailleurs, mais montrent un certain lissage induit par la création d'une zone de mélange entre les zones saturées d'une part par le fluide visqueux et d'autre part par le fluide peu visqueux.

Comme mentionné plus haut, la méthodologie proposée permet une caractérisation unidimensionnelle de l'hétérogénéité. Pour s'affranchir de cette limitation, nous envisageons, dans le chapitre suivant, d'aborder le problème à partir de techniques de calage itératives.

# Chapitre 4

## Caractérisation tridimensionnelle de l'hétérogénéité de la perméabilité

### 4.1 Introduction

L'objectif de ce chapitre est de mettre en place une boucle de calage pour caractériser la répartition spatiale des perméabilités dans un échantillon. Les données disponibles sont celles enregistrées lors des expériences de déplacement miscible introduites dans le chapitre précédent : l'évolution de la pression différentielle au cours du temps ainsi que des cartes 3D spécifiant la répartition spatiale des concentrations à différents temps. Par ailleurs, des mesures scanner sont aussi réalisées pour déterminer la distribution des porosités dans l'échantillon. Il s'agit donc ici d'être capable de construire un modèle 3D de perméabilité représentatif de l'échantillon et de contraindre la distribution des valeurs de perméabilité dans ce modèle par les données citées ci-dessus.

### 4.2 Paramétrage du modèle de perméabilité

Le modèle de perméabilité est représenté par une grille. L'objectif est d'attribuer une valeur de perméabilité à chaque maille de la grille. Pour paramétrer le modèle de perméabilité, nous utilisons la relation suivante :

$$\log_{10}[k(\mathbf{x})] = A\phi(\mathbf{x}) + b(\mathbf{x}) \quad (4.1)$$

$A$  est une constante.  $b(\mathbf{x})$  est une réalisation d'une fonction aléatoire caractérisée par une moyenne  $m$ , une variance  $\sigma^2$  et une fonction de covariance données. Le vecteur  $\mathbf{x}$  indique la position. Le champ de porosité  $\phi(\mathbf{x})$  est connu.  $b(\mathbf{x})$  est un champ tridimensionnel de mêmes dimensions que  $\phi(\mathbf{x})$ . Les paramètres dont dépend le champ 3D de perméabilité  $k$  sont donc :

1. Le coefficient  $A$  ;



2. le germe utilisé pour générer  $b(\mathbf{x})$  ;
3. La moyenne  $m$  ;
4. La variance  $\sigma^2$  ;
5.  $L_x$ ,  $L_y$  et  $L_z$  les longueurs de corrélation suivant les trois axes principaux. Ces paramètres interviennent au niveau du variogramme.

En modifiant ces divers paramètres, on peut changer très significativement la relation entre les porosités et les perméabilités. En outre, la structure spatiale obtenue au final pour le champ de perméabilité peut différer fortement de celle du champ de porosité.

### 4.2.1 Définition de la fonction objectif

Brièvement, lorsqu'on lance une procédure de calage, on modifie les paramètres d'un modèle jusqu'à ce que la simulation d'écoulement pour le modèle modifié fournisse une réponse compatible avec les données dynamiques collectées sur le terrain. Mathématiquement, ce problème équivaut à minimiser une fonction, dite fonction objectif.

Dans notre cas, la fonction objectif mesure l'écart entre les données dynamiques acquises (à savoir l'évolution de la pression différentielle en fonction du temps et les cartes 3D de concentration mesurées à différents temps), et les réponses numériques correspondantes fournies par le simulateur d'écoulement.

La fonction objectif s'écrit donc :

$$\begin{aligned}
 J(\Theta) = & \frac{1}{2} \frac{w^p}{ntimes} \sum_{i=1}^{ntimes} \left( \frac{p_i^{obs} - p_i^{sim}(\Theta)}{\sigma^p} \right)^2 \\
 & + \frac{1}{2} \sum_{j=1}^{ndata} \frac{w_j^S}{nvalues_j} \sum_{i=1}^{nvalues_j} \left( \frac{S_{i,j}^{obs} - S_{i,j}^{sim}(\Theta)}{\sigma_j^S} \right)^2
 \end{aligned} \tag{4.2}$$

où  $J$  est la fonction objectif et  $\theta$  l'ensemble des paramètres inconnus du modèles.  $ntimes$  est le nombre de mesures pour la pression,  $ndata$  le nombre de cartes 3D de concentration et  $nvalues$  le nombre de valeurs de concentration par carte.  $\sigma$  est l'écart type. Les notations  $p$  et  $S$  se réfèrent respectivement aux pressions et concentrations. Les notations "obs" et "sim" sont utilisées pour identifier les valeurs observées et simulées.

La mise en place d'une boucle de calage nous amène à définir un workflow pour construire un modèle et à calculer pour ce modèle la valeur de la fonction objectif. Puis, un processus itératif modifie les paramètres inconnus jusqu'à ce que la fonction objectif atteigne une valeur minimale.

## 4.3 Boucle de calage

Deux boucles de calage ont été élaborées en s’aidant des fonctionnalités développées dans le logiciel prototype de recherche Condor : une avec une optimisation simple et une avec une optimisation graduelle.

### 4.3.1 Optimisation simple

L’optimisation simple s’appuie sur le workflow présenté sur la Figure 5.2 (voir annexe). On construit un premier modèle de perméabilité et on implémente un processus de recherche pour identifier les paramètres qui minimisent la fonction objectif.

Pour cette première boucle de calage, les paramètres à ajuster sont :  $A$ ,  $m$  et  $\sigma^2$ .

Les étapes du workflow sont les suivantes.

1. On attribue des valeurs initiales raisonnables aux paramètres à déterminer.
2. On construit une grille cartésienne 3D qu’on remplit avec les valeurs de porosité estimées par scanner.
3. A partir d’un germe, on génère un bruit blanc Gaussien  $z_1$ .
4. A partir de ce bruit blanc Gaussien, on génère la réalisation  $b$  [34].
5. Connaissant la valeur de  $A$ , on construit le champ 3D de perméabilité (équation 4.1).
6. Les champs de porosité et de perméabilité sont tous les deux mis à l’échelle.
7. Une simulation d’écoulement reproduisant les conditions des expériences menées en laboratoire (voir chapitre 3) est lancée.
8. On calcule la fonction objectif (équation 4.2) en comparant les données mesurées aux réponses simulées. Si la fonction objectif est suffisamment petite, le processus de minimisation s’arrête : les paramètres donnant la plus petite fonction objectif sont les paramètres optimaux. Si la fonction objectif est trop grande, on modifie les paramètres et on revient à l’étape 4.

On notera que  $z_1$  étant invariable, la répartition spatiale des hétérogénéités de perméabilité ne change pas.

### 4.3.2 Optimisation graduelle

Cette nouvelle boucle de calage (Figure 5.3, voir annexe) intègre un degré de complexité ou flexibilité supplémentaire par rapport à l’optimisation simple introduite dans la section précédente. Il s’agit ici de se donner les moyens de modifier la répartition spatiale des hétérogénéités de perméabilité dans l’échantillon. Pour ce faire, on applique la méthode

de déformation graduelle [27, 35]. Cette technique permet de modifier le bruit blanc Gaussien à partir d'un ou plusieurs paramètres, dits de déformation.

Pour cette deuxième boucle de calage, les paramètres à ajuster sont :  $A$ ,  $m$ ,  $\sigma^2$ ,  $L_x$ ,  $L_y$ ,  $L_z$  et  $\theta$ , le paramètre de déformation graduelle.

La procédure d'optimisation passe par les étapes présentées ci-après.

1. On attribue des valeurs initiales raisonnables aux paramètres à déterminer.
2. On construit une grille cartésienne 3D qu'on remplit avec les valeurs de porosité estimées par scanner.
3. A partir d'un germe, on génère un bruit blanc Gaussien  $z_1$ .
4. On génère un deuxième bruit blanc Gaussien  $z_2$ .
5. On combine  $z_1$  et  $z_2$  suivant les principes de la méthode de déformation graduelle. Cette combinaison dépend d'un paramètre  $\theta$  de déformation. On obtient un nouveau bruit blanc Gaussien  $z(\theta)$ .
6. A partir de ce bruit blanc Gaussien, on génère la réalisation  $b$ .
7. Connaissant la valeur de  $A$ , on construit le champ 3D de perméabilité (équation 4.1).
8. Les champs de porosité et de perméabilité sont tous les deux mis à l'échelle.
9. Une simulation d'écoulement reproduisant les conditions des expériences menées en laboratoire (voir chapitre 3) est lancée.
10. On calcule la fonction objectif (équation 4.2) en comparant les données mesurées aux réponses simulées. Si la fonction objectif est suffisamment petite, le processus de minimisation s'arrête : les paramètres donnant la plus petite fonction objectif sont les paramètres optimaux. Si la fonction objectif n'a pas convergé et n'est pas assez petite, on modifie les paramètres ( $A$ ,  $m$ ,  $\sigma^2$ ,  $L_x$ ,  $L_y$ ,  $L_z$  et  $\theta$ ) et on revient à l'étape 5. Si la fonction objectif a convergé, mais n'est pas assez petite, on modifie les paramètres ( $A$ ,  $m$ ,  $\sigma^2$ ,  $L_x$ ,  $L_y$ ,  $L_z$  et  $\theta$ ), on remplace  $z_1$  par  $z$  et on revient à l'étape 4.

## 4.4 Validation numérique

### 4.4.1 Modèles numériques

Afin de valider la méthodologie, on construit deux modèles numériques. Les champs de perméabilité sont donc connus pour ces deux modèles. Une simulation d'écoulement pour chacun des deux modèles fournit les pressions différentielles et les cartes de concentration. On considère ces réponses comme des données de référence.

Les modèles numériques sont appelés modèle 3 et modèle 4. Ils sont caractérisés par le fait qu'ils présentent une hétérogénéité longitudinale, mais aussi transversale. Ils sont constitués

de 4 blocs de porosité et perméabilité moyennes différentes. Les champs de porosité sont générés aléatoirement. Leurs paramètres stochastiques sont rappelés dans le tableau 3.1 (voir annexe). Pour le modèle 3, on génère un champ de perméabilité indépendant de la porosité. Pour le modèle 4, le champ de perméabilité se déduit du champ de porosité à l'aide de la relation 4.1.

Le modèle 3 est discrétisé sur une grille de  $20 \times 30 \times 30$  mailles et le modèle 4 sur une grille de  $20 \times 90 \times 90$  mailles.

#### 4.4.2 Méthodologie

A ce stade, on suppose que les champs de perméabilité des modèles 3 et 4 ne sont pas connus. On ne dispose comme information que des cartes de porosité, de l'évolution des pressions en fonction du temps et des cartes 3D de concentration. A partir de ces données de référence, nous cherchons à construire des modèles de perméabilité que nous pourrions comparer par la suite aux modèles 3 et 4.

Les données de pression, nous l'avons vu dans le chapitre 3, dépendent du profil de perméabilité le long de la direction d'écoulement. Elles ne sont pas sensibles à l'hétérogénéité transversale. Au contraire, les concentrations sont très sensibles aux hétérogénéités transverses. En conséquence, nous proposons de faire une première procédure de calage en ne considérant que les données de pression. La boucle de calage correspond alors à l'optimisation simple introduite plus haut. Puis, dans un deuxième temps, en partant du modèle contraint par les données de pression, nous utilisons le schéma d'optimisation complexe pour contraindre aussi le modèle de perméabilité aux cartes 3D de concentration.

#### 4.4.3 Résultats des tests de validation

Que ce soit pour le modèle 3 et le modèle 4, le calage préliminaire des données de pression est excellent. Les paramètres optimaux obtenus pour le modèle 3 sont reportés sur la Figure 7.3 (voir annexe). Cette première étape de calage permet d'ajuster les valeurs de  $A$  et  $m$ , mais pas celle de  $\sigma^2$ . On notera qu'à ce stade, la fonction objectif est limitée au terme des pressions.

Partant des modèles calés en pression, on cherche à présent à intégrer aussi les données de concentration pour caractériser les modèles 3D de perméabilité. On ne considère pour chaque modèle qu'une unique carte de concentration (Figures 7.5 et 7.11, voir annexe). La fonction objectif est donnée par l'équation 4.2. Les résultats du calage des concentrations sont présentés sur les Figures 7.8 et 7.15 (voir annexe) : les concentrations simulées pour les modèles optimaux sont très proches des concentrations mesurées. Il apparaît que les longueurs de corrélation sont des paramètres influents des modèles. Pour le modèle 3, le paramètre  $A$  tend vers 0, ce qui signifie qu'on retrouve bien que les porosités et perméabilités ne sont pas corrélées. On peut montrer que pour les deux tests, on obtient des valeurs

optimales pour les paramètres proches des valeurs utilisées pour créer les modèles de référence (voir pas exemple tableau 7.5 en annexe).

## 4.5 Application aux expériences en laboratoire

Nous considérons à présent le composite 2 et un grès, nommé “SG20”. Pour ces échantillons, on dispose de la carte 3D de porosité, de la pression différentielle au cours du temps et de cartes 3D de concentration mesurées à différents temps.

On applique alors la méthodologie de calage introduite dans la section précédente pour élaborer pour ces deux échantillons des modèles 3D décrivant la répartition spatiale des perméabilités. Comme précédemment, on utilise l’optimisation simple pour caler les pressions, puis l’optimisation complexe pour caler aussi les concentrations.

### 4.5.1 Résultats pour le composite 2

Bien que le composite 2 soit formé de 4 petits échantillons mis bout à bout, on montre qu’il faut distinguer 5 zones différentes dans le composite : le deuxième échantillon est subdivisé en deux zones. Ce faisant, la procédure de calage simple amène à un modèle reproduisant très bien l’évolution de la pression différentielle.

Dans un deuxième temps, nous intégrons les données de concentration. Les données considérées sont celles acquises pour un PVI de 0,02 : elles sont donc ajoutées à la fonction objectif. L’optimisation complexe basée sur la méthode de déformation graduelle permet d’affiner le modèle optimal obtenu pendant l’étape de calage des pressions : le nouveau modèle optimal donne une carte de concentration plus proche (Figure 7.21, voir annexe) de la carte de référence que ne l’était la carte de concentration obtenue pour le premier modèle optimal. A nouveau, il apparaît que  $A$  et les longueurs de corrélation sont les paramètres les plus influents dans cette deuxième étape de calage.

### 4.5.2 Résultats pour le grès SG20

La pression différentielle mesurée pour cette échantillon fait apparaître 4 zones distinctes. On intègre donc cette information dans la procédure de calage : le modèle est découpé en 4 zones perpendiculaires à la direction d’écoulement. Dans ces conditions, l’optimisation conduit à un modèle de perméabilité capable de très bien approcher la réponse en pression mesurée pendant l’injection du fluide très visqueux (Figure 7.23, voir annexe).

En ce qui concerne les concentrations, on cherche à intégrer les cartes de concentration obtenues sous scanner pour  $PVI = 0,25$  et  $PVI = 0,47$ . On applique l’optimisation complexe présentée plus haut en la raffinant : en plus de la déformation graduelle, on ajoute des points pilotes pour se donner plus de flexibilité dans le processus de déformation du champ

de perméabilité. Les résultats du calage des concentrations sont illustrés par la Figure 7.33 (voir annexe). Excepté pour la première section, le calage des concentrations est très correct.

## 4.6 Conclusion

Dans ce chapitre, nous avons développé une méthodologie itérative de calage des pressions et des concentrations. Cette méthode passe par deux étapes : une optimisation simple pour caler les pressions qui permet de capturer l'hétérogénéité dans la direction de l'écoulement et une optimisation complexe pour caler les concentrations pour capturer l'hétérogénéité transverse dans la zone éclairée par le fluide injecté.

Cette méthode a été validée à partir de tests numériques, ce qui permet de contrôler le potentiel de reconstruction du modèle de perméabilité. Les deux cas considérés ont été positifs. Enfin, la méthode a été appliquée à des expériences d'injection de fluide visqueux que nous avons réalisées en laboratoire sur deux échantillons. Nous avons pu déterminer des modèles de perméabilité représentant les échantillons capables de reproduire assez bien les données de pression et de concentration acquises pendant l'injection.

# Conclusions et perspectives

Dans ce travail, nous avons essayé de caractériser l'hétérogénéité du champ de perméabilité à l'échelle de l'échantillon. L'étude a été divisée en trois parties principales. L'objectif de la première partie a été de sélectionner les échantillons naturels ayant différents degrés d'hétérogénéité, notamment, l'hétérogénéité longitudinale et transversale. Dans ce but, nous nous sommes référés à des procédures de sélection qui sont souvent utilisées pour séparer les échantillons homogènes des échantillons hétérogènes. Des images CT scan ont été acquises pour explorer l'hétérogénéité transversale. Elles ont aussi été utilisées afin de calculer le nombre de CT moyen par tranche. Observer ces valeurs moyennes le long de l'échantillon nous a aidé à quantifier rapidement les hétérogénéités longitudinales. Puis, on a créé deux échantillons hétérogènes artificiels composés de quatre bouts d'échantillon. Nous avons aussi sélectionné quatre échantillons qui présentaient des hétérogénéités macroscopiques. Quatre modèles numériques ont également été créés avec différents types d'hétérogénéité pour des raisons de validation.

Dans la deuxième partie de cette étude, nous avons présenté une nouvelle méthodologie afin d'obtenir un profil 1D de perméabilité absolue le long de l'échantillon. L'idée était d'injecter de la glycérine visqueuse dans un échantillon saturé au préalable par une saumure soixante fois moins visqueuse. Les deux fluides étaient miscibles dans toutes les proportions. Nous avons supposé un déplacement de type piston, puisque le rapport de viscosité était très favorable. Cette hypothèse a été validée en visualisant l'interface entre les deux fluides par des images CT. Nous avons étudié l'évolution de la pression différentielle en fonction du temps jusqu'au moment de la percée de la glycérine. Un profil continu de la perméabilité a été estimé le long de l'échantillon en supposant qu'il était constitué d'un nombre infini de tranches perpendiculaires à la direction d'écoulement : une valeur de la perméabilité absolue a été déterminée pour chaque tranche. La méthodologie a été validée par des expériences numériques. L'écoulement numérique a été effectué pour deux modèles qui représentaient nos deux échantillons composites. Ces modèles étaient constitués de quatre blocs, chacun d'eux ayant une perméabilité absolue différente. L'hétérogénéité transversale était négligeable dans ces deux modèles. Nous avons simulé la pression différentielle (entrée-sortie) en considérant un écoulement miscible et un second immiscible. La procédure d'interprétation a montré son efficacité en reproduisant plus ou moins les perméabilités de référence. Les erreurs relatives

entre les perméabilités estimées et perméabilités réelles ont été de moins de 13% pour ces deux modèles. Nous avons noté un effet de lissage dans le cas du déplacement miscible, qui est dû à la création d'une zone de mélange entre les deux fluides.

La méthode a également été appliquée à des expériences en laboratoire. Le processus a bien fonctionné pour les faibles perméabilités. L'erreur relative entre les perméabilités estimées et les perméabilités absolues a été inférieure à 5%. Dans le cas d'échantillons perméables, la pression différentielle est inversement proportionnelle à la perméabilité, ce qui conduit à une estimation de perméabilité très fluctuante. La détermination de la perméabilité a été améliorée par une injection inverse. Les résultats obtenus pour les échantillons hétérogènes ne sont pas aussi bons que pour l'expérience numérique et montrent plus de 40% d'erreur. Toutefois, nous avons montré que la perméabilité estimée suit les variations de la perméabilité réelle (quantifiée à partir d'autres mesures).

Dans la méthodologie que nous avons développée pour déterminer le profil 1D de la perméabilité, nous avons supposé que la perméabilité est homogène par tranche (transversale), ce qui signifie que l'hétérogénéité est unidimensionnelle. Cette hypothèse est par trop réductrice. Dans la troisième partie de cette étude, nous nous sommes concentrés sur le développement d'une nouvelle procédure en mesure de capturer l'hétérogénéité tridimensionnelle dans les échantillons. Nous avons sélectionné des échantillons avec des hétérogénéités locales. On connaissait leurs champs 3D de porosité : ils ont été créés pour les modèles numériques et ont été mesurés (sous scanner) pour les échantillons naturels. La pression différentielle (entrée-sortie) a été mesurée au cours de tests de déplacements miscibles visqueux en déplaçant une saumure à faible viscosité avec de la glycérine à forte viscosité. Les cartes de concentration ont été obtenues pour différents temps pendant la manipulation. Les champs 3D de perméabilité ont été modélisés en utilisant une relation du type  $\log(k(\mathbf{x})) = A\phi(\mathbf{x}) + b(\mathbf{x})$ , où  $A$  est une constante et  $b(\mathbf{x})$  est une réalisation d'une fonction aléatoire caractérisée par une moyenne, une variance et un variogramme.

Nous avons développé un processus de calage d'historique pour modéliser l'hétérogénéité du champ de perméabilité dans l'échantillon tout en utilisant le champ de porosité 3D ainsi que les données de pression et de concentration. Les paramètres inconnus étaient  $A$ , la moyenne et la variance de  $b(\mathbf{x})$ , le paramètre de déformation graduel et les longueurs de corrélation de  $b(\mathbf{x})$ . Nous avons développé une méthodologie itérative de calage des pressions et des concentrations. Cette méthode passe par deux étapes : une optimisation simple pour caler les pressions qui permet de capturer l'hétérogénéité dans la direction de l'écoulement et une optimisation complexe pour caler les concentrations pour capturer l'hétérogénéité transverse dans la zone éclairée par le fluide injecté.

La méthode proposée a été appliquée à deux séries d'expériences numériques et deux autres séries d'expériences en laboratoire. La mesure  $\Delta p(t)$  pour tous les échantillons a été parfaitement calée en utilisant le processus d'optimisation simple. La fonction objectif a montré plus de 95% de baisse pour tous les cas. Le calage des données de concentration a été beaucoup plus difficile en raison du bruit dans les images CT. La réduction de la fonction objectif a été



d'environ de 60% pour les expériences numériques et de 20% pour les expériences en laboratoire. Il a été montré que  $\Delta p(t)$  était seulement une fonction de la perméabilité moyenne et qu'un bon calage des données de concentration ne pouvait être réalisé sans prendre en compte les hétérogénéités transversales. Le paramètre  $A$  a été un bon indicateur pour montrer les corrélations perméabilité-porosité. Ce paramètre et la moyenne de  $b(\mathbf{x})$  étaient dépendants : une augmentation du paramètre  $A$  entraîne une diminution de la moyenne de  $b(\mathbf{x})$ . Enfin, nous avons montré que les longueurs de corrélation de  $b(\mathbf{x})$  sont les paramètres les plus influents pendant le calage des données de concentration.

Comme dans toutes les études pratiques, notre modélisation est fondée sur des hypothèses et des simplifications. L'amélioration de ces hypothèses théoriques et expérimentales peut conduire à une modélisation plus réaliste et à de meilleurs résultats. Ici, nous discutons de quelques-unes des futures améliorations possibles.

- Dans notre technique de caractérisation 1D de perméabilité, le rapport de viscosité est favorable, ce qui nous permet de supposer un déplacement de type piston dans l'échantillon. Nous avons aussi émis l'hypothèse qu'il n'y a pas de zone de mélange entre les deux fluides. L'une des améliorations possibles est d'envisager trois zones à l'intérieur de l'échantillon : une zone de pure glycérine, une de pure saumure et une mixte entre les deux. Il serait intéressant de développer une nouvelle formulation considérant la pression différentielle relative à la zone mixte et de ces effets sur l'estimation de la perméabilité.
- Une autre possibilité serait d'effectuer un écoulement immiscible visqueux au lieu d'un déplacement miscible. Les conditions d'écoulement seraient les mêmes que précédemment sauf qu'il n'y aurait pas de zone mixte entre les deux fluides. L'hypothèse de déplacement piston pourrait être alors vérifiée de façon plus précise.
- Afin d'améliorer la qualité des données recueillies au cours des mesures CT scan, on peut augmenter la durée de mesure de chaque images CT et en parallèle réduire le nombre de tranches le long de l'échantillon. Le processus d'optimisation peut être réalisé en utilisant les données de concentration 2D observées à certains endroits de l'échantillon. La validation de notre méthodologie dépend de la qualité des données recueillies. Des données non bruitées seraient beaucoup plus utiles, même si elles ne sont disponibles que sur certaines parties de l'échantillon.
- Dans ce travail, nous avons toujours supposé que le variogramme de notre modèle de perméabilité est le même que celui des données de la porosité. Une autre possibilité serait de changer le variogramme de notre modèle et d'étudier son effet sur la fonction objectif et le processus de calage.
- Il serait intéressant de pouvoir tester la relation  $k = A(\phi - \phi_0)^\beta$  suggéré par la théorie de la percolation. Dans cette formulation,  $\phi_0$  est la porosité minimale au cours de laquelle les canaux microscopiques sont connectés. Le paramètre  $A$  est une constante qui détermine la grandeur de  $k$ .  $\beta$  est un exposant lié à la géométrie des canaux

microscopiques. Ici, les paramètres  $A$  et  $\beta$  sont inconnus.  $\phi_0$  peut être déterminé en laboratoire.

- Dans notre étude, les modèles de perméabilité sont mis à l'échelle à l'aide d'un calcul de moyenne arithmétique-arithmétique-harmonique et d'un ratio de mise à l'échelle constant. Plus d'études peuvent être réalisées sur le ratio de mise à l'échelle et ses effets sur le calage final. Il serait également intéressant de travailler sur l'effet de mise à l'échelle sur le paramètre  $\beta$ , quand on utilise la loi de puissance  $k - \phi$  suggérée par la théorie de la percolation.
- L'effet de la miscibilité sur les données de concentration doit être étudié dans le détail. Dans ce travail, nous avons utilisé un modèle immiscible et ignoré la zone mixte lors de la simulation de notre déplacement miscible visqueux. Cette hypothèse peut être révisée en utilisant, par exemple, le coefficient de mélange de Todd et Longstaff.

# Annexe

# Chapter 1

## Introduction

According to the International Energy Outlook (IEO2007, May 2007), world petroleum consumption will increase from 83 million barrels per day in 2004 to 118 million barrels per day in 2030. If the world keeps using subsurface hydrocarbon reserves, then industry and academia have to invent and explain better ways to find and produce them. The primary objective of a reservoir study is to determine the optimum conditions needed to maximize the economic recovery with an acceptable degree of certainty. Reservoir engineers should describe various reservoir characteristics using available data. Reservoir modeling is the most sophisticated technique for achieving this goal. The reservoirs are modeled as 3D grids, whose grid cells are populated by petrophysical properties such as porosity and permeability and other required rock data. Reservoir properties have different weights and importance due to their various impacts on fluid flow. Permeability is one of the most important properties of a reservoir rock. It strongly affects fluid flow by creating flow barriers and preferential flow paths. Although engineers have been producing oil and gas from reservoirs for more than a century, they are still inadequately informed about the distribution of permeability (or porosity) inside reservoir rocks. Ideally, if reservoirs were homogeneous, measuring a reservoir property at any location would allow a full description of the reservoir. Unfortunately, reservoirs are heterogeneous. Rock formations are the product of different geological events such as sedimentation, diagenetic evolution and mechanical stresses. These geological phenomena can occur sequentially or simultaneously, which makes rock formation very complex and non homogeneous. The knowledge about reservoir heterogeneity is very incomplete due to the sparsity of the direct observations. The information about reservoir heterogeneity is limited to a few well data and a limited number of seismic survey studies. Being aware of the influence of reservoir rock heterogeneities on fluid flow and production is critical for a proper reservoir management. Different reservoir characterization methods are developed to integrate the available static and dynamic data into the reservoir model and reduce the uncertainties of the model predictions.

## 1.1 Heterogeneity from the core to the entire reservoir

Reservoir heterogeneity can be measured at different scales from pore to the entire reservoir. Although reservoir properties may vary over different continuous scales, it is convenient to divide heterogeneity into four different levels [25] shown in Figure 1.1.

1. *Microscopic Heterogeneities.* These type of heterogeneities are measured at a micro level. They are also called pore-level heterogeneities. Microscopic heterogeneities include pore and grain size distribution, throat opening and rock lithology.
2. *Macroscopic Heterogeneities.* Macroscopic heterogeneities are observed at the core level. They are also called core-level heterogeneities. They impact core properties such as permeability and porosity, petrophysical properties such as relative permeability and capillary pressure and some log data.
3. *Megascopeic Heterogeneities.* The order of magnitude of these types of heterogeneities is roughly the same as that of a reservoir simulator grid cell, that is a few meters in both vertical and horizontal directions. The properties measured at this scale include log data and reservoir formation test data. Seismic data are sometimes considered to be characteristics of this scale [31].
4. *Gigascopeic Heterogeneities.* Gigascopeic heterogeneities are measured at reservoir scale. They include the data measured from tracer tests, well tests, surface seismic and major fault locations.

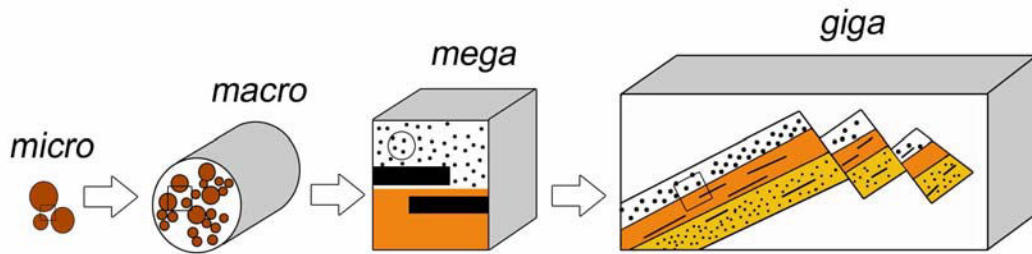
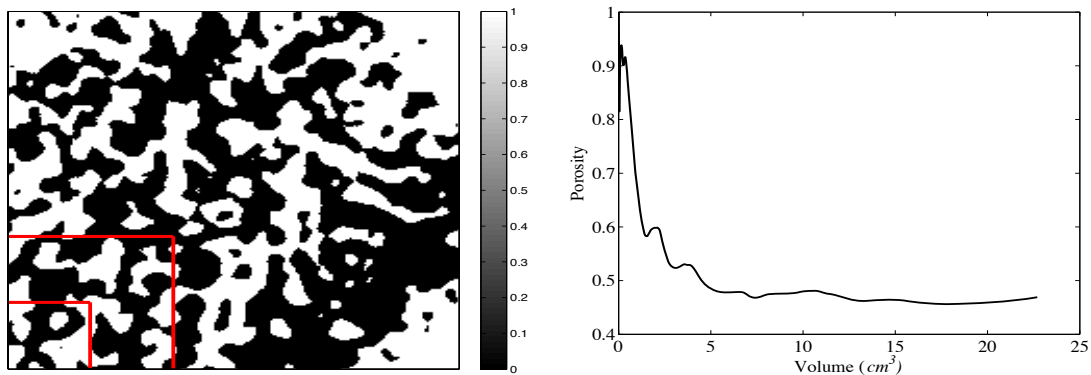


Figure 1.1: Heterogeneity from micro to gigascopeic scales (after Kelkar and Perez, 2002).

When describing reservoir heterogeneities, the heterogeneity has to be defined at the proper scale to be truly representative of this scale [18]. In a reservoir study, different measurements are conducted at different levels. Relative permeabilities are measured at the core scale while well test permeability is measured at the reservoir scale. At microscopic scale, a natural porous system is always heterogeneous due to the spatial variability of pore morphology [18]. Therefore, any measurement over this scale shows significant variations in the measured

property. For example, porosity at microscopic level can be either one in the pore or zero in the grain. When the measurement is made at larger scale, the variations in the properties observed at a smaller level are reduced because they are averaged [31]. In other words, the variations in a given measured property decrease as the scale of measurement increases. This scale dependence is called the support effect. Figure 1.2 shows a classical example. Figure 1.2(a) shows a cross section of a synthetic sandstone rock with  $3.8 \times 3.8 \times 1.0 \text{ cm}^3$  dimensions. The variations in the computed porosity of the given porous volume decrease when the measurement volume increases (Figure 1.2(b)). Another example is about permeability measurement. Core permeability is measured over a  $0.00001 \text{ m}^3$  core sample. On the other hand, well test permeability is measured over a volume of  $10^4$  to  $10^6 \text{ m}^3$ . There are at least 10 orders of magnitude difference between the volume over which permeability is measured at the core scale versus the volume over which it is measured with well test data. This difference has to be carefully considered when defining the permeability value for a simulator grid cell. Proper permeability adjustment (respecting the grid cell volume) by accounting for the support effect is needed before simulator grid cell values can be represented correctly. Just as for permeability, the support effect also influences porosity values derived from core and log data.



a. A symbolic sandstone sample. The white spaces are the voids. The color bar shows the porosity. b. Variations of porosity with the volume considered.

Figure 1.2: Computed porosity as a function of the volume considered for a numerical sandstone sample. The variations in porosity are consistent with the support effect. As the considered volume increases, the calculated porosity reaches a constant level.

## 1.2 Reservoir data and heterogeneity

In a reservoir study, two kinds of data are usually available. “Static data”, which are generally collected before reservoir production and “dynamic data”, which are acquired during production and thus change with time. Static data provide information about the attribute

of interest at given locations. Therefore, they change when the measuring locations change. Depending on the measurement types, static data are affected with different heterogeneity scales. For example, permeability or porosity can be obtained from laboratory measurements on core samples extracted from a given well. In this case, the measured properties are influenced by macroscopic heterogeneities. Permeability and porosity can also be obtained from well-log measurements around the wells. Here, the measured properties are affected with megascopic heterogeneities. Seismic data prior to any reservoir production or outcrop studies can be used to locate the major faults. They are influenced by gigascopic heterogeneities. Static data such as porosity and permeability always exhibit spacial variations at the reservoir scale. Statistical analyses are carried out to describe the observed spatial variations in these measured properties [35, 31]. Statistical techniques are also used to model pore-scale heterogeneities inside core sample [50, 17, 2].

Dynamic data such as bottom-hole pressure or hydrocarbon production are time-dependent. As fluid moves during production, dynamic data vary. They are usually measured in wells. Today, time lapse seismic data are also used to measure the changes in hydrocarbon saturation during production. Depending on the types of flow that take place in the reservoir, different heterogeneities may have different effects. During primary recovery, the natural energy of the reservoir is used. When the natural energy is depleted, the reservoir may be subjected to water flooding,  $CO_2$  injection, surfactant flooding or polymer flooding. Kelkar and Perez [31] indicate that as the flow process becomes more complex, the effect of small scale heterogeneities increases. Gigascopic heterogeneity impact overall reservoir performance during primary recovery. As the flow process changes to secondary recovery, additional levels of heterogeneities can affect fluid flow and production. Megascopic and core level heterogeneities create preferential flow paths. As a result, the displacing fluids take preferential flow paths, which contributes to reduce the sweeping efficiency and hence oil recovery. During an enhanced oil recovery (EOR), even the microscopic levels of heterogeneity can affect reservoir production. Due to the complexity of the flow process at this stage of recovery, small scale heterogeneities can affect the way in which the interface between the displacing fluid and hydrocarbon is established and moved [31].

### 1.3 Numerical modeling and heterogeneity

As mentioned before, reservoir modeling is the most sophisticated technique for describing various reservoir properties based upon the available data. The purpose of reservoir simulation is to predict the performance of a reservoir as accurately as possible. Commercial reservoir simulators (*e.g.*, ECLIPSE, PumaFlow) use finite difference formulation in order to simulate fluid flow inside reservoirs. In this approach, the reservoir is discretized over a finite number of cells. In each cell, a material balance is written based upon Darcy's law [12], mass conservation and capillary pressure equations. Equations 1.1 to 1.5 describe multiphase flow

inside a grid cell:

$$\nabla \cdot [\lambda_i(\nabla p_i - \gamma_i \nabla z)] = \frac{\partial}{\partial t} \left[ \frac{\phi S_i}{B_i} \right] + q_i \quad i = o, w \quad (1.1)$$

$$\begin{aligned} \nabla \cdot [R_s \lambda_o(\nabla p_o - \gamma_o \nabla z) + \lambda_g(\nabla p_g - \gamma_g \nabla z)] \\ = \frac{\partial}{\partial t} \left[ \phi \left( \frac{R_s}{B_o} S_o + \frac{S_g}{B_g} \right) \right] + R_s q_o + q_{fg} \end{aligned} \quad (1.2)$$

$$S_o + S_w + S_g = 1 \quad (1.3)$$

$$p_{cow} = p_o - p_w \quad (1.4)$$

$$p_{cog} = p_g - p_o \quad (1.5)$$

Transmissibility  $\lambda_i$  is defined by  $\lambda_i = \frac{k_{ri}}{\mu_i B_i} k$ ,  $i = o, w, g$  and  $\gamma_i$  is defined by  $\gamma_i = \rho_i \mathbf{g}$ ,  $i = o, w, g$ . In the given equations,  $k$  is the absolute permeability tensor,  $k_{ri}$  is the relative permeability of phase  $i$ ,  $\mu$  is the fluid viscosity,  $\mathbf{g}$  is gravity,  $\rho$  is the fluid density,  $z$  is the vertical downward direction,  $p$  is the pressure,  $B_i$  is the formation factor of phase  $i$ ,  $\phi$  is porosity,  $S$  is saturation,  $R_s$  is solution gas-oil ratio,  $t$  is time,  $p_c$  is the capillary pressure and  $q$  is the flow rate.  $q_{fw}$  stands for free gas flow rate. Details about reservoir simulation techniques can be found in Aziz and Settari [1].

As it can be seen in the above equations, both fluid and rock data are required as inputs to numerically simulate the flow behaviors. The rock data are directly related to reservoir characterization techniques. They include [18]:

- |                               |                          |
|-------------------------------|--------------------------|
| 1. Formation elevation        | 2. Formation thickness   |
| 3. Porosity                   | 4. Permeability          |
| 5. Capillary pressure         | 6. Relative permeability |
| 7. Formation fluid saturation | 8. Compressibility       |

A value for each of these parameters must be given to each cell of the reservoir grid. Obviously, the finer the reservoir grid, the more detailed and the more time-consuming the numerical simulation. To make flow simulations tractable in terms of CPU time, one has to reduce the number of grid cells. Therefore, on one hand, reservoir heterogeneity must be represented as accurately as possible and, on the other hand, the number of grid cells must be as reduced as possible. Which target is the most crucial is a debatable subject, which is out of the scope of this study.

Let us recall that permeability is one of the most important properties of a reservoir rock when focusing on flow problems. Permeability heterogeneity can induce preferential flow path and barrier to flow at both core and reservoir scale flooding.

Permeability heterogeneity inside a reservoir can vary vertically or laterally. A stratified reservoir rock is a good example of permeability heterogeneity in the vertical direction. Figure 1.3 represent a schematic reservoir that contains three strata of different permeabilities.



The amount of displacing water going into each zone is proportional to the permeability of this zone if the injected water has the same mobility (*i.e.*  $k_{rw}/\mu_w$ ) as the displaced oil [51]. In such a case, the displacing water moves preferentially through high permeability region, leaving behind a huge amounts of oil in the lower permeability layers. With simple calculations, we can show that at water breakthrough, which occurs in the 100 *mD* zone, only about 30% of the mobile oil has been produced.

Microscale permeability heterogeneity affects the calculation of relative permeability data from experimental core flooding. In special core analysis techniques (SCA), relative permeabilities are defined through a system of equations describing flow inside porous media:

$$\vec{v}_i = -\frac{kk_{ri}}{\mu_i}(\nabla p_i - \rho_i \vec{g}) \quad (1.6)$$

$$\frac{\partial \phi \rho_i S_i}{\partial t} = -\nabla \cdot (\rho_i \vec{v}_i) \quad (1.7)$$

$v_i$  is Darcy velocity of phase  $i$ . Relative permeabilities are determined from experiments involving unsteady state immiscible displacements. For a two phase system, the core is flooded with one of the phases. Typically the flood phase is water or gas since in the reservoir one (or both) of these phases displaces oil. If one assumes that 1) the porous medium is homogeneous, 2) flow is one dimensional and incompressible, and 3) capillary forces and gravity effects are negligible, the above system of equations can be inverted explicitly and relative permeabilities can be calculated directly from the time series of production and pressure drop data [10, 28]. Several authors discussed that core analysis data are usually influenced by both capillary pressures and heterogeneity patterns and hence, that the above assumptions are frequently violated [54, 65, 44, 22]. Calculating relative permeability data while considering small scale heterogeneity can have an immediate impact on predicted reservoir performance [65].

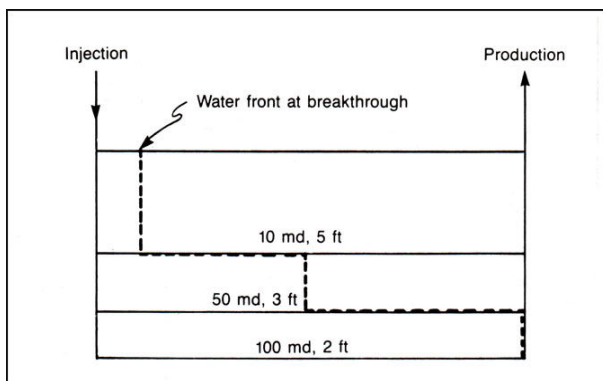


Figure 1.3: Schematic of vertical permeability variation in a reservoir (after Slider, 1983).

## 1.4 Geostatistics and heterogeneity

One of the main goals of reservoir characterization is to capture the actual geology of reservoirs. It is clearly hopeless to obtain a detailed image of the reservoir from a few number of well data and limited seismic surveys. Reservoirs are heterogeneous in the sense that even permeabilities measured on cores extracted from the same well can vary by orders of magnitude. Thus, populating a 3D grid representing the reservoir by permeability and porosity values is not an easy task due to the limited deterministic information about reservoirs. Today, a stochastic description of the reservoir is preferred by both reservoir engineers and geologists. Derived from statistical techniques, different images of the reservoir are created based on the information observed at wells. Many images (or realizations) of the reservoir, containing millions of grid blocks, can be generated honoring the data collected in wells or the data derived from seismic surveys. Details about the method used to generate these images can be found in specialized monographs [31, 35]. Geostatistics takes advantage of the fact that, in many natural phenomena, variable values measured close to each other are similar. As the distance between the measured values increases, the similarity between two measurements decreases [31]. Based on this fact, geostatistics capture the spatial relationship between the sample data. As sufficient amounts of data are not available within the reservoir, geostatistics are used to interpolate the properties of interest at unsampled locations. In such cases, geostatistical techniques generate probable images of reservoirs representing geological models. These models are finely gridded and constrained to static data. As flow simulation over a fine gridded model is very time-consuming, the number of grid cells must be reduced. It is done using upscaling techniques. A flow simulation is run for the coarse grid model and simulated dynamic data are compared to the reservoir data. Obviously, the fine geological model must be modified in order to provide dynamic results similar to reservoir behaviour. This modification procedure known as history-matching involves “optimization techniques”.

## 1.5 Objectives of the study

The main object of this study is to provide tools to improve the interpretation of laboratory experiments carried out on heterogeneous rock samples. As it was stated before, the assumption of homogeneity when interpreting petrophysical properties such as relative permeabilities is not appropriate in all cases.

At the reservoir scale, a huge amount of work has been dedicated to the characterization of permeability fields in the framework of history-matching. The developed methodologies are concerned with both geostatistics and optimization. We aim at taking advantage of this background in constrained modeling to propose new methodologies for characterizing the permeability field at the core scale. The following topics are considered.

**Laboratory experiments.** Viscous miscible displacements are performed and analyzed using CT scan data. The considered samples present different heterogeneities along and perpendicular to flow axis. X-ray CT measurements are expressed in terms of 3D porosity maps plus a few 3D concentration maps obtained at successive time steps. In addition, inlet-outlet pressure drop is measured while the flow rate is constant. These detailed data are complemented by conventional petrophysical measurements.

**One dimensional permeability mapping technique.** We investigate the evolution of the pressure drop as a function of time. A continuous permeability profile is estimated along the flow direction from the pressure drop assuming that the core sample is a stack of infinitely thin cross sections perpendicular to flow direction. Thus, we determine a permeability value for each cross section. Numerical and laboratory experiments are carried out to validate the method. Flow simulations are performed for numerical models representing core samples to estimate the pressure drop. The selected models are sequences of plugs with constant permeabilities. In addition, laboratory displacements are conducted for both low permeability and high permeability core samples. To investigate whether there is dispersion inside the porous medium, CT scan measurements are performed during fluid displacement: the location of the front is observed at successive time intervals.

**Three dimensional permeability characterization.** Last, we focus on the 3D distribution of permeability inside core samples. A 3D grid is constructed and porosity and permeability values are assigned to each grid cell. These porosity and permeability maps are heterogeneous at the core scale, but homogeneous at the grid cell scale. To determine a permeability model, which validates all available data, we use an optimization process. Briefly, we generate an initial permeability field referring to static data. Then, this initial field is iteratively modified until honoring the dynamic data. Data integration is ensured following two processes. The dynamic data are accounted for through the minimization of an objective function. This function measures the mismatch between the laboratory dynamic data and the corresponding numerical simulation results. Static data are directly integrated in the model using a relationship such as  $\log(k(\mathbf{x})) = A\phi(\mathbf{x}) + b(\mathbf{x})$  where  $A$  is a constant and  $b(\mathbf{x})$  is a realization of a random function characterized by a mean  $m$ , a variance  $\sigma^2$  and a given variogram. An initial realization  $b(\mathbf{x})$  is generated assuming reasonable values for its mean, variance and correlation lengths. Given an initial value for  $A$ , we build a 3D permeability field. Then an optimization process is run to modify the unknown parameters  $A$ ,  $m$  and  $\sigma^2$  while honoring the observed pressure variations along flow axis. Second, the so-obtained calibrated permeability field is modified using a gradual deformation based optimization workflow until the mismatch between the observed dynamic data (both  $\Delta p(t)$  and concentration data) and the fluid flow simulation results is minimized. In this second optimization process, the optimization parameters are the same as before plus the correlation lengths of  $b(\mathbf{x})$  and a gradual deformation parameter.

## Nomenclature

$B_g$	gas formation volume factor	$p_o$	oil pressure
$B_i$	phase $i$ formation volume factor	$p_w$	water pressure
$B_o$	oil formation volume factor	$q_{fg}$	free gas flow rate
$R_s$	solution gas-oil ratio	$q_i$	phase $i$ flow rate
$S_g$	gas saturation	$t$	time
$S_i$	phase $i$ saturation	$v_i$	Darcy velocity of phase $i$
$S_o$	oil saturation	$\phi$	porosity
$S_w$	water saturation	$\gamma_g$	$= \rho_g \mathbf{g}$
$\mathbf{g}$	gravity	$\lambda_g$	gas transmissibility
$k$	permeability	$\mu_i$	viscosity of phase $i$
$k_{ri}$	phase $i$ relative permeability	$\rho$	density
$m$	mean	$\sigma^2$	variance
$p_c$	capillary pressure		
$p_{cog}$	oil-gas capillary pressure		
$p_{cow}$	oil-water capillary pressure		
$p_g$	gas pressure		

# Chapter 2

## Literature Review

Reservoir rocks have different properties. The simplest but the most important one of such properties is permeability. Permeability variations in natural rocks can strongly affect the way fluids displace through them. Any realistic modeling of porous media must correctly represent these natural permeability variations. To do so, permeability heterogeneity must be characterized depending on the scale of porous media that we wish to model [50]. In this chapter, we review and discuss various techniques developed to characterize permeability heterogeneity. We consider methods, which incorporate three fundamental degrees of heterogeneities namely pore level, core level and field scale heterogeneities. For the sake of simplicity, the chapter is divided into two sections. Field scale heterogeneity characterization is addressed in section 2.1. Both pore and core level heterogeneity characterization are covered in section 2.2. The chapter is finished with some concluding remarks.

### 2.1 Field scale permeability characterization

A classical approach to characterize permeability heterogeneity at the field scale was introduced by Matthews and Russell [38]. It was further developed and improved by Bourdet *et al.* [9]. This method, which is widely used in well test analysis, gives the average formation permeability on the scale of well spacing. The method is based on the inversion of pressure data under single phase flow conditions. The surface flow rates of specified wells are changed and their corresponding bottom hole pressures are monitored. The pressure change  $\Delta p(\Delta t)$  and its derivative  $\frac{\partial \Delta p}{\partial \Delta t}$  are plotted in a log-log scale as a function of elapsed time  $\Delta t$ . It is then compared to reference type curves. A type curve model is an analytical representation of the pressure response for a given well and reservoir configuration. Once a match is found for both the pressure change and its derivative, the average permeability of the formation can be calculated.

Feitosa *et al.* [20] presented a new characterization algorithm, which can be applied to

estimate reservoir permeability distributions as a function of the distance from the well. They considered pressure data from drawdown and buildup tests. The well is located at the center of a radially heterogeneous reservoir where permeability varies with distance from well. With their proposed algorithm, permeability variations can be directly estimated from well test pressure data. Authors validated their methodology with two synthetic cases, one with  $k = k(\mathbf{x})$  and another one with  $k = k(\mathbf{x}, \mathbf{y})$ .  $\mathbf{x}$  and  $\mathbf{y}$  are locations along axes  $X$  and  $Y$ . They showed that if the permeability profile is smooth, the estimated permeabilities can be accurate. For sharp permeability variations, their method gives the right permeability trend, but the estimated permeability profile represents a smoothed approximation of the true distribution.

Kaczmaryk and Delay [29] used interference pumping test data to infer the hydraulic parameters of a fractured limestone aquifer. The authors assumed that this aquifer can be modeled with a dual-medium approach. They used an inversion procedure in order to match the experimental drawdown pressure data with their analytical model. They showed that fracture permeability is almost constant over the scale of the aquifer ( $\simeq 200 m$ ). Bernard *et al.* [6] characterized the same aquifer using different interference pumping test data. They used an analytical method, which was developed earlier by Delay [15] and reached the same results as Kaczmaryk and Delay [29]. The fracture permeability was rapidly homogenized for distances of  $100 - 200 m$ .

To date, most of the field scale permeability characterization method, use optimization techniques [48, 24, 49]. Basically, the permeability or porosity field is unknown except for a few well (static) data. Geostatistical tools are used to generate an initial reservoir model constrained to the available static data. The model is upscaled and flow simulation is run. The reservoir dynamic data are then compared to the simulated dynamic response of the reservoir model [35]. Generally, the simulated answers do not reproduce the reservoir dynamic data. The fine geological model has to be modified in order to minimize the mismatch between the numerical answers and the dynamic data. This modification or history-matching procedure involves optimization techniques. It is obvious that the number of unknown parameters (*i.e.*, permeability or porosity) is at least equal to the number of grid cells. The question is how to handle hundreds of thousand of unknown variables. This difficulty has motivated the development of specific parametrization techniques, which ensure the preservation of spatial structure and, which decrease the number of parameters. One of these geostatistical parametrization technique was introduced by de Marsily [14]. It is often referred to as the pilot point or master location method. Another geostatistical parametrization technique was suggested by Hu [27]. This method is called the gradual deformation method (GDM). Using GDM, the permeability and porosity fields can be modified from one or a few number of deformation parameters while preserving the spatial variability. Both the pilot point and gradual deformation methods are discussed in details in chapter 5.

## 2.2 Core scale permeability characterization

A huge amount of research works are concerned with the modeling of macroscopic porous media. These models are simple enough to make flow simulations tractable in terms of CPU time, while they also contain the essential features of the porous media [50]. A complete discussion about various models including “spatially-periodic” models, “Bethe Lattice” models, “network” models, “continuum” models etc. can be found in Sahimi [50] and Dullien [18]. In this section, we only review the state of the art pore scale network modelling and its application to heterogeneity characterization. Different techniques of core scale permeability characterization are then presented.

Pore scale network modeling has been used for many years to predict multiphase flow properties as a complementary tool to special core analysis [50, 5]. Normally, pore scale network models represent simplified pore configuration, for which a given transport process can be solved analytically. Typical configurations include regular lattice structures, such as a cubic lattice, with pore bodies corresponding to the vertices of the lattice, and pore throats connecting the pore bodies [64]. Pore bodies are often assigned spherical shapes. Similarly, pore throats may be cylindrical with circular cross sections [43]. The details of procedure for deriving a network model for a given pore space can be found in Sahimi [50]. Network models are the state of the art in the oil industry and are extensively used to relate the macroscopic behavior of porous media to the physics of flow and displacement at the pore scale. They are useful for understanding the effect of pore scale heterogeneity on dispersion, relative permeability and capillary pressure measurements. See for instance the works of Laroche and Vizika [33], Dijeljcic and Blunt [7], Blunt and King [8] and Xu *et al.* [62].

In order to generate a network model that describes the pore and throat system of a reservoir rock, a 3D representation of the rock void space has to be determined first. Micro-CT scanning can provide two-dimensional images of the three-dimensional pore space of sandstones and some granular carbonates with a resolution of a few microns [17]. Several methods have been proposed to generate three-dimensional pore space images from these 2D micro-CT images. All these methods are based on the statistical properties of the porous medium derived from 2D sections. Bakke and Oren [2] used an object base simulation to analyze the grain-size distribution in 2D. Then, they reconstructed a 3D pack of spheres with the same size distribution as in 2D. They used various alteration schemes, such as cementation and clay particle deposition to better simulate realistic sediments.

Kameda [30] selected natural and artificial sandstone samples and produced several 2D micro-CT images for each sample. this author used a pixel-based simulation to reconstruct the 3D pore space from these 2D images. He stated that porosity and correlation lengths estimated from the 2D images should be used together to honor the shape, size, or the scale of the pores and grains in the resulting 3D pore spaces. Fluid flow was simulated for each 3D

model and its absolute permeability was computed. Kameda [30] showed that cross-plotting the simulated permeabilities versus porosities can lead to a single trend, which can be used to estimate permeability if porosity is known.

Okabe and Blunt [45] used a multiple-point statistics to generate 3D pore space representations. They used two-dimensional micro-CT slices as training images. Similar to Kameda's work [30], these authors used pixel-based simulation to generate 3D images that preserve the typical patterns of the void space seen in the thin sections. They stated that multiple-point statistics predicts long-range connectivity of the structures better than standard two-point statistics methods. They also discussed that a proper selection of multiple-point statistics can lead to satisfactory 3D images.

Analytical modeling of macroscopic porous media is not the only way toward their characterization. A lot of routine core analysis techniques are used to characterize the natural rock samples. Improvements in these techniques have led to a better understanding of small scale heterogeneities and their effects on the field scale production. Baraka-Lokmane *et al.* [3] used different routine core analysis methods to fully characterize sandstone core samples. They used X-ray CT scanning, magnetic resonance imaging (MRI), thin section studies etc. to characterize different sandstone sample with different grain size, porosity and mineralogy. The authors found out that these methods are consistent with each other, and that a combination of them allows a full characterization of the rock samples. These authors concluded that combining different petrophysical measurement techniques adds significant value toward a better description of reservoir properties.

Louis *et al.* [37] selected a Vosges sandstone core sample and analyzed its pore level properties. Thin section image analysis provided the grain size and orientation and pore space anisotropy. Pore space anisotropy was estimated from anisotropy of magnetic susceptibility (AMS). The inner structure of the sample was imaged by X-ray CT scanning. All these data helped the authors to detect two internal zones: a loose zone and a tight zone with a porosity of about half of the loose zone. They estimated the permeability of each zone from Kozeny-Carman equation and the microstructural parameters of each layer. Their results were in agreement with laboratory brine permeability measurement. These authors concluded that microstructural data can help to constrain the variations in petrophysical properties such as permeability.

Menéndez *et al.* [39] came to the same conclusion from the microstructural analysis of an artificial granular sample. Two similar sintered glass beads samples were considered. One of them was altered by hot water during 20 hours. Both altered and unaltered samples were observed under laser scanning confocal microscopy (LSCM). LSCM provides images at depth from 0 to 100  $\mu m$ . The microstructural and petrophysical properties such as pore size distribution, porosity and permeability were calculated for both samples. It was shown



that the permeability of the altered sample dropped by more than 6 orders of magnitude. Menéndez *et al.* [39] showed that the pore size decreases with alteration and that tortuosity increases resulting in a pore system much more complex than that of unaltered sample. Again, it was concluded that pore-level heterogeneity can explain the variations in permeability.

Zweers *et al.* [65] outlined that core scale heterogeneity can be safely ignored if the heterogeneity in the reservoir is much larger or much smaller than the scale of the core samples. The difficulty arises when heterogeneity is at the core scale. During the past decades, engineers and researchers have tried to develop different practical and theoretical techniques to obtain a map of permeability variations inside the core sample. Withjack [60] pointed out very early the interest in using CT scanning for special core analysis. Withjack *et al.* [61] then estimated a permeability field for cores from measured CT porosity maps. They assumed that flow was associated to a bundle of stream tubes with constant properties along each stream tube. These authors showed that in-situ permeability variations strongly influence physical dispersion as well as the characteristic shape of the effluent profile.

In a recent publication, Olivier *et al.* [46] used the same correlation technique as Withjack [60] and pointed out the small scale heterogeneity effects over relative permeability measurements. These authors selected a vuggy carbonate rock and performed both steady and unsteady state imbibition tests. Using CT scan porosity data, they characterized the small scale heterogeneities (vugs and carbonate matrix) of the core sample and mapped them to a finely gridded model. They demonstrated that the resulting 3D heterogeneous model provides relative permeability curves much more meaningful than those obtained from the usual 1D homogeneous model. These authors also indicated that imaging techniques favor the understanding of how water sweeps out within porous media at millimeter scale.

deZabala *et al.* [16] studied the brine injection into a vuggy carbonate saturated with oil. Two steady and unsteady state drainage experiments were performed and saturation profiles along flow axis were obtained. Although X-ray CT porosity and saturation maps were available, these authors only used the conventional capillary number and capillary end effect calculation to characterize the flow process inside their sample. It was shown that these methods are inadequate. Xu *et al.* [62] tried to improve the interpretation of the experimental results of deZabala *et al.* using a pore network model. They concluded that their model must represent the CT porosity spatial correlation in order to reproduce the experimental data.

An adequate study of core scale heterogeneity parallel and perpendicular to flow axis was presented by Hamon and Roy [26]. Different experimental methods for measuring core scale permeability heterogeneity were reviewed by these authors (*e.g.*, tracer tests, minipermeameters, CT scanning). They indicated that most of these methods are useful to characterize

heterogeneities perpendicular to flow axis. They examined the effect of small scale permeability heterogeneity on relative permeability calculations. It was pointed out that unsteady state flood experiments are very sensitive to permeability heterogeneities parallel to flow axis even if capillary forces are negligible.

Moctezuma *et al.* [41] studied a highly vugular core sample. A 3D porosity map was obtained for this sample from X-ray CT measurements. Tracer tests were performed and effluent dispersion profiles were obtained. The authors considered a porosity cut-off and generated a core scale 3D grid cell. Cells with porosity higher than the cut-off were considered as high permeability vugs and cells with porosity lower than the cut-off were considered as low permeability matrix. Moctezuma *et al.* [41] concluded that the observed dispersion profiles could be reproduced by adjusting the vug/matrix permeability ratio.

Characterization of heterogeneous porous media using tracer tests was also developed by Fourar [22]. He proposed to model a heterogeneous porous sample by using an equivalent stratified medium. The theoretical model for the displacement of a tracer through a perfectly stratified porous medium gives the tracer flux as:

$$F(\mathbf{x}, t) = 0.5C_0 \times Q \times \operatorname{erfc}\left(\frac{\ln\left(\frac{\mathbf{x}}{vt} \frac{1}{\sqrt{1+H^2}}\right)}{\sqrt{2 \ln(1+H^2)}}\right) \quad (2.1)$$

where  $F(\mathbf{x}, t)$  is the tracer flux at location  $\mathbf{x}$  and time  $t$ ,  $C_0$  is the injected fluid concentration,  $\operatorname{erfc}$  is the complementary error function and  $v = \frac{Q}{Ar\phi}$  is the tracer front velocity, with  $Q$  the flow rate,  $Ar$  the cross sectional area, and  $\phi$  the porosity. In this expression,  $H$  is the heterogeneity factor. It characterizes the degree of the stratified formation heterogeneity. Fourar [22] performed several miscible displacements and measured tracer concentration as a function of time and distance using an X-ray CT instrument. He concluded that  $H$  is a decreasing function of the distance from the inlet of the medium for different samples and proposed an empirical equation for it. He showed that the tracer transport can be predicted along the heterogeneous porous media using the proposed model.

Dauba *et al.* [13] showed that core samples with longitudinal heterogeneity can be characterized using a simple miscible displacement and the concentration profile deduced from CT scan measurements. These authors modeled different heterogeneous core samples and considered two mobile regions. The permeability contrast and volume proportion of each region were then adjusted using history matching techniques. They mentioned that their heterogeneous models result in a better definition of relative permeabilities.

An alternative approach to identify core scale permeability map is based on the analysis of the arrival times of a tracer test. If the front position is known at different times (*e.g.*, through visual or tomographic techniques), arrival time methods can provide a direct map

of the permeability heterogeneity [61]. This approach was extensively studied by Zhan and Yortsos [63]. These authors developed a methodology, which provides permeability at once from the solution of a nonlinear boundary-value problem. This method is based on the direct inversion of the data, rather than on the optimization of an initial random guess of the permeability field. Assuming that Darcy's law [12] is valid for single phase flow in an isotropic porous medium and that the dispersion of the concentration of the injected tracer is negligible, they obtained a nonlinear equation for flow potential  $\Phi$ :

$$\nabla \cdot \left[ \frac{\phi(\mathbf{x}) \nabla \Phi}{\nabla \Phi \cdot \nabla f} \right] = 0 \quad (2.2)$$

where  $\phi(\mathbf{x})$  is the porosity and  $f(\mathbf{x})$  is the arrival time function. The above equation is a partial differential equation, which leads to  $\Phi$ , given appropriate boundary conditions and information about porosity  $\phi(\mathbf{x})$  and arrival time function  $f(\mathbf{x})$ . When  $\Phi$  is known, the permeability field is straightforwardly derived from:

$$k(\mathbf{x}) = \frac{\phi(\mathbf{x})}{\nabla \Phi \cdot \nabla f} \quad (2.3)$$

The suitability of this method was studied for various types of permeability heterogeneity and for various permeability contrasts. When the permeability contrast is low to moderate and the permeability field is spatially correlated, this method was found to work well. Zhan and Yortsos [63] stated that the proposed technique is suitable for laboratory applications. However, their methodology was only validated with synthetic data.

A heterogeneity detection test was introduced by Watson *et al.* [59] based on an immiscible displacement test. Its purpose was to measure the pressure drop across the core during a two phase immiscible displacement. Watson *et al.* [59] assumed that capillary pressure, compressibility and gravitational effects were negligible. They demonstrated that for a constant flow rate, the pressure drop is linear with time provided that the core is homogeneous. They also stated that their method can approximately determine the location where non-uniformity starts in a composite sample. This method was validated by both synthetic and laboratory experiments. Fincham and Gouth [21] used the same technique to measure effective permeability to oil within unconsolidated cores saturated with a low viscosity brine. The method is based on the pre-breakthrough differential pressure measurement during a viscous oil flood. The variations in the slope of the differential pressure curve are used to identify different areas along the flow axis and to estimate their permeability values.

Besides all these experimental methods for permeability characterization, minipermeameters can also be used to study the air permeability structure of the rock samples. Minipermeameters involve a localized flow by injecting gas into a sample through a small tip seal. The resulting pressure transient is monitored and the local permeability is calculated based on

mathematical models [56]. The experiment is fast and yields a map of permeability heterogeneity at the external surface of samples [57, 26, 46].

## 2.3 Concluding remarks

Although well test data provide significant information about permeability variations around wells, stochastic methods are mostly used to obtain an acceptable image of permeability heterogeneity within reservoirs. Using statistical techniques, different images of the reservoir can be created based on the information observed at wells.

Several methods are proposed to characterize core scale heterogeneities, but there is still a lot to do. Engineers use microscopic models such as pore network modeling to characterize core scale fluid flow. In this technique, two-dimensional micro-CT images are used to generate three-dimensional pore space images [2, 30, 45]. These images help to construct pore scale network models [18, 8, 62].

Tracer test results are also used to characterize core scale heterogeneities. In this method, the core model is divided into different regions (*i.e.*, mobile and immobile, stratified, vugs and matrix) and an average permeability or porosity value is assigned to each region [13, 22, 41]. The X-ray CT measurements are used to produce a permeability field from CT porosity data [60, 46, 41]. Minipermeameters can also reveal the surface map of permeability heterogeneity. They are used for a fast and approximate air permeability detection of consolidate core samples [57, 26, 46].

Last, immiscible displacements are used to determine the location of non-uniformities along the core samples from the slope of pressure drop curves [59, 21].

## Nomenclature

$A_r$	cross sectional area	$t$	time
$C_0$	injected fluid concentration	$v$	tracer front velocity
$H$	heterogeneity factor	$\mathbf{x}$	location
$F(\mathbf{x}, t)$	tracer flux at location $\mathbf{x}$ and time $t$	$\Delta p$	pressure change
$Q$	flow rate	$\Delta t$	elapsed time
$erfc$	complementary error function	$\Phi$	flow potential
$f(\mathbf{x})$	arrival time function	$\phi$	porosity
$k$	permeability		

# Chapter 3

## Core Analysis and Measurements

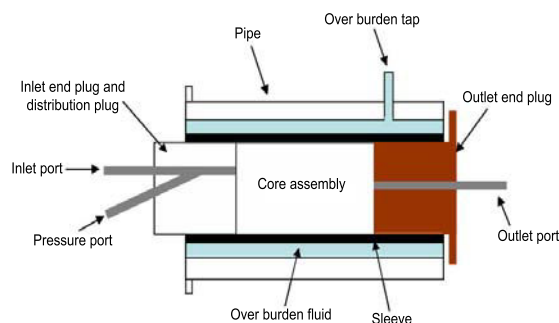
Core samples can be obtained from a porous media such as an outcrop rock or a reservoir long core. They usually have a cylindrical form, 3.0 to 5.0 *cm* in diameter and up to 10.0 *cm* long. Measurements made on core plugs can be subdivided into “routine core analysis” or “special core analysis”. Routine core analysis generally includes measurements of porosity, permeability, fluid saturation, NMR etc. Special core analysis concerns reservoir properties such as wettability, relative permeability and capillary pressure (summarized from online Schlumberger oilfield glossary). In this chapter, we describe both natural and numerical core samples, that we used to validate the methodology proposed in chapters 4 and 5. In section 3.1, the laboratory devices used to perform our experiments are introduced. A short description is given for each device. The experimental procedure followed for each viscous miscible displacement is provided in this section. Section 3.2 is dedicated to the geological description of the natural core samples and the numerical ones. Different core data are collected prior to our viscous miscible displacement. These data are discussed in section 3.3. First, two important rock properties namely porosity and permeability are defined. Then, a short description of how they are measured is given. The porosities and permeabilities measured for the different natural core samples are then reported. Second, some basic statistical definitions are recapped. These definitions are used to provide a two-order statistical analysis of the measured core data.

### 3.1 Laboratory experiments

As mentioned earlier, we aim at performing laboratory experiments, which provide data similar to reservoir scale data. We perform a viscous miscible displacements in heterogeneous core samples and measure the evolution of pressures and fluid concentrations against time. These data are dynamic data since they depend on fluid movements. We also perform laboratory experiments to measure petrophysical properties of our core samples. These data are static as they do not change with time. In this section, we first present the different



a. The X-ray core-holder used for CT imaging during our experiments.



b. Schematic of a core-holder.

Figure 3.1: The core-holder assembly, which is used to accommodate consolidated core samples.

laboratory devices that we used to perform our experiments and then provide a complete laboratory procedure.

### 3.1.1 Experimental devices and setup

The leading idea of our experiment is to inject a high viscosity fluid into a core sample saturated by a low viscosity fluid. The equipment has been designed to conduct an unsteady state miscible flow experiment on consolidated core samples under room conditions. Inlet-outlet pressure drops and X-ray CT images can be collected at successive times. The experimental setup is shown in Figure 3.4. The main components of the experimental setup are introduced below.

**The core-holder.** The core-holders are either a standard Hassler type or X-ray core holder. Both core-holders are designed so that the differential pressure can be measured as a function of time during fluid injection. They can accommodate consolidated cores of 4.0 cm in diameter and up to 15.0 cm long. The appropriate valves are designed so that different measurements (*e.g.*, fluid temperature, fluid conductivity, inlet-outlet resistivity) can be conducted at the same time (Figure 3.1(b)). Hassler core-holder is routinely used for gas and liquid permeability measurements as well as for core flooding experiments. X-ray core-holder is suitable for CT-scan measurements. For both core-holders, a radial pressure is applied to the core sample so that fluids flow only inside the core sample and not around. Due to the special design of these core holders, core samples can be easily interchanged. When the confining pressure is released, the outlet end plug and the distribution plugs are removed and the core sample is easily removed from the sleeve. Spacers are provided to accommodate undersized cores. The distribution plugs located at the inlet face of the sample ensure a more

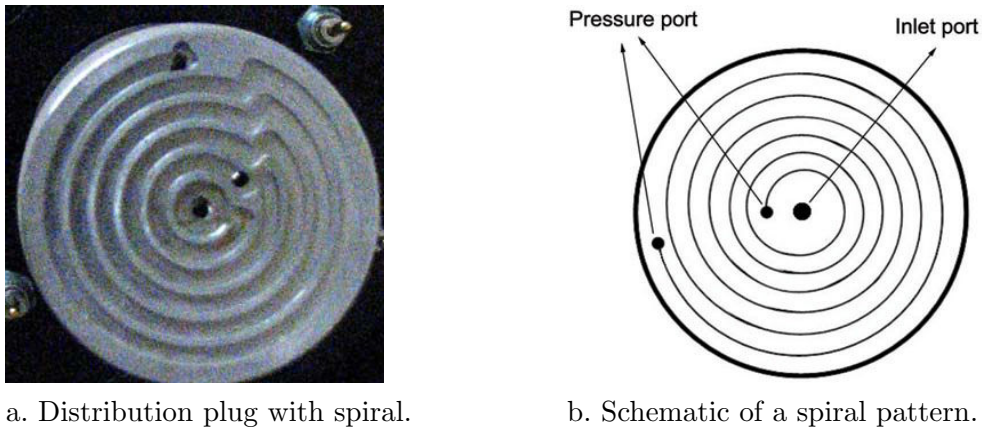


Figure 3.2: The distribution plug with spiral pattern for a full inlet face injection.

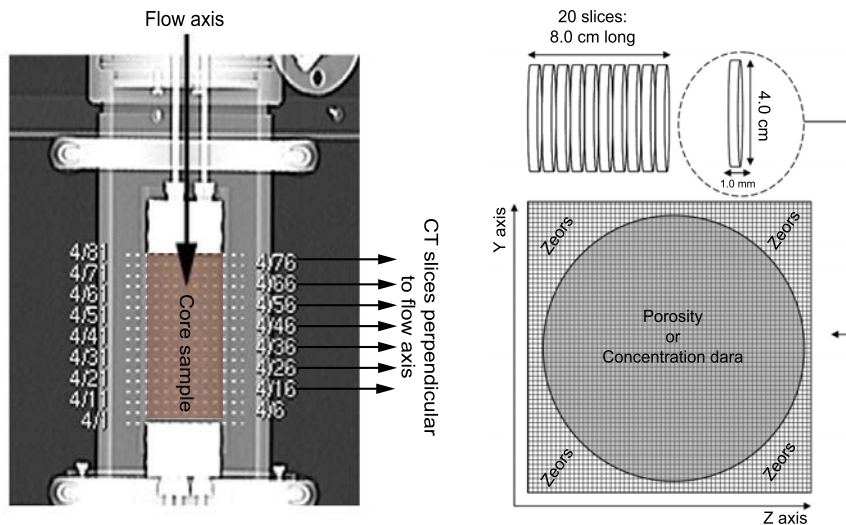
and less homogeneous distribution of the injected fluids thanks to spiral pattern (Figure 3.2).

**The injection system.** The injection system consists in a syringe pump. This pump is designed especially for conducting high pressure fluid flow experiments with limited pulse effect. These pumps can provide continuous injection either at a constant flow rate or a constant pressure.

**The production system.** The purpose of the experiment is to measure the pressure difference between the inlet and outlet faces as a function of time. The pressure at the outlet face should be the atmospheric pressure. The in-place low viscosity fluid (30% NaCl brine) is degassed (see section 3.3.1). However, to avoid difficulties related to gas release in the outlet pipe, a moderate back pressure was applied at the outlet port of the core holder.

**The displacing and displaced fluids.** To avoid any kind of reaction between fluids and clay contents, a 30% NaCl brine is selected as the in-place phase and the core cleaning solvent. At room temperature, the brine has a viscosity of 1.0 *cp*. The invading fluid is a glycerin-brine mixture (pure glycerin and 30% NaCl brine), which is miscible with brine whatever the proportions. To select the glycerin-brine (hereafter named glycerin for simplicity) viscosity, we perform two miscible injection tests with different viscosity ratios, 60 and 200 *cp*. The preliminary results show similar pressure drop behaviors. Meanwhile, most of our available pressure transducers and core holders have pressure limits (maximum 20 bars for pressure transducer and 50 bars for core holders). That is why we decide to perform our experiments with a 60 *cp* glycerin, which implies a lower pressure drop during displacement.

**The X-ray CT scan.** X-ray CT scanning is used to characterize porosity and concentration distributions inside core samples. It is out of the scope of this text to discuss all



a. Radiography of core sample inside the core-holder. b. Schematic 2D matrix of CT data.

Figure 3.3: X-ray CT scanning and the resulting two-dimensional matrix of CT data.

the details of acquisition, optimization and interpretation of X-ray computed tomography techniques. But in general, acquisition of CT data consists of four steps: sample preparation, calibration, data collection and data reconstruction [32]. In this study, we use a Hispeed FX/i medical scanner to perform our X-ray CT measurements. Each scanning consists of data acquisition at several successive locations along the flow axis. The lag space between each two CT images is  $3.0\text{ mm}$  (Figure 3.3(a)). After data acquisition, CT data (in Hounsfield unit) are converted into two-dimensional reconstructed images. A CT image is typically called a slice, as it corresponds to a certain thickness of the sample being scanned. Because of the resolution of IFP scanner ( $100\mu\text{m} \times 100\mu\text{m}$  for a transverse section and each section of  $1.0\text{ mm}$  in thickness), each volume pixel (voxel) represents a volume of  $0.01\text{ mm}^3$ . The original images are masked and cropped. The cropped images consist of approximately  $300 \times 300$  voxels. More than 80% of these voxels have nonzero porosity or concentration values (*i.e.*, active voxels).

**Data Logger.** During injection, the differential pressure  $\Delta p(t)$ , is continuously monitored and recorded by a laboratory computer. As mentioned above, the differential pressure is the difference between the inlet pressure and the outlet pressure. It is recorded by a sensitive differential pressure transducer. The signal of the transducer is converted to a digital form by the data logger. The data logger transmits the digital output to the PC. It is possible to select the time interval between two pressure measurements during the experiment (one second, one minute or one hour).



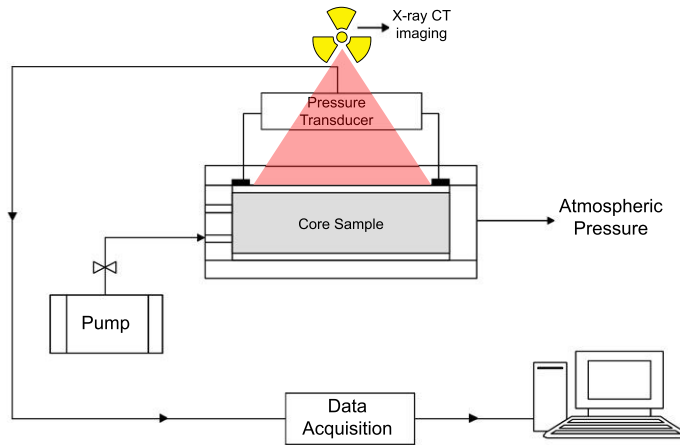


Figure 3.4: The experimental setup.

### 3.1.2 Experimental procedure

This section describes the general procedure followed to conduct our experiments. The core samples used in this study were either limestone or sandstone (see section 3.2). We select samples with a wide range of permeabilities. Our selection criterion mainly involved homogeneity, which is estimated from CT profiles. The core samples are dried in a furnace at temperatures between 50 and 60°C. Then, they are slowly cooled to room temperature. We saturate each dry sample with 30% NaCl brine and measure its porosity and absolute permeability (see section 3.3.1). Then, the viscous miscible displacement is performed based upon the following principles.

*Initial condition:* samples are fully saturated with the 30% NaCl brine at room temperature. Initial pressure is uniform and assumed to be  $10^5 Pa$ .

*Boundary condition:* the core-holder strongly seals the circumference boundary of the core. The flow is assumed to be one dimensional with no flow boundaries.

*Injection period:* the viscous glycerin is injected through one end of the core ( $x = 0$ ) at constant filtration velocity. The escaping fluids are collected at the other end ( $x = L$ ) at atmospheric pressure. The pressure drop across the core is measured as a function of time. CT measurements are also performed for some experiments. The injection period varies between 60 to 80 min depending on the sample pore volume. The injection is stopped after pressure stabilization.

## 3.2 Core description

We use both natural and numerical core samples to validate our methodology. In laboratory, it is a common practice to build composite cores in order to introduce permeability variations along the flow direction [26]. A composite core is a stack of several individual core plugs, which may differ both in porosity and permeability. Thus, we may generate high permeability contrasts in a composite core. In reality, permeability or porosity can vary by a factor of 10 within a single core sample with small scale heterogeneities such as laminae and cross bedding [54]. Computed tomography (CT) adsorption profiles along flow axis provide useful insights about the longitudinal heterogeneity. Generally speaking, a homogeneous core sample has a stable absorption profile while heterogeneity imposes fluctuations. Moreover, cross sectional X-ray CT images make it possible to visualize the surface features and internal structures within the core samples. They are helpful for a rapid heterogeneity characterization of natural core samples.

In this work, we use CT adsorption profile along flow axis to characterize longitudinal heterogeneity. CT slices are taken from the dry core samples every 1.0 *mm* along the sample main axis. The arithmetic average of CT numbers per slice (in Hounsfield unit) is calculated and plotted against location (see Figure 3.6). Variations in the CT profile are attributed to the presence of heterogeneities along the flow direction. The cross sectional CT slices are also generated and displayed in grey scale color-map. Based on our CT scanner resolution, the following features can be characterized: bedding features and sedimentary structures, natural and coring-induced fractures, small scale grain size variations and density distributions [3]. In a grey-scale image, gray to white represent higher density zones (matrix) and dark to very dark grey represent lower density zones (pores). Details are given in section 3.2.1.

In brief, the following samples are used in this study:

1. Two composite core samples made of small plugs stacked together;
2. Four heterogeneous core samples;
3. Four numerical models representing both longitudinal and transverse heterogeneities.

### 3.2.1 Natural core samples

Two artificially heterogeneous core sample named “composite 1” and “composite 2” and four individual heterogeneous samples named “Lavoux”, “LJ001”, “K13” and “SG20” are selected. The composite samples are made of small cylindrical plugs stacked together. To build these composite samples, we select several sandstone and limestone core samples that are 38 *mm* in diameter and up to 80 *mm* long. We only keep the ones considered as homogeneous, that is those whose CT adsorption profiles are stable along flow axis. Small

plugs of maximum 2.0 *cm* length are cut from these homogeneous samples and used to create composites 1 and 2.

### Composites 1 & 2

**Composite 1** is made of four small cylindrical plugs stacked together. These plugs have different geological properties and pore structures.

The first plug (plug1-1) is extracted from a Meule sandstone rock collected from a quarry in north-eastern France (town of Rothbach). The rock is a quartz sandstone with notable clay and micaceous content. Its porosity is largely inter-granular, but altered feldspar also exhibits abundant micro-porosity. Figure 3.5(a) shows a thin section photograph of Meule sandstone under natural light.

The second plug (plug2-1) is extracted from a Lavoux limestone rock collected from a quarry in west central France (Poitiers). The block is a pelotoidal limestone bounded by micro-crystalline calcite. It contains inter-granular macro-porosity resulted from cementation and micro-porosity inside its pellet. Figure 3.5(b) shows a thin section photograph of Lavoux limestone under natural light.

The third plug (plug3-1) is extracted from a limestone rock collected from a quarry in north-eastern France (town of Brauvilliers). The block is an oolitic limestone with high micro-porosity resulted from dissolution of oolites. Figure 3.5(c) shows a thin section photograph of Brauvilliers limestone.

The fourth plug (plug4-1) is extracted from a Meule sandstone rock collected from a quarry in north-eastern France (town of Rothbach). It has the same characteristic as plug1-1 with altered feldspar and clay.

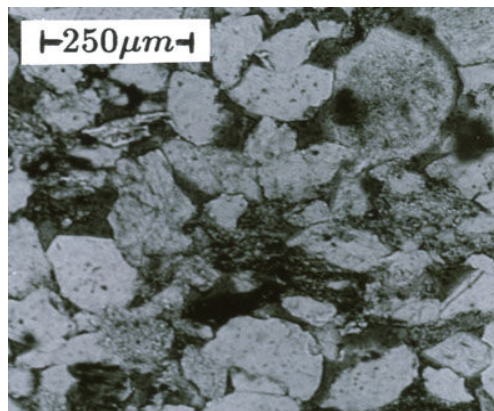
Figure 3.6(a) shows the CT adsorption profile of composite 1. As we can see, the CT profile of each small plug is horizontal with no fluctuations along axis *X*. Some cross sectional CT images related to different plugs of composite 1 are shown in Figure 3.7 and 3.8. Obviously, the Meule sandstone of plug1-1 exhibits millimetric beddings perpendicular to flow axis. The dark gray is related to minerals of quartz and feldspar. The Meule sandstone of plug4-1 and Lavoux limestone of plug2-1 exhibit no obvious heterogeneities. Some white spots are observed in plug2-1, which are related to calcite minerals. The Brauvilliers limestone of plug3-1 shows variations of dark and light gray (macro-pores and calcite, respectively), which are uniformly distributed inside the sample.

**Composite 2** is also made of four small cylindrical plugs stacked together. These plugs exhibit different geological properties and pore structures.

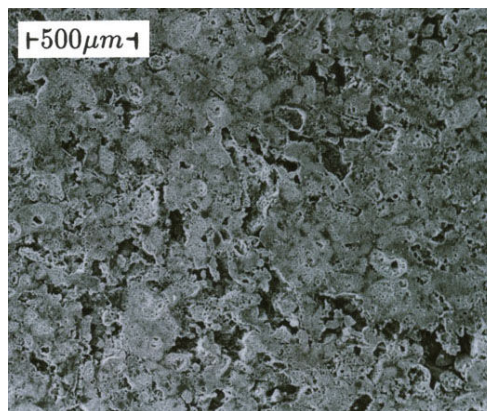
The first plug (plug1-2) is the same as plug1-1.

The second plug (plug2-2) is extracted from a Lavoux limestone rock collected from a quarry in west central France (Poitiers). It has the same geological characteristics as plug2-1.

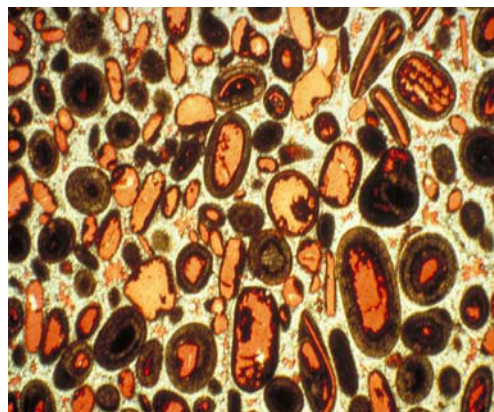
The third plug (plug3-2) is extracted from a sandstone rock collected in a Fontainebleau quarry located near Paris, in France. The rock is entirely composed of quartz grains with



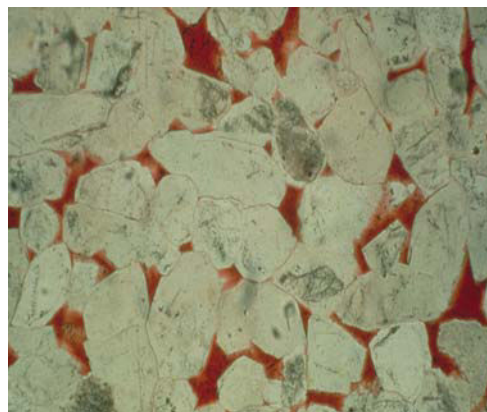
a. Thin section of Meule sandstone under natural light.



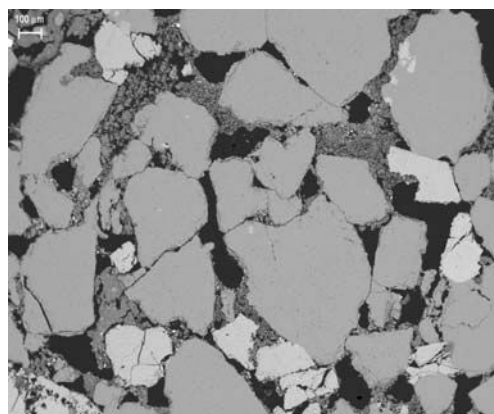
b. Thin section of Lavoux limestone under natural light.



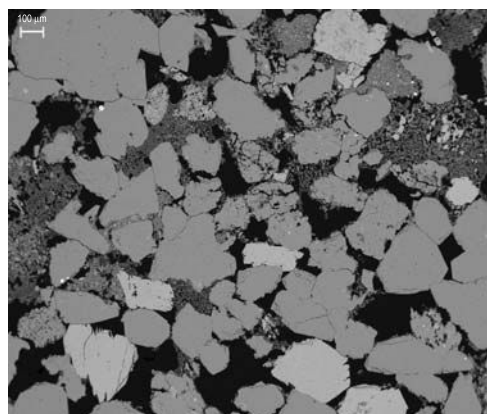
c. Thin section of Brauvilliers limestone.



d. Thin section of epoxy pore cast Fontainebleau sandstone.



e. Thin section of epoxy pore cast sandstone K13.



f. Thin section of epoxy pore cast sandstone SG20.

Figure 3.5: Thin sections of the core samples used in this study (from IFP laboratory of core analysis).

syntactic quartz cementation. Its porosity is inter-granular. Figure 3.5(d) shows a thin section of this Fontainebleau sandstone under natural light.

The fourth plug (plug4-2) is extracted from a Meule sandstone rock collected in a quarry in north-eastern France (Rothbach). It has the same characteristic as plug1-4.

Figure 3.6(b) shows the CT adsorption profile measured for composite 2. The CT profile of each small plug is horizontal with no fluctuations along axis  $X$ . Some of X-ray CT images related to plug3-2 is shown in Figure 3.9. No obvious heterogeneity effect is pointed out.

**The Lavoux** core sample is extracted from a Lavoux limestone rock collected in a quarry in west central France (Poitiers). It is characterized by a low permeability. Its geological characteristics are same as those of Plug2-1. The CT profile (Figure 3.6(c)) measured for this sample shows two distinct regions. We believe that the second half of the sample close to the outlet face contains more clay. No cross sectional CT image is available for this sample.

**The LJ001** core sample is extracted from a Lavoux limestone block originating from a quarry in west central France (Poitiers). This sample is permeable and has the same geological characteristics as Plug2-1. Sample heterogeneity is primarily enhanced through a  $CO_2$  injection: heterogeneity occurs along the flow axis, but also in cross sections. The CT profile of LJ001 is shown in Figure 3.6(d). Porosity close to the injection face is increased due to calcite dissolution, resulting in obvious voidage and small CT numbers. Four cross sectional CT images of LJ001 are shown in Figure 3.10(a1-a4). Dissolution patterns can be observed along flow axis.

**K13** is a clayey sandstone sample extracted from Paris Basin. It contains lots of quartz and feldspar (Figure 3.5(e)). The sample is porous and kaolinitic clay can be easily observed. It is very friable and contains a wide range of grain size (from very fine to very coarse). The CT profile of K13 is shown in Figure 3.6(e). Its cross sectional CT images are shown in Figure 3.10(b1-b4). Dark spots are related to minerals of quartz and kaolinite.

**SG20** is a heterogeneous sandstone sample from Paris Basin. This sample shows numerous insights of alteration of kaolinitic clays. It contains lots of quartz and feldspar (Figure 3.5(f)). Small scale heterogeneities are evidenced by its CT adsorption profile, which shows fluctuations along axis  $X$  (Figure 3.6(f)). The SG20 cross sectional CT images are shown in Figure 3.10(c1-c4). Dark spots are related to kaolinitic minerals or the pores.

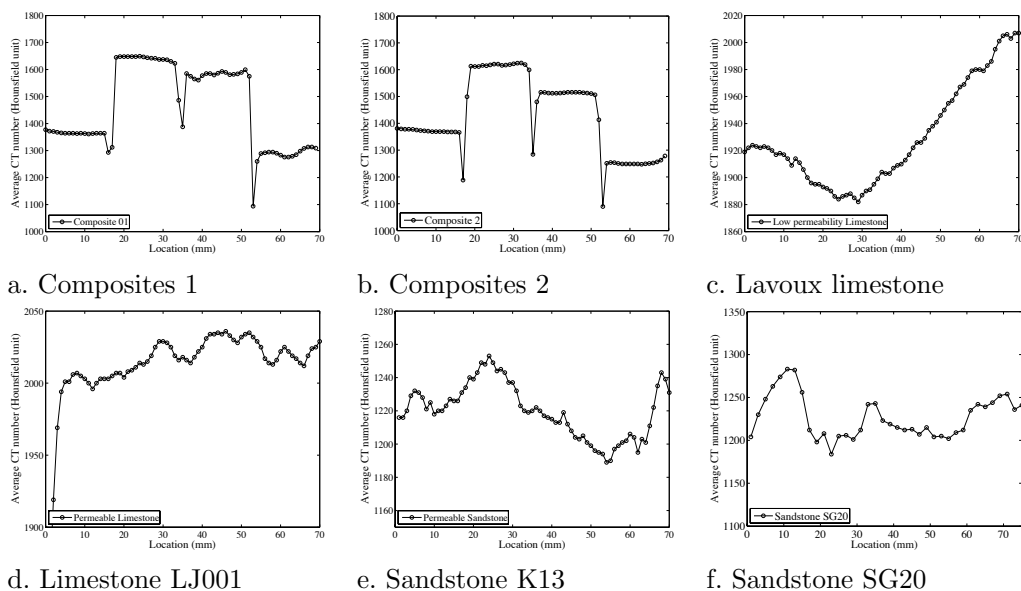


Figure 3.6: Tomography profiles computed for different core samples used in this study. The profiles of composite 1 and 2 evidence that there are still some voids in between the stacked plug.

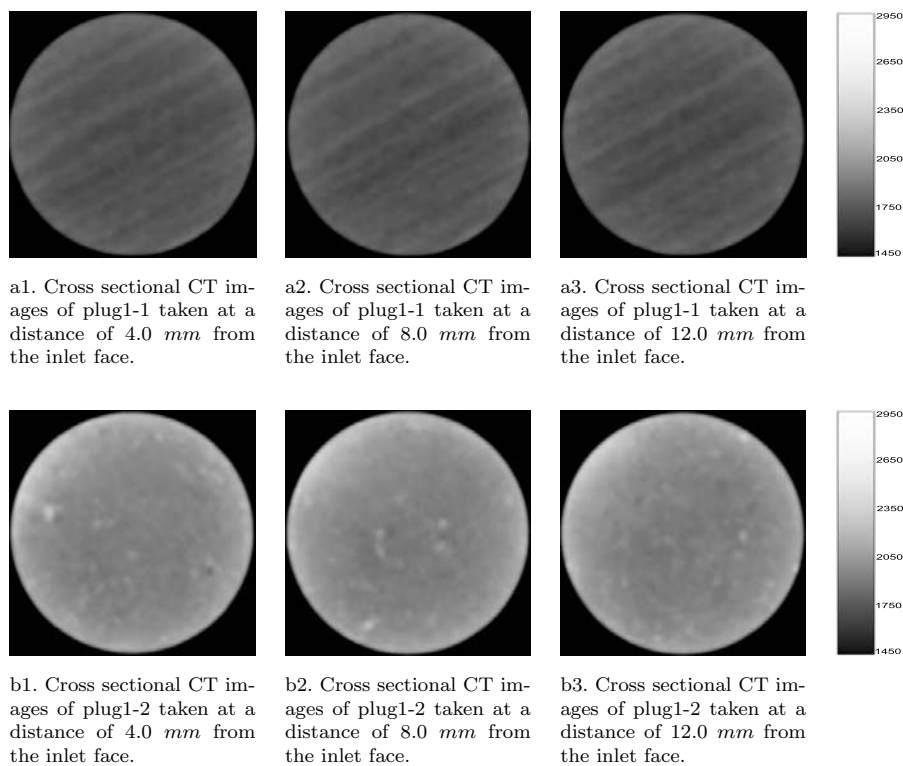


Figure 3.7: Cross sectional CT images of plug1-1 and plug1-2 used to create composite 1. The color bars show CT values in Hounsfield unit.

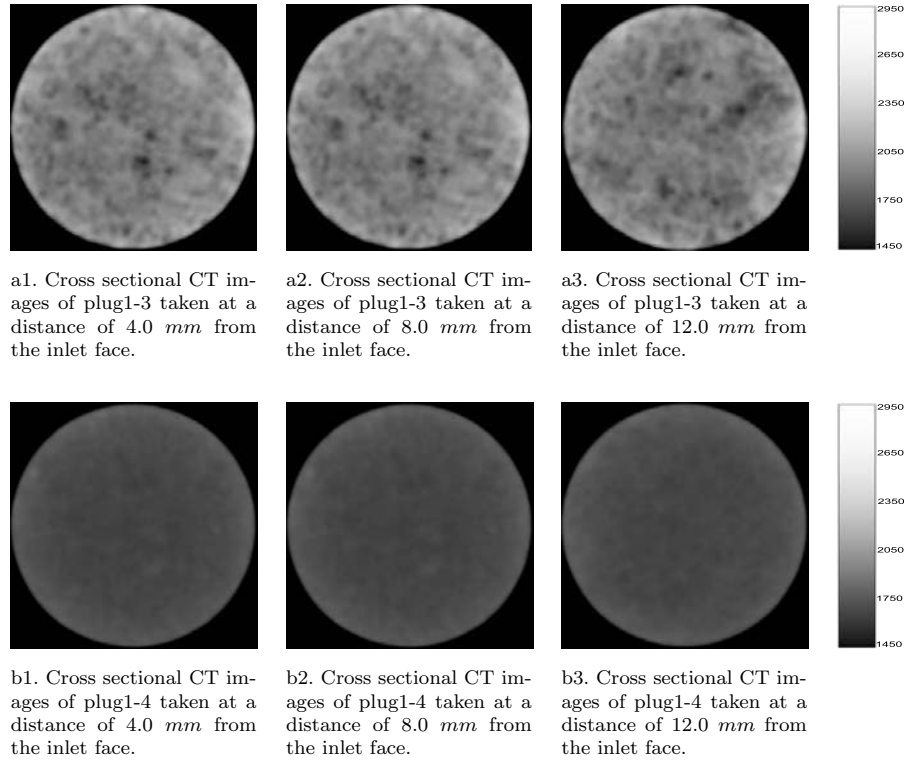


Figure 3.8: Cross sectional CT images of plug1-3 and plug1-4 used to create composite 1. The color bars show CT values in Hounsfield unit.

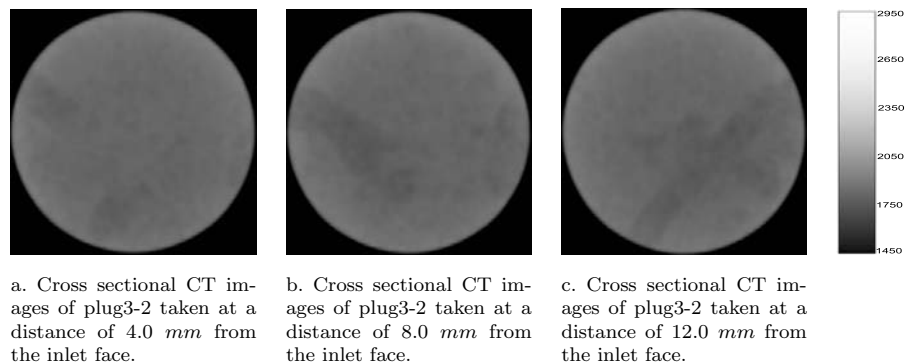


Figure 3.9: Cross sectional CT images of Fontainebleau plug used inside composite 2. The color bars show CT values in Hounsfield unit.

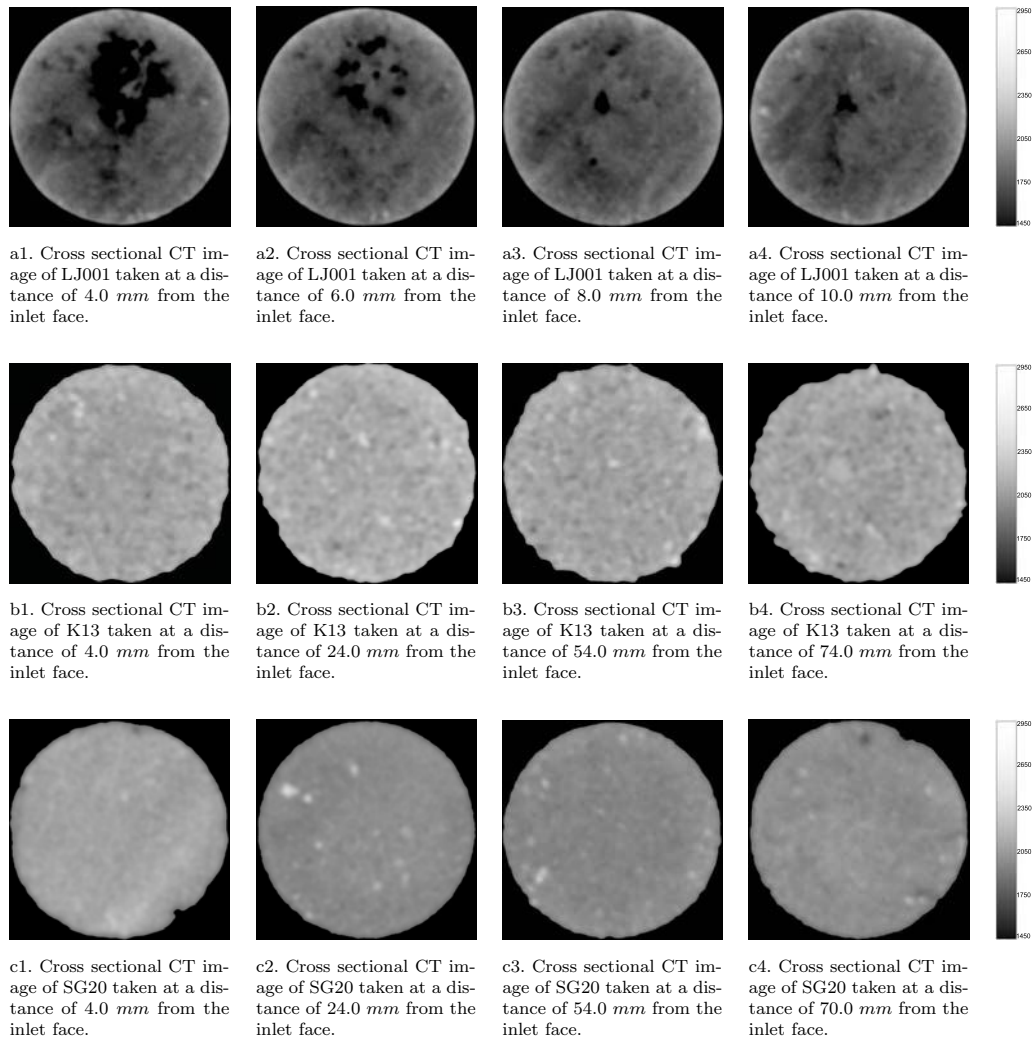


Figure 3.10: Cross sectional CT images of samples LJ001, K13 and SG20. The color bars show CT values in Hounsfield unit.

### 3.2.2 Numerical core samples

Four heterogeneous numerical samples are considered in this study. Two of them named “Model-1” and “Model-2”, exhibit longitudinal heterogeneities only and two of them, named “Model-3” and “Model-4”, present both longitudinal and transverse heterogeneities.

*Model-1* and *Model-2* are constituted of four blocks. The longitudinal heterogeneity is represented by defining these four blocks perpendicular to flow axis with distinct absolute permeability per block. The log-permeability field of each block is generated using the FFTMA geostatistical simulator [34]. It is a random field characterized by a variogram with



small correlation lengths (see Table 3.1). The transverse permeability heterogeneity is ignored. Porosity is constant per block.

**Model-3** and **Model-4** are also constituted of four blocks. In both models, the porosity field is generated from the FFTMA geostatistical simulator. They are random fields with moderate heterogeneity. The permeability field is independent of porosity in Model-3, but it is correlated with porosity in Model-4. Both permeability fields are characterized by longitudinal and transverse heterogeneities. The longitudinal heterogeneity is represented by defining four blocks perpendicular to the flow axis with distinct absolute permeability per block. The transverse heterogeneity is created randomly (by increasing the values of correlation lengths along axes  $Y$  and  $Z$ ). For more information see chapter 6.

Table 3.1: Petrophysical properties considered to generate the numerical core samples.

		Cross sectional area ( $cm^2$ )	Length (cm)	Porosity field					Permeability field				
				$\phi$	$L_x$ (m)	$L_y$ (m)	$L_z$ (m)	$\sigma^2$	$k$ mD	$L_x$ (m)	$L_y$ (m)	$L_z$ (m)	$\sigma^2$
Model-1	block1-1	11.22	1.82	0.17	-	-	-	0.0	70	0.002	0.002	0.003	1.0
	block2-1	11.22	1.78	0.25	-	-	-	0.0	3	0.002	0.002	0.003	1.0
	block3-1	11.22	1.84	0.27	-	-	-	0.0	29	0.002	0.002	0.003	1.0
	block4-1	11.22	1.80	0.22	-	-	-	0.0	62	0.002	0.002	0.003	1.0
Model-2	block1-2	11.22	1.82	0.17	-	-	-	0.0	70	0.002	0.002	0.003	1.0
	block2-2	11.22	1.78	0.24	-	-	-	0.0	4.5	0.002	0.002	0.003	1.0
	block3-2	11.22	1.78	0.09	-	-	-	0.0	106	0.002	0.002	0.003	1.0
	block4-2	11.22	1.78	0.23	-	-	-	0.0	62	0.002	0.002	0.003	1.0
Model-3	block1-3	11.22	1.82	0.19	0.01	0.003	0.002	0.0093	70	0.014	0.02	0.02	0.1386
	block2-3	11.22	1.78		0.01	0.003	0.002	0.0093	4.5	0.014	0.02	0.02	0.1386
	block3-3	11.22	1.78		0.01	0.003	0.002	0.0093	106	0.014	0.02	0.02	0.1386
	block4-3	11.22	1.78		0.01	0.003	0.002	0.0093	29	0.014	0.02	0.02	0.1386
Model-4	block1-4	11.22	1.82	0.19	0.01	0.003	0.002	0.0093	70	-	0.009	0.0143	0.1818
	block2-4	11.22	1.78		0.01	0.003	0.002	0.0093	4.5	-	0.009	0.0143	0.0833
	block3-4	11.22	1.78		0.01	0.003	0.002	0.0093	106	-	0.009	0.0143	0.1448
	block4-4	11.22	1.78		0.01	0.003	0.002	0.0093	29	-	0.009	0.0143	0.1548

### 3.3 Preliminary data analysis

The data collected prior to our laboratory viscous miscible displacement are preliminary analyzed in this section. First, the petrophysical properties of different samples are presented. To do so, we define some basic petrophysical properties and their laboratory measurement techniques. The results of these measurements are tabulated for different natural and synthetic samples in section 3.3.1. Second, some statistical definitions and their numerical calculation techniques are given. The statistical analysis of the available data is presented in section 3.3.2 for some of our natural samples.

#### 3.3.1 Petrophysical analysis

As mentioned in the previous chapter, porosity and permeability are the most important petrophysical properties of porous media.

### Definitions:

**Porosity**  $\phi$  also called “voidage”, is the fraction of the bulk volume that is occupied by pore and void space [18]. Depending on the type of porous medium, porosity may vary from near zero to almost 0.4. Above 0.4, porosity is reached a mechanical percolation threshold, for which the rock sample desegregates. Porosity does not have a practical unit.

**permeability**  $k$ , is a measure of the ability of the fluid to go across the porous medium. It has a great importance in determining the flow characteristics of oil and gas reservoirs and aquifers. Its practical unit is the Darcy. Depending on the type of porous medium, permeability may vary from less than 1.0 milli-Darcy (in granites) to more than 10.0 Darcy (in unconsolidated sandstones).

### Laboratory measurement of porosity

Various experimental methods used to determine porosity have been adequately discussed by Dullien [18]. In this work, we used the “weighting” technique and X-ray CT imaging to measure the porosity of our core samples. The weighting technique is very simple. Porosity is considered as the ratio of the void volume to the total volume of the core sample. As the samples are cylindrical, their total volume can be easily calculated knowing their physical dimensions. For void volume measurement, we proceed as described below.

1. The core sample is weighted when completely dry.
2. The 30 g/l NaCl brine is degassed and filtered by a 0.24 micrometer filter in order to prevent possible plugging phenomena by salt grains during saturation. The salt grains or any other particles in the brine solution can plug the pores and prevent a full saturation (or fluid flow through the connected pores).
3. The sample is evacuated with a vacuum pump for a few hours and then saturated by brine for a sufficiently long time.
4. The saturated sample is weighted and porosity is derived from  $\frac{(W_{saturated}-W_{dry})/\rho_{brine}}{Sample\ Volume}$ , where  $W$  is the sample weight and  $\rho_{brine}$  is the brine density.

The weighting technique, if done with sufficient care, can yield an exact value of the sample porosity [18].

The CT imaging technique can also yield the average porosity of the core samples. To obtain a map of porosity along flow axis, each samples is scanned using our medical scanner. Two series of several CT slices are obtained from the sample under two different states: dry and fully saturated by the 30 g/l NaCl brine. A porosity map is deduced from  $\frac{CT_{dry}-CT_{saturated}}{CT_{air}-CT_{brine}}$  where  $CT_{air}$  and  $CT_{brine}$  are the measured CT of pure air and pure brine [60], respectively. This map is a three-dimensional matrix of porosity values. As porosity is an additive variable, The average porosity value can be calculated using an arithmetic average of the resulting

3D porosity data.

### Laboratory measurement of permeability

Permeability is usually calculated from Darcy's law [12]. Considering the one-dimensional flow of a single-phase fluid through a core sample, Darcy's law [12] is:

$$Q = \frac{kAr}{\mu} \frac{\Delta p}{L} \quad (3.1)$$

where  $Q$  is the flow rate,  $Ar$  is the cross sectional area of the sample,  $\mu$  is the viscosity of the fluid,  $\Delta p$  is pressure drop along the core sample,  $L$  is the sample length and  $k$  is the absolute permeability of the sample. This law states that for a macroscopically homogeneous core sample, there is a linear relationship between flow rate and pressure drop, whose slope provides permeability  $k$ . To measure the permeability of our natural samples, we proceed as recapped below.

1. The sample, which is fully saturated by 30 g/l NaCl brine is clamped between the two distribution end plugs in the core holder. The overburden fluids are either distilled water or Nitrogen. Whatever the fluid, a 30 bar confining pressure is applied to ensure that the brine flows only inside the sample.
2. The brine is filtered by a 0.24 micrometer filter in order to prevent any plugging by salt grains during displacement. It has been also degassed with a simple water pump for 30 min to avoid any gas release during the injection process.
3. The brine is then injected through one end of the core at a constant flow rate. The escaping brine is collected at the other end at atmospheric pressure. The pressure drop across the core is measured when stabilized.
4. The injection flow rate is changed and the stabilized pressure drop is measured again. This process is repeated several times with different flow rates.
5. The pressure drops are plotted against flow rates. The slope of their best linear fit provides  $Q/\Delta p$ . The absolute permeability is then calculated from Equation 3.1.

The porosity and permeability values measured for our samples are reported in Table 3.2. The petrophysical properties of the small plugs used to produce composite 1 and composite 2 are reported in Table 3.3.

### 3.3.2 Statistical analysis

In this section, we will briefly discuss some basic statistical concepts. This concepts are used to derive information from collected porosity data. We will discuss "descriptive statistics", which can be used to understand the characteristics of sample data sets. Then, the

Table 3.2: Petrophysical properties of the core samples studied in this work.

Sample name	Diameter (cm)	Length (cm)	Porosity	Permeability (mD)
Composite 1	3.80	7.24	0.23	10.2
Composite 2	3.80	7.19	0.18	15.4
Lavoux	3.79	7.73	0.23	4
LJ001	4.87	6.22	19	240
K13	3.81	7.88	0.24	170
SG20	3.89	7.96	0.27	33.5

Table 3.3: Petrophysical properties of the small plugs used to create composites 1 and 2.

		Diameter (cm)	Length (cm)	Porosity	Permeability (mD)
Composite 1	plug1-1	3.80	1.82	0.17	70
	plug2-1	3.80	1.78	0.25	3
	plug3-1	3.81	1.84	0.27	29
	plug4-1	3.80	1.80	0.22	62
Composite 2	plug1-2	3.80	1.82	0.17	70
	plug2-2	3.80	1.78	0.24	4.5
	plug3-2	3.80	1.78	0.09	106
	plug4-2	3.80	1.78	0.23	62

“inferential statistics” is introduced in order to get familiar with random variables and its functions. Last, we present statistical tools used to describe spatial relationships. Many standard statistics book cover these topics. See for instance Kelkar [31] or Le Ravalec-Dupin [35].

In statistics, a measured data is called variable as it can change with time or location. Porosity and permeability are two well-known variables in analyzing reservoir characteristics. They are collected at different locations and they usually show spatial variability. In this study, the local porosity of core samples is measured using an X-ray CT imaging technique. For the selected samples, more than two million porosity values are available with a resolution of 3.0 mm along axis  $X$  and 100  $\mu m$  along axes  $Y$  and  $Z$ . This is our sample data. There are several techniques for analyzing these data.

**The frequency distribution** is probably the simplest way to analyze sample data. It summarizes the data in a more compact way. To construct a frequency distribution, the data are divided into intervals called class intervals. The number of measurements falling within a particular class is called a class frequency. The relative frequency can be calculated by normalizing the class frequency by the total number of samples.

**The mean** represents the arithmetic mean of sample data. In other words, the sample mean represents the central tendency of the sample data.

**The variance** represents the spread of the data. It is a quantitative measure of how widely the data are distributed. Mathematically, variance is calculated as:

$$\sigma^2 = \frac{\sum_{i=1}^n x_i^2 - nm^2}{(n-1)} \quad (3.2)$$

where  $n$  is total number of samples,  $x$  is the sample value and  $m$  is the mean of the sample data.

In order to make a conclusion about larger populations from its sample data, we use inferential statistics. A method towards statistical inference is “Estimation”. In estimation, a sample from a population is studied and an inference is made about the population based on the sample. The key to make an accurate inference about a population is random sampling where each possible sample of the same size has the same probability of being selected from the population.

**The random variable** is a variable whose value is generated by a random experiment.

**The probability function**, also called probability density function (PDF), describes the probability that a random variable takes a certain value. The probability function is closely related to the relative frequency distribution, which describes the chance that a value falls within a certain class.

**The distribution function**, also called the cumulative density function (CDF), describes the probability that a variable takes on a value less than or equal to a number. Knowing the distribution function, we can calculate the probability that a random variable falls within a certain interval.

**The Gaussian distribution**, also called “normal distribution”, is the most famous distribution in the field of statistics. Its probability function has a bell-shaped curve and is given by:

$$f(x) = \frac{1}{\sigma\sqrt{2\pi}} \exp\left[-\frac{1}{2}\left(\frac{x-m}{\sigma}\right)^2\right] \quad -\infty < x < \infty \quad (3.3)$$

This distribution has a mean of  $m$  and a variance of  $\sigma^2$ .

**The log-normal distribution** is closely related to normal distribution. If the logarithm of a variable is normally distributed, then the variable itself is log-normally distributed. Its probability function can be written as:

$$f(x) = \frac{1}{x\beta\sqrt{2\pi}} \exp\left[-\frac{1}{2}\left(\frac{x-\alpha}{\beta}\right)^2\right] \quad x > 0 \quad (3.4)$$

This distribution has a mean  $m$  and a variance  $\sigma^2$  as follows:

$$m = \exp\left[\alpha + \frac{\beta^2}{2}\right] \quad (3.5)$$

$$\sigma^2 = m^2[e^{\beta^2} - 1] \quad (3.6)$$

The CT porosity data are available for composite 2, sample K13 and sample SG20. We first analyze their frequency distribution. The number of classes are estimated using the square root of the total number of porosity data [31]. Thus, we divide the sample data into classes of equal width. Calculated relative frequencies of these three samples are plotted in Figure 3.11. For composite 2, two different class frequencies are observed. They are related to different small plugs. As the mean porosity value of some plugs are close to each other, their class frequencies are superimposed. All relative frequencies of porosity data show a bell-shaped form distributed about the mean porosities. If we assume porosity is a continuous variable, then it can be characterized by a Gaussian distribution function. Contrary to porosity, permeability is usually characterized by a log-normal distribution function [31]. The mean and variance of porosity data are reported in Table 3.4.

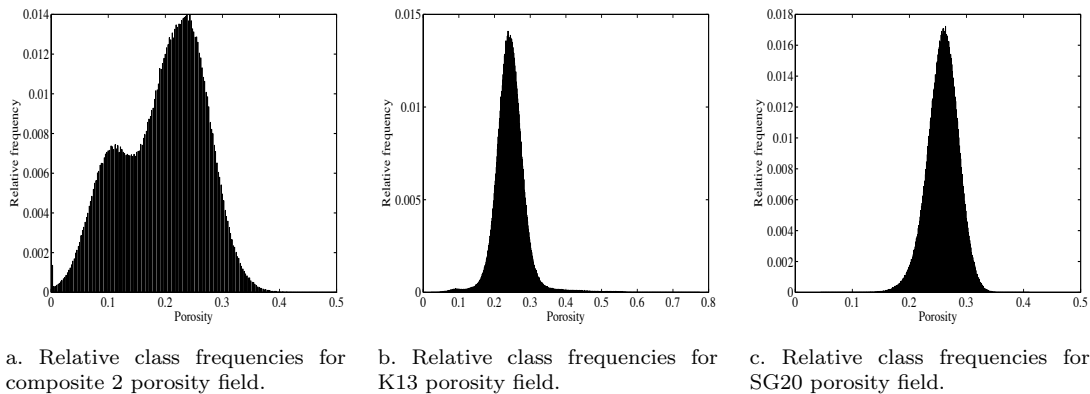


Figure 3.11: The relative class frequencies of porosity data for composite 2, sample K13 and SG20.

Table 3.4: The mean and variance of porosity data.

Sample name	Mean porosity	variance
Composite 2	0.18	0.01
K13	0.23	0.002
SG20	0.26	0.004

We can also analyze statistics of two variables. When several core samples are available from a reservoir, the variations in porosity values may explain the variations in absolute

permeabilities. A similar relation exists between the width and the thickness of channel sand [31]. These information may help to capture a non-unique relationship between two variables. Several tools are used to summarize the statistics between two variables.

**The covariance** is a measure of the relationship between two variables. It is defined as:

$$C(x, y) = \frac{1}{n} \sum_{i=1}^n x_i y_i - \frac{1}{n} \sum_{i=1}^n x_i \frac{1}{n} \sum_{i=1}^n y_i \quad (3.7)$$

where  $x$  and  $y$  are variables,  $n$  is the total number of sample pairs. If  $x$  and  $y$  are positively related (*i.e.*,  $x$  increases with  $y$ ), the covariance has a positive value. If  $x$  increases when  $y$  decreases, the covariance has a negative value. If there is no relation between  $x$  and  $y$ , then the covariance has a value close to zero. The covariance reduces to variance if  $x = y$ .

**The correlation coefficient** is a dimensionless form of the covariance. It is defined as:

$$r(x, y) = \frac{C(x, y)}{\sigma_x \sigma_y} \quad (3.8)$$

where  $C(x, y)$  is the covariance between  $x$  and  $y$  and  $\sigma$  is the square root of the variance (*i.e.*, the standard deviation). The value of the correlation coefficient belongs to  $[-1 \ +1]$ . A strong relation between  $x$  and  $y$  leads to a correlation coefficient close to  $+1$ .

**The variogram** is the most commonly used geostatistical technique for describing the spatial variability. A variogram describes the degree of spatial dependence of the sample values at different locations. It is defined as:

$$\gamma(h) = \frac{1}{2n_h} \sum_{i=1}^{n_h} [x(u_i) - x(u_i + h)]^2 \quad (3.9)$$

where  $\gamma(h)$  is the estimated (or experimental) variogram,  $n_h$  is the number of pairs at lag distance  $h$ ,  $x(u_i)$  and  $x(u_i + h)$  are the data values for the  $i^{th}$  pair located  $h$  lag distance apart. In a qualitative way, the variogram assumes that the data closely located to each others have similar values. The difference between two values increases as distance increases. The variogram starts with a zero value (at  $h = 0$ ) and increases as the lag distance between the values increases. As expected, the variogram is closely related to covariance. Both capture the spatial variability. The variogram increases as the covariance decreases. Referring to the definition of covariance, Equation 3.9 becomes [35]:

$$\gamma(h) = C(0) - C(h) \quad (3.10)$$

where  $C(0)$  is the variance. Figure 3.12(a) shows the experimental variogram of composite 2 porosity data in  $Y$  direction. The variogram starts with a value of zero and increase

sharply. At approximately  $h = 0.002 \text{ m}$ , the variogram reaches a constant level (*i.e.*, sill). This distance is called the “range” of the variogram. This range represent the distance to which neighboring porosities are related to each other. The relationship gets weaker as the lag distance increases. For lag distance greater than the range, the neighboring values are uncorrelated. The experimental variogram for composite 2 and sample SG20 are shown in Figure 3.12. The lack of sufficient pairs does not allow us to estimate their variograms in the  $X$  direction.

We approximate our experimental variograms by models and use these models when correlating permeability with porosity. Details about variograms models can be found in standard statistics books [31, 35]. Here, we only present two models we used in our work.

**Exponential Model.** The equation for the exponential model is as follows:

$$\gamma(h) = C_0[1 - \exp(\frac{-3h}{a})] \quad (3.11)$$

where  $C(0)$  is the variance,  $h$  is the lag distance and  $a$  is the range. This model behaves linearly at short distances near the origin.

**Gaussian Model.** The equation for the Gaussian model is as follows:

$$\gamma(h) = C_0[1 - \exp(-3(\frac{h}{a})^2)] \quad (3.12)$$

where  $C(0)$  is the variance,  $h$  is the lag distance and  $a$  is the range. The variogram changes very gradually at the origin and exhibits an S-shaped curve before reaching a constant value. This variogram is often used to describe very continuous phenomena [35].

Figure 3.13 shows the modeled variograms for sample SG20 and composite 2. The sample SG20 is approximated by an exponential variogram. For composite 2, both exponential and Gaussian can be used. In Figure 3.13, composite 2 is modeled with a Gaussian variogram. The details related to the variogram ranges are given in Table 3.5.

Table 3.5: The ranges related to modeled variograms.

Sample name	$L_y$ (m)	$L_z$ (m)
Composite 2	0.0021	0.0013
SG20	0.0039	0.0033



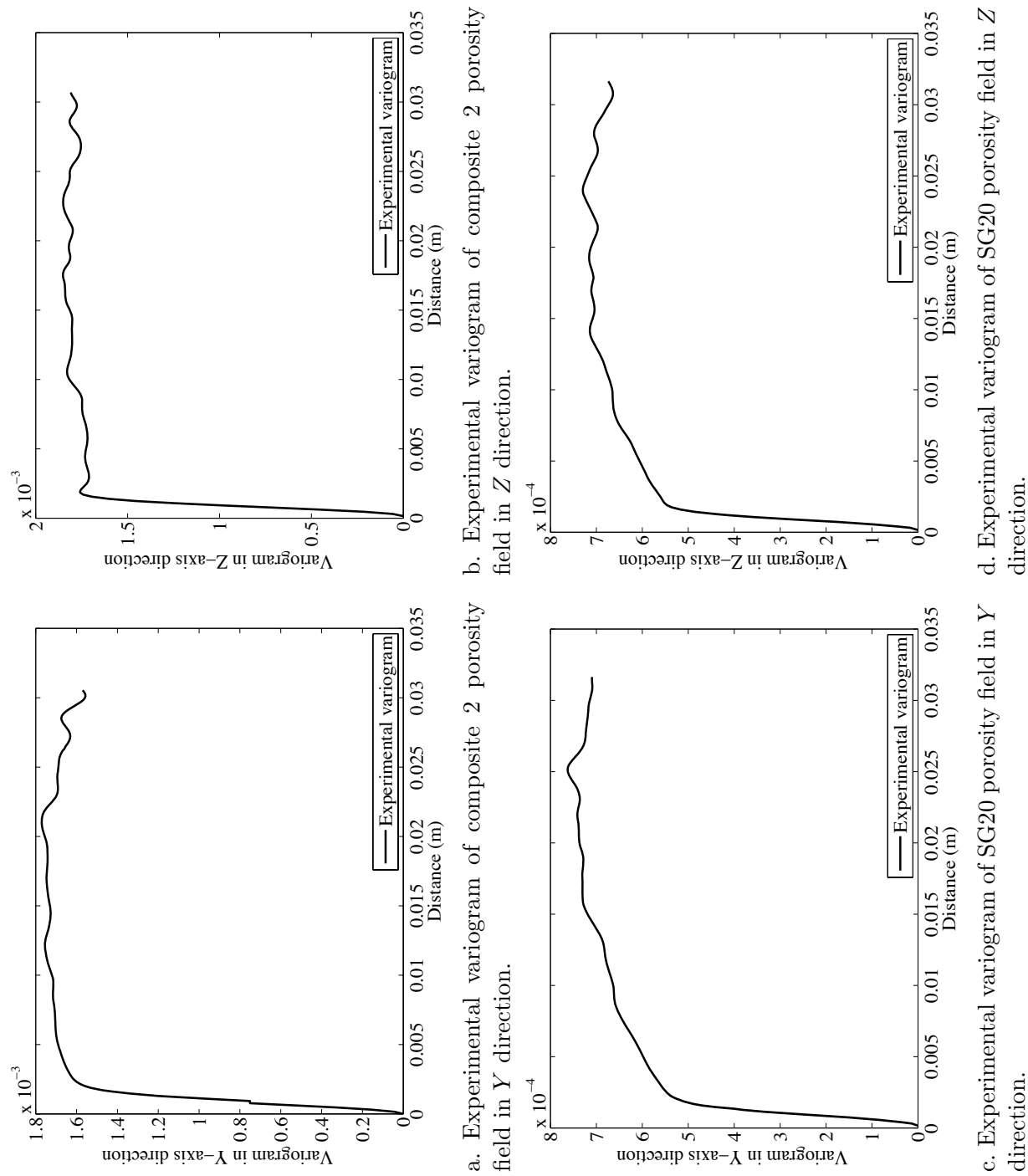


Figure 3.12: The experimental variograms of porosity data for composite 2 and sample SG20. They are calculated using ISATIS geostatistical software package, developed by the Centre de Geostatistique at Fontainebleau in France.

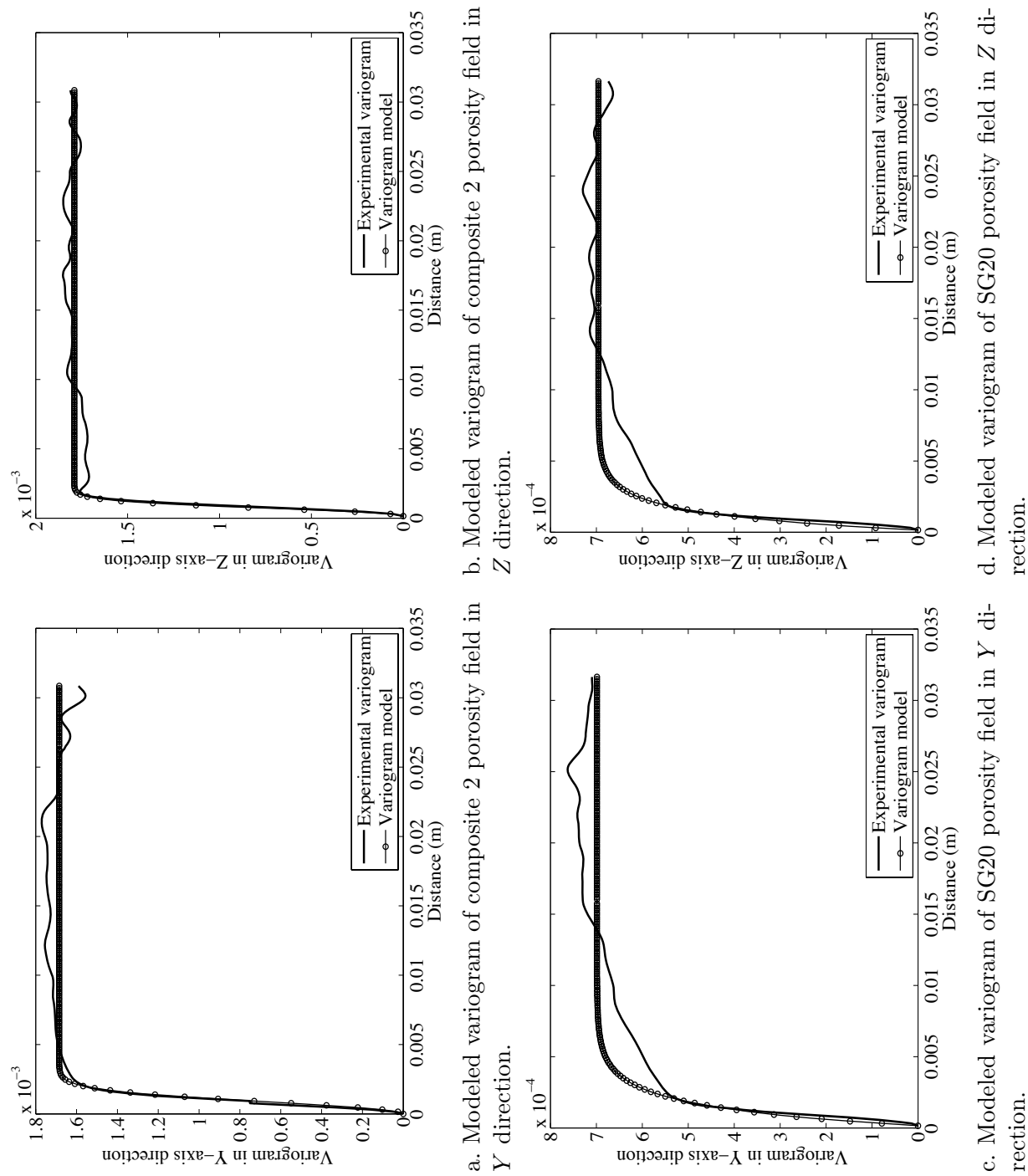


Figure 3.13: The modeled variograms of porosity data for composite 2 and sample SG20. They are calculated using ISATIS geostatistical software package, developed by the Centre de Geostatistique at Fontainebleau in France.

### 3.4 Chapter summary

In this chapter, we first reviewed the experimental setup and procedure followed to collect the petrophysical data and static (porosity) data for different core samples. Different laboratory devices and different steps for performing a viscous miscible displacement were discussed. Then, we briefly described our natural and numerical core samples. A medical CT device was used to reveal small scale heterogeneities along the flow direction axis. Two-dimensional CT images were used to visualize the interior surface of the samples. The petrophysical properties of these samples were measured and reported. The only available static data are the CT porosities of three core samples. The three-dimensional matrix of porosity data were used to find variogram models capable of describing their spatial variability.

### Nomenclature

$A_r$	cross sectional area	$n$	total number of samples
$C(x, y)$	covariance between $x$ and $y$	$r(x, y)$	correlation coefficient between $x$ and $y$
$Q$	flow rate	$x, y$	sample values
$f(x)$	distribution function	$\Delta p$	pressure change
$h$	lag distance	$\phi$	porosity
$k$	permeability	$\gamma(h)$	experimental variogram
$L$	length	$\mu$	viscosity
$m$	mean	$\sigma^2$	variance

# Chapter 4

## One-Dimensional Permeability Characterization

In this chapter, we develop a physical approach to directly assess the one-dimensional core scale permeability profile from a viscous miscible displacement (see also Soltani *et al.* [52]). In section 4.1, we present the methodology to estimate the permeability variations along the flow direction axis. In section 4.2, the proposed methodology is validated through numerical experiments. Our methodology is also applied to data collected during some laboratory experiments. The results are given in section 4.3.

### 4.1 Description of the methodology

To quantify cross bedding heterogeneity inside an unconsolidated core sample, Fincham and Gouth [21] used a drainage process: a core is initially saturated with a low viscosity brine. A viscous oil displaces the brine and the pressure drop across the core is recorded. The pressure variations provide to oil permeability as far as capillary pressure is ignored and the front is very sharp.

In this study, we refer to similar concepts, but we focus on the characterization of the profile of absolute permeabilities. Therefore, we consider the injection of a high viscosity miscible fluid into a core sample initially saturated by a low viscosity fluid. We assume that the two fluids are incompressible and that the temperature is uniform and constant (*i.e.*, porosity, densities and viscosities are constants). The viscose fluid is injected through one end of the core ( $x = 0$ ) at constant filtration velocity. The escaping fluids are collected at the other end ( $x = L$ ) at atmospheric pressure. The pressure drop across the core is measured as a function of time. The following assumptions are made.

1. The fluid movement is dominated by viscous forces. The displacement is miscible: there is no capillary pressure effect.

2. The displacing front is assumed to be very sharp (due to a high viscosity ratio).
3. The absolute permeabilities of the core sample for both the invading and defending fluids are the same. With this assumption we make sure that the local permeability is independent of fluid characteristics.

Considering the one-dimensional flow of a single-phase fluid through a porous medium, the differential form of Darcy's law [12] is:

$$Q = -\frac{kAr}{\mu} \frac{dp}{dx} \quad (4.1)$$

where  $Q$  is the flow rate,  $Ar$  is the cross sectional area,  $\mu$  is the viscosity of the invading fluid,  $p$  is the pressure,  $x$  is the coordinate axis along the flow direction and  $k$  is the absolute permeability of the porous medium. This law states that for a strictly homogeneous core sample, there is a linear relationship between flow rate and pressure drop, whose slope provides permeability  $k$ . The viscous displacement considered here is unsteady-state, which means that the pressure drop along the medium is a function of time. The integration of the above equation with respect to any location  $x$  gives:

$$\Delta p(t) = \int_0^x \frac{-Q\mu}{Ark(x)} dx \quad (4.2)$$

In Equation 4.2, permeability  $k$  is the only variable depending on  $x$ . If we assume that the displacement is piston-like (Figure 4.1), then the pressure drop across the core can be written as the sum of the pressure drop in the invading fluid (high viscosity fluid) and the pressure drop in the defending fluid (low viscosity fluid):

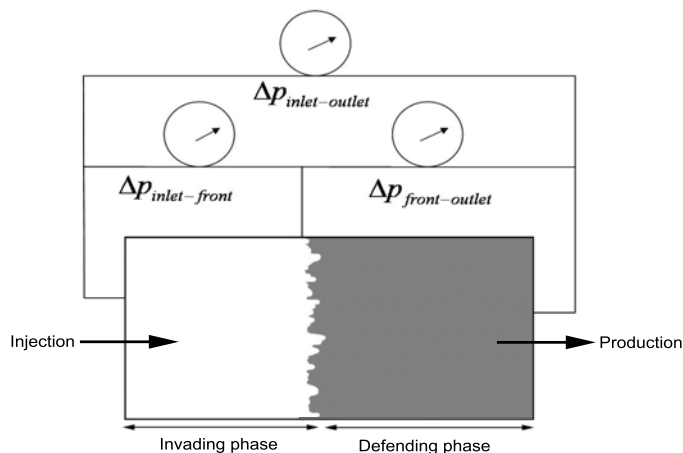


Figure 4.1: Schematic view of the pressure drop across the core sample.

$$\Delta p_{inlet-outlet} = \Delta p(t) = \Delta p_{inlet-front} + \Delta p_{front-outlet} \quad (4.3)$$

Rewriting Equation 4.2 for the invading and defending fluid pressure drops and substituting the results in Equation 4.3 gives:

$$\Delta p(t) = \int_0^{x_f} \frac{-Q\mu_{invading}}{Ark(x)} dx + \int_{x_f}^L \frac{-Q\mu_{defending}}{Ark(x)} dx \quad (4.4)$$

where  $x_f$  is the front location. The concept of Buckley-Leverett frontal theory [10] and our second assumption provides the following relationship between front location and time:

$$x_f = \frac{Q}{Ar\phi} t \quad (4.5)$$

$\phi$  is the porosity. As shown above, the absolute permeability is a function of front location. Referring to Equation 4.5, it is also a function of time. We compute the time derivatives of both sides of Equation 4.4:

$$\frac{\partial \Delta p(t)}{\partial t} = \frac{-Q}{Ar\phi} \left( \frac{Q\mu_{invading}}{Ark(x_f)} - \frac{Q\mu_{defending}}{Ark(x_f)} \right) \quad (4.6)$$

Therefore, we obtain the following formulation for  $k(x_f)$ :

$$k(x_f) = k = \frac{Q^2(\mu_{invading} - \mu_{defending})}{-Ar^2\phi \frac{\partial \Delta p(t)}{\partial t}} \quad (4.7)$$

We thus obtain the variations in  $k$  when the step front moves inside the porous medium. As the front location is a function of time, we can deduce the permeability profile versus injection time.

## 4.2 Numerical validation

We consider two models to numerically validate our methodology. Numerical simulations are performed using a streamline simulator (3DSL, streamsim technologies, Inc). 3DSL is very fast compared to conventional finite difference simulators and suffers less from numerical dispersion [4]. Before going to numerical validation, sensitivity analyses are performed in order to study the effect of the time step size and the grid cell size on simulation results.

### 4.2.1 Sensitivity analysis

A numerical simulation must always respect the physical flow properties of interest. In our laboratory displacement, we displace a low viscosity brine with a high viscosity glycerin. Brine ( $H_2O$ ) and glycerin ( $C_3H_8O_3$ ) are one contact miscible and the viscosity ratio is very

favorable. Thus, the displacement process is very simple and efficient. The displaced fluid moves ahead of the displacing fluid with a stable front. There is also a mixed zone between the pure displacing and displaced fluid regions [50]. Aziz and Settari [1] mentioned that a miscible displacement can be simulated with an immiscible flow model provided that surface tensions are ignored and that the two fluids move at the same velocity. They also added that one can use the Todd and Longstaff [58] parameter to represent the viscosity and density of the mixed zone. In this section, we assume that the extent of miscibility is null and thus, ignore the mixed (transition) zone. We consider numerical conditions identical to those of the laboratory experiments.

1. An immiscible black oil model with only oil and water phases is used. Capillary pressures are ignored.
2. An incompressible mode is used so that viscosities and densities do not change with pressure.
3. The PVT data are defined to represent the laboratory scale displacement. Gravity and all formation volume factors are ignored.
4. Straight line relative permeability curves with end points of 1 are defined. We have  $k_{rw}$  for  $S_w$  and  $k_{ro}$  for  $1 - S_w$ . Thus,  $k_{rw} + k_{ro} = 1$ , whatever  $S_w$ .
5. The water/oil viscosity ratio is set at 60.
6. Wells are defined at inlet and outlet faces of the numerical model in order to mimic a line-drive injection consistent with the homogeneous fluid distribution of spirals.
7. The injection period depends on the model pore volume and varies between 60 and 80 *min*.

These conditions are general. They are respected in almost all of our numerical simulations. For conventional finite difference simulation, a proper time step size and grid cell size must be used to ensure both stability and accuracy (*i.e.*, less truncation error) of the solution [19, 1]. 3DSL does not suffer from instability problem and the solution is always stable no matter the size of the time steps [4]. Truncation error, however, must be taken into account. Truncation errors are often called “numerical dispersion” [1]. They result from time and space discretization and lead to smeared gradient of saturation or concentration profile and early breakthrough. Depending on the technique used to solve the numerical problem, the effects of grid size and time step size are different. Let us consider a one-dimensional reservoir with length  $L$  and uniform cross section  $Ar$ . If the reservoir is regularly discretized with  $\frac{L}{\Delta x}$  blocks between injector and producer, the numerical dispersion  $D^{numerical}$  can be represented as [19]:

$$D^{numerical} \equiv \frac{v}{2} \left( \Delta x \pm \frac{v \Delta t}{\phi} \right) \quad (4.8)$$

$D^{numerical}$  depends on grid cell size  $\Delta x$ , time step size  $\Delta t$ , front velocity  $v$ , porosity  $\phi$  and numerical formulation. The + sign applies to the fully implicit method and the – sign applies to IMPES (implicit in pressure, explicit in saturation). The 3DSL simulator is based on IMPES method. Equation 4.8 tells us that increasing  $\Delta x$  will increase numerical dispersion. The relation between the number of time steps, the grid cell size and the simulation results is complicated. Sensitivity tests must be performed to quantify their effects on numerical dispersion and recovery.

### Effect of time step size

As mentioned above, there is no stability criterion for 3DSL and any desired time step size can be taken. However, a proper number of time steps over a fixed total time is required to capture the non-linearity of the displacement [4]. The non-linearity (convergence) is captured when there is no additional change in recovery when increasing the number of time steps (the simulation time is constant). Non-linearity is a function of mobility ratio, displacement type and heterogeneity. We consider a 3D coarse model constituted of 98000 grid cells ( $80 \times 35 \times 35$ ). The simulation conditions are the same as those described in the previous section. The model is populated with porosity and permeability values. The 3D log-permeability field is generated from the FFTMA geostatistical simulator [34]. It is considered as a random field characterized by an exponential variogram with correlation lengths  $L_x = 0.01 \text{ m}$ ,  $L_y = 0.002 \text{ m}$  and  $L_z = 0.003 \text{ m}$ . The model properties are recapped in Table 4.1. The resulting 3D permeability field is shown in Figure 4.2. Porosity is constant for the entire grid.

Figure 4.3(a) illustrates the convergence in recovery of the streamline method as the time

Table 4.1: Properties of the numerical model with  $80 \times 35 \times 35$  grid cells.

	Cross sectional area ( $cm^2$ )	Length (m)	Porosity	Permeability field				
				$k \text{ mD}$	$L_x$ (m)	$L_y$ (m)	$L_z$ (m)	$\sigma^2$
Model with $80 \times 35 \times 35$ grid cells	11.22	0.072	0.19	15.40	0.01	0.002	0.003	1.0

steps size increases (or number of pressure solves decrease). This figure shows that more than 80 pressure solves (a time step size of  $1.098 \text{ min}$ ) lead to convergence. Increasing the number of time steps results also in a decrease in numerical dispersion and a sharper front (Figure 4.3(c)). Both recovery and watercut are calculated from Equation 4.9.

$$\begin{aligned}
 Watercut^i &= \frac{q_w^i}{q_w^i + q_o^i} \\
 CP^i &= \frac{V_o^i}{V_{oip}} \\
 t_D^i &= \frac{(q_w^i + q_o^i) \times t^i}{V_p} \quad i = \text{time step number}
 \end{aligned} \tag{4.9}$$



In this Equation,  $q_w$  is the water production rate,  $q_o$  is the oil production rate,  $CP$  is the cumulative production,  $V_o$  is the total volume of produced oil,  $V_{oip}$  is the total volume of oil in place,  $t_D$  is the dimensionless time,  $t$  is the injection period and  $V_p$  is the model pore volume. Let us notice that more non-linear problems require greater numbers of time steps to ensure convergence.

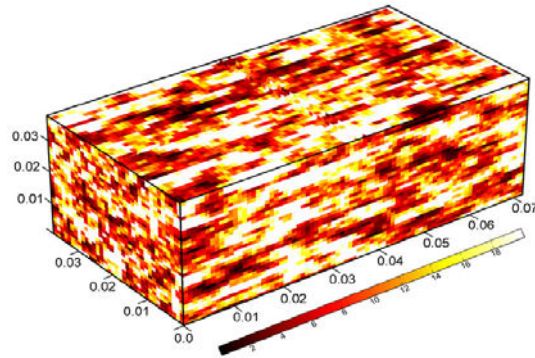


Figure 4.2: The permeability field for the numerical model with  $80 \times 35 \times 35$  grid cells. The color bar shows permeability in mD. The model is  $0.072 \text{ m}$  long.

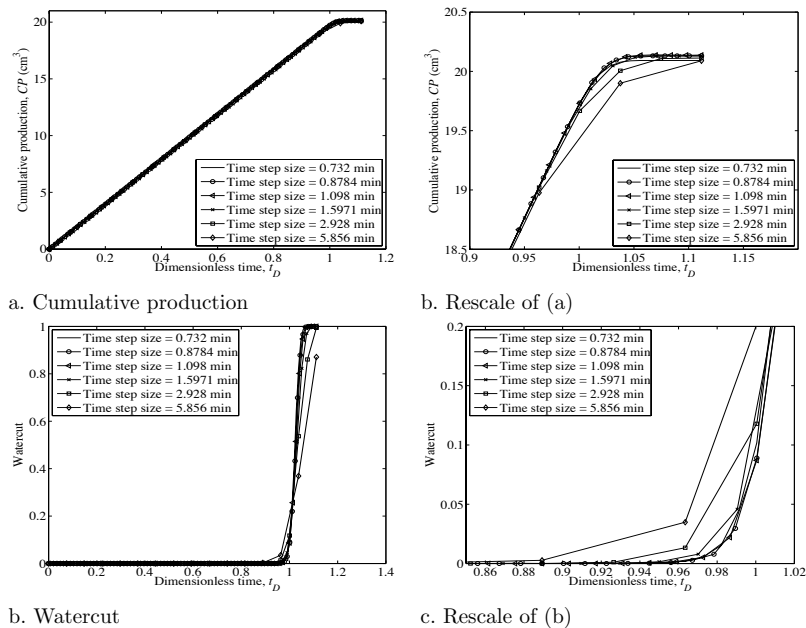


Figure 4.3: Cumulative production and watercut against dimensionless time. Simulations are run for the  $80 \times 35 \times 35$  model while changing the time step size. Total simulation time is  $87 \text{ min}$ .

### Effect of grid cell size

As mentioned in chapter 1, a fine scale model results in a more detailed simulation, but also more CPU time. Increasing the number of grid cells between wells allows for improving the description of front displacement. In this section, we study the effect of grid cell size on numerical dispersion and cumulative recovery. We consider a 3D numerical model constituted of 915920 grid cells ( $80 \times 107 \times 107$ ). The simulation conditions are the same as those explained in section 4.2.1. The model is populated by porosity and permeability values. The 3D log-permeability field is generated from the FFTMA geostatistical simulator. It is considered as a random field characterized by an exponential variogram with correlation lengths  $L_x = 0.01 \text{ m}$ ,  $L_y = 0.002 \text{ m}$  and  $L_z = 0.003 \text{ m}$ . The model properties are reported in Table 4.2. Porosity is constant for the entire grid. The resulting 3D permeability field is shown in Figure 4.4. The time step size is set at  $1.098 \text{ min}$  for all simulations.

**First case.** The simulation is run for the fine scale model and the resulting watercut and

Table 4.2: Properties of the numerical model with  $80 \times 107 \times 107$  grid cells.

	Cross sectional area ( $cm^2$ )	Length (m)	Porosity	Permeability field				
				$k \text{ mD}$	$L_x$ (m)	$L_y$ (m)	$L_z$ (m)	$\sigma^2$
Model with $80 \times 107 \times 107$ grid cells	11.22	0.072	0.19	15.40	0.01	0.002	0.003	1.0

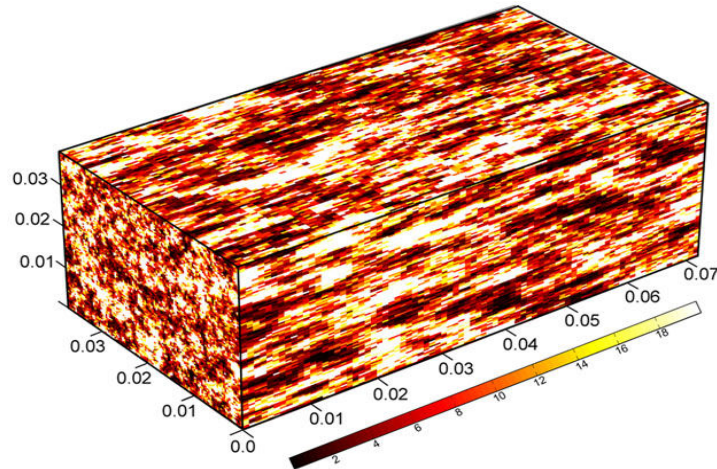


Figure 4.4: The permeability field with  $80 \times 107 \times 107$  grid cells. The color bar shows permeability in mD. The model is  $0.072 \text{ m}$  long.

cumulative production are calculated from Equations 4.9. The model is then upscaled to a coarse grid of  $40 \times 107 \times 107$  cells, the upscaling ratio being  $2 : 1$  for cells along axis  $X$ . The flow simulation is run and the resulting watercut and cumulative production are computed. The same process is repeated with another upscaled model of  $20 \times 107 \times 107$  cells. Note that a simple geometric upscaling is used to derive the coarse models. The results are given

in Figure 4.5. The numerical dispersion increases as the grid cell size increases. This is in agreement with Equation 4.8. The upscaled models underestimate recovery by 2 to 4% in comparison to the fine scale results. Remember that the cumulative production depends on the upscaling algorithm: it changes when changing the upscaling algorithm.

**Second case.** The simulation is run for the fine scale model and the resulting watercut and cumulative production are computed. The model is then upscaled to a coarse grid of  $80 \times 53 \times 53$  cells, the upscaling ratio being 2 : 1 for cells along axes  $Y$  and  $Z$ . The flow simulation is run and the resulting watercut and cumulative production are calculated. The same process is repeated for a coarse grid of  $80 \times 35 \times 35$  cells. Note that a simple arithmetic upscaling is used to derive coarse models because the cells along axes  $Y$  and  $Z$  are perpendicular to flow. The results are plotted in Figure 4.6. The interesting point is that upscaling along axes  $Y$  and  $Z$  does not have a considerable effect on watercut. The front resolution mostly depends on grid cell size between wells. The upscaled models overestimate recovery by 2% in comparison to the fine scale results.

As a conclusion, time step size must be small enough to have a converged solution. The grid cell size must be small in the flow direction to better represent the front. Increasing the number of grid cells along axes  $Y$  and  $Z$  only increase the CPU time. For these reasons, we select a grid with  $78 \times 40 \times 40$  grid cells and proceed with numerical validation.

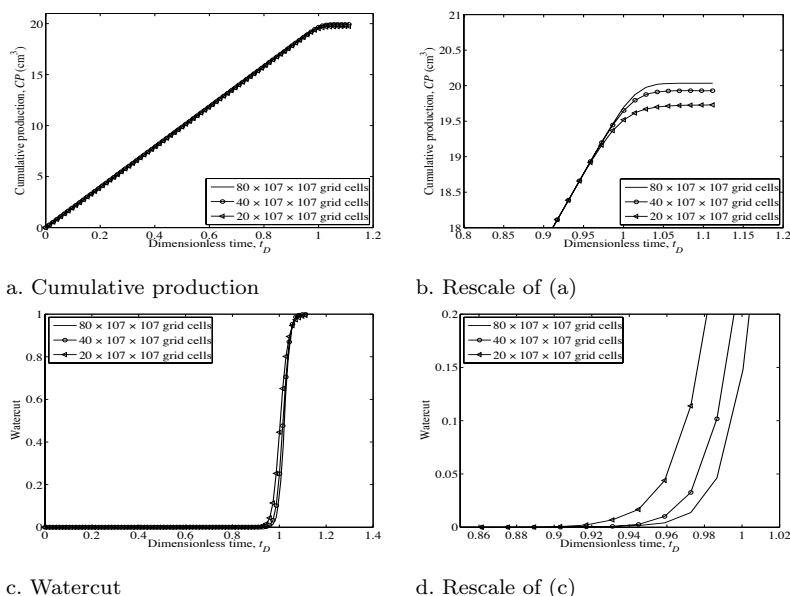


Figure 4.5: Cumulative production and watercut against dimensionless time. The fine model ( $80 \times 107 \times 107$ ) is upscaled, for cells along axis  $X$ . The time step size is fixed to 1.098 min.

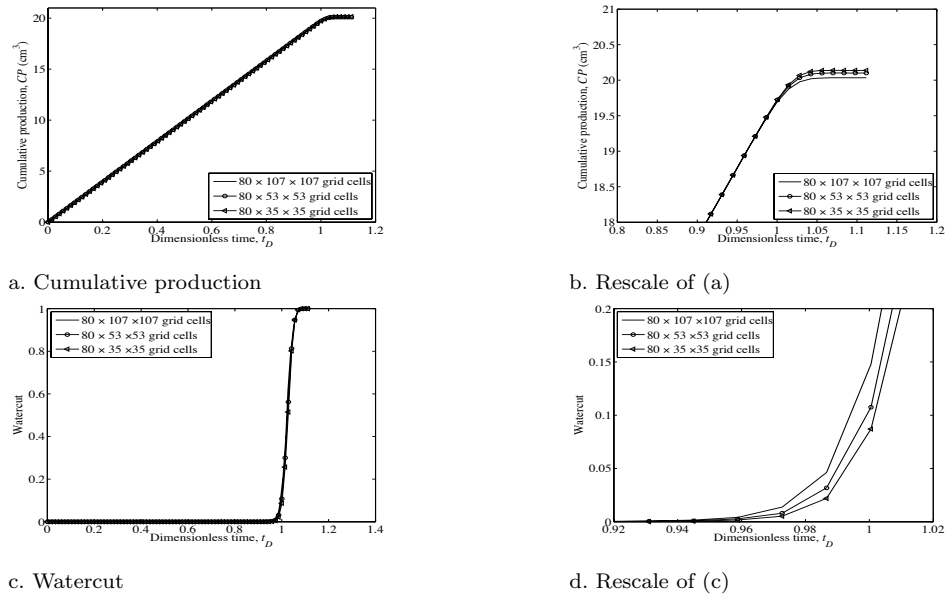


Figure 4.6: Cumulative production and watercut against dimensionless time. The fine ( $80 \times 107 \times 107$ ) model is upscaled for cells along axis  $Y$  and  $Z$ . The time step size is fixed to  $1.098 \text{ min}$ .

## 4.2.2 Numerical differentiation

In order to estimate the derivative of a vector, we usually use numerical differentiation techniques. A simple technique is a two-point derivative estimation. The derivative of a function  $f$  at  $x$  is the slope of a line through points  $(x, f(x))$  and  $(x + h, f(x + h))$  as  $h$  approaches zero. A three-point or five-point estimation can also provide the derivative of a function with smaller truncation errors. In our work, we need to calculate the derivative of the inlet-outlet pressure changes as a function of time (see Equation 4.7). The time lag ( $\Delta t$ ) between each recorded  $\Delta p(t)$  is usually fixed by the data logger in the laboratory. It is consistent with time step size in numerical simulations. Therefore,  $\Delta p(t)$  is a single vector argument. The derivative approximation of this vector can be obtained using two-point estimation at the ends of the vector and three-point (or centered) estimation in the interior. Let us look at an example.

A 3D model of  $78 \times 40 \times 40$  grid cells is built. The grid dimensions are the same as those given in Table 4.1. The grid is populated by homogeneous porosity and permeability fields (*i.e.*,  $k = 10 \text{ mD}$  and  $\phi = 0.25$ ). The simulation conditions are the same as those described in section 4.2.1. The injection flow rate is  $15 \text{ cc/hr}$ . The time step size is set at  $0.9 \text{ min}$  and the flow simulation is run for a duration of  $85 \text{ min}$ . For each time step, the pressure drop

between inlet and outlet faces is derived from Equation 4.10:

$$\Delta p(t) = \frac{\sum_{i=1}^{N_y \times N_z} p_i^{\text{inlet face}}}{N_y \times N_z} - \frac{\sum_{i=1}^{N_y \times N_z} p_i^{\text{outlet face}}}{N_y \times N_z} \quad (4.10)$$

where  $N_y$  and  $N_z$  are the number of grid cells along axes  $Y$  and  $Z$ .  $\Delta p(t)$  is plotted in Figure 4.7(a). A closer look at this  $\Delta p(t)$  (Figure 4.7(b)) indicates that inlet-outlet pressure change is not a monotonic function of time. Even though  $\Delta p(t)$  increases with time, there are small scale fluctuations. Small  $\Delta t$  can lead to more fluctuations especially in laboratory experiments. Figure 4.7(c) shows the derivative estimation of the given  $\Delta p(t)$ . It would be a horizontal line (*i.e.*,  $\partial \Delta p(t) / \partial t = 3 \times 10^{-3}$ ) if no pressure fluctuations existed. To reduce the observed fluctuations in  $\frac{\partial \Delta p(t)}{\partial t}$ , we can apply a smoothing algorithm (*e.g.*, moving average technique). Smoothing techniques require a span, which can have different sizes. A large span increases the smoothness, but decreases the resolution of data, while a small span does not have any considerable effect (Figures 4.8(a) to (c)).

Last, we use a data picking technique, which can effectively reduce the noise. We simply increase the time lag and pick the related  $\Delta p(t)$ . With this method, we change the observation scale and ignore small scale pressure fluctuations. Figure 4.8(d) to (e) shows the calculated  $\frac{\partial \Delta p(t)}{\partial t}$  using this technique.

The methodology presented in section 4.1 is used to derive the model permeability profile along the flow direction axis. The results (Figure 4.9) perfectly duplicate the absolute permeability of the model.

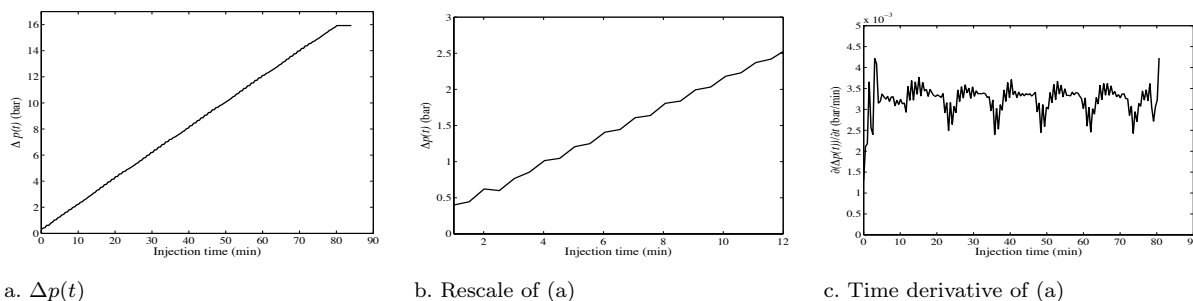


Figure 4.7:  $\Delta p(t)$  and its time derivative fluctuations. The time derivative of inlet-outlet pressure drop would be a horizontal line (*i.e.*,  $\partial \Delta p(t) / \partial t = 3 \times 10^{-3}$ ) if no pressure fluctuations existed.

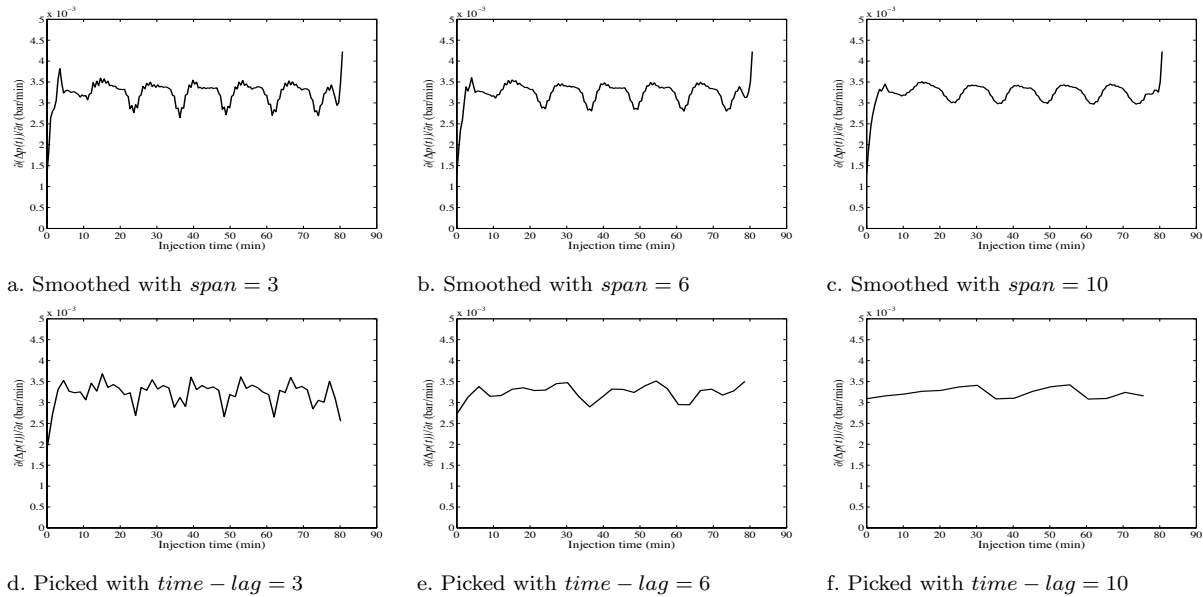


Figure 4.8: Filtering small scale  $\Delta p(t)$  time derivative fluctuations.

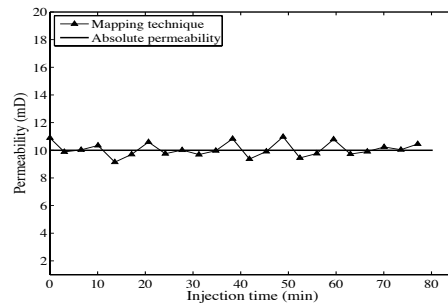


Figure 4.9: Comparison of the processed permeabilities (triangles) with the absolute permeability (line) for the homogeneous model.

### 4.2.3 Numerical immiscible displacement

Two models constituted of  $78 \times 40 \times 40$  grid cells are considered (Figure 4.10). These models named “Model-1” and “Model-2” are created based on two laboratory samples “composite 1” and “composite 2”, respectively (see section 4.3). The properties of each model are reported in Table 3.1. The simulation conditions are given in section 4.2.1. The time step size is set at  $0.8 \text{ min}$ . During the numerical simulations, the injected fluid invades the blocks one after another. Numerical simulation provides pressure and saturation data for all grid cells at different time steps. For each time step, the pressure drop between inlet and outlet faces is derived from Equation 4.10. The numerical pressure drops are plotted for both Model-1 and Model-2 in Figure 4.11. The  $\Delta p(t)$  behaviour clearly shows the existence of four different

layers in both models. Two-dimensional images of the three-dimensional saturation maps (Figure 4.12) show a sharp front at different injected pore volumes ( $PVI$ ). One should notice that the front sharpness can change when the range of the permeability variogram changes.

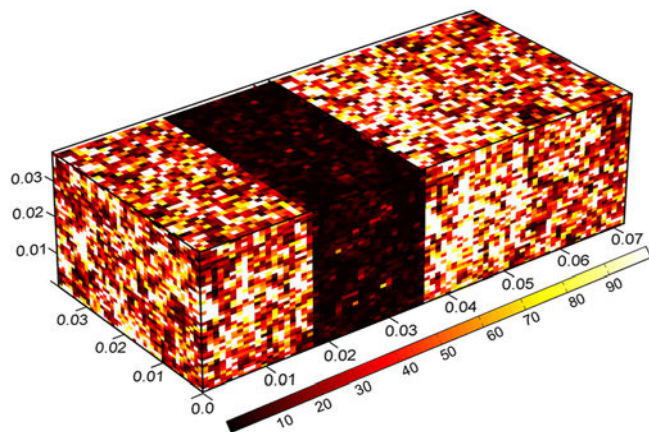


Figure 4.10: The permeability field for the numerical Model-2 ( $78 \times 40 \times 40$  grid cells). The color bar shows permeability in mD. The model is  $0.072\text{ m}$  long.

The methodology presented in section 4.1 is applied to estimate permeability variations

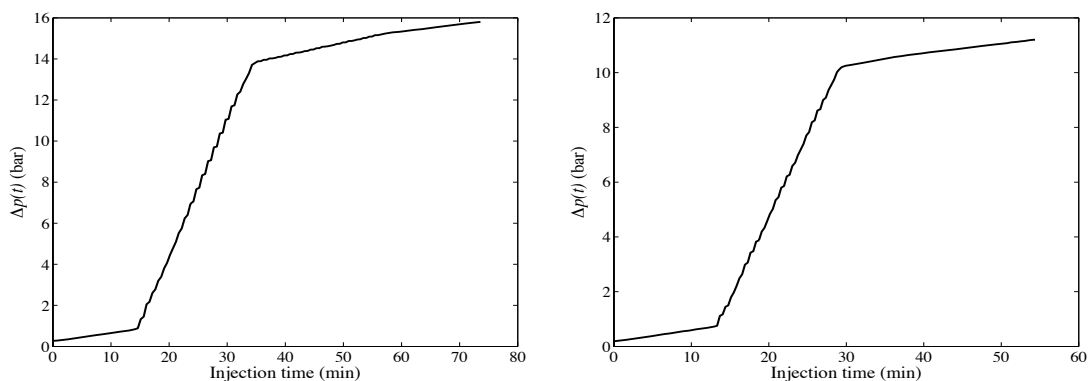


Figure 4.11: Numerical pressure drop data for Model-1 (left) and Model-2 (right) when performing immiscible displacement.

along the flow direction axis from the simulated pressure drop. The processed results are compared to the absolute permeabilities in Figure 4.13. For Model-1, the permeabilities derived from our methodology duplicate the actual permeabilities of the plugs. For Model-2, the estimated permeability of the third plug is slightly overestimated. This is because the inlet-outlet pressure changes are less sensitive to high permeability values ( $\Delta p(t)$  is inversely proportional to permeability). Small variations in  $\Delta p(t)$  results in high variations in estimated permeabilities. One should not forget the effect of permeability variations

perpendicular to flow axis. Here, we ignore the transverse permeability heterogeneity and simply check that the local permeability values derived from our methodology reproduce the actual permeabilities of the different blocks in our numerical models. The result of our 1D permeability mapping technique shows a good agreement with the absolute permeability of the selected blocks. To measure the difference between actual and estimated permeabilities,

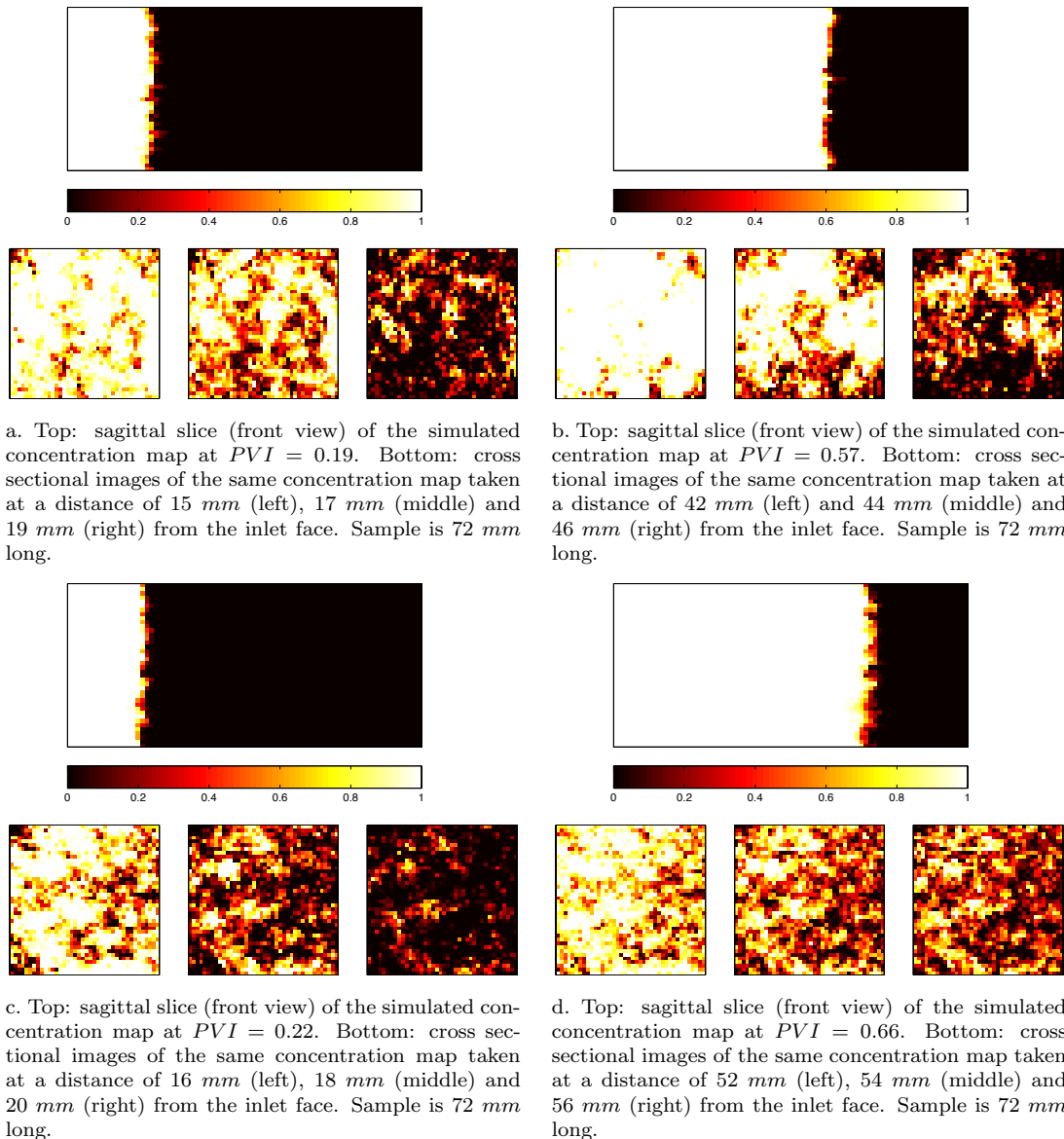


Figure 4.12: 2D images of the 3D simulated concentration maps at different times for numerical Model-1 (top) and Model-2 (bottom) when performing immiscible displacement. The color bars show the injected fluid concentrations.



we define a relative error  $\epsilon^{relative}$  as:

$$\epsilon^{relative} = \left( \frac{\sum_{i=1}^{nvalues} |k_i^{estimated} - k_i^{actual}|^2}{\sum_{i=1}^{nvalues} (k_i^{actual})^2} \right)^{0.5} \quad (4.11)$$

In this Equation,  $nvalues$  is the number of permeability values,  $k_i^{estimated}$  is the local permeability calculated from Equation 4.7 and  $k_i^{actual}$  is the average permeability of the block where the displacement front is located. In such conditions, the relative error between the actual permeabilities and estimated ones is less than 0.13 for both Model-1 and Model-2 (ignoring the overestimation in the third block of Model-2).

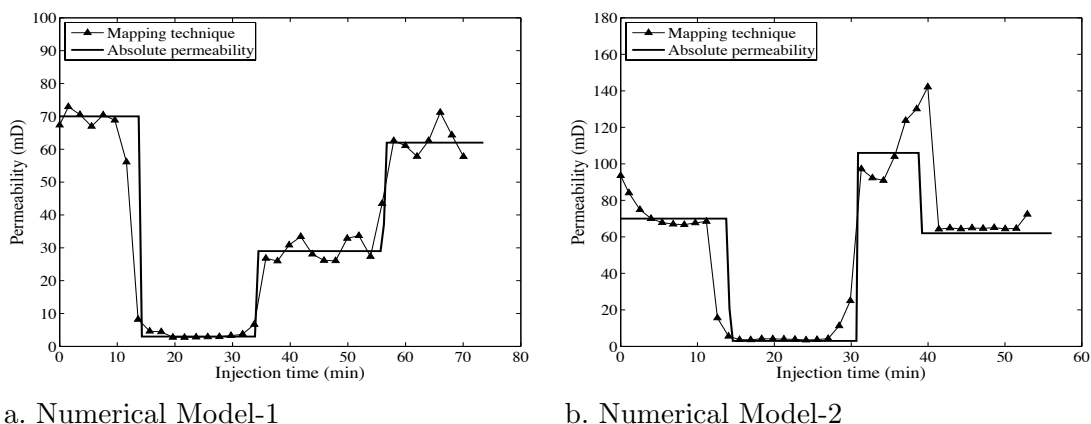


Figure 4.13: Comparison of the processed numerical permeabilities (triangles) with the absolute permeability of each block (lines) for Model-1 (a) and Model-2 (b) when performing immiscible displacement.

#### 4.2.4 Numerical miscible displacement

We also simulate miscible displacements to investigate the influence of miscibility on the pressure drop. If the displacing and displaced fluids are first contact miscible and viscosity ratio is favorable, then the displacement process is simple and efficient. The displaced fluid moves ahead of the displacing fluid, the displacement front is stable and there is a mixed zone between the pure displacing and displaced fluid regions [50]. In the previous section, we simply ignored the mixed zone. In this section, we use a modified form of the Todd and Longstaff miscibility coefficient defined in 3DSL. 3DSL's miscible model assumes that the invading phase is miscible with the defending phase, whatever the pressures. In our case,

the extent of miscibility is limited due to the high viscosity ratio. We assume that 10% of the invading phase components dissolve into the defending phase. 3DSL calculate the mixed zone viscosity from a quarter-power mixing rule [4]. Miscible displacements are simulated for the two models described above with flow conditions identical to those of the immiscible case. The numerical pressure drops are plotted for both Model-1 and Model-2 in Figure 4.14. The existence of the mixed zone between the invading and defending fluids results in smoother transitions in pressure profile. Two-dimensional images of the three-dimensional saturation maps (Figure 4.16) show that the front remains sharp and the effect of miscibility is negligible. The estimated permeabilities along the flow axis are shown in Figure 4.15. The miscibility results in minor change in the slope of the pressure drop curve and slight underestimation of permeability values (Model-1). The overestimation in the third block of Model-2 is again observed. A strong agreement is still observed between the actual and estimated permeabilities.

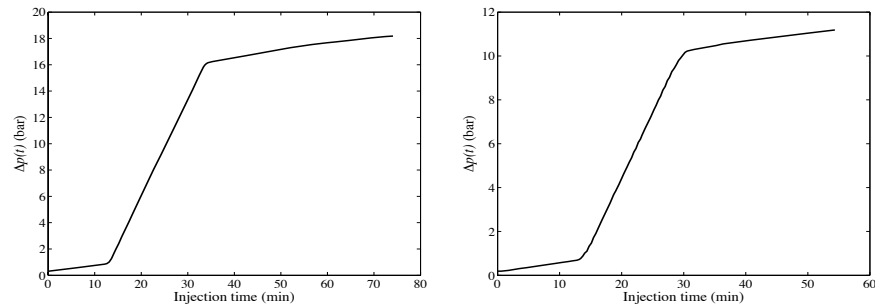
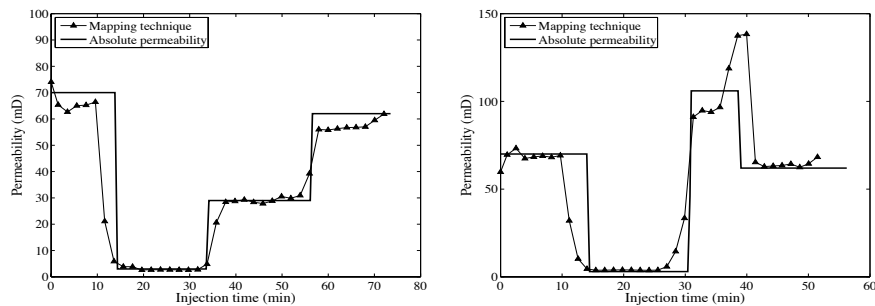


Figure 4.14: Numerical pressure drops for Model-1 (left) and Model-2 (right) when performing miscible displacement.



a. Numerical Model-1

b. Numerical Model-2

Figure 4.15: Comparison of the processed numerical permeabilities (triangles) with the absolute permeability of each block (lines) for Model-1 (a) and Model-2 (b) when performing miscible displacement.

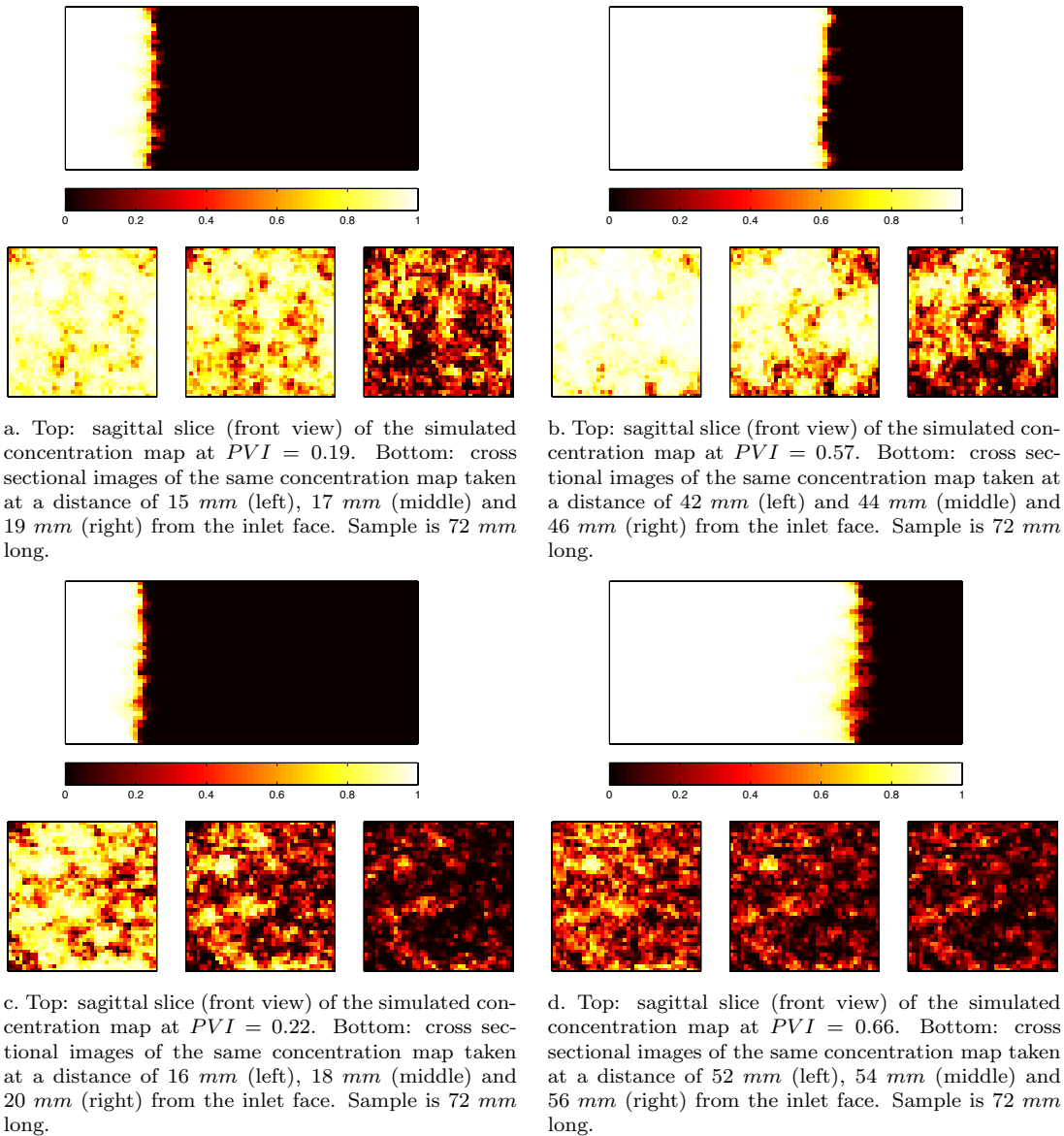


Figure 4.16: 2D images of the 3D simulated concentration maps at different times for numerical Model-1 (top) and Model-2 (bottom) when performing miscible displacement. The color bars show the injected fluid concentrations.

### 4.3 Experimental validation

We use an experimental device thought up to conduct unsteady state flow experiments inside consolidated core samples submitted to room pressure and temperature condition (see section 3.1.1). During the experiments, we handle two types of samples: two artificially

heterogeneous samples built from plugs stacked together and three heterogeneous cores. For a complete discussion about these samples, see chapter 3. The following parameters are measured for each sample.

1. Its physical and petrophysical properties (length, diameter, weight, porosity and absolute permeability) are measured prior to any experiment.
2. The viscous miscible displacement is performed and  $\Delta p(t)$  is recorded. An inverse injection is also performed if necessary.
3. The concentration maps are collected at successive times according to CT scan availability. The CT concentration data are calculated from  $\frac{CT-CT_b}{CT_g-CT_b}$  where  $CT_b$  is the measured CT of the core saturated with brine and  $CT_g$  is the measured CT of the core saturated with glycerin. The use of this equation requires an accurate CT slice positioning: two-dimensional CT slices for the brine saturated sample and the sample submitted to the miscible displacement experiment must be collected at the same location. This is discussed in details in chapters 6.

In the following sections, we present the results of our interpretation technique to derive the permeability profile from the pressure drop data.

### 4.3.1 Experimental results

#### Composite samples

The two artificially heterogeneous samples (composite 1 and composite 2) are initially saturated by a 30 g/l NaCl brine at room temperature. The initial pressure is uniform and assumed to be  $10^5$  Pa. A strong core-holder seals the circumference boundary of the core samples so that flow is linear with no flow boundary conditions. For any stable miscible displacements, convection should control dispersion. The results of tracer tests are usually used to determine convenient flow rates. However, Fourar *et al.* [23] showed that for heterogeneous core samples, the effluent concentration profiles do not depend on flow rates (*i.e.*, convection dominates the dispersion) and molecular diffusion can be ignored. Our experiments are performed with flow rates, which correspond to the optimal flow rate allowed by our laboratory devices (core holder and pressure transducers). For the composite samples, a 60 cp glycerin is injected at a constant flow rate of 15 cc/hr. The pressure drop is recorded until stabilization.

Our methodology is based on an important assumption, which states that the front is sharp during displacement. To check this assumption, CT scan measurements are collected for composite 2. Selected CT images (Figure 4.17) show that fluid displacement is quite stable and the assumption relative to the sharpness of the front is reasonable. A complete discussion about the noise and CT image processing is given in chapter 6.

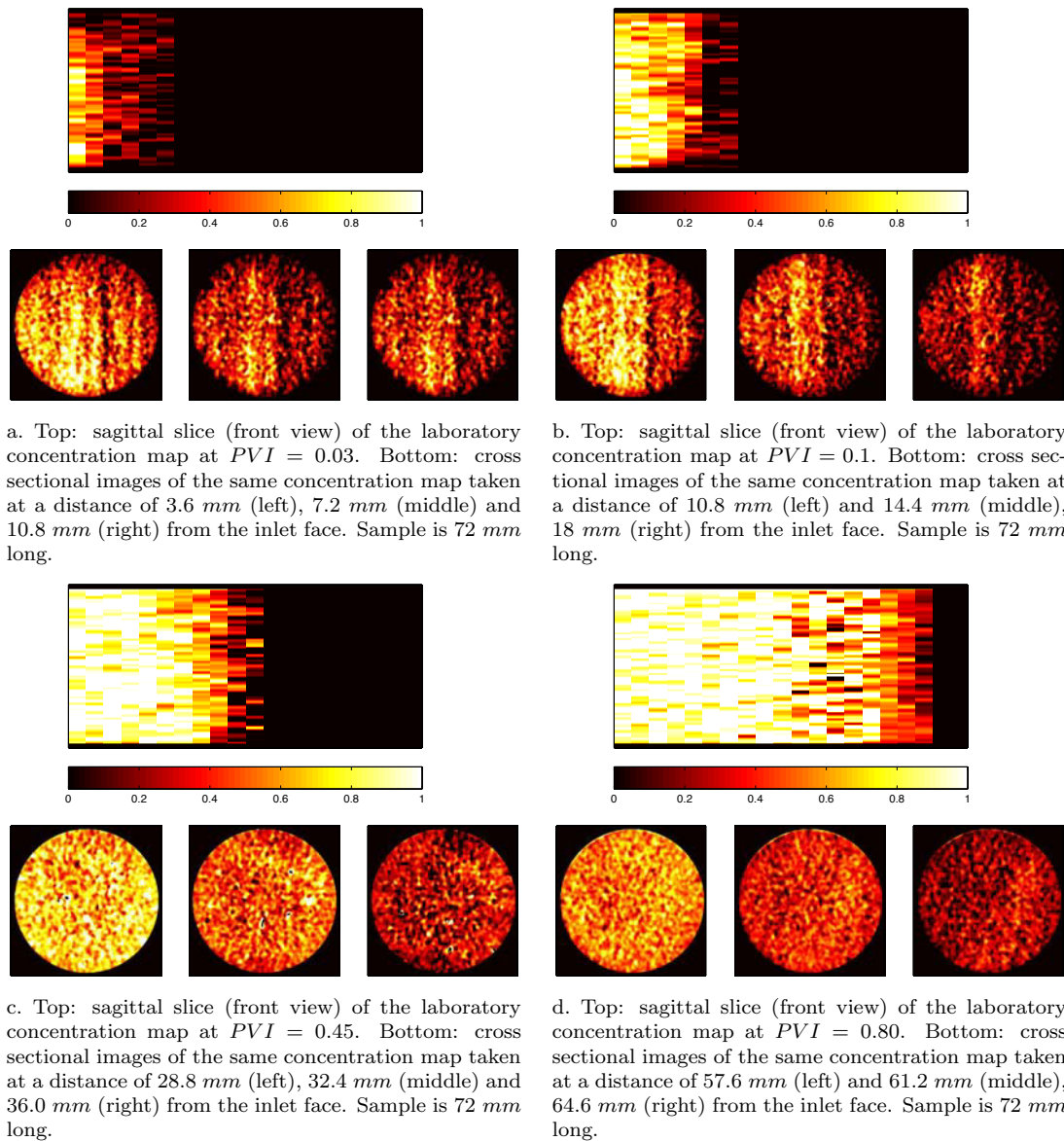


Figure 4.17: 2D images of the 3D concentration maps at different times for composite 2 when performing laboratory viscous miscible displacement. The color bars show the injected fluid concentrations.

The permeability profiles determined from Equation 4.7 are compared to the absolute permeabilities of the two composites in Figure 4.18. The agreement is not as good as the one pointed out for numerical experiments, but the estimated permeabilities still follow the permeability variations of the stacked plugs. The dead volume inside the inlet port and spiral of the core holder is not purged to facilitate the identification of the pressure jump when

viscous fluid starts to invade the core sample. It takes some time for viscous fluid to fill the spiral and enter the porous medium. High permeability values observed at the beginning of the estimated profiles are related to this period of time (when  $\Delta p(t)$  variations is not pronounced). Additional remarks can be emphasized.

**First**, low viscosity brine is still produced after the breakthrough and as a result,  $\Delta p(t)$  increases. The measured  $\Delta p(t)$  must be rescaled to be consistent with the pressure drop related to the absolute permeability of the sample. The measured injection time does not affect the calculated permeabilities, but it has also to be consistent with the theoretical sweeping time. Equation 4.12 is used to rescale the recorded data. The results are illustrated in Figure 4.19.

$$\begin{aligned}\Delta p_{scaled} &= \Delta p_{recorded} \times \frac{\Delta p_{theoretical} (PVI = 1)}{\Delta p_{recorded} (PVI = 1)} \\ \Delta t_{scaled} &= \Delta t_{recorded} \times \frac{\Delta t_{theoretical} (PVI = 1)}{\Delta t_{recorded} (PVI = 1)}\end{aligned}\quad (4.12)$$

**Second**, the derivative vector is much noisier than the one calculated in numerical cases.  $\Delta p(t)$  is recorded every 6.0 sec. This imposes more pressure fluctuations due to smaller  $\Delta t$ . As for the numerical simulation results,  $\Delta p(t)$  is not a monotonic function of time. This phenomenon is more pronounced in very permeable zones due to the fact that pressure variations are inversely proportional to permeability. Here, we should also consider the measurement errors when recording inlet-outlet pressure changes. Data post processing is required to smooth out pressure variations and remove the noise (see section 4.2.2).

**Third**, after the first pressure jump, the viscous fluid continues to invade the sample and  $\Delta p(t)$  increases progressively till breakthrough. Just before breakthrough, the recorded  $\Delta p(t)$  varies very slowly during the so-called pressure stabilization period. The small variations in

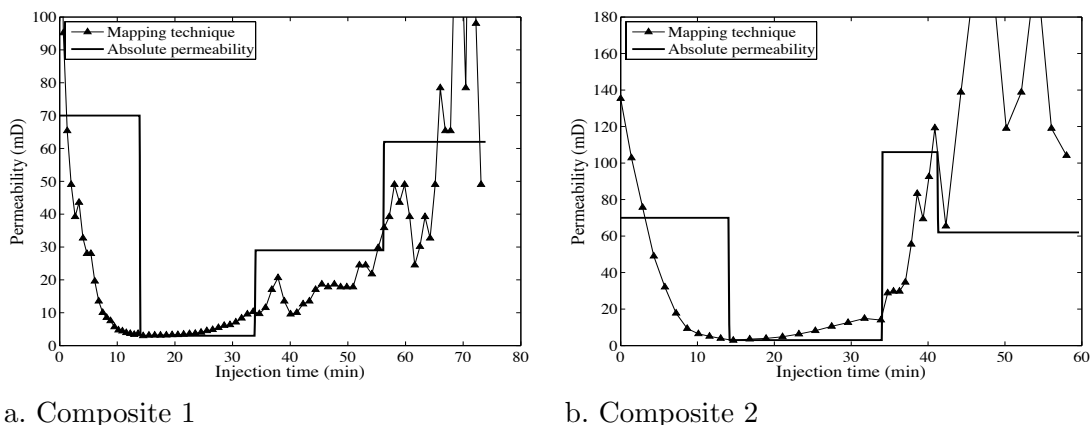


Figure 4.18: Comparison of the processed experimental permeabilities (triangles) with absolute permeability variations between plugs (lines) for composite 1 and composite 2 when performing laboratory viscous miscible displacement.

$\Delta p(t)$  at the end of the experiment explain why the method does not succeed in estimating the local permeabilities close to the outlet face of our composite samples (Figure 4.18). An inverse injection under the same conditions can help to capture the permeability variations of this part.

**Fourth**, the permeability variations from one plug to another are not as sharp as those observed with the numerical simulation results. The miscibility of the two fluids reduces the viscosity of the transition zone and thus, reduces the sharpness of the pressure variations when passing from plug to another one. We should not forget the effect of transverse heterogeneity on  $\Delta p(t)$  and the estimated permeabilities. Figure 4.17 shows the cross sectional images of the concentration distribution close to the front location. As it is obvious, the natural core plugs are not uniform in perpendicular directions to flow and this reality is ignored in our 1D mapping technique.

Neglecting the extreme values in estimated permeabilities, the relative error between the actual permeabilities and the estimated ones is calculated from Equation 4.11. It is less than 0.33 for composite 1 and about 0.48 for composite 2.

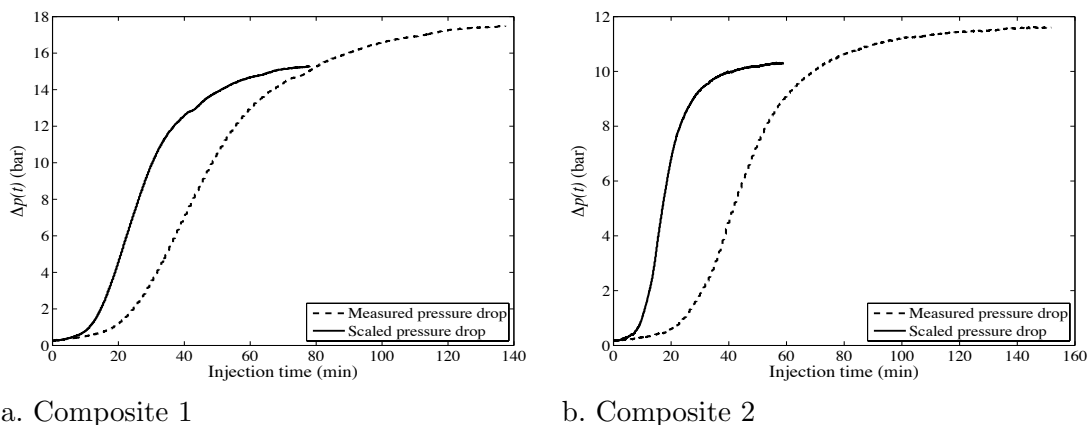


Figure 4.19: Inlet-outlet pressure drop before and after scaling for composite 1 and composite 2. The recorded  $\Delta p(t)$  should be rescaled to be consistent with absolute permeability of the sample.

### Low permeability limestone sample

We now consider a heterogeneous limestone Lavoux, with an absolute permeability of  $4.0 \text{ mD}$ . Its properties are reported in Table 3.2. The CT profile (Figure 3.6, (c)) of this sample shows two distinct regions. The sample is initially saturated with  $30 \text{ g/l}$  NaCl brine. The high viscosity glycerin ( $60 \text{ cp}$ ) is injected at a constant flow rate of  $6 \text{ cc/hr}$ . Since the sample permeability is very low, the flow rate cannot exceed this value to make sure that pressure respects transducers limit. The inlet-outlet pressure drop is shown in Figure 4.20(b). Once the miscible displacement is over, the sample is cut into two plugs based on the observed sharp change in its CT absorption profile. We measure the absolute permeability of each

small part. Figure 4.20(a) shows that there is a good agreement between the processed permeability profile and the absolute permeabilities of the cut plugs. As stated for composite samples, the permeability values cannot be perfectly estimated at the end of the displacement. The relative error between the measured permeabilities and the estimated permeabilities is around 0.05

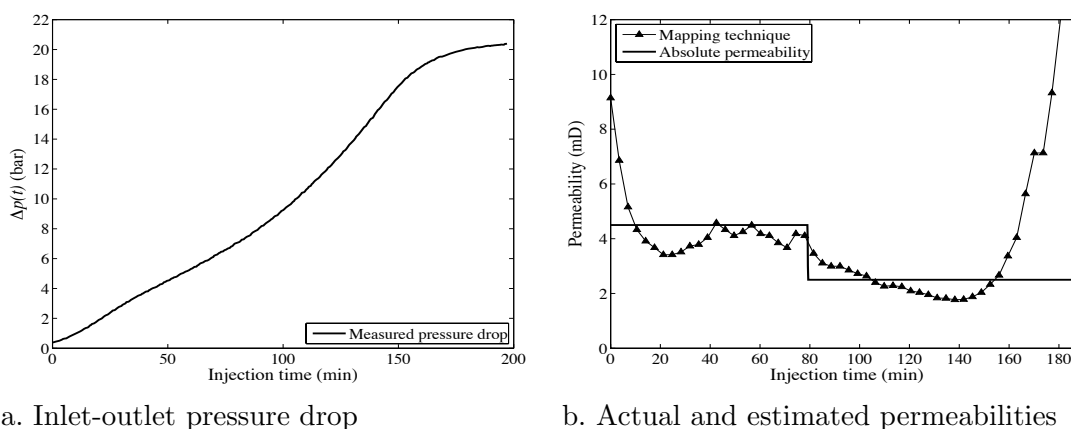


Figure 4.20: Comparison of the processed permeabilities (triangles) with the absolute permeabilities for two cut parts of the low permeability limestone sample (lines).

### High permeability limestone sample

The second heterogeneous core sample LJ001 is a limestone with an absolute permeability of 240  $mD$ . Its properties are reported in Table 3.2. Sample heterogeneity was primarily enhanced through a  $CO_2$  injection: heterogeneity occurs along the flow axis, but also in cross sections (see Figure 3.10). Like previous samples, the core is initially saturated with 30  $g/l$  NaCl brine. As the sample is permeable, we perform two injection experiments both with a flow rate of 85  $cc/hr$ : one from left to right (normal injection), which allows us to capture the permeability profile in the first half of the sample and one from right to left (reverse injection), which allows us to capture the permeability profile in the second half. The pressure drop curves for both normal and inverse injections are plotted in Figure 4.21. The inverse injection is preferred whenever the absolute permeability of the sample is more than 100  $mD$ . With the inverse injection, we hope to overcome the difficulties related to the noise intrinsic to the estimation of permeability values, especially at the end of displacement. For comparison purposes, 32 minipermeameters are located along the core. They yield a mean surface permeability for 8 cross sections. Results are reported in Figure 4.22. They stress the capabilities of the methodology proposed in this work. The error calculation is more delicate in this case because of minipermeameter error measurement. The relative error



between the surface permeabilities and estimated permeabilities is around 0.40 ignoring the minipermeameter error measurement.

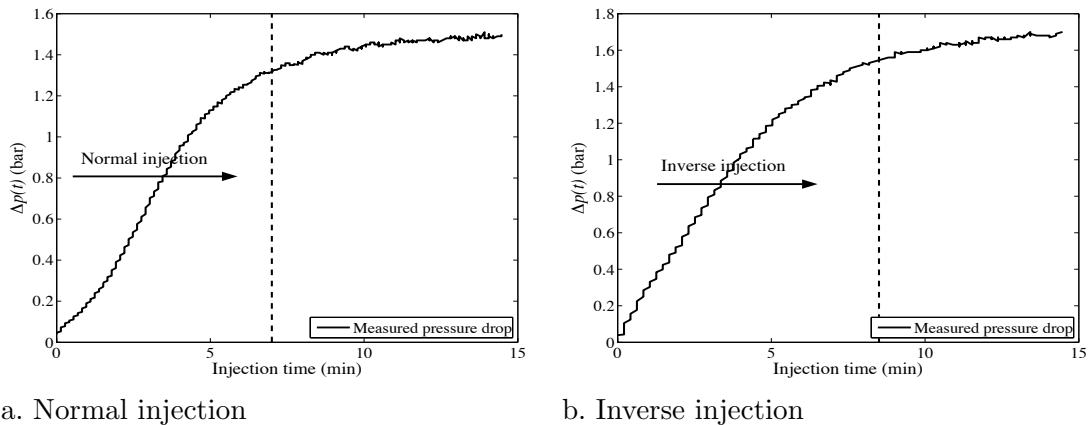


Figure 4.21: Inlet-outlet pressure drop data against injection time for sample LJ001.  $\Delta p(t)$  data on left hand side of dotted line are used to estimate the permeability values.

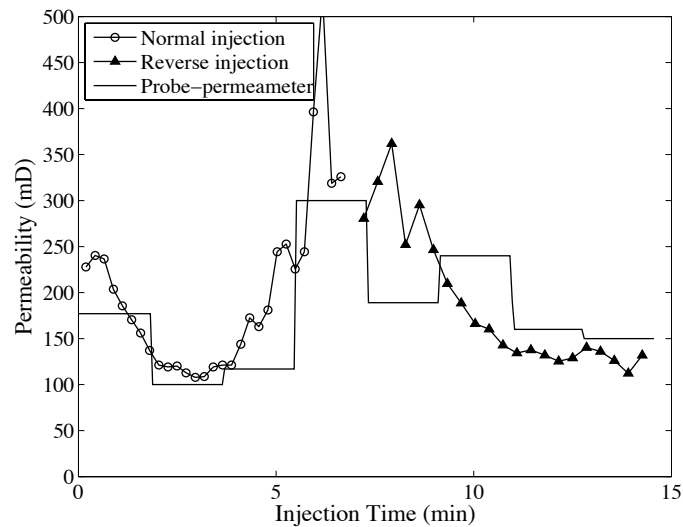


Figure 4.22: Comparison of processed permeabilities (dots and triangles) with the minipermeameter results (lines) for the sample LJ001. Dots indicate that the injection is performed from left to right and triangles from right to left.

### Permeable coarse-grained sandstone

The third heterogeneous sample is a coarse-grained sandstone K13, with an absolute permeability of 170  $mD$ . Its properties are reported in Table 3.2. It contains a distinct layer

of about 1.5 *cm* width, whose nature is not clearly identified. Small scale heterogeneity is evidenced when looking at the sample's CT profile (Figure 3.6 (e)). X-ray CT imaging is primarily performed during a tracer test in order to capture better the impact of heterogeneity. The sample is saturated with 30 *g/l* NaCl brine. A 70 *g/l* KI brine is injected into the sample with a flow rate of 60 *cc/hr*. The collected images point out a very dispersed front. Figure 4.24 (top) shows the KI brine concentration at different injected pore volumes (*PVI*). No stratification or barrier to the flow is easily observed, but it seems that the lower part of the sample is more permeable than the upper part. After the tracer test, the sample is again saturated with 30 *g/l* NaCl. We decide to increase the viscosity of glycerin to 200 *cp* in order to have a more stable front. The glycerin is injected into the sample with a flow rate of 60 *cc/hr*, inlet-outlet pressure drop is recorded and X-ray CT images are taken at successive times. Figure 4.24 (bottom) shows the front shape and the glycerin concentration at different *PVI* similar to what was observed with the tracer test. Thus, we are able to compare the displacing fluid concentration from two miscible displacements. Even though the injection rate is the same for both experiments, the dispersion due to diffusion seems to be suppressed in the second experiment.

As the sample is permeable, the experiment is repeated twice: injection of 200 *cp* glycerin from left to right and from right to left. The collected data are processed to estimate the 1D permeability profile. The result is shown in Figure 4.23. The calculated permeabilities vary between 70 and 220 *mD*. As the sample is very friable, no other measurement could be collected to crosscheck our results.

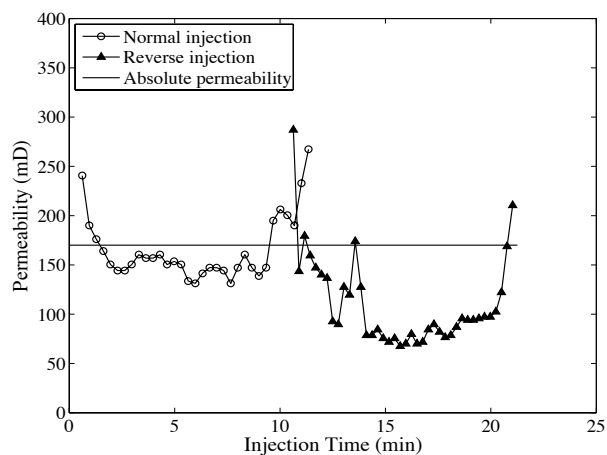


Figure 4.23: The processed permeabilities (dots and triangles) for the coarse-grained sandstone K13. Dots indicate that the injection is performed from left to right and triangles from right to left.

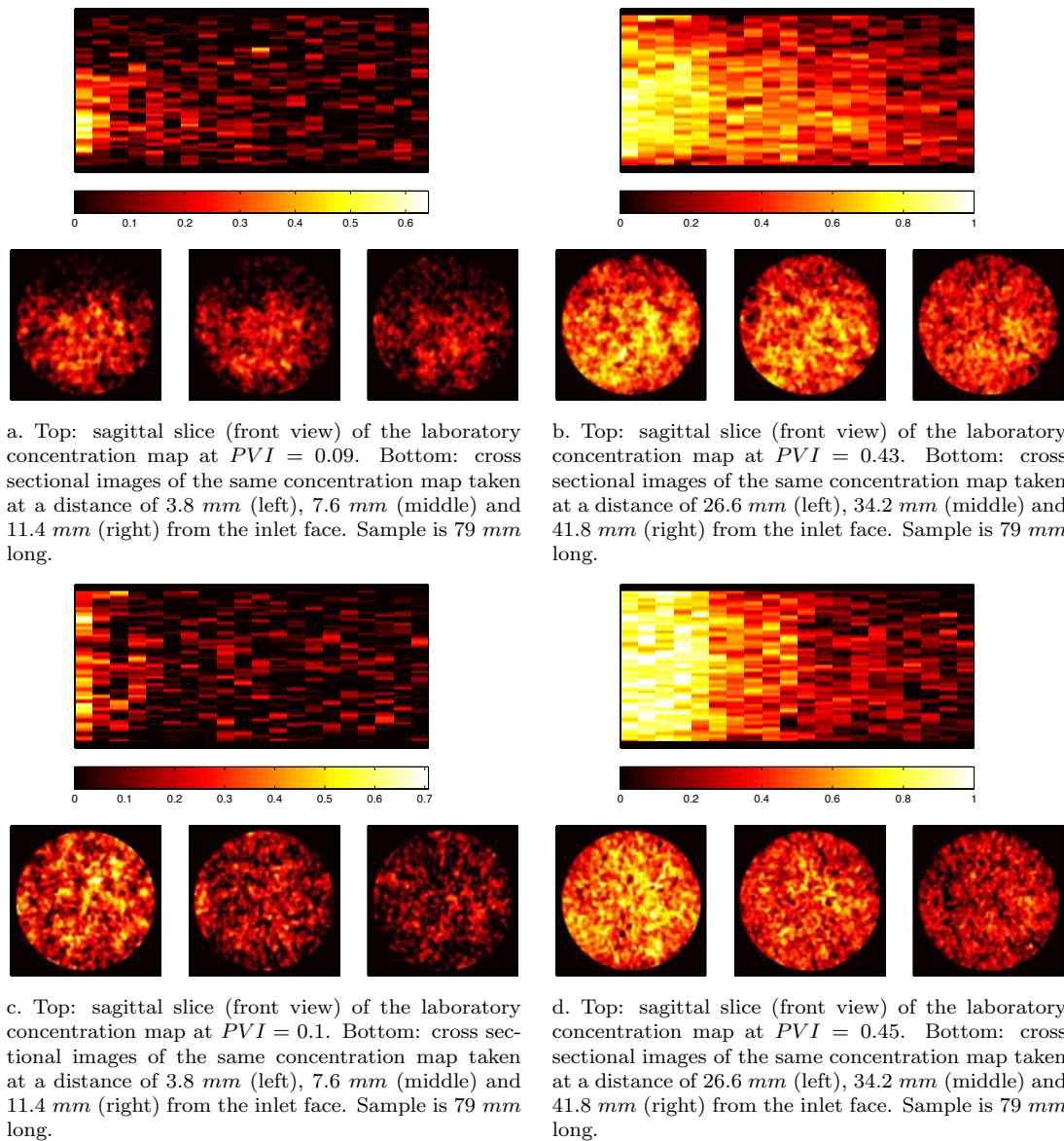


Figure 4.24: Top: 2D images of the 3D concentration maps for the coarse-grained sandstone K13 when performing a laboratory tracer displacement. Bottom: 2D images of the 3D concentration maps for the same sample when performing a laboratory viscous miscible displacement. The color bars show the injected fluid concentrations.

## 4.4 Concluding remarks

In this chapter, we presented a methodology to characterize the permeability profile in cores along the flow direction axis. It involves the injection of a high viscosity miscible fluid into a

core sample initially saturated by a low viscosity fluid. We derived the permeability profile from the variations in the pressure drop across the core.

The methodology was validated through numerical experiments. Flow simulations were performed for numerical models representing core samples. The models studied were sequences of blocks with given mean permeabilities. We simulated the pressure drop between the inlet and outlet faces considering both miscible and immiscible fluids. The interpretation procedure provided the expected permeability profile. However, we pointed out a smoothing effect in the case of miscible fluids, which is due to the mixing zone between the invading and defending fluids.

The methodology was also validated by laboratory experiments. The process works well for low permeabilities. In the case of permeable samples, as the pressure drop is inversely proportional to permeability, the estimated permeabilities are very noisy. The determination of the permeability profile was improved by performing a reverse injection.

The analysis of the results obtained for the heterogeneous cores pointed out another difficulty. The proposed methodology assumes that permeability is homogeneous per cross section, which means that heterogeneity is one-dimensional. In the next chapter, we focus on a new procedures able to capture three-dimensional heterogeneity.

## Nomenclature

$A_r$	cross sectional area	$k$	permeability
$CP$	cumulative production	$k_{ro}$	oil relative permeability
$D^{numerical}$	numerical dispersion	$k_{rw}$	water relative permeability
$L$	length	$p$	pressure
$L_x$	correlation length along axis $X$	$q_o$	oil production rate
$L_y$	correlation length along axis $Y$	$q_w$	water production rate
$L_z$	correlation length along axis $Z$	$t$	time
$N_y$	number of grid cells in $Y$ direction	$t_D$	dimensionless time
$N_z$	number of grid cells in $Z$ direction	$v$	front velocity
$PVI$	injected pore volume	$x$	location
$Q$	flow rate	$x_f$	front location
$S_w$	water saturation	$\epsilon^{relative}$	relative error
$V_{oip}$	total volume of produced oil	$\phi$	porosity
$V_{ot}$	oil in place volume	$\mu$	viscosity
$V_p$	pore volume		

# Chapter 5

## Three Dimensional Permeability Characterization: Theory

As mentioned in chapters 3 and 4, two sets of dynamic data and a set of static data are collected during our viscous miscible displacement experiment: experimental inlet-outlet pressure drop as a function of time, several three-dimensional concentration maps and a three-dimensional porosity map. In this chapter, we explain how to calibrate a three-dimensional permeability field to these available data. The theoretical background of our methodology is given in this chapter, which is organized as follows. The optimization problem is introduced in section 5.1. We define our objective function and show how to numerically formulate an objective function. In section 5.2, some brief explanations are given about numerical algorithms, which are usually used to solve optimization problems. In section 5.3, we have a look at two well-known geostatistical parameterization techniques and explain why one should use them. In section 5.4, the workflows used to solve our specific problem are described. The inversion parameters are defined and the iteration and optimization loops are explained in details.

### 5.1 Optimization problem

As already mentioned, a reservoir model is a grid populated with properties such as porosity and permeability. Geostatistical methods are used to populate the reservoir grid with porosity or permeability realizations. These realizations must respect the measured data (*e.g.*, well data) and the spatial variability model inferred from static data (*e.g.*, variograms). The final goal of a reservoir characterization study is to get a reservoir model consistent with all static and dynamic data. This issue is addressed as a “history-matching” process. The reservoir model is unknown, but we know it reacts to production history (*i.e.*, inverse problem). Basically, a reservoir model is proposed as an initial estimate. A numerical fluid flow is then performed to obtain simulated dynamic data. The suitability of the proposed model

is measured by an objective function. When simulating a multiphase flow experiment, the relation between the model properties and the dynamic data is highly non-linear [36]. Thus, the method to find a solution must be iterative. A solution can be reached through an optimization procedure. In such a case, the objective function, which measures the mismatch between simulated and actual dynamic data has to be minimized.

### 5.1.1 Definition of the objective function

The purpose of the optimization problem is to minimize an objective function  $J$ , which measures the mismatch between the observed dynamic data and the corresponding simulated answer:

$$J(\Theta) = \frac{1}{2} (g(\Theta) - \mathbf{d}^{obs})^T C_D^{-1} (g(\Theta) - \mathbf{d}^{obs}) \quad (5.1)$$

However, this problem is ill-posed, which means that its solution does not exist or its solution is not unique or its solution is not stable under perturbations on data [42]. To regularize the optimization problem, that is to make it “less ill-posed”, one may add *a priori* information into the objective function [55]. The resulting objective function is:

$$J(\Theta) = \frac{1}{2} (g(\Theta) - \mathbf{d}^{obs})^T C_D^{-1} (g(\Theta) - \mathbf{d}^{obs}) + \frac{1}{2} (\Theta - \Theta^o)^T C_\Theta^{-1} (\Theta - \Theta^o) \quad (5.2)$$

where:

- $J$  is the objective function;
- $\Theta$  is the set of model parameters;
- $g$  is the operator mapping  $\Theta$  to data space;
- $\mathbf{d}^{obs}$  is the vector of observed values to be matched;
- $C_D^{-1}$  is the inverse of a covariance matrix, which characterize the errors between the observed and the simulated data;
- $\Theta^o$  is a vector of *a priori* parameter values;
- $C_\Theta^{-1}$  is the inverse of the covariance matrix, which characterize the uncertainties in  $\Theta^o$ .

The first term on the right-hand side of  $J(\Theta)$ , called the likelihood constraint, measures the mismatch between the simulated and the observed data. The second part, which is called *a priori* constraint, evaluates the discrepancy between the current estimated parameters and the likelihood parameters. Minimizing  $J$  becomes extremely difficult when the reservoir model consists of a huge number of grid cells, each of them attributed to unknown porosity and permeability values. As the dimension of *prior* covariance matrix  $C_\Theta$  is the number of unknowns, computing its inverse may be just intractable [35].

Another possibility to ensure regularization is to narrow the search space. We chose to regularize our objective function by narrowing the space wherein we search for the solution.

To do so, we use a geostatistical parametrization technique, named the gradual deformation method (GDM). We will provide more details about this technique in section 5.3. Using the GDM, we account for the *prior* constraint while keeping only the data mismatch term in the objective function. Such a parametrization technique allows for narrowing the input parameter space and regularizing the optimization problem. The focus of this work is the matching of pressure and concentration data. If we assume that the vector of pressure data is represented by  $p$  and the matrix of concentration data is represented by  $S$ , then our objective function  $J$  can be expressed as follows:

$$\begin{aligned}
J(\Theta) = & \frac{1}{2} \frac{w^p}{ntimes} \sum_{i=1}^{ntimes} \left( \frac{p_i^{obs} - p_i^{sim}(\Theta)}{\sigma^p} \right)^2 \\
& + \frac{1}{2} \sum_{j=1}^{ndata} \frac{w_j^S}{nvalues_j} \sum_{i=1}^{nvalues_j} \left( \frac{S_{i,j}^{obs} - S_{i,j}^{sim}(\Theta)}{\sigma_j^S} \right)^2
\end{aligned} \tag{5.3}$$

where:

- $J$  is the objective function;
- $\Theta$  is the set of model parameters;
- $ntimes$  is the number of measurement times for pressure data;
- $p_i^{obs}$  is an observed pressure data value at time  $i$ ;
- $p_i^{sim}$  is the simulated data at the same time;
- $\sigma^p$  is the standard deviation of pressure data errors;
- $ndata$  is the number of concentration data series to be matched;
- $nvalues_j$  is the number of observed concentration data values for the data series  $j$ ;
- $S_{i,j}^{obs}$  is an observed concentration data value at time  $i$  for the data series  $j$ ;
- $S_{i,j}^{sim}$  is the simulated concentration data at the same time;
- $\sigma_j^S$  is the standard deviation of concentration data (series  $j$ ) errors;

$w^p$  and  $w_j^S$  are weighting coefficients. The standard deviations are used to normalize errors between simulated and observed responses by uncertainty ranges. Therefore, different types of data can be combined in a single objective function.  $\sigma^p$  and  $\sigma_j^S$  are calculate as follows:

$$\begin{aligned}
\sigma^p &= \frac{1}{10} \frac{1}{ntimes} \sum_{i=1}^{ntimes} p_i \\
\sigma_j^S &= \frac{1}{10} \frac{1}{nvalues_j} \sum_{i=1}^{nvalues_j} S_{i,j}
\end{aligned} \tag{5.4}$$

Using Equation 5.4, we normalize our data considering a constant confidence interval, which is 10% of their mean value. The local weights  $w^p$  and  $w_j^S$  are constant for a given data series

and are computed as follows:

$$\begin{aligned} w^p &= \frac{1}{[\sigma^p]^2} \\ w_j^S &= \frac{1}{[\sigma_j^S]^2} \end{aligned} \quad (5.5)$$

It is often necessary to adjust the relative contributions of the production and concentration data so that they impact similarly the optimization process. The weighting coefficients applied to production and concentration data series are used to balance the influence of the different terms of the objective function [48].

## 5.2 Optimization methods

In order to match the available pressure and concentration data with the corresponding simulated answers, one has to identify the unknown model parameters. The identification of the unknown parameters is based on the solution of a constrained optimization problem minimizing the defined objective function. The idea is to construct an optimal set of parameters  $\Theta^*$  such that:

$$\Theta^* = \arg \min_{\Theta \in D} J(\Theta) \quad (5.6)$$

where  $D$  is the feasible domain determined by a set of constraints on parameters. The flow equations that we consider are nonlinear, which makes the optimization problem very complex. Therefore, finding the optimal parameters is an iterative search process: parameters are sequentially perturbed. In each iteration, the parameters are changed in order to satisfy the following condition:

$$J(\Theta^{(itn+1)}) < J(\Theta^{(itn)}) \quad (5.7)$$

$$\Theta^{(itn+1)} \in D \quad \Theta^{(itn)} \in D$$

where  $itn$  is the iteration number. Optimization algorithms are subdivided into two families: gradient-based and non-gradient-based. Gradient-based methods have often been found to be most effective in terms of CPU time. However, they do converge to local minima [40]. In our study, we use gradient-based methods, mainly because the algorithms in this category converge faster. Well-known gradient-based algorithms are:

- Steepest-Descent
- Gauss-Newton
- Levenberg-Marquardt
- Powell Dog-Leg
- BFGS



All these methods involve similar ideas for the minimization of the objective function [35]. We assume that the objective function  $J(\Theta_1, \Theta_2, \dots, \Theta_n,)$  is a continuous function and can be differentiated twice. The gradient of  $J$  is defined as the derivatives of  $J$  with respect to the unknown parameters  $\Theta_i$ :

$$\nabla J = \left( \frac{\partial J}{\partial \Theta_1}, \frac{\partial J}{\partial \Theta_2}, \dots, \frac{\partial J}{\partial \Theta_n} \right) \quad (5.8)$$

The Hessian matrix of  $J$  consists of its second derivatives with respect to the unknown parameters  $\Theta_i$ :

$$\mathbf{H}(J) = \begin{bmatrix} \frac{\partial^2 J}{\partial \Theta_1^2} & \frac{\partial^2 J}{\partial \Theta_1 \partial \Theta_2} & \cdots & \frac{\partial^2 J}{\partial \Theta_1 \partial \Theta_n} \\ \frac{\partial^2 J}{\partial \Theta_2 \partial \Theta_1} & \frac{\partial^2 J}{\partial \Theta_2^2} & \cdots & \frac{\partial^2 J}{\partial \Theta_2 \partial \Theta_n} \\ \vdots & \vdots & \ddots & \vdots \\ \frac{\partial^2 J}{\partial \Theta_n \partial \Theta_1} & \frac{\partial^2 J}{\partial \Theta_n \partial \Theta_2} & \cdots & \frac{\partial^2 J}{\partial \Theta_n^2} \end{bmatrix} \quad (5.9)$$

The minimization of  $J$  is achieved step by step: the first iteration starts with model  $\Theta^i$ . Then, one successively moves from one step of length  $r$  into direction  $\mathbf{p}$ , so that the modified model is  $\Theta^{i+1} = \Theta^i + r\mathbf{p}$  [35]. Direction  $\mathbf{p}$  depends on  $\nabla J$  and  $\mathbf{H}(J)$ . The step  $r\mathbf{p}$  has to be chosen to sufficiently reduce the objective function. The identification of suitable directions calls for the computation of gradients or derivatives. Each of the above algorithms has advantages and disadvantages. In this study, the Powell's "dogleg" algorithm [47] is used for matching both production and concentration data. This algorithm combines the advantage of the Steepest Descent algorithm, which is very robust when starting far away from the solution, and those of the Gauss-Newton algorithm, which has a good convergence rate when approaching the solution. Exhaustive reviews of all these algorithms can be found in the literature (see for instance, Tarantola [55] or Le Ravalec-Dupin [35]).

### 5.3 Parametrization techniques

The purpose of our optimization problem is to identify a parameter (*e.g.*, permeability) value for each grid cell from the available pressure and concentration data. As there are many grid cells, the optimization process can be extremely slow and inefficient. This problem has motivated researchers to introduce different parametrization techniques. The idea is to find better ways for describing a reservoir model with less unknown parameters. However, the solution must be consistent with the reservoir spatial structure. The optimization cost in terms of CPU time must also be reasonable. The two well known parametrization techniques, which are usually used in reservoir engineering studies are "the pilot point technique" and "the gradual deformation method".

### 5.3.1 Pilot point technique

This method applies to Gaussian realizations. It was initially developed by de Marsily [14]. The idea is to introduce some control points inside the grid in order to better tune the geostatistical model. We consider some grid cells as pilot points and try to modify their values while reducing the data mismatch. These modifications allow us to locally perturb the realization around the selected grid cells. The pilot points should be selected respecting the variogram model correlation lengths [35].

Assume that  $n$  permeability data are known at  $n$  given locations (well locations) inside the reservoir grid.  $m$  grid cells are also selected as pilot points and are given initial values. The procedure is as follows:

1.  $y$ , an unconditional permeability field is generated. The geostatistical model is populated with  $y$ .
2. The unconditional  $y$  field is conditioned to the  $n$  known permeability values plus the  $m$  initial pilot point values using kriging.
3. A fluid flow simulation is run with the resulting conditional field. The objective function and its gradients with respect to pilot point values are calculated.
4. If the objective function is not small enough, the pilot points values are modified and the process is repeated (iteration process).

In such conditions, the number of inversion parameters are reduced to the number of pilot points. In this technique, perturbations are limited to pilot point neighborhood. The spatial extent of these perturbations depend on the correlation lengths. Pilot point method is a local parametrization technique. The most subjective feature of this method is the choice of the locations of the pilot points [35]. The use of time lapse seismic (or saturation) data in the objective function could be a guideline for an optimal location of the pilot points. In fact, the seismic term in the objective function gives directly the zones of the reservoir with the largest mismatch between data and simulation results. Pilot points should be located within these unmatched zones to enhance a local flexibility on the geological model perturbation [40].

### 5.3.2 Gradual deformation method

The gradual deformation method (GDM) is a stochastic parametrization technique just as the pilot point method, which allows to narrow the search space. This method was initially developed by Hu [27] for gradually changing Gaussian stochastic reservoir models while preserving their spatial variability.

The simplest gradual deformation scheme consists in combining two independent standard Gaussian random functions  $B_1$  and  $B_2$  with identical variograms:

$$(B(\theta) - m) = (B_1 - m) \cos(\theta) + (B_2 - m) \sin(\theta) \quad (5.10)$$

$\theta$  is a deformation parameter and  $m$  is the mean of  $B_1$  and  $B_2$ . This relation ensures that  $B(\theta)$  is also a random Gaussian function with the same mean and variogram as  $B_1$  and  $B_2$ , whatever the value of the deformation parameter. Given two independent realizations  $b_1$  and  $b_2$  of  $B_1$  and  $B_2$ , we get a continuous chain of realizations  $b(\theta)$ :

$$(b(\theta) - m) = (b_1 - m) \cos(\theta) + (b_2 - m) \sin(\theta) \quad (5.11)$$

$b_1$  is considered as our initial realization.  $b_2$  is just a randomly drawn independent realization. Varying the deformation parameter induces the continuous deformation of realization  $b$ . When  $\theta$  is zero,  $b = b_1$  and when it is equal  $\frac{\pi}{2}$ ,  $b = b_2$ . Applying Equation 5.11 leads to the gradual deformation of the whole initial realization. As a result, the deformation is said global. The gradual deformation principles can be extended to the combination of more than two independent realizations [49]. In this case, the number of deformation parameters equals the number of complementary realizations added to the starting one.

When observations are scattered in different zones of the studied field, calibration using global deformation may be inefficient [27]. In such cases, we can consider local gradual deformation processes. One should notice that a Gaussian white noise  $z$  is used to produced  $b$ . There is a big difference between the Gaussian white noise  $z$  and  $b$ :  $b$  is a realization with a continuous spatial structure while  $z$  exhibits a chaotic behavior [36]. This difference is essential when using local gradual deformation method. Local gradual deformation processes cause a discontinuity between the modified zone and the non modified one. If we locally apply the gradual deformation process to  $b$ , we severely perturb its continuous spatial structure. If  $z$  is locally changed, it is still chaotic and the spatial continuity of the resulting  $b$  realization is preserved. Therefore, we must apply the local gradual deformation to  $z$  instead of  $b$ . We can select a group of grid cells and modify their normal deviates through the following formulation [35]:

$$z^{zone}(\theta) = z_1^{zone} \cos(\theta) + z_2^{zone} \sin(\theta) \quad (5.12)$$

$z_1$  and  $z_2$  yield realizations  $b_1$  and  $b_2$ , respectively. The superscript “zone” stands for the selected grid cells. When applying Equation 5.12 to the selected normal deviates only, the neighboring grid cells (*i.e.*, closer than one correlation length) are also impacted by the deformation process [27].

Again, the coefficient  $\theta$  is estimated through an optimization process so that the resulting realization  $b$  reproduce the observed data as well as possible. A schematic diagram depicting the deforming process for  $b$  is shown in Figure 5.1. During the  $n$  iterations of the first optimization, parameter  $\theta$  is changed and the optimized realization  $b^{1optim}$  is identified.  $b^{1optim}$  is uploaded to the second optimization loop and a new search process is implemented. In our study, we use a gradual deformation based optimization to calibrate our core model to both concentration and pressure data.

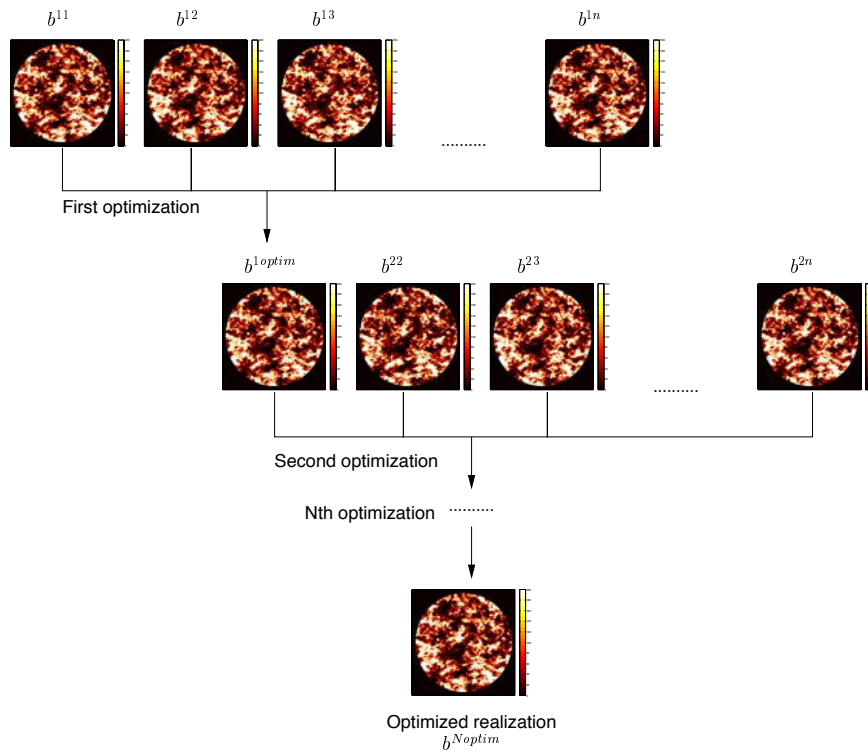


Figure 5.1: Schematic of realization chain during a gradual deformation based optimization.

## 5.4 Optimization workflow

We use the CONDOR research prototype software to construct our optimization workflow. The main difficulty is to determine how to modify the permeability field. To parametrize our 3D permeability field we use:

$$\log_{10}[k(\mathbf{x})] = A\phi(\mathbf{x}) + b(\mathbf{x}) \quad (5.13)$$

where  $A$  is a constant and  $b(\mathbf{x})$  is a realization of a random function  $B$  characterized by a mean  $m$ , a variance  $\sigma^2$  and a given variogram. Vector  $\mathbf{x}$  indicates location. Porosity  $\phi(\mathbf{x})$  is a known three-dimensional field.  $b(\mathbf{x})$  is also a three-dimensional field with the same size of  $\phi(\mathbf{x})$ . The parameters, which can change the resulting 3D permeability field are:

1. Coefficient  $A$ ;
2. The seed used to generate  $b(\mathbf{x})$ ;
3.  $m$ , the mean of  $b(\mathbf{x})$ ;
4.  $\sigma^2$ , the variance  $b(\mathbf{x})$ ;

5.  $L_x$ , the range of  $b(\mathbf{x})$  variogram along axis  $X$ ;
6.  $L_y$ , the range of  $b(\mathbf{x})$  variogram along axis  $Y$ ;
7.  $L_z$ , the range of  $b(\mathbf{x})$  variogram along axis  $Z$ .

By varying any of these parameters, we can significantly change the relation between permeability and porosity data. Even if the porosity field shows randomness in its spatial distribution (*i.e.*, small correlation lengths), we are capable of generating a heterogeneous permeability field with very distinct geostatistical properties. In the following sections, we describe two workflows, which are used during our optimization processes.

### 5.4.1 Simple optimization

During a simple optimization process, we use the workflow shown in Figure 5.2. A realization is built and a search process is implemented to determine the inversion parameters. The workflow is as follows.

1. A 3D regular numerical grid is built. This grid has the same size as the 3D CT porosity map.
2. Given a random seed, a Gaussian white noise termed  $z_1$  is generated.  $z_1$  has the same size of the 3D numerical grid and exhibits a chaotic behavior.
3. The Gaussian white noise  $z_1$  is used to produce a  $b(\mathbf{x})$  field from the FFTMA simulator [34]. Here, the following five parameters are given reasonable values: two values for the mean and variance of  $b(\mathbf{x})$  and three values for the correlation lengths of  $b(\mathbf{x})$  along the three main axes  $X$ ,  $Y$  and  $Z$ .  $b(\mathbf{x})$  is a random field with a continuous spatial structure: It has a mean and variance and it is characterized by a given variogram.
4. Starting from an initial value for  $A$ , a 3D permeability field is produced from Equation 5.13. Both permeability and porosity fields are upscaled. The upscaling techniques are described in chapter 7.
5. A new 3D grid is constructed and populated with upscaled porosity and permeability data. This grid has the same size as the upscaled 3D porosity map. The flow simulation is performed and the appropriate dynamic answers are extracted from the simulation outputs.
6. The objective function is calculated from Equation 5.3. Here,  $w_j^S = 0$ . If the objective function value is less than or equal to the selected threshold value, then the optimization process stops and the 3D permeability field is printed. Otherwise, the search process is started to determine the inversion parameters minimizing the objective function.

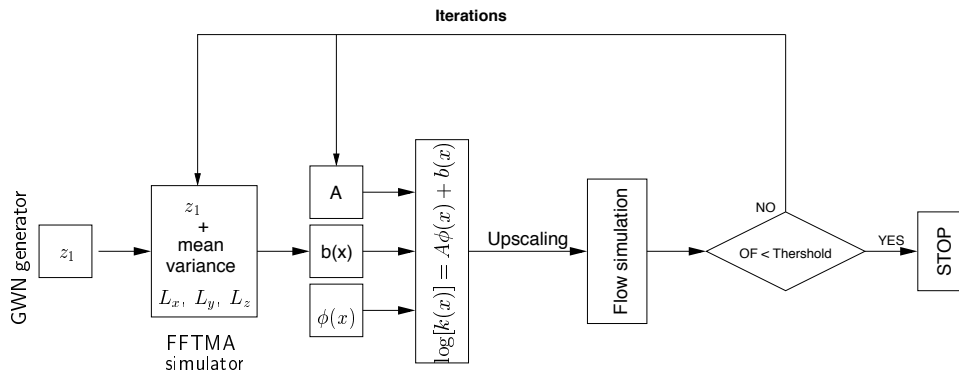


Figure 5.2: CONDOR workflow used for calibration of the 3D permeability field to pressure data only.

The maximal number of iterations depends on the number of parameters and is user defined. This simple optimization workflow is used to calibrate permeability field to pressure data only. When calibrating the permeability field to both pressure and concentration data, we use a gradual deformation based optimization workflow.

### 5.4.2 Gradual optimization

The gradual deformation based optimization workflow consists of two loops (see Figure 5.3). In the **Internal loop**, a realization chain is built and a search process is implemented to determine the inversion parameters minimizing the objective function. The **Internal loop** can be seen as a simple optimization process. A single realization chain allows us to only explore a tiny part of the realization space. Updating the optimal parameters when moving to the **External loop** and constructing new chains of realizations help to further explore the realization space [35]. The workflow is as follows.

#### External loop:

1. A 3D regular numerical grid is built. This grid has the same size as the 3D CT porosity map.
2. Given a random seed, a Gaussian white noise termed  $z_1$  is generated.  $z_1$  has the same size as the 3D numerical grid and exhibits a chaotic behavior.
3. Once  $z_1$  is produced, the procedure enters the internal loop.

#### Internal loop:

1. Given a random seed, a second Gaussian white noise termed  $z_2$  is generated.  $z_2$  has the same size as the 3D numerical grid and exhibits a chaotic behavior.

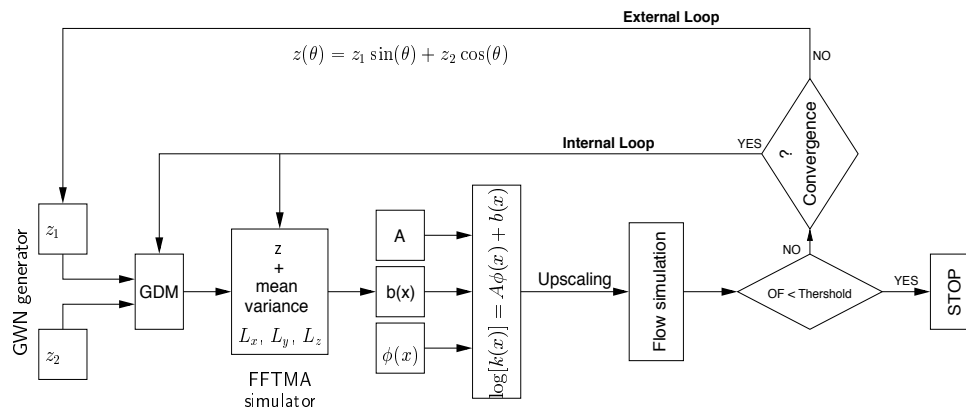


Figure 5.3: CONDOR workflow used for calibration of the 3D permeability field with both pressure and concentration data.

2. The gradual deformation method (Equation 5.11) is used to produce a Gaussian white noise  $z$ . Then, the FFTMA simulator generates the random field  $b(\mathbf{x})$  from  $z$ . Here, the following six parameters are given reasonable values: two values for the mean and variance of  $b(\mathbf{x})$ , three values for the correlation lengths of  $b(\mathbf{x})$  and an initial value for  $\theta$ .  $b(\mathbf{x})$  is a random field with a continuous spatial structure: it has a mean and variance and it is characterized by a given variogram.
3. Starting from an initial value for  $A$ , a 3D permeability field is produced from Equation 5.13. Both permeability and porosity fields are upscaled. The upscaling techniques are described in chapter 7.
4. A new 3D grid is constructed and populated with the upscaled porosity and permeability data. A flow simulation is performed and the simulated  $\Delta p(t)$  and concentration maps are extracted from the simulation outputs.
5. The objective function is calculated from Equation 5.3. If its value is less than or equal to the selected threshold value, then the optimization process stops and the 3D permeability field is printed. Otherwise, a search process is started to determine the inversion parameters minimizing the objective function. The maximal number of iterations depends on the number of parameters and is user defined.
6. If the fit is still unsatisfactory, the optimal Gaussian white noise  $z$  identified at the end of the previous step is used as a new starting point instead of  $z_1$  and a new  $z_2$  is generated. Other parameters are also updated based on their optimal values derived during step 5. A new search process is started in the **Internal loop**.

The number of **External loops** (optimization loops) is user defined. The optimization process is stopped when one of the stopping criteria is reached.

## 5.5 Concluding remarks

This chapter was a general introduction to our optimization problem. We stated that static and dynamic data are available from our viscous miscible displacement. As for the reservoir scale matching problem, one has to construct a 3D grid and populate it with known CT scan porosity data. To determine a 3D permeability field, which can reproduce the observed laboratory dynamic data, an inverse problem must be solved. We defined an optimization process and explained its objective function and related inversion parameters. We discussed a general method used to minimize the objective function and mentioned that the Powell's Dog-Leg method is used in our specific case. We also introduced a geostatistical parametrization techniques named gradual deformation method (GDM). This method is used to reduce the search space while preserving the spatial model. Finally, we discussed two optimization workflows, which are used in our work. The simple optimization workflow is used to match pressure data only. The gradual deformation based optimization workflow is used to calibrated the permeability model to both pressure and concentration data.

## Nomenclature

$A$	correlation coefficient	$g(\Theta)$	operator mapping $\Theta$ to data space
$B$	random function	$k$	permeability
$H$	Hessian matrix	$w$	weighting coefficient
$J$	objective function	$z$	Gaussian white noise
$C$	covariance matrix	$\Delta p(t)$	pressure drop as a function of time
$L_x$	correlation length along axis $X$	$\Theta$	model parameter
$L_y$	correlation length along axis $Y$	$\phi$	porosity
$L_z$	correlation length along axis $Z$	$\theta$	deformation parameter
$p$	production data	$m$	mean
$S$	concentration data	$\sigma$	standard deviation
$b$	realization of a random function	$\sigma^2$	variance



# Chapter 6

## Three Dimensional Permeability Characterization: Dynamic Data

In the previous chapter, we reviewed the main points related to our optimization problem and its solutions. In this chapter we present the dynamic data that we want to match. These data are divided into two groups: the dynamic data related to our numerical models and the ones collected during our laboratory experiments.

In section 6.1, we discuss the dynamic data for two numerical models: Model-3 and Model-4. First, their reference porosity and permeability fields are illustrated and discussed. Second, a flow simulation is performed for each model populated with its reference porosity and permeability fields. The resulting simulated  $\Delta p(t)$  and concentration data are then presented. These data are regarded as the measured data. We will use them in chapter 7 to numerically validate our proposed methodology.

In section 6.2, the laboratory measured data including  $\Delta p(t)$  and the three-dimensional porosity and concentration maps are discussed for two core samples: composite 2 and sandstone SG20. It is shown that these data require processing before being used within an optimization process. Our proposed methodology is applied to these data in chapter 7 for validation purposes.

### 6.1 Numerical models and the available data

As discussed in chapter 3, we use two numerical samples named Model-3 and Model-4 to numerically validate our proposed technique for characterizing a three-dimensional permeability field at the core scale. A brief description of these models is given in Table 3.1. The 3D porosity fields for Model-3 and Model-4 are generated using the FFTMA simulator. They are considered as random fields characterized by an exponential variogram with moderate heterogeneity. Their average porosity value is 0.19. On the other hand, the permeability fields are characterized by both longitudinal and transverse heterogeneities. They

are discussed in the following sections. The porosity and permeability are not correlated for Model-3. With this model, we verify the capability of the proposed technique in determining the coefficient  $A$  in Equation 5.13. On the contrary, the permeability data for Model-4 are correlated with porosity. Again, we check the existence of this correlation when applying our methodology.

Note that these porosity and permeability data are considered as our reference cases. A flow simulation is performed for each populated with its reference porosity and permeability fields. The resulting simulated  $\Delta p(t)$  and concentration maps are then regarded as the observed laboratory data.

### 6.1.1 Numerical data analysis

#### Model-3

A regular  $20 \times 30 \times 30$  coarse grid is considered. The model dimensions are similar to those of our core samples and are reported in Table 3.1. Both 3D porosity and log-permeability fields are generated using the FFTMA geostatistical simulator. Figure 6.1 shows some cross sectional images of the 3D porosity field for Model-3. It is characterized by an exponential variogram with correlation lengths similar to those of the experimental variogram of the porosity field for sample SG20 (see Table 3.5).

In order to represent the longitudinal heterogeneity, the grid is divided into four blocks of  $5 \times 30 \times 30$  grid cells perpendicular to the flow axis. A 3D log-permeability field is generated for each block. It is characterized by an exponential variogram with correlation lengths much bigger than those of the porosity field. They are reported in Table 3.1. The effective permeabilities of these four blocks are selected to be similar to the absolute permeabilities of different plugs in composite 1 and 2. Figure 6.2 shows some 2D images of the permeability fields for block1-3 and block2-3 (first and second block). The permeability fields computed for other blocks exhibit similar distributions.

We saw in section 3.3.2 that a simple tool for measuring the relationship between log-permeability  $\log(k)$  and porosity  $\phi$  is their correlation coefficient  $r(\log(k), \phi)$ . We use Equations 3.8 and 3.9 to calculate the correlation coefficient of porosity and log-permeability fields of block1-3 (first block):

$$\begin{aligned} C(\log(k), \phi) &= \frac{1}{4500} \sum_{i=1}^{4500} \log(k_i) \phi_i - \frac{1}{4500} \sum_{i=1}^{4500} \log(k_i) \frac{1}{4500} \sum_{i=1}^{4500} \phi_i \\ &= -0.0019 \\ r(\log(k), \phi) &= \frac{C(\log(k), \phi)}{\sigma_\phi \times \sigma_{\log(k)}} \\ &= -0.052 \end{aligned}$$

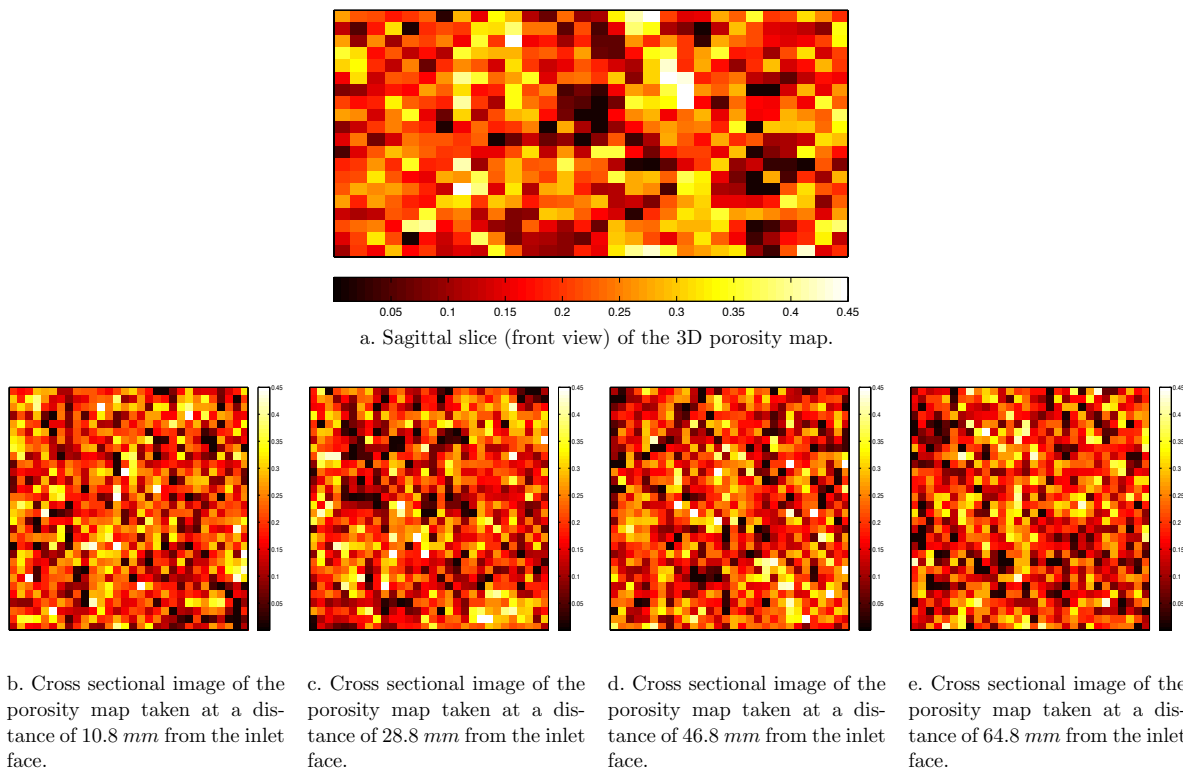


Figure 6.1: Cross sectional images of the 3D porosity map for Model-3. The Model is 72.0 mm long. The color bars show porosity.

The same calculation is repeated for all blocks. Results are reported in Table 6.1. The correlation coefficient values are close to zero, which means that there is no correlation between porosity and permeability. A flow simulation is run for this model and the simulated  $\Delta p(t)$  and two three-dimensional concentration maps are extracted. The details of the numerical simulation are given in the following chapter. Figure 6.3 shows the simulated inlet-outlet pressure drop data. Figure 6.4 depicts 2D images of the 3D concentration maps. These data are used as our reference data inside the optimization process presented in chapter 7.

Table 6.1: The correlation coefficient values for different blocks in Model-3.

		$C(\log(k), \phi)$	$r(\log(k), \phi)$
Model-3	block1-3	-0.0019	-0.052
	block2-3	0.00091	0.025
	block3-3	-0.00011	-0.0029
	block4-3	0.00084	0.024

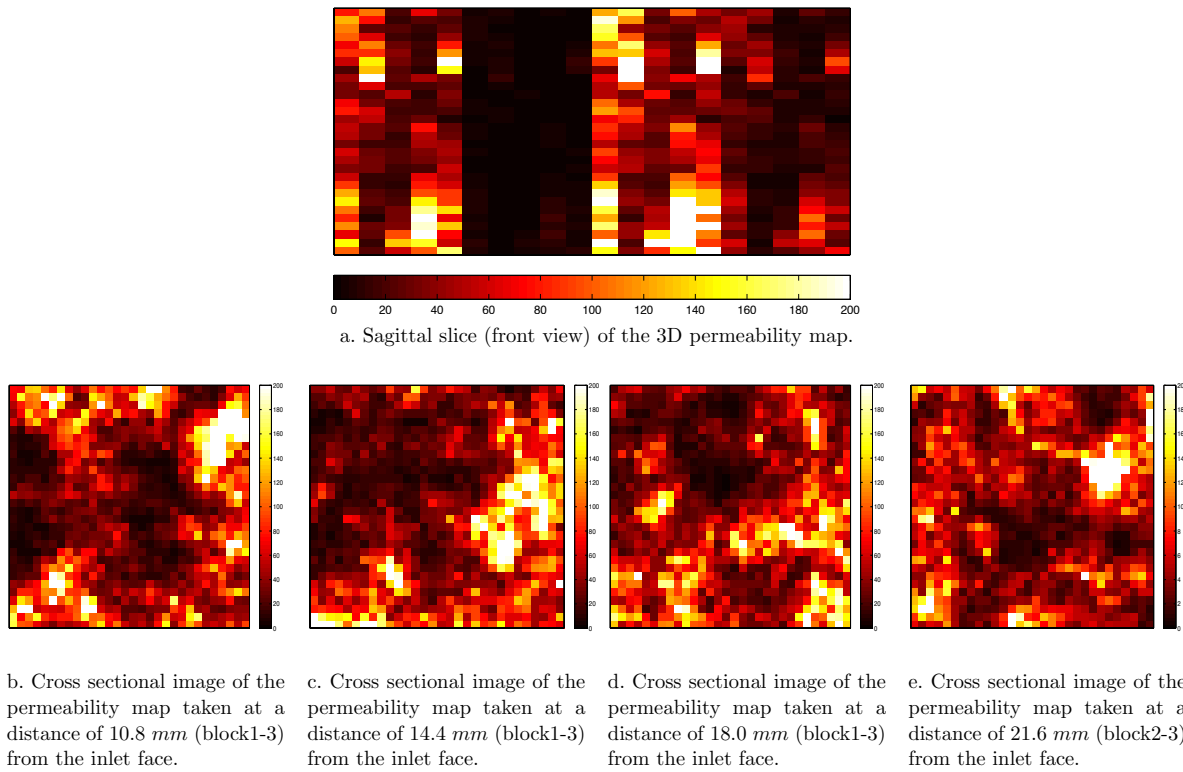


Figure 6.2: Cross sectional images of the 3D permeability map for Model-3. The Model is 72.0 mm long. The color bars show permeability.

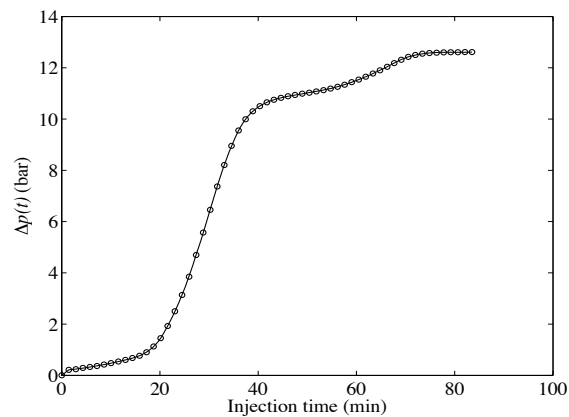
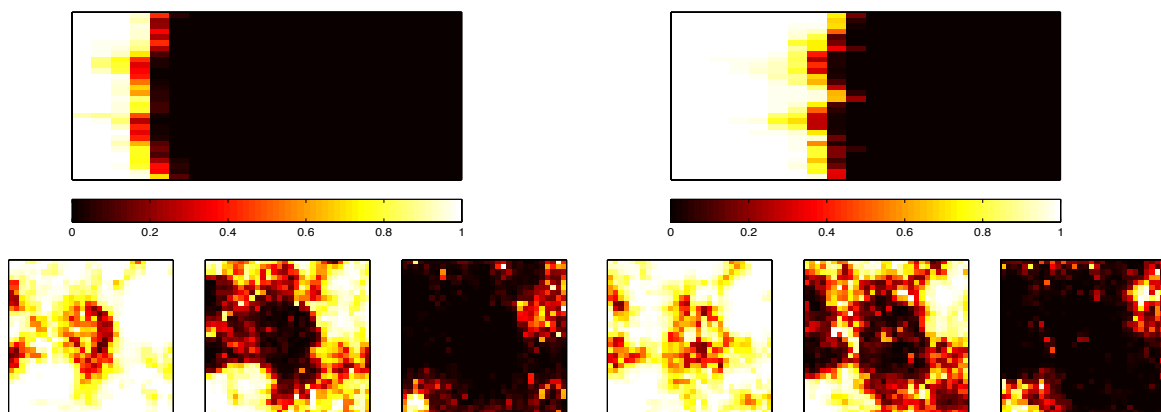


Figure 6.3: Reference inlet-outlet pressure drop data for numerical Model-3 when simulating a viscous miscible displacement. These data will be used to numerically validate our proposed methodology (see the next chapter).



a. Top: sagittal slice (front view) of the simulated concentration map at  $PVI = 0.22$ . Bottom: cross sectional images of the same concentration map taken at a distance of 14.4 mm (left), 18.0 mm (middle) and 21.6 mm (right) from the inlet face. Sample is 72 mm long.

b. Top: sagittal slice (front view) of the laboratory concentration map at  $PVI = 0.42$ . Bottom: cross sectional images of the same concentration map taken at a distance of 28.8 mm (left) and 32.4 mm (middle), 36 mm (right) from the inlet face. Sample is 72 mm long.

Figure 6.4: Reference concentration maps for numerical Model-3 when simulating a viscous miscible displacement. These data will be used to numerically validate the proposed methodology (see the next chapter). The color bars show the injected fluid concentrations.

## Model-4

A regular  $20 \times 90 \times 90$  grid is considered. The model dimensions are similar to those of our core samples and are reported in Table 3.1. The 3D porosity field is generated from the FFTMA geostatistical simulator. It has the same characteristics as for Model-3. Model-4 is also divided into four blocks of  $5 \times 90 \times 90$  grid cells perpendicular to the flow axis. A realization  $b(\mathbf{x})$  characterized by a mean  $m$ , a variance  $\sigma^2$ , and an exponential variogram is generated for each block. Then, a 3D permeability field is computed for each block using Equation 5.13 and setting a value for coefficient  $A$ . Details are reported in Table 6.2. Figure 6.5 shows some 2D images of the permeability fields for block1-4 and block2-4 (first and second block). The permeability fields for other blocks exhibit similar distributions.

Table 6.2: Statistical properties of  $b(\mathbf{x})$  for different blocks in Model-4.

		$b(\mathbf{x})$					$A$
		$m$	$\sigma^2$	$L_x$ (m)	$L_y$ (m)	$L_z$ (m)	
Model-4	block1-4	1.203	0.1	0.0144	0.02	0.02	3.28
	block2-4	0.305	0.1	0.0144	0.02	0.02	1.85
	block3-4	1.522	0.1	0.0144	0.02	0.02	2.64
	block4-4	0.897	0.1	0.0144	0.02	0.02	2.93

As for Model-3, the correlation coefficient for porosity and log-permeability fields for block1-4

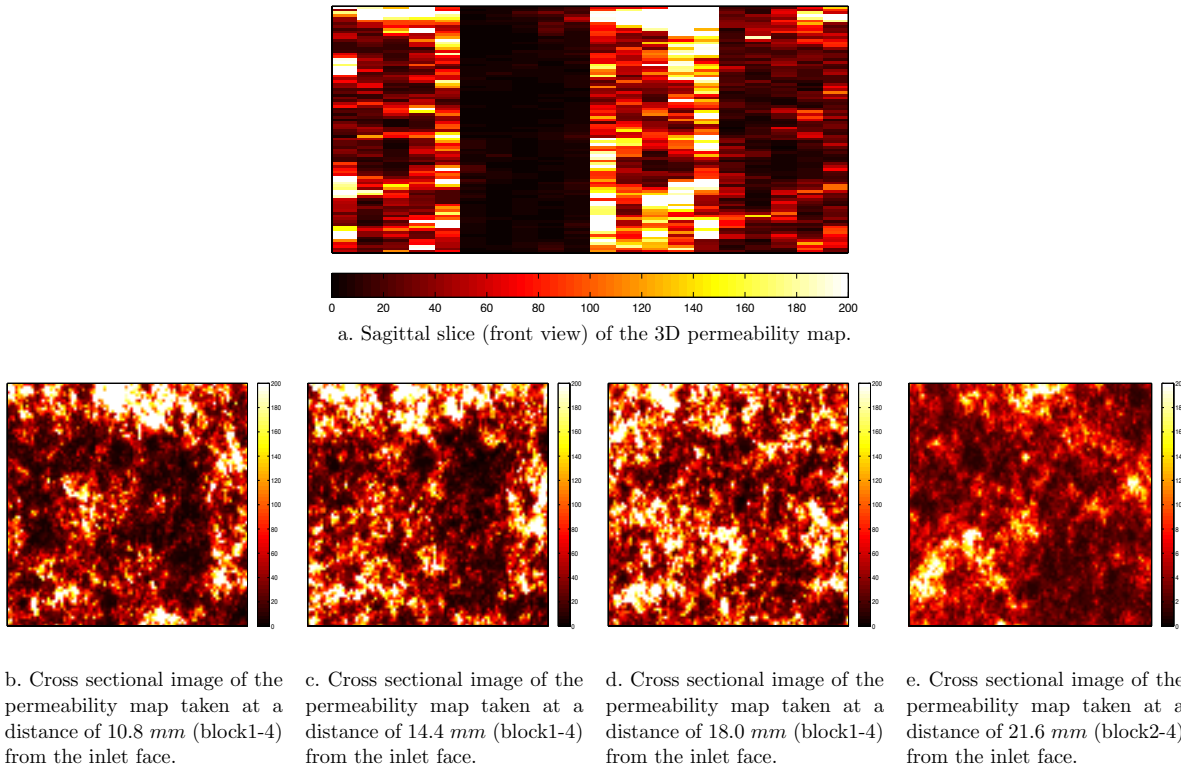


Figure 6.5: Cross sectional images of the 3D permeability map for Model-4. The Model is 72.0 mm long. The color bars show permeability.

(first block) is:

$$\begin{aligned}
 C(\log(k), \phi) &= \frac{1}{40500} \sum_{i=1}^{40500} \log(k_i) \phi_i - \frac{1}{40500} \sum_{i=1}^{40500} \log(k_i) \frac{1}{40500} \sum_{i=1}^{40500} \phi_i \\
 &= 0.032 \\
 r(\log(k), \phi) &= \frac{C(\log(k), \phi)}{\sigma_\phi \times \sigma_{\log(k)}} \\
 &= 0.76
 \end{aligned}$$

The same calculations are done for all blocks and are reported in Table 6.3. The correlation coefficient values are positive and more than 0.5 meaning that there is a strong correlation between porosity and permeability data. A flow simulation is run for this model. The simulated  $\Delta p(t)$  and two concentration maps are extracted. Figure 6.6 shows the simulated inlet-outlet pressure drop data. Figure 6.7 provides 2D images of the 3D concentration maps. These data are used as our reference data inside the optimization process presented in the following chapter.

Table 6.3: The correlation coefficient values for different blocks in Model-4.

		$C(\log(k), \phi)$	$r(\log(k), \phi)$
Model-4	block1-4	0.032	0.76
	block2-4	0.018	0.64
	block3-4	0.025	0.68
	block4-4	0.027	0.71

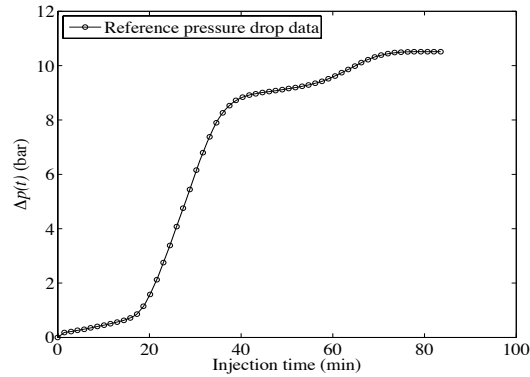
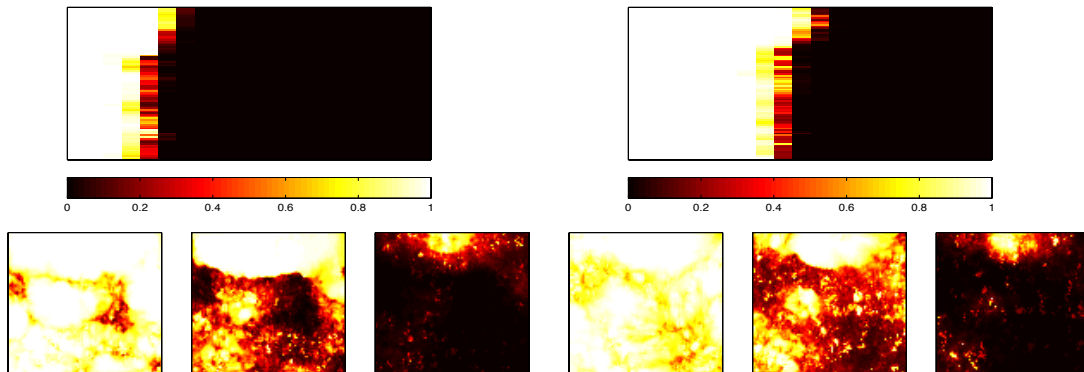


Figure 6.6: Reference inlet-outlet pressure drop data for numerical Model-4 when simulating a viscous miscible displacement. These data will be used to numerically validate the proposed methodology (see the next chapter).



a. Top: sagittal slice (front view) of the simulated concentration map at  $PVI = 0.22$ . Bottom: cross sectional images of the same concentration map taken at a distance of  $14.4 \text{ mm}$  (left),  $18.0 \text{ mm}$  (middle) and  $21.6 \text{ mm}$  (right) from the inlet face. Sample is  $72 \text{ mm}$  long.

b. Top: sagittal slice (front view) of the laboratory concentration map at  $PVI = 0.42$ . Bottom: cross sectional images of the same concentration map taken at a distance of  $28.8 \text{ mm}$  (left) and  $32.4 \text{ mm}$  (middle),  $36 \text{ mm}$  (right) from the inlet face. Sample is  $72 \text{ mm}$  long.

Figure 6.7: Reference concentration maps for numerical Model-4 when simulating a viscous miscible displacement. These data will be used to numerically validate the proposed methodology (see the next chapter). The color bars show the injected fluid concentrations.

## 6.2 Laboratory experiments and the available data

Let us come back to our laboratory experiments and the collected data. Although we considered several core samples, we only use two of them: composite 2 and the sandstone SG20. For detailed description of these two samples, see chapter 3. Physical and petrophysical properties of the samples are measured prior to any experiment. They are reported in Table 3.2. The samples are then scanned using a medical scanner. Two series of several CT slices are obtained from each sample under two different states: dry and fully saturated with 30 g/l NaCl brine. The space between CT slices is 3.0 mm and each slice has a 1 mm thickness. A porosity map is deduced from  $\frac{CT_{dry}-CT_{saturated}}{CT_{air}-CT_b}$  where  $CT_{air}$  and  $CT_b$  are the measured CT of pure air and pure brine, respectively. Each porosity map is a 3D matrix of more than  $2 \times 10^6$  data.

Then, we use an experimental device to conduct viscous miscible displacement inside the core samples. A strong core-holder seals the circumference boundary of the brine saturated samples so that flow is linear with no flow boundary conditions. The initial pressure and temperature are uniform and assumed to be  $10^5 Pa$  and  $19^\circ C$ , respectively. A 60 cp glycerin is injected into the samples with a constant flow rate. The pressure drop is recorded and CT slices are taken at successive times until stabilization of  $\Delta p(t)$ . An inverse injection is also performed for sample SG20. Concentration CT slices are taken at the same exact locations as the porosity CT slices. The concentration maps are obtained from  $\frac{CT-CT_b}{CT_g-CT_b}$  where  $CT_b$  is the measured CT of the core when 100% saturated with brine and  $CT_g$  is the measured CT of the core when 100% saturated with glycerin. Several 3D matrices each with more than  $2 \times 10^6$  concentration data are obtained at the end of each experiment. In brief, the available data for each sample are:

1. A three-dimensional porosity map.
2. Inlet-outlet pressure drop against injection time.
3. Several three-dimensional concentration maps collected at successive times.

### 6.2.1 Laboratory data analysis and processing

The experimental data recapped above are analyzed in this section. We show that all the data collected need processing before being used within our optimization workflows. We divide this section into three subsections: pressure data, porosity data and concentration data. In each subsection, the data collected for both composite 2 and sandstone SG20 are described, analyzed and processed in details.

#### Pressure data

The inlet-outlet pressure drop is recorded against time using an automatic data logger. The time lag between each recording is fixed to 6.0 sec. As the injected glycerin is very viscous,



the inlet-outlet pressure drop increases with time until breakthrough. The duration of injection depends on sample pore volume. We use two criteria before stopping the injection. First, the inlet-outlet pressure drop must reach stabilization. This means no additional increase in  $\Delta p(t)$ . Second, the CT scan concentration profiles must exhibit full glycerin saturation (*i.e.*, a horizontal line along flow axis).

**Composite 2.** 1515 data (pressure drop against time) are recorded during 170 *min* of injection. As explained in chapter 4, section 4.3.1, these data have to be rescaled to be consistent with the absolute permeability of the core sample. Moreover, we use the technique explained in chapter 4 and remove the small scale pressure fluctuations. A time lag of 2.8 *min* is used for this sample. As a result, the number of recorded data are reduced to 53. Figure 6.8 shows that the trend of processed  $\Delta p(t)$  is identical to original data set. The final processed data are used as the reference pressure drop data in our optimization workflows.

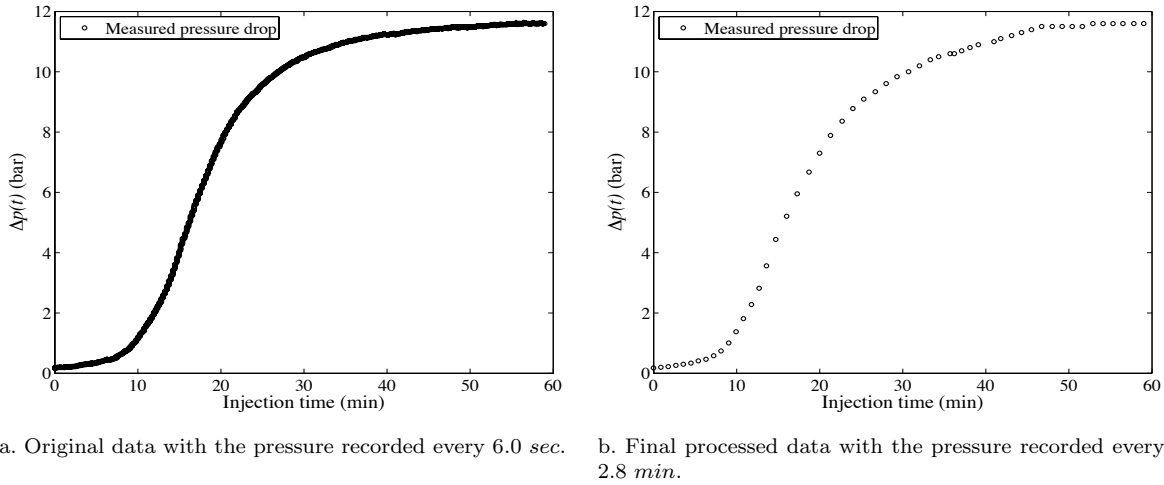


Figure 6.8: The inlet-outlet pressure drop data against injection time for composite 2.

As discussed in the previous chapter, the standard deviations are used to normalize the difference between simulated and measured data. For the pressure drop data of composite 2, the standard deviation  $\sigma_{Composite2}^p$  and the weighting coefficient  $w_{Composite2}^p$  are calculated from Equation 5.4 and 5.5:

$$\sigma_{Composite2}^p = \frac{1}{10 \times 53} \sum_{i=1}^{53} p_i = 1.81$$

$$w_{Composite2}^p = \frac{1}{[\sigma_{Composite2}^p]^2} = 0.31$$

$w_{Composite2}^p$  is the local weight. The final weighting coefficient is calculated by dividing the local weight by the number of pressure-time measurements (see Equation 5.3).

**Sandstone SG20.** Two displacement tests are performed for this sample: One from left to right (normal injection) and one from right to left (inverse injection). The collected pressure drop data are much noisier than those obtained for composite 2.

During normal injection experiment, 650 data pairs (pressure drop against time) are recorded during 156 *min*. They are rescaled to be consistent with the absolute permeability of the sample. Figure 6.9(a) shows the normal inlet-outlet pressure drop against time for this sample. The measured  $\Delta p(t)$  shows small fluctuations after about 23 minutes of the beginning of the injection. 37 minutes after injection, a sudden negative jump in  $\Delta p(t)$  is observed. These pressure behaviors can not be clearly explained. As we mentioned earlier, the injected glycerin is very viscous compared to in-place NaCl brine. Therefore, the pressure drop must be an increasing monotonic function of time. We believe that the electrical pump malfunctioning caused these negative jumps. In our optimization process, we ignore the pressure data associated to negative jumps by assigning zero local weights to them.

For the normal injection, the number of pressure drop data is reduced to 78. We calculate the standard deviation  $\sigma_{SG20-N}^p$  and the weighting coefficient  $w_{SG20-N}^p$  as follows:

$$\sigma_{SG20-N}^p = \frac{1}{10 \times 78} \sum_{i=1}^{78} p_i = 0.58$$

$$w_{SG20-N}^p = \frac{1}{[\sigma_{SG20-N}^p]^2} = 2.91$$

The collected pressure drop data show more fluctuations when performing the inverse injection. More than 450 pairs of  $\Delta p(t)$  data are recorded during 100 *min*. Figure 6.9(b) shows the inverse inlet-outlet pressure drop data against time. We rescale these data and only consider the ones obtained during the first 14 *min* of the injection. The remaining data are neglected due to their erratic behavior. The number of recorded data is then reduced to 41. Similarly to normal injection, we calculate the standard deviation  $\sigma_{SG20-I}^p$  and the weighting coefficient  $w_{SG20-I}^p$  as follows:

$$\sigma_{SG20-I}^p = \frac{1}{10 \times 41} \sum_{i=1}^{41} p_i = 0.63$$

$$w_{SG20-I}^p = \frac{1}{[\sigma_{SG20-I}^p]^2} = 2.51$$

Zero local weights are assigned to data showing negative pressure jumps. We will see in the following chapter that the SG20 numerical model consists of 25 grid cells along the flow axis. We divide this model into two sub-grid: one with 18 grid cells and the other one with 7 grid cells along the flow axis (Figure 6.9, top). The normal pressure drop data will be used to find a permeability model for the first sub-grid. The inverse pressure drop data will be used to find a permeability model for the second sub-grid. For more details, see chapter 7.

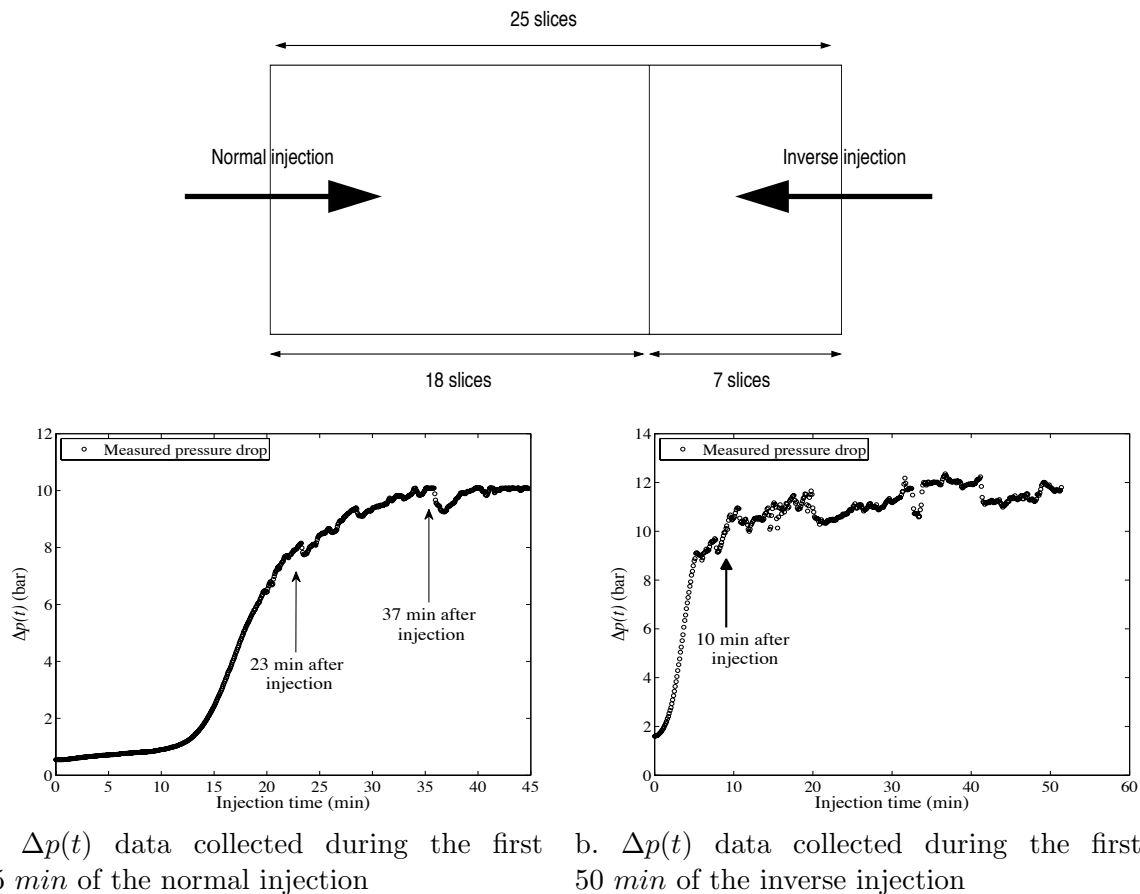


Figure 6.9: Top: the SG20 numerical model is divided into two sub-grid: one with 18 grid cells along flow axis and the other one with 7 grid cells. Bottom: normal and inverse  $\Delta p(t)$  data are used to find a permeability model for the each sub-grid. More explanation are given in the next chapter.

## Porosity data

In chapter 3, we discussed the statistical properties of the three-dimensional porosity fields for both composite 2 and SG20 sample. In this chapter, we take a closer look at porosity data and discuss the data processing required before including these porosity data to our optimization workflows.

**Composite 2.** 20 CT porosity slices are obtained at 20 successive locations along the flow direction axis. The space between CT slices is 3.0 mm. Therefore, the resolution of porosity data along the flow axis is 3 mm. Notice that the number of CT slices along the flow axis is automatically optimized for both porosity and concentration acquisitions. As mentioned earlier, the CT slices of porosity and concentration data must correspond to the

same exact locations. Increasing the number of slices, decreases the CT scan efficiency in acquiring several series of transverse concentration images over a short period of time (*i.e.*, injection time). Each CT slice is a two-dimensional matrix of  $512 \times 512$  porosity data with a resolution of  $100\mu\text{m} \times 100\mu\text{m}$ . As the slice thickness is  $1.0\text{ mm}$ , each voxel (volume pixel) represent a volume of  $0.01\text{ mm}^3$ . The original slices are masked and cropped. The final images consist of  $329 \times 329$  voxels. Eventually, we get a three-dimensional matrix of  $20 \times 329 \times 329$  porosity data. Figure 6.10 shows some 2D slices of this 3D porosity field.

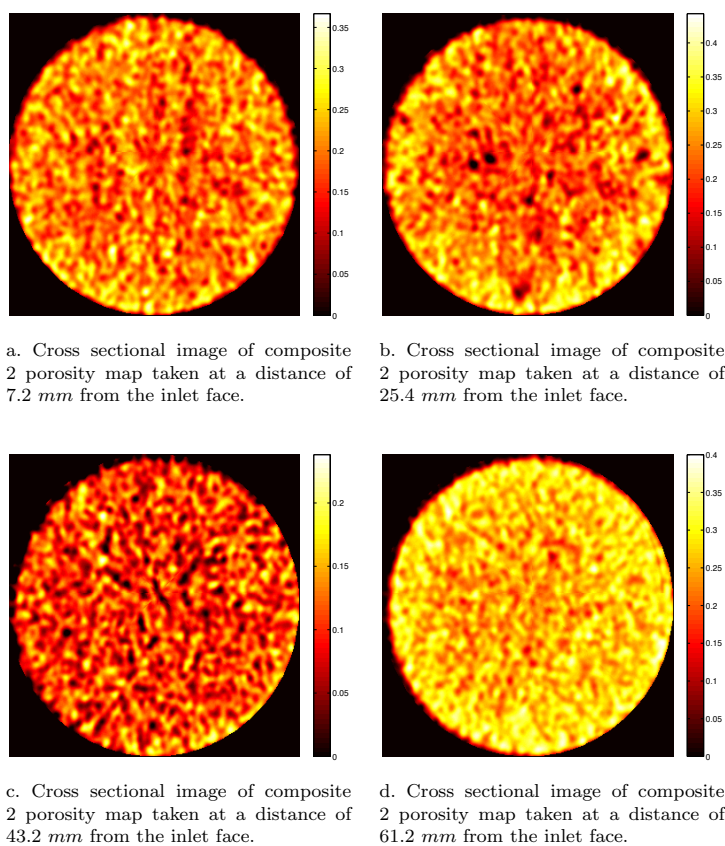


Figure 6.10: Cross sectional images of the 3D porosity map for composite 2. The core is  $72.4\text{ mm}$  long. The color bars show porosity.

A thin red boundary can be observed around the 2D images in Figure 6.10. This is a scanning artifact known as beam hardening. In general, the low-energy, high attenuating X-rays are adsorbed more easily near the edge of the sample resulting in higher attenuation coefficients. Using the IFP scanner, the beam hardening artifact is reduced by optimizing the X-ray beam energy and using beam filtration. However, it still can be observed in our X-ray CT images. We use a simple visual inspection and remove this bright boundary by replacing its values with zeros. We ensure that the sample diameter is uniform along the flow axis and is consisted with its laboratory measured value (see Table 3.2). Figure 6.11 shows the 2D

porosity images after removing this artifact. The average porosity per slice is also calculated before and after removing the artifact and is shown in Figure 6.12. The maximum difference is 0.0093. The arithmetic average of the 3D porosity data has changed from 0.1982 to 0.2046, a difference of 0.0064, which is negligible.

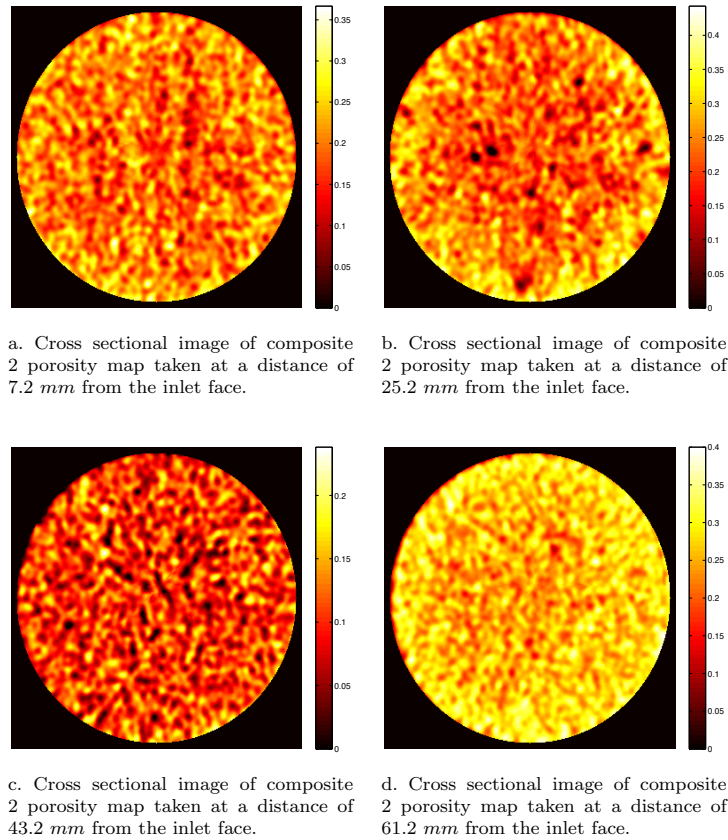


Figure 6.11: Cross sectional images of the 3D porosity map for composite 2. The core is 72.4 mm long. The color bars show porosity.

We saw earlier that with the resolution of our medical CT scanner, each voxel represents a volume of  $0.01 \text{ mm}^3$ . This volume is bigger than a pore size. Therefore, a voxel cannot represent a pore and its porosity is always less than 1.0. The minimum and the maximum values for the CT porosity of composite 2 are 0.002 and 0.50, respectively. More than 80% of the porosity voxels of composite 2 are non zeros (*i.e.*, active voxels). CT porosity values are generally noisy. When scanning the core sample, one should pay enough attention to CT slice positioning: two-dimensional CT slices for the dry or saturated sample must be collected at the same exact locations. However, there is still some perturbation. It can be visualized by comparing two images  $I_1$  and  $I_2$ , which are taken from a dry core sample at the same location one after another (Figures 6.13(a) and 6.13(b)). We expect  $CT_{I_2} - CT_{I_1}$  to be a 2D Null matrix but Figure 6.13(c) shows that its values vary between  $-60$  and  $+60$ ,

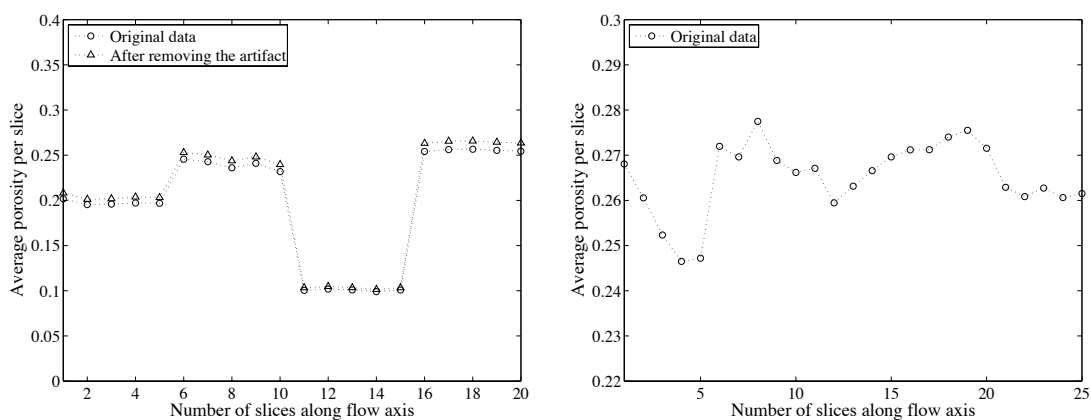


Figure 6.12: Left: the arithmetic average of composite 2 porosity values per slice along flow axis. The average values are calculated for the original data and after removing the beam hardening effect. Right: same calculation for sample SG20. The hardening effect is negligible for this sample.

which represents an error of about 3% compared to the CT values of  $I_1$  and  $I_2$ . Data post processing such as moving average filter could slightly smooth the noise, but it would never remove it. As the arithmetic average of the 3D porosity data for composite 2 is very close to the laboratory measured porosity, CT porosity noise is neglected.

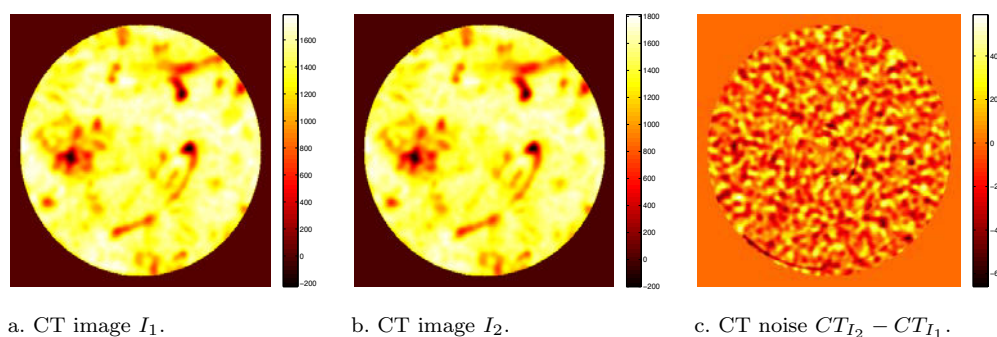


Figure 6.13: Visualization of CT noise by comparing two images  $I_1$  and  $I_2$ , which are taken from a dry core sample at the same position one after another.  $CT_{I_2} - CT_{I_1}$  is the noise. The color bars show the CT values in Hounsfield unit.

**Sandstone SG20.** 25 CT porosity slices are obtained at 25 successive locations along the flow direction axis. The space between CT slices is 3.0 mm. Each CT slice is a two-dimensional matrix of  $512 \times 512$  porosity data with a resolution of  $100\mu\text{m} \times 100\mu\text{m}$ . The original slices are masked and cropped. The final images consist of  $334 \times 334$  volume elements. As for composite 2, we have a final three-dimensional matrix of  $25 \times 334 \times 334$  porosity data. At first glance, the beam hardening artifact is much limited in sandstone

SG20. Figure 6.14 shows some of its 2D porosity images. The average porosity per slice is also calculated and plotted in Figure 6.12. The minimum and the maximum values of SG20 CT porosity values are 0 and 0.7, respectively. Again, the arithmetic average of the 3D porosity data for this sample is very close to the laboratory measured porosity. Thus, the CT porosity noise is neglected.

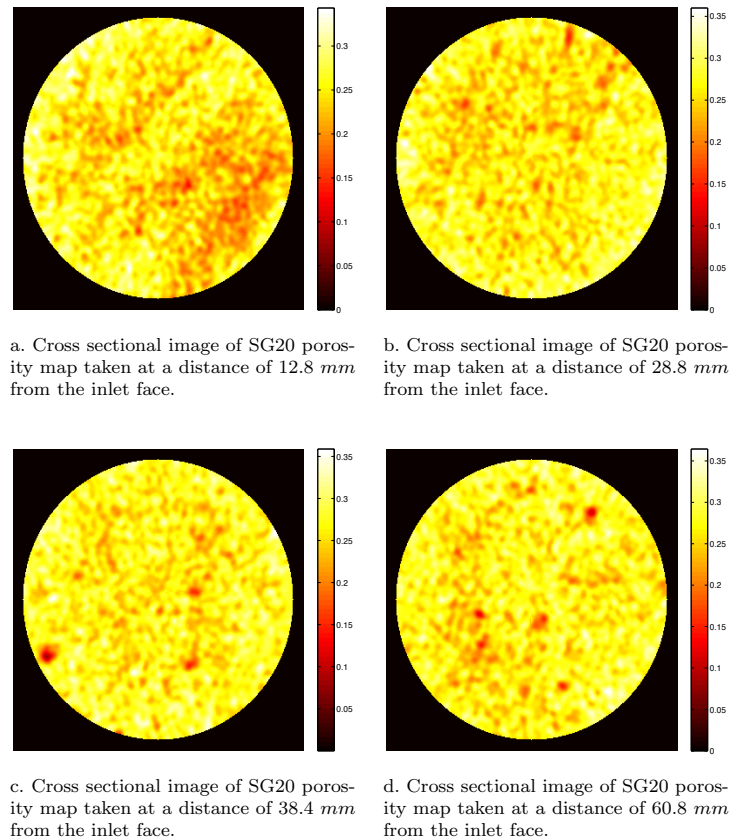


Figure 6.14: Cross sectional images of the 3D porosity map for sample SG20. The core is 79.6 mm long. The color bars show porosity.

### Concentration data

During viscous miscible injection, CT slices are recorded at successive times until the sample is fully saturated and exhibits a horizontal CT concentration profile. Concentration CT slices are taken at the same exact locations as the porosity CT slices. Several 3D matrices of concentration data are obtained at the end of the experiment. The beam hardening artifact is not strong during the acquisition. However, to make 3D concentration maps consistent with the 3D porosity map, we create a binary mask from porosity data. Multiplying each 3D concentration map by this mask leads to new 3D matrices of concentration data nicely

aligned with the 3D pattern of porosity map. With this technique, we make sure that each 3D concentration matrix has the same size of the 3D porosity matrix of the sample, with the same number of active voxels.

The main difficulty when processing concentration data is the noise inherent to CT images. The capability of scanner to differentiate between neighboring volume elements with similar attenuation is limited. This phenomenon is even stronger during a miscible displacement, because there is a mixed zone between displacing and displaced fluids. The noise evidenced in our work originates from several sources. The most significant one is the short duration of each intensity measurement (1.0 sec), which is required to capture the rapid front movement inside the porous medium. Figure 6.15 shows the front shape and the concentration distribution for composite 2 during four successive times. The first plug exhibits small scale heterogeneities in the form of beddings. This can be visualized in the first two concentration maps (Figures 6.15(a) and (b)). As the front enters the second plug, the concentration distribution becomes homogeneous and no obvious heterogeneity can be observed.

For an injected pore volume of 0.45 ( $PVI = 0.45$ ), the front is still inside the second plug (see Figure 6.15(c)). However, the third and fourth plugs show non zero concentration values. This is noise.

The frequency distribution of concentration data is calculated for the 2D slices of this concentration map (at  $PVI = 0.45$ ). Three different distributions are observed. They are plotted in Figure 6.16. The first one is related to the fully glycerin saturated part of the sample (Figure 6.16(a)). In this case, the concentration values vary between 0.6 and 1.0. The second distribution is related to the partly glycerin saturated zones (Figure 6.16(b)) and the last one is related to non saturated part of the sample (Figure 6.16(c)). The concentration values vary between 0.0 and 0.3 for the later case, while they are expected to be zeros.

In such a condition, removing the noise is not simple. We can use a moving average filter to reduce the noise and smooth the CT images. This is shown in Figure 6.17. A non glycerin saturated 2D slice of the same concentration map (Figure 6.15(c)) is selected and filtered with a moving average technique. Two averaging windows of  $8 \times 8$  and  $16 \times 16$  voxels are applied. In both cases, we still observed non zero concentration values.

The arithmetic average of concentration values is calculated for each slice of this concentration map (Figure 6.15(c)). It is plotted in Figure 6.18(a). Another difficulty is pointed out. The average concentration of the fully glycerin saturated slices is less than 1.0. It is probably due to the mixing of glycerin and brine. Furthermore, the third plug shows the average concentration values higher than the expected values (near zero). The same concentration profile can be observed even at the beginning of injection. Enough attention has been paid to keep the sample clean. However, the only cause, which can explain this phenomenon, is the existence of non NaCl particles inside this plug. We process the concentration data base on following procedure:



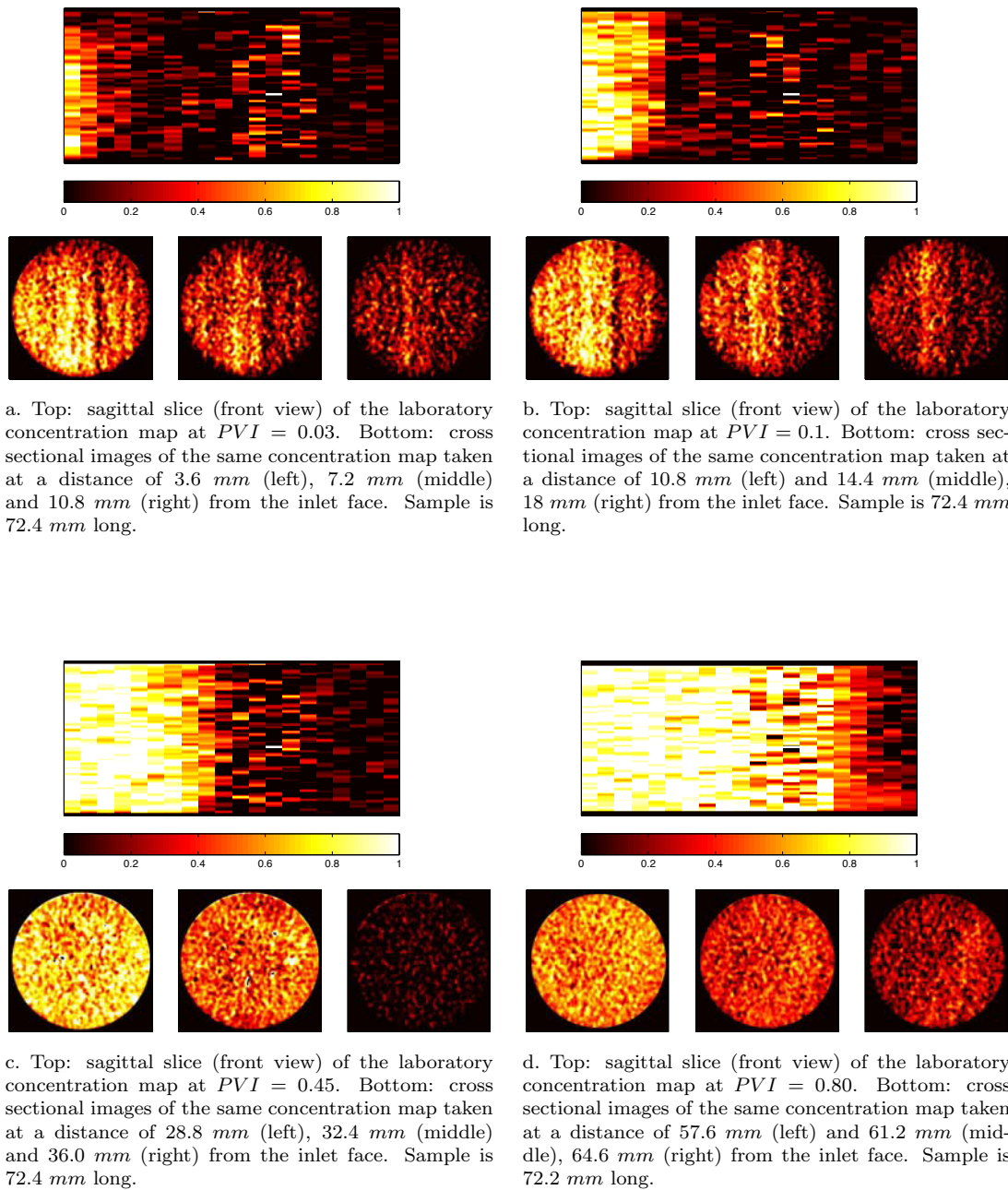


Figure 6.15: 2D images of the 3D concentration maps obtained at successive times for composite 2 when performing laboratory viscous miscible displacement. In (a) and (b), the displacement front is located inside the first plug. In (c) it is located inside the second plug and in (d) inside the third plug. The color bars show the injected fluid concentrations.

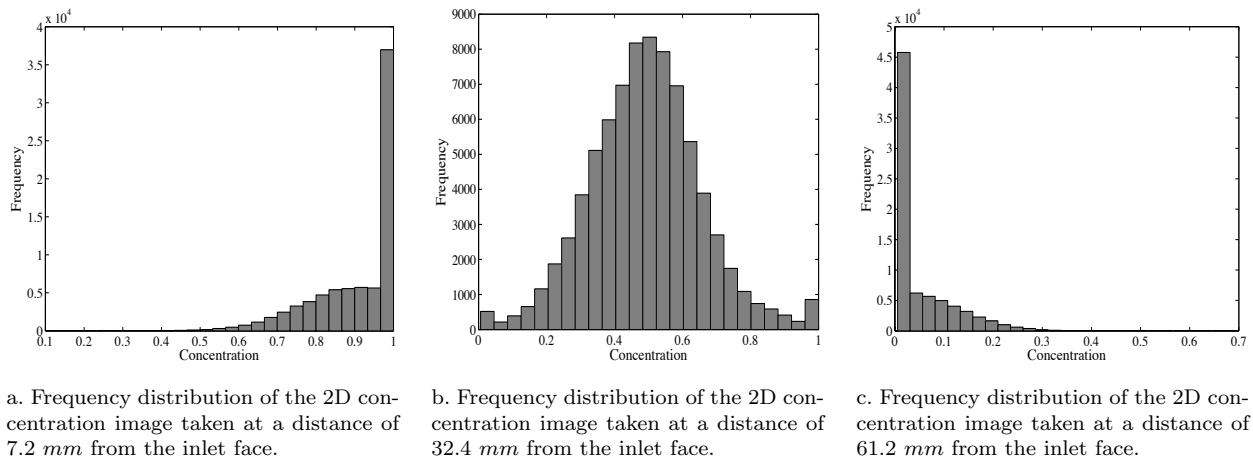


Figure 6.16: The frequency distribution of some concentration images obtained at  $PVI = 0.45$  for composite 2.

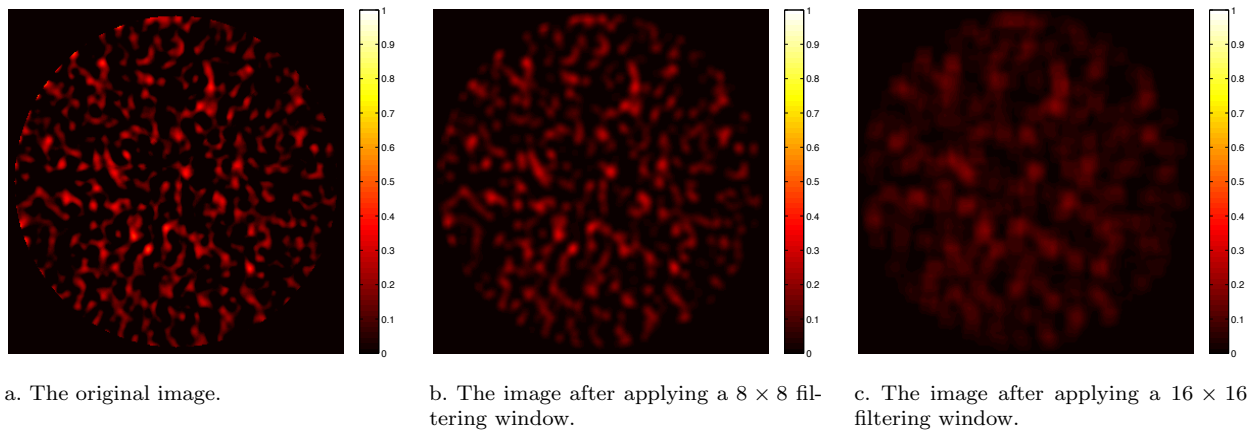


Figure 6.17: A 2D concentration image taken at a distance of 61.2 mm from the inlet face of composite 2 (at  $PVI = 0.45$ ). The image noise is smoothed using a moving average technique. The color bars show the injected fluid concentrations.

1. The pure glycerin zone plus the mixed zone are approximately detected in 3D concentration maps using the concentration gradient profile with the help of three-dimensional visual inspection and frequency distribution plots.
2. The concentration values of the 2D slices located in the pure brine zone are turned to zeros.
3. The 2D concentration slices located in pure glycerin zone and the slices which are partly saturated, are not processed.

Using this technique, we remove the noise in the non swept areas. The slices, which are located close to the front are not processed to keep the natural form of the concentration distribution. The results of this processing is shown in Figure 6.18(b) for the concentration map obtained at  $PVI = 0.45$ .

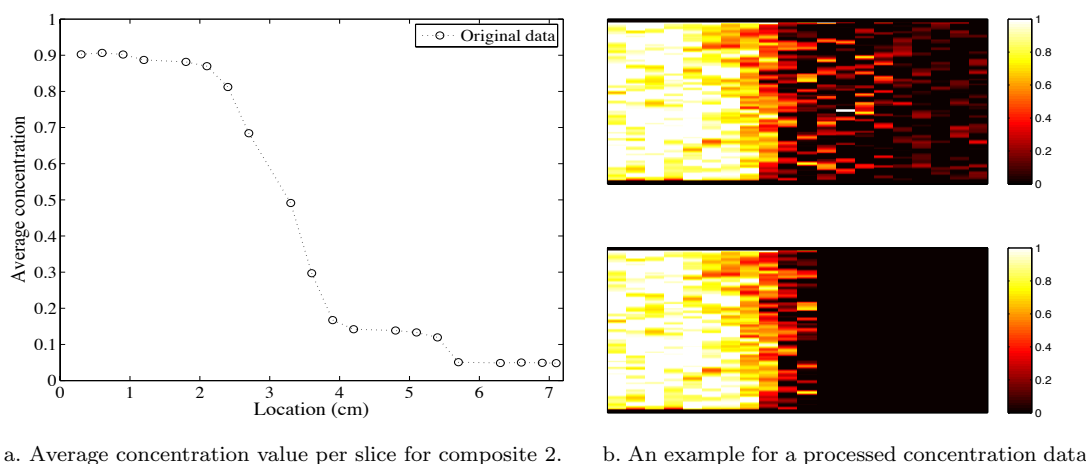


Figure 6.18: Left: Average concentration value calculated for 20 slices of composite 2 along flow axis at ( $PVI = 0.45$ ). The axis  $X$  indicates location of CT slices. Right: sagittal slice (front view) of the original concentration map compared with the same image after removing the noise. The original concentration data are obtained from composite 2 at  $PVI = 0.45$ . The color bars show the injected glycerin concentrations.

The concentration data obtained for sandstone SG20 show characteristics similar to composite 2. The processing of SG20 concentration data is similar to those of composite 2. For this sample, the concentration distribution is not homogeneous inside the slices, which are fully saturated with glycerin. In such slices (*e.g.*, Figure 6.21(a)), there are zones, which are fully saturated and zones, which are not saturated at all. We keep the original data and only remove the noise in the non swept zones.

**Normal injection:** for the injection from left to right, we could not obtain the concentration data during the first 15 *min* of the injection (scanner technical problems). Six concentration maps, which are obtained during the injection are shown in Figures 6.19 and 6.20. In the first half of the sample, the areas close to the boundary seem less saturated resulting in a conic front shape (Figures 6.19(b) and (c)). One may relate this to the edge effect. For slow flow rates, the fluid velocity is maximum at the center and reduces slightly towards the sample edges. The edge effect is minimized with high flooding rate. Sample SG20 is flooded with a flow rate of 30 *cc/hr*, which is twice the flow rate of composite 2. As the edge effect was not observed in composite 2, it is less probable to happen for sandstone SG20.

The concentration distribution for the second half of the sample is different. First, no

boundary is clearly identified. Second, as the front approaches to sample's end, small scale heterogeneities can be observed. Figures 6.19(d) and 6.20 show that the sample is composed of inclined bedding with different permeabilities. This heterogeneities are better observed during the inverse injection.

**Inverse injection:** several concentration maps are acquired during the injection from right to left. Eight of them are shown in Figures 6.21–6.23. The small scale bedding can be easily observed in the first half of the sample. A piece of hard material (probably iron) is also observed near inlet face of the sample, resulting in a circular non saturated area. It is visualized in the lower half of the first CT slice in Figure 6.22(a). As the displacement front approaches the second half of the sample, the bedding effects vanish and again one can see a less saturated boundary near the edges of the sample. These results are in complete agreement with the results of normal injection.

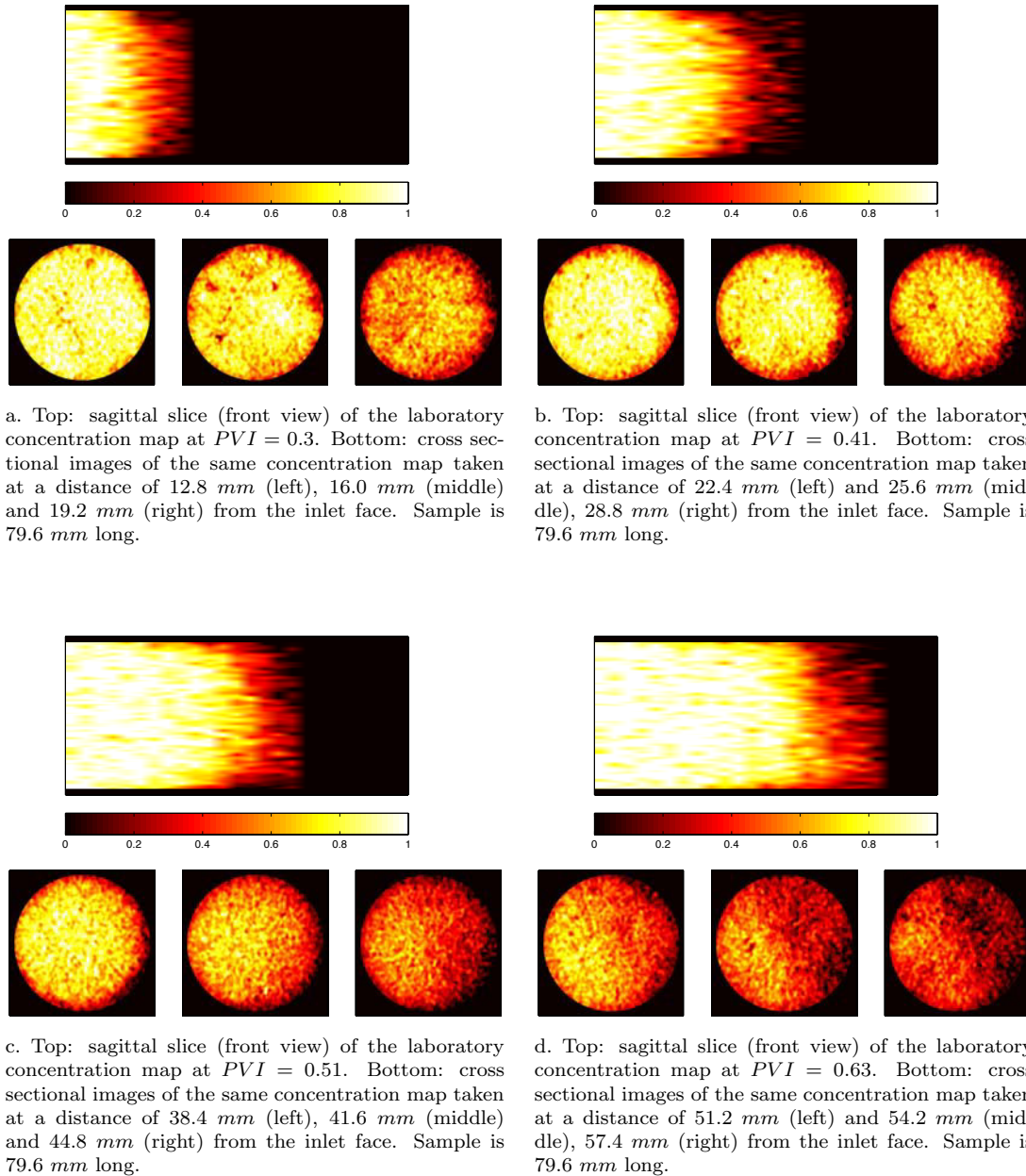


Figure 6.19: 2D images of the 3D concentration maps for sandstone SG20 taken at two successive times after injection. The viscous miscible injection is performed from left to right (normal injection). The color bars show the injected glycerin concentrations.

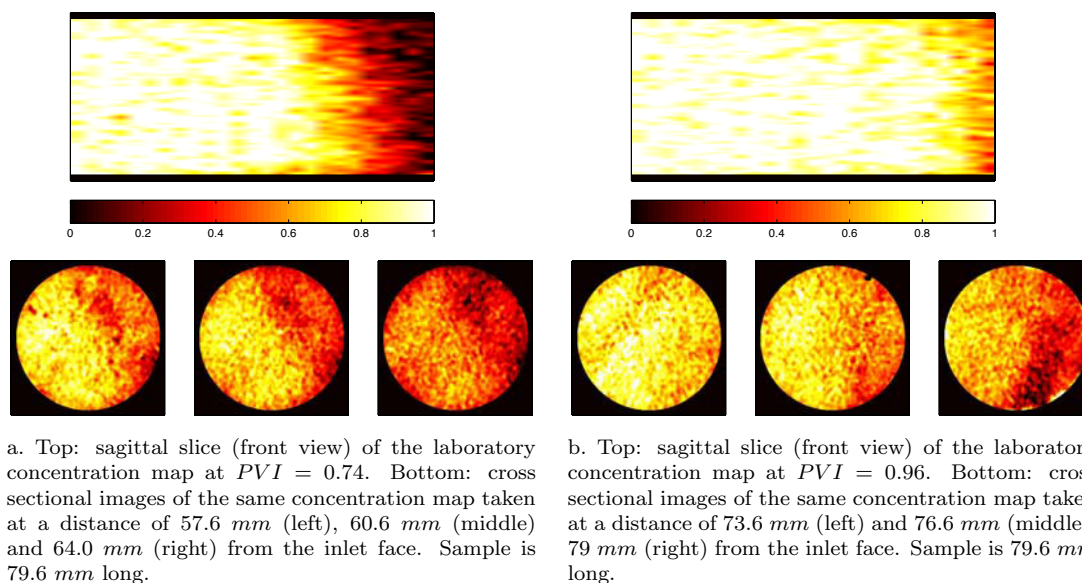


Figure 6.20: 2D images of the 3D concentration maps for sandstone SG20 taken at two successive times after injection. The viscous miscible injection is performed from left to right (normal injection). The color bars show the injected glycerin concentrations.

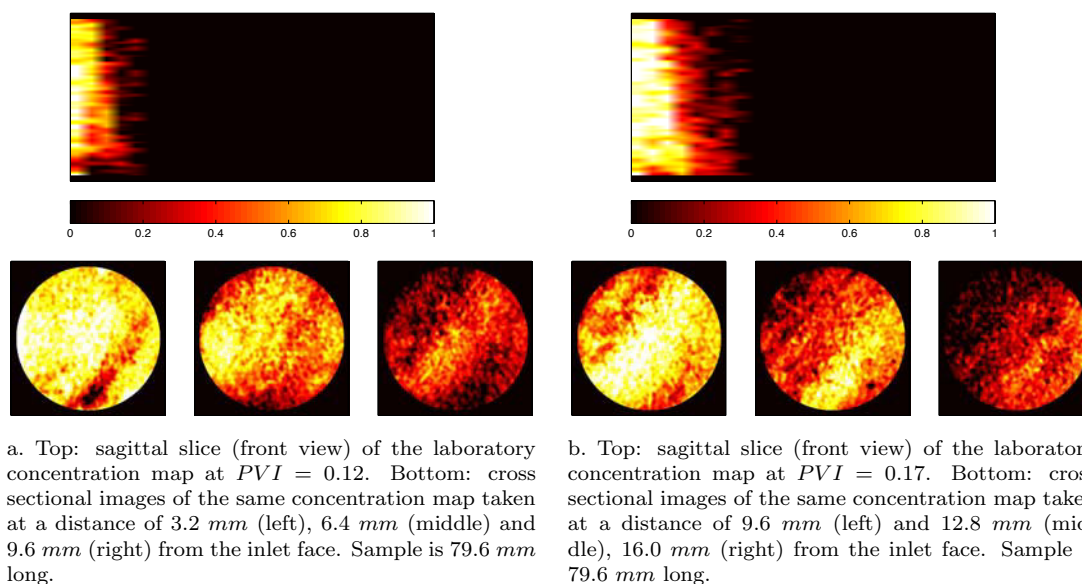


Figure 6.21: 2D images of the 3D concentration maps for sandstone SG20 taken at two successive times after injection. The viscous miscible injection is performed from right to left (inverse injection), but the images are reversed to be consistent with other Figures. The color bars show the injected glycerin concentrations.

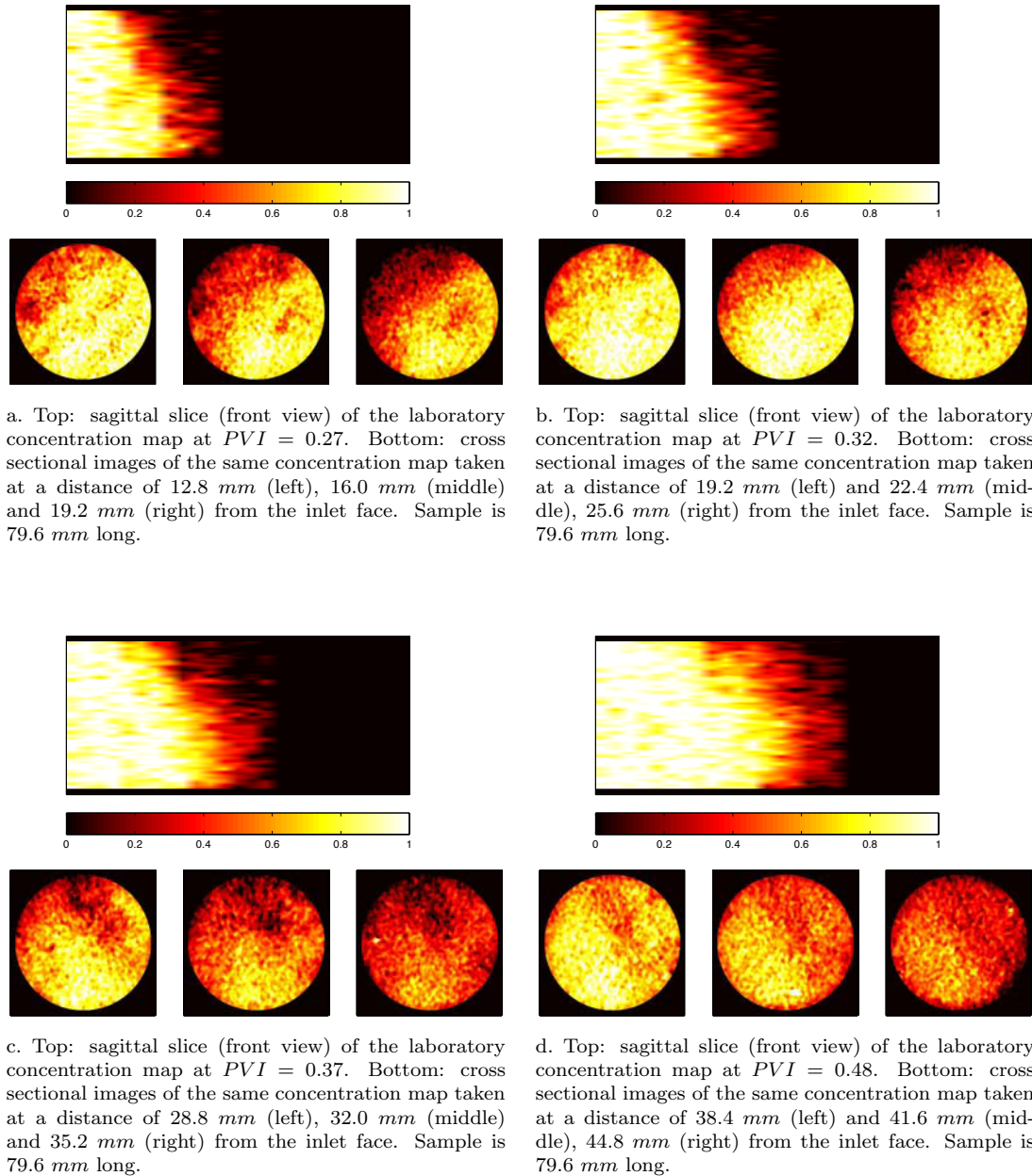


Figure 6.22: 2D images of the 3D concentration maps for sandstone SG20 taken at two successive times after injection. The viscous miscible injection is performed from right to left (inverse injection), but the images are reversed to be consistent with other Figures. The color bars show the injected glycerin concentrations.

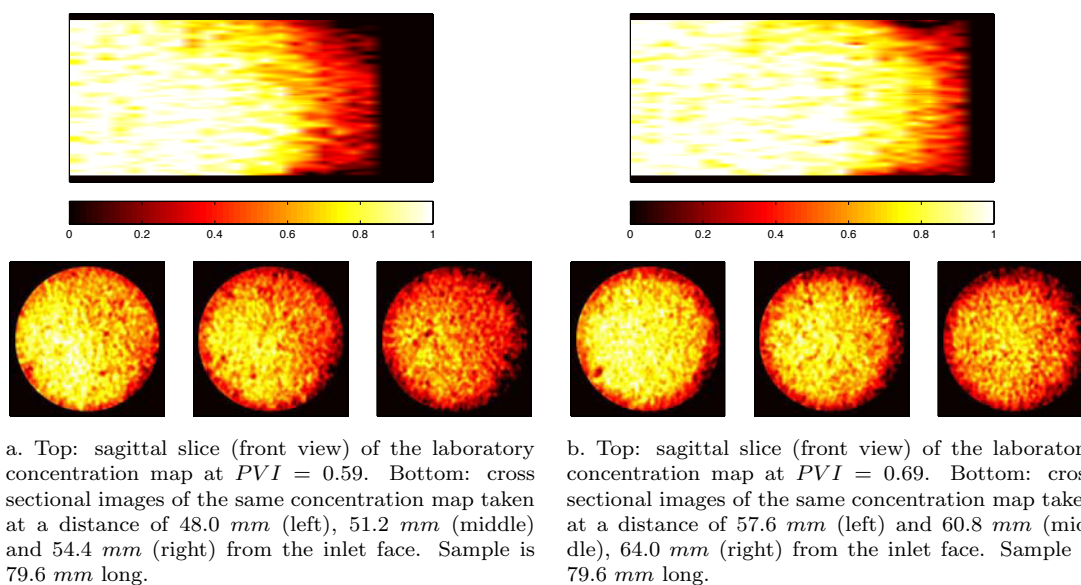


Figure 6.23: 2D images of the 3D concentration maps for sandstone SG20 taken at two successive times after injection. The viscous miscible injection is performed from right to left (inverse injection), but the images are reversed to be consistent with other Figures. The color bars show the injected glycerin concentrations.

### 6.3 Concluding remarks

In this chapter, we presented the available dynamic data, which will be used in the following chapter to characterize more precisely permeability distribution inside core samples. In the first part, we focused on the numerical models that will be used to validate our methodology. We discussed the numerical porosity and permeability data, which are used to produce the reference  $\Delta p(t)$  and concentration maps. We showed that with the two models considered here, heterogeneity was evidenced in both directions, parallel and perpendicular to flow axis. In the second part, we discussed in details, the  $\Delta p(t)$ , porosity and saturation data obtained during our laboratory measurements for composite 2 and sandstone sample SG20. We showed that both porosity and concentration data are noisy. This noise can be ignored for porosity data, but it has to be reduced or removed for concentration data. The 3D concentration maps for composite 2 showed that small scale heterogeneities are visible only for the first plug. The concentration data were homogeneously distributed for the remaining of the core sample. The sandstone sample exhibited small scale heterogeneities when observing its concentration distribution for both normal and inverse injections.



# Chapter 7

## Three Dimensional Permeability Characterization: Application

In chapter 5 we discussed the workflows used in this study to calibrate a three-dimensional core scale permeability field to both static and dynamic data. These data were introduced and discussed in chapter 6. In this chapter, we aim at applying our proposed methodology to these data within the framework of field scale history-matching techniques (see also Soltani *et al.* [53]). We use CONDOR, which is a prototype software developed at IFP, to perform our optimizations. Within CONDOR, we perform flow simulations using PumaFlow (also developed at IFP). Some extra programmings are necessary to design CONDOR workflows to core scale optimizations. In section 7.1, we briefly introduce the PumaFlow simulator and the modifications of its input file for performing core scale miscible displacements. In section 7.2, the proposed methodology is validated referring to numerical samples, Model-3 and Model-4. These samples were already discussed in the previous chapter. In section 7.3, we first apply our methodology to the data collected for composite 2. The influence of the inversion parameters on the matching process is discussed in details. The evolution of the objective function with both pressure drop and concentration terms is also illustrated and discussed. Then, the same study is carried out for sandstone sample SG20.

### 7.1 PumaFlow numerical simulator

PumaFlow is a finite difference numerical simulator developed at IFP. The reason for which we use this simulator instead of any other one is its availability in terms of licenses. IFP is equipped with a computer cluster and it is possible to perform several simulations at the same time. Thus, we effectively reduce the computation time.

One should notice that PumaFlow is a field scale reservoir simulator. In order to run this simulator for core scale optimization purposes, we must modify its input file. Most of these modifications were explained earlier in chapter 4. However, there are still some important

points to be mentioned.

**First**, as discussed in chapter 4, we can simulate a miscible displacement with an immiscible flow model by neglecting capillary pressures and defining straight line relative permeability functions. In PumaFlow, it is mandatory to define a table of saturation against capillary pressure data. However, we can choose the capillary pressure values to be extremely small and nullify their effect. Note that hereafter, the word “saturation” is identical to “concentration”. We also denote the miscible phases glycerin and brine by “gly” and “w”, respectively. Relative permeability data are defined in order to better represent the glycerin-water displacement process. From Todd and Longstaff [58] empirical model for miscible displacements, one assume  $\frac{k_{rw}}{k_{ro}} = \frac{S_w}{1-S_w}$  and consider a mixing parameter  $\omega$  to calculate the effective phase viscosities from Equation 7.1.

$$\begin{aligned}\mu_{ew} &= \mu_w^{1-\omega} \mu_m^\omega \\ \mu_{egly} &= \mu_{gly}^{1-\omega} \mu_m^\omega\end{aligned}\tag{7.1}$$

where  $\mu_{ei}$  is the effective viscosity of phase  $i$ ,  $\mu_i$  is the viscosity of pure phase  $i$  and  $\mu_m$  is the mixture viscosity determined from a quarter-power mixing rule [58, 1, 50, 4]. Once the effective viscosities are determined, the fraction of each phase  $i$  inside the mixed zone can be calculated [58]. In their formulation, miscibility is considered through parameter  $\omega$ . When it equals zero, there is no miscibility (or dispersion) and when it equals one, there is a complete mixing within the grid cell. For our purpose, the miscibility is defined through relative permeability data instead of parameter  $\omega$ . The miscibility implies that  $k_{rgly} + k_{rw} = 1$  whatever the saturation  $S_{gly}$  is. We ignore the 30 g/l NaCl dissolved in water and use a standard pure water-glycerin mixture curve as presented in Figure 7.1(a). Relative permeabilities against saturation data are calculated as follows.

1. The mass percentage of glycerin (presented in axis  $X$  in Figure 7.1(a)) is converted to saturation from  $S_{gly} = \frac{m_{gly}/\rho_{gly}}{m_{gly}/\rho_{gly} + m_w/\rho_w}$ . Here,  $\rho_i$  is the density of phase  $i$ .
2. For each  $S_{gly}$ , a glycerin-water mixture viscosity  $\mu_m$  is derived from the reference curve in Figure 7.1(a).
3. Relative permeability data are obtained from  $1/\mu_m(S_{gly}) = k_{rgly}/\mu_{gly} + k_{rw}/\mu_w$  and  $k_{rw} = 1 - k_{rgly}$  with end points of 1.  $\mu_{gly}$  is the viscosity of pure glycerin and  $\mu_w$  is the viscosity of pure brine.

The resulting relative permeability curves are plotted in Figure 7.1(b).

**Second**, with a regular grid definition, the simulator performs calculations for all grid cells including non active cells (*i.e.*, zero porosity grid cells) around the core sample. This will consume a lot of CPU time. We set the grid type to non regular to avoid these extra computations. In PumaFlow, different algorithms can be used to solve the numerical problems. We select fully implicit method, which is the PumaFlow default numerical algorithm.

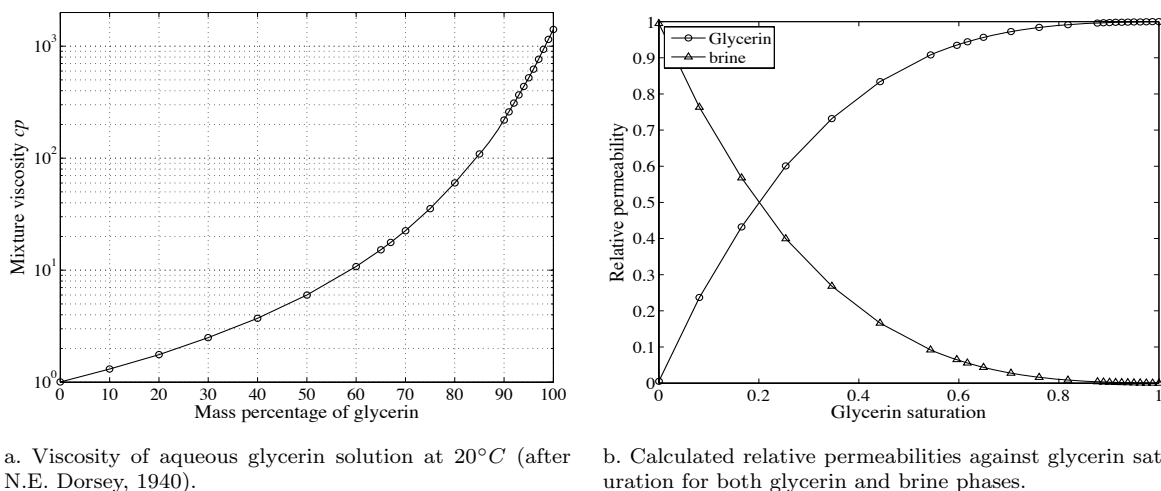


Figure 7.1: The relative permeability data calculated from the standard pure water-glycerin mixture curve presented in (a). They are used to better represent the glycerin-water displacement process.

**Third**, in the conventional finite difference simulators, proper time step size must be selected to ensure: (a) stability of the solution, and (b) acceptable truncation errors. Both of these requirements are related to the rate of change of pressure and saturation inside grid cells [1]. PumaFlow uses an automatic time step selection algorithm by defining maximum pressure and saturation changes PVAR and SVAR, respectively. If the pressure or saturation exceeds these user defined limits, time step size is divided by two and the calculations are repeated.

**Fourth**, PumaFlow provides pressure and saturation data for all grid cells at different time steps. The inlet-outlet pressure drop data are calculated from Equation 4.10 for each time step. It is also possible to print the simulated saturation data for any desired time during the injection period. This is specially important when comparing the simulation results with the laboratory measured concentration data: they must correspond to the same exact time.

**Fifth**, sensitivity analyses are required to estimate the effect of time step size and grid cell size on flow simulation results. From sensitivity analysis performed with 3DSL, (chapter 4, section 4.2.1) we concluded that time step size must be small enough to ensure convergence. We also concluded that the grid cell size must be small in the flow direction to better represent the front resolution. As stated above, in PumaFlow, time step size is selected automatically and thus, no sensitivity analysis is required. The number of grid cells along the flow axis is equal to the number of X-ray CT slices taken along the flow direction. Thus, no sensitivity analysis is performed for the grid cell size in this direction. The upscaling of grid cells perpendicular to flow axis was studied with 3DSL. The results are also valid for the PumaFlow simulator. The reason for which we perform upscaling within our optimization workflows is to reduce the optimization cost in terms of computation time and memory. Assuming an upscaling ratio of  $n : 1$ , the following upscaling technique is used for the grid

cells perpendicular to flow axis:

$$\begin{aligned}\bar{k} &= \frac{\sum_{i=1}^n \sum_{j=1}^n k_{i,j}}{n \times n} \\ \bar{\phi} &= \frac{\sum_{i=1}^n \sum_{j=1}^n \phi_{i,j}}{n \times n}\end{aligned}\tag{7.2}$$

In this formulation,  $k$  is permeability,  $\phi$  is porosity,  $\bar{k}$  is the upscaled permeability,  $\bar{\phi}$  is the upscaled porosity and  $i$  and  $j$  are the grid cell indices in  $Y$  and  $Z$  directions, respectively. Note that the effective permeability of the grid should be calculated from the harmonic average of the upscaled grid cells along the flow direction axis [11].

## 7.2 Numerical validation

The proposed methodology in chapter 5 is applied to two numerical models for validation purposes. These models and their numerical pressure drops and concentration maps are illustrated and discussed in the previous chapter. Let us remind that the unknown parameters when producing a permeability field are: deformation parameter  $\theta$ , coefficient  $A$ , mean  $m$ , variance  $\sigma^2$  and the correlation lengths of  $b(\mathbf{x})$  (see chapter 5). Considering Equation 5.13, the influence of each parameter on the final permeability map is different. From basic statistics we have:

$$\begin{aligned}E[\log_{10}(k(\mathbf{x}))] &= A \times E[\phi(\mathbf{x})] + E[b(\mathbf{x})] \\ V[\log_{10}(k(\mathbf{x}))] &= A^2 V[\phi(\mathbf{x})] + V[b(\mathbf{x})] + 2A \times C(\phi(\mathbf{x}), b(\mathbf{x}))\end{aligned}\tag{7.3}$$

where symbols  $E$  and  $V$  stand for expected value and variance, respectively.  $C$  is the covariance. The following remarks can be emphasized.

1.  $\phi(\mathbf{x})$  and  $b(\mathbf{x})$  are independent variables and thus,  $C(\phi(\mathbf{x}), b(\mathbf{x})) = 0$ .
2.  $A$  is a correlation coefficient. A strong  $A$  means a strong correlation between permeability and porosity. If  $A$  equals zero, porosity and permeability become independent variables.
3. If we assume that  $\phi(\mathbf{x})$  and  $b(\mathbf{x})$  are stationary variables, then the average permeability of the model can be predicted from the average values of  $\phi(\mathbf{x})$  and  $b(\mathbf{x})$ .
4. As the variances of our porosity fields are small, the variances of permeability model are strong functions of  $b(\mathbf{x})$  variance and weak function of  $A$ .

5. We assume that the porosity field is characterized by an exponential variogram. If  $b(\mathbf{x})$  is a Gaussian white noise, then the permeability field can be characterized by the same variogram as the one of the porosity field plus a discontinuity at the origin (nugget effect). If  $b(\mathbf{x})$  is characterized by the same variogram as the one of the porosity field, then the variogram of the permeability field becomes a linear combination of two exponential variograms.
6. The small scale permeability heterogeneity of the model is a direct function of natural heterogeneity of porosity map and correlation lengths of  $b(\mathbf{x})$ . Increasing the correlation lengths of  $b(\mathbf{x})$  leads to a heterogeneous permeability field even if the porosity field is statistically homogeneous.

For a large number of inversion parameters, the optimization process can be intensive in terms of CPU time. Therefore, depending on the optimization purposes, we should only consider the most influential parameters. A simple solution is to compare the gradients of the objective function with respect to each parameter (*i.e.*,  $\frac{\partial J}{\partial \Theta}$ ). Regarding the remarks made above, we categorize our inversion parameters into two groups:

1. parameters  $A$ ,  $\mu$  and  $\sigma^2$ , which are somehow related to the average permeability of the grid cells along the flow direction axis;
2. Deformation parameter  $\theta$ , and correlation lengths  $L_x$ ,  $L_y$  and  $L_z$ , which influence the spatial permeability distribution.

The following sections are dedicated to the application of our optimization workflows when characterizing the three-dimensional permeability fields at the core scale.

### 7.2.1 Model-3

When analyzing reservoir well test results, the bottom hole pressure drop can be inverted to infer well blocks permeability. This means that pressure drop is mostly a function of average rock permeability. On the contrary, the fluid distributions provide information about geological heterogeneities. These remarks are also valid for our core scale displacements. The inlet-outlet pressure drop for a core sample is a function of permeability variations along the flow direction axis. Therefore, for calibrating the permeability field to the pressure data, no specific permeability distribution is required. However, the reference concentration data cannot be reproduced without accounting for small scale transverse heterogeneities in our permeability models.

## History matching of pressure data

In the first part, we calibrate the Model-3 permeability field to the reference pressure data. The unknown parameters are coefficient  $A$  as well as the mean  $m$  and variance  $\sigma^2$  of  $b(\mathbf{x})$ . We know that Model-3 consists of four blocks perpendicular to flow axis. We assume that the correlation lengths of  $b(\mathbf{x})$  are similar to the correlation lengths of the reference 3D porosity data and construct a permeability field for each block. Having three unknown parameters for each permeability field, we get 12 parameters for the entire model.

As the average permeability and porosity of the blocks are known, we can approximate the initial values of  $A$ ,  $m$  and  $\sigma^2$  for each block using equation 7.3. Let us consider the first block of Model-3. From Table 3.1, its average permeability is  $70 \text{ mD}$ . Its average porosity is calculated from an arithmetic average and equals 0.1982. Assuming  $A = 3.0$ , then:

$$E[b(\mathbf{x})] = E[\log_{10}(70)] - 3.0 \times E[0.1982] = 1.25$$

One may wonder why to select this value for parameter  $A$ . Clearly, we should be able to take any initial value for this parameter. However, when looking at Equation 7.3, a negative  $A$  means a negative correlation between porosity and permeability. For  $A \geq 6$ , the permeability field shows nonsensical values (*e.g.*,  $10^6 \text{ mD}$ ). For these reasons, we have to define proper initial values (with upper and lower bounds) for  $A$  as well as for the other parameters. In addition, we define two permeability cutoffs: permeability values lower than  $0.01 \text{ mD}$  are set to 0.01 and those bigger than  $4000 \text{ mD}$  are set to  $4000 \text{ mD}$ . These cutoff values are selected after a few sensitivity tests when changing cutoff values and comparing simulation CPU times.

The calculation of the variance of permeability field is also straightforward. From Table 3.1, the variance of the Model-3 porosity field is 0.0093. Assuming  $A = 3.0$  and  $V[b(\mathbf{x})] = 0.2$ , we get:

$$V[\log_{10} k(\mathbf{x})] = 3.0^2 \times 0.0093 + 0.2 = 0.2837$$

As the variance of porosity data is small, the variance of permeability field becomes a strong function of  $V[b(\mathbf{x})]$ . Note that the initial  $V[b(\mathbf{x})]$  has been randomly selected. The initial values for our 12 unknown parameters are reported in Table 7.1.

Table 7.1: The initial inversion parameters used to calibrate the 3D permeability field of Model-3 to pressure data.

		$b(\mathbf{x})$					$A$
		$\mu$	$\sigma^2$	$L_x$ (m)	$L_y$ (m)	$L_z$ (m)	
Model-3	Block1-3	1.25	0.2	0.01	0.003	0.002	3.0
	Block2-3	0.028	0.2				2.0
	Block3-3	1.45	0.2				3.0
	Block4-3	0.73	0.2				4.0

We use our primary optimization workflow described in chapter 5, section 5.4.1 to calibrate

the Model-3 permeability field to pressure data only. Model-3 consists of 18000 grid cells: no upscaling is required. The optimization details are summarized below.

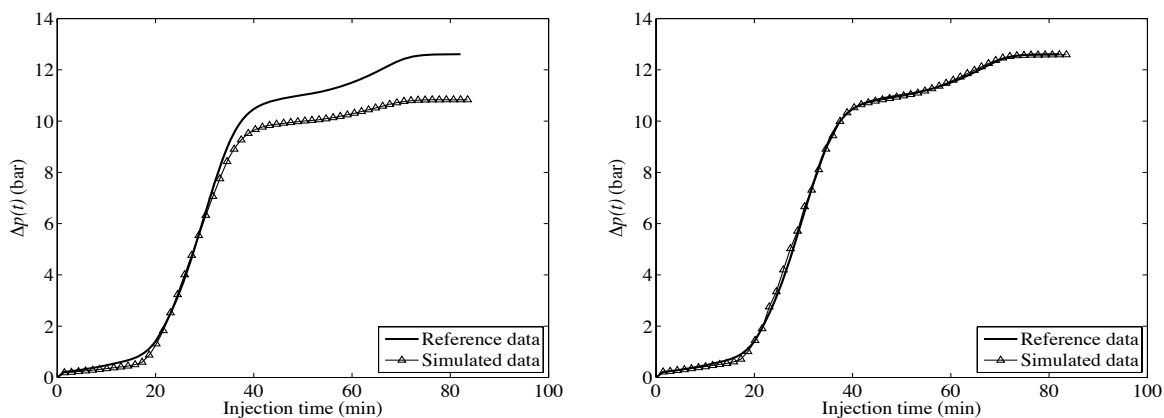
1. A perturbation is applied to each parameter  $\Theta$  to compute the objective function derivatives.
2. The parameters are then updated moving to the optimal direction calculated from the Powell's Dog-Leg algorithm.
3. A new iteration is performed with the updated parameters. Several perturbations can be applied to get new derivatives at some iterations until the simulated  $\Delta p(t)$  duplicates as well as possible the reference inlet-outlet pressure drop.

Step 3 is repeated until a convergence criterion is reached. It can be the decreasing ratio of the objective function or the maximum number of simulations. They are both user defined. The results show that after 12 iterations (43 simulations), we are capable of perfectly reproducing the reference  $\Delta p(t)$  curve. This is illustrated in Figure 7.2. The evolution of the parameters against the number of iterations is depicted in Figure 7.3.

As can be seen, the parameters  $A$  and  $m$  show minor changes after 12 iterations. They are dependent parameters: increasing one results in decreasing the other one. On the other hand, the variations in the variance of  $b(\mathbf{x})$  are strong. Because we work with a numerical case, the variance of the true permeability field is known (see Table 3.1). Thus, we hope the parameter  $\sigma^2$  to get close to its reference value at the end of the optimization. This is not the case. For block1-3, the optimized variance of the permeability field is 27% higher than its reference value (see Table 7.2). A similar behavior is observed for the variance of other permeability zones: our linear  $\log(k) - \phi$  correlation is not capable of reproducing the reference variance of the permeability fields. In other words, the true variance of  $b(\mathbf{x})$  can not be determined from pressure drop data.

The effective permeability of a 3D permeability field  $\bar{k}$ , can be calculated from Cardwell and Parsons method [11]. In this method, the effective permeability is calculated from the harmonic average of the arithmetic average of the grid cells perpendicular to flow axis.  $\bar{k}$  is calculated for each block of Model-3 for both the reference and the optimized permeability data. The results are reported in Table 7.2. Although the simulated pressure data are perfectly matched with the reference pressure data, an average error of 8.5% is still observed between the optimized and the reference effective permeability values.

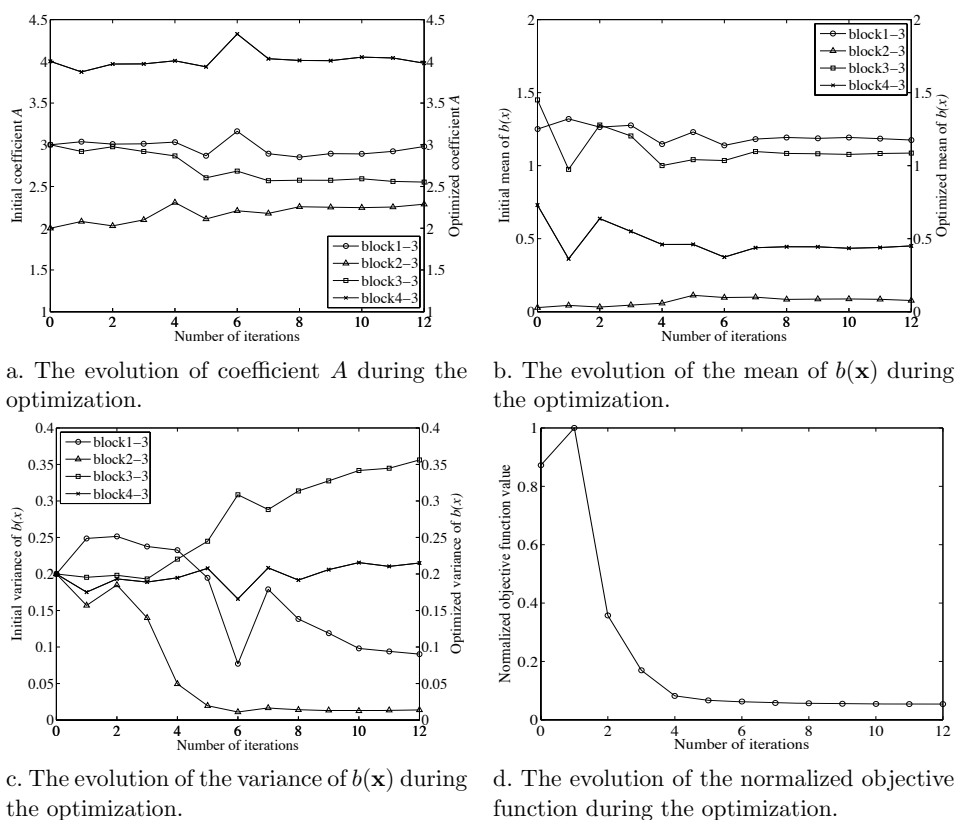
The evolution of the normalized objective function against the number of iterations is illustrated in Figure 7.3(d). It is reduced to more than 5% of its initial value.



a. Beginning of the optimization.

b. End of optimization.

Figure 7.2: Comparison of the reference pressure drop data with the simulated ones for the numerical Model-3 before and after the primary optimization process.

a. The evolution of coefficient  $A$  during the optimization.b. The evolution of the mean of  $b(\mathbf{x})$  during the optimization.c. The evolution of the variance of  $b(\mathbf{x})$  during the optimization.

d. The evolution of the normalized objective function value during the optimization.

Figure 7.3: The evolution of different parameters and the normalized objective function for the numerical Model-3 during the primary optimization process.



Table 7.2: Comparison of the  $\sigma^2$  and the average permeability for the reference data with the calibrate ones for Model-3. Permeability fields are calibrated to only pressure data. Notice that  $\bar{k}$  is calculated from the harmonic-arithmetic-arithmetic average of 3D permeability data in  $XYZ$  directions.

		$\sigma_{\log_{10}(k)}^2$ (ref)	$\sigma_{\log_{10}(k)}^2$ (optim)	% error $_{\sigma^2}$	$k_{ref}$ (mD)	$k_{optim}$ (mD)	% error $_{\bar{k}}$			
Model-3	Block1-3	0.1386	0.1763	27	70	14.3	90.89	13.05	29	8.5
	Block2-3	0.1386	0.0614	55	4.5		3.82		15	
	Block3-3	0.1386	0.4005	188	106		114.08		7.6	
	Block4-3	0.1386	0.3552	156	29		40.29		38	

An important question may be raised here: are the optimized parameters unique? An answer is provided by repeating the same optimization process with different initial parameters. Let us remember that the seed used to generate the Gaussian white noise is always the same and the new initial parameters are still calculated as explained at the beginning of this section. Another simple optimization is performed with new initial parameters (Figure 7.4). After 8 iterations (45 simulations), the optimization is stopped and the optimized parameters are printed. The results show that the pressure match is as good as the first simple optimization and that the objective function is reduced to more than 1% of its original value. The so optimized parameters are not the same as those of the previous optimization. This means that there is no unique response for this optimization process. The behavior of parameters  $A$ ,  $m$  are similar to those of the first optimization. But, parameter  $\sigma^2$  behaves differently. No general trend can be observed for this parameter.

In brief, using our simple calibration process with three unknown parameters  $A$  and  $m$  and  $\sigma^2$ , a 3D permeability field is produced, which can perfectly duplicate the reference inlet-outlet pressure data. The parameters  $A$  and  $m$  can be determined from the reference pressure data. However, there is not enough information in the pressure drop data to retrieve the parameter  $\sigma_{b(x)}^2$ . Less than 40 numerical simulations are required to calibrate the permeability field of this model with pressure data. Each simulation consumes approximately 4.8 *min* of CPU time. Therefore, the duration of a simple optimization is around than 2.5 *hr*. Using a computer cluster with 8 nodes (8 simultaneous simulations), this time is reduced to 35 *min*. Is this calibration enough? The answer is given in the next section.

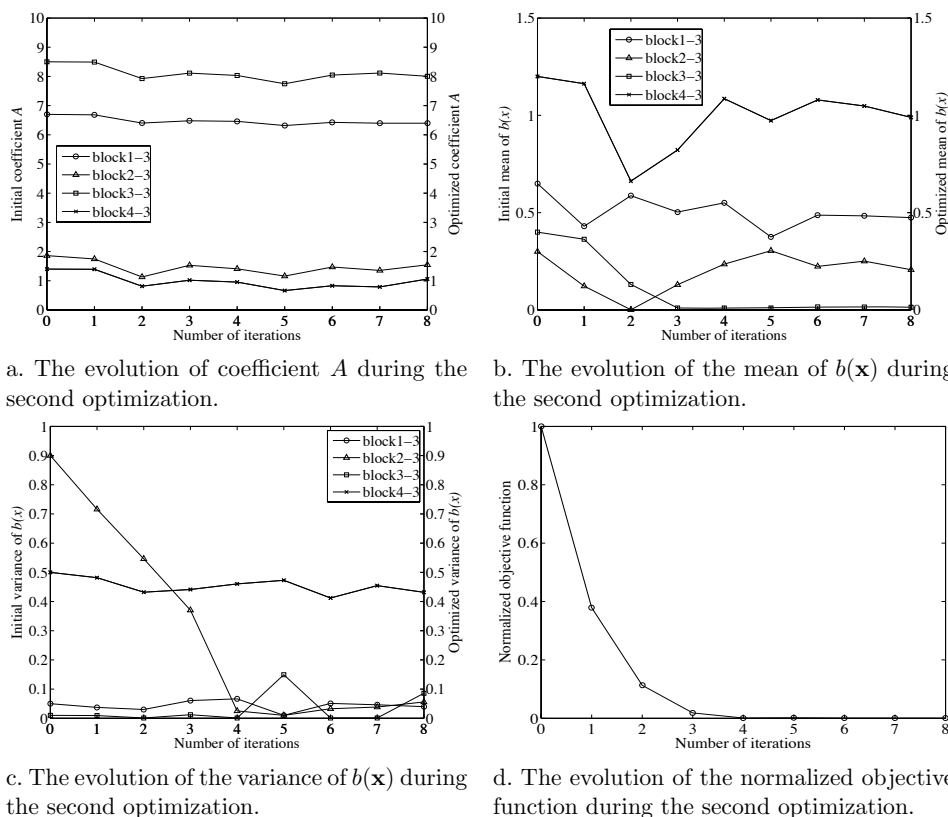


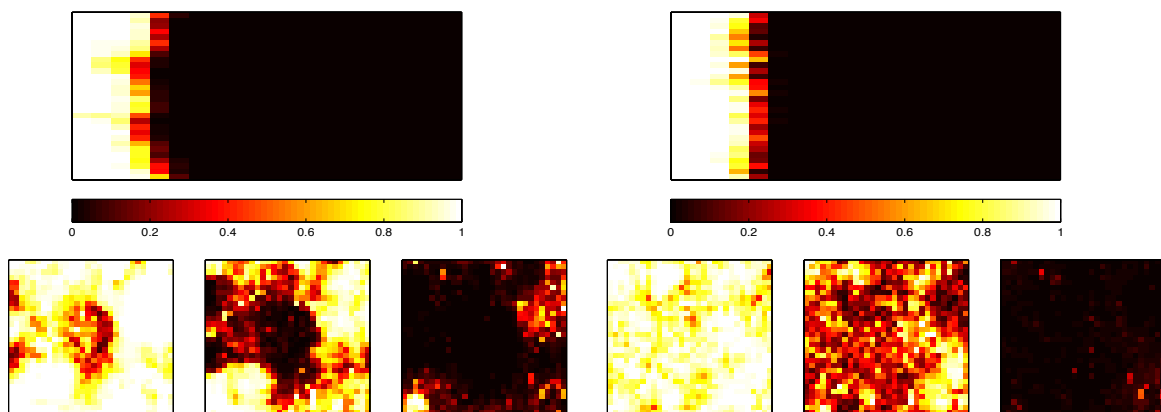
Figure 7.4: The evolution of different parameters and the normalized objective function for the numerical Model-3 during the second simple optimization process. The only difference between this optimization and the one presented in Figure 7.3 is the initial values for the inversion parameters.

## History matching of concentration data

When calibrating the permeability field of Model-3 to pressure data only, the optimal value for parameter  $A$  indicates that there is a good correlation between porosity and permeability. This is in obvious contrast to our results obtained in chapter 6. There, we demonstrated that the correlation coefficient between  $k(\mathbf{x})$  and  $\phi(\mathbf{x})$  of Model-3 is equal zero. That is one reason why our primary calibration is not sufficient. Additionally, the concentration maps extracted from the primary calibrated model are very different compared to the reference ones (see Figure 7.5).

The following step consists in matching the pressure data together with concentration data. Here, we mainly aim at reproducing the reference concentration map using our proposed  $\log(k) - \phi$  correlation.

Naturally, several successive reference concentration maps should be used to produce a detailed permeability map for the entire model. The number of selected reference concentration maps depends on the purpose of the optimization. Our purpose is to validate the proposed



a. Top: sagittal slice (front view) of the reference concentration map at  $PVI = 0.22$ . Bottom: cross sectional images of the same concentration map taken at a distance of  $14.4\text{ mm}$  (left),  $18.0\text{ mm}$  (middle) and  $21.6\text{ mm}$  (right) from the inlet face. Sample is  $72\text{ mm}$  long.

b. Same images when calibrating the 3D permeability field to pressure data only.

Figure 7.5: Comparison of a reference concentration map for Model-3 with the optimized one when calibrating the three-dimensional permeability field to pressure data only. The color bars show the injected fluid concentrations.

methodology. Therefore, we only use one reference concentration map for Model-3, that is the one obtained at  $PVI = 0.22$  (Figure 7.5(a)). Clearly, we cannot reproduce this map without accounting for transverse heterogeneities in our permeability model. Therefore, we use a gradual deformation based optimization process and consider the deformation parameter and the correlation lengths of  $b(\mathbf{x})$  as parameters. Adding the three parameters already considered during the first matching process, we get 7 parameters for each block. This means 28 parameters for the entire model. However, we do not need to tune all these parameters. For the reference concentration map obtained at  $PVI = 0.22$ , the displacement front is located inside the first block. Therefore, we focus on the permeability field of block1-3 and its unknown parameters. The other parameters are fixed to their optimal values from previous optimization. Finally, we get 7 inversion parameters to tune.

Starting from the model constrained to  $\Delta p(t)$  data, it is expected that the integration of 3D concentration data improves the model predictions. After 102 simulations, the objective function is reduced to 39% of its initial value (Figure 7.6). The following remarks can be emphasized.

- Convergence to solution is very fast. The objective function reduces to 50% of its initial value after the first iteration (9 simulations). The influence of correlation lengths of  $b(\mathbf{x})$  is huge.
- The reduction in objective function term is mostly related to the concentration term. The pressure term changes slightly, but stays close to zero.

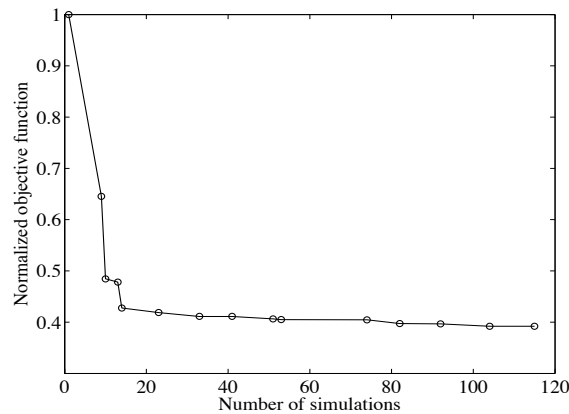


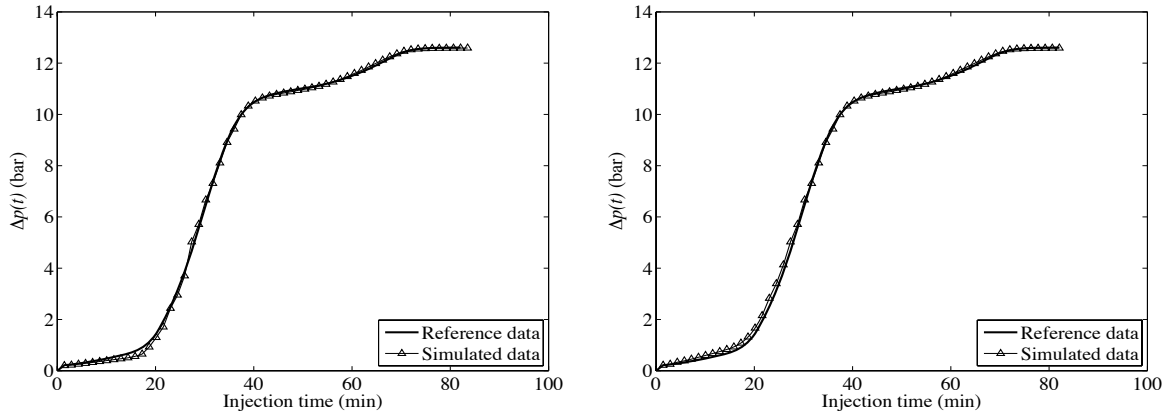
Figure 7.6: Evolution of the objective function against the number of simulations for the numerical Model-3. A gradual deformation based optimization process is used to calibrate the permeability field to both pressure and concentration data.

- After 20 simulations, correlation coefficient  $A$  reduces to its lower bound 0.0001. This proves that there is no correlation between porosity and permeability.

Figure 7.7 shows the pressure data match at the beginning and the end of this optimization process. Figure 7.8 compares the optimized concentration map with the reference one. In both cases, simulated results duplicate very well the reference data.

The evolution of the inversion parameters during optimization is shown in Figure 7.9. As expected, the correlation lengths of  $b(\mathbf{x})$  increase while the mean remains stable. The variance of  $b(\mathbf{x})$  shows a sudden drop at the beginning of the optimization. Then, its value increases monotonically until the end of optimization. However, the variance of the optimized permeability field is still 34% lower than its reference value (see Table 7.3). Although a good match is observed for both pressure and concentration data, the variance of the reference permeability field is not reproduced. The gradient of the objective function with respect to  $\sigma^2$  indicates that this parameter does not influence the objective function. The same result was also obtained at the end of our primary optimization process. Again, there is not enough information in the both  $\Delta p(t)$  and the concentration data to retrieve the parameter  $\sigma_{b(\mathbf{x})}^2$ . One may refer to the increasing trend of the variance of  $b(\mathbf{x})$  and discuss that continuing the optimization process may result in a variance closer to its reference value. Later, we will see that no general conclusion can be drawn from the variations in this parameter and its behavior remains unpredictable.

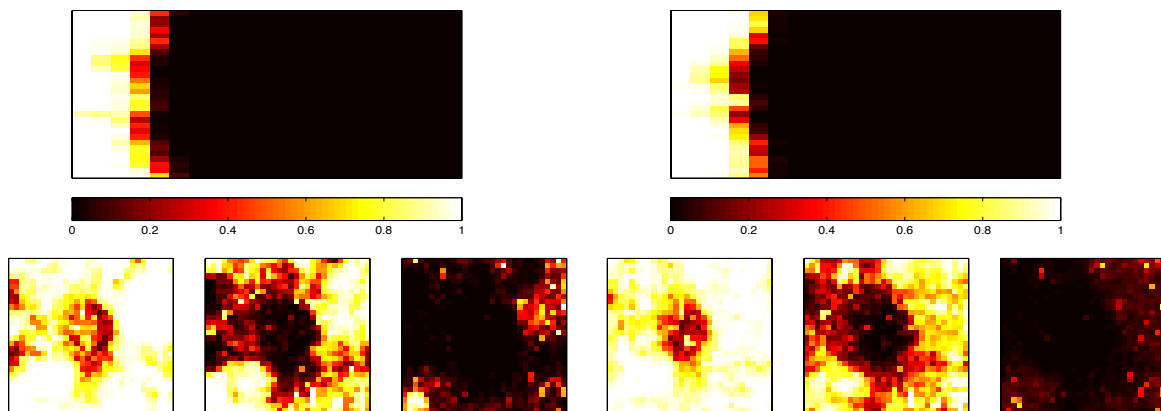
The matches are so far satisfactory. Meanwhile, the reducing rate of the objective function becomes very slow after 102 simulations. Therefore, we stop the optimization at this stage.



a. Beginning of the optimization.

b. End of optimization.

Figure 7.7: Comparison of the reference pressure drop data with the simulated ones for the numerical Model-3 before and after the gradual deformation based optimization process.



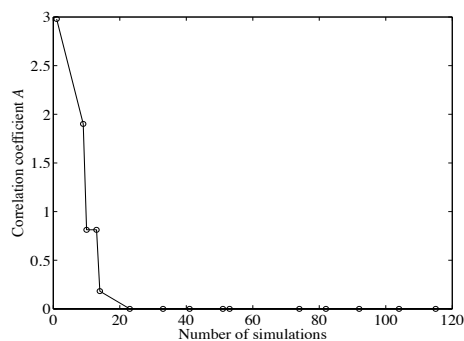
a. Top: sagittal slice (front view) of the reference concentration map at  $PVI = 0.22$ . Bottom: cross sectional images of the same concentration map taken at a distance of  $14.4\text{ mm}$  (left),  $18.0\text{ mm}$  (middle) and  $21.6\text{ mm}$  (right) from the inlet face. Sample is  $72\text{ mm}$  long.

b. Same images when calibrating the 3D permeability field to both pressure and concentration data.

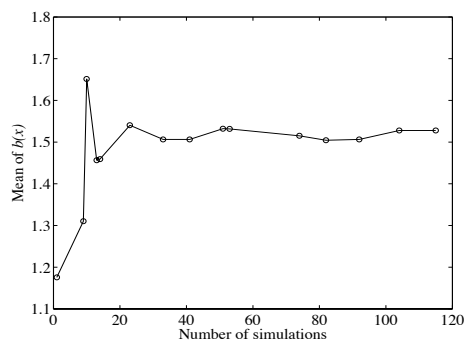
Figure 7.8: Comparison of the Model-3 reference concentration map with the optimized one when calibrating the three-dimensional permeability field to both pressure and concentration data. The color bars show the injected fluid concentrations.

Table 7.3: Comparison of the  $\sigma^2$  and the average permeability for the reference permeability data with the calibrate ones of block1-3 in Model-3. The permeability field is calibrated to both pressure and concentration data. Notice that  $\bar{k}$  is calculated from the harmonic-arithmetic-arithmetic average of 3D permeability data in  $XYZ$  directions.

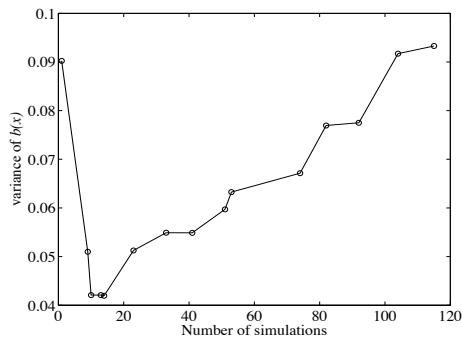
	$\sigma_{\log_{10}(k)}^2$ (ref)	$\sigma_{\log_{10}(k)}^2$ (optim)	% error $_{\sigma^2}$	$k_{ref}$ (mD)	$k_{optim}$ (mD)	% error $_{\bar{k}}$
Block1-3	0.1386	0.0917	34	70	41.21	41



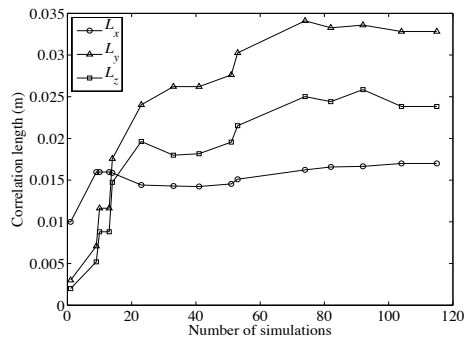
a. The evolution of coefficient  $A$  during the gradual based optimization.



b. The evolution of the mean of  $b(\mathbf{x})$  during the gradual based optimization.



c. The evolution of the variance of  $b(\mathbf{x})$  during the gradual based optimization.



d. The evolution of the correlation lengths of  $b(\mathbf{x})$  during the gradual based optimization.

Figure 7.9: The evolution of different parameters for the numerical Model-3 (block1-3) during the gradual deformation based optimization process.

## 7.2.2 Model-4

In this section, we apply the same methodology as the one described above, but to another numerical core. The three-dimensional permeability field is constrained to the reference pressure drop and concentration data, simulated for our Model-4. Contrary to Model-3, the reference porosity and permeability data of this model are correlated. We first calibrate our permeability field to the pressure data. Then, this calibrated model is further constrained to both pressure and concentration data within a gradual deformation based optimization process.

## History matching of pressure data

Again, the unknown parameters are coefficient  $A$  and the mean  $m$  and variance  $\sigma^2$  of  $b(\mathbf{x})$ . Model-4 consists of four blocks (zones) perpendicular to the flow axis. We assume that the correlation lengths of  $b(\mathbf{x})$  are similar to the correlation lengths of the reference porosity data and construct a permeability field for each of the four blocks. Having three unknown parameters for each permeability zone, we get 12 unknown parameters for the entire model. This model has  $20 \times 90 \times 90$  grid cells. To make the flow simulation faster, the model is upscaled. The upscaled model consists of  $20 \times 30 \times 30$  grid cells, the upscaling ratio being 3 : 1 for cells along axes  $Y$  and  $Z$ . As a result, the CPU time reduces from 40 *min* to around 5.2 *min* for a single flow simulation. Simulation CPU time is also a function of permeability heterogeneity and may increase when heterogeneity increases.

A simple optimization is performed and the parameters are sequentially perturbed until the numerically simulated  $\Delta p(t)$  duplicates as well as possible the reference inlet-outlet pressure drop data. The results show that after 6 iterations (43 simulations), we are capable of perfectly reproducing the observed  $\Delta p(t)$  curve (Figure 7.10).

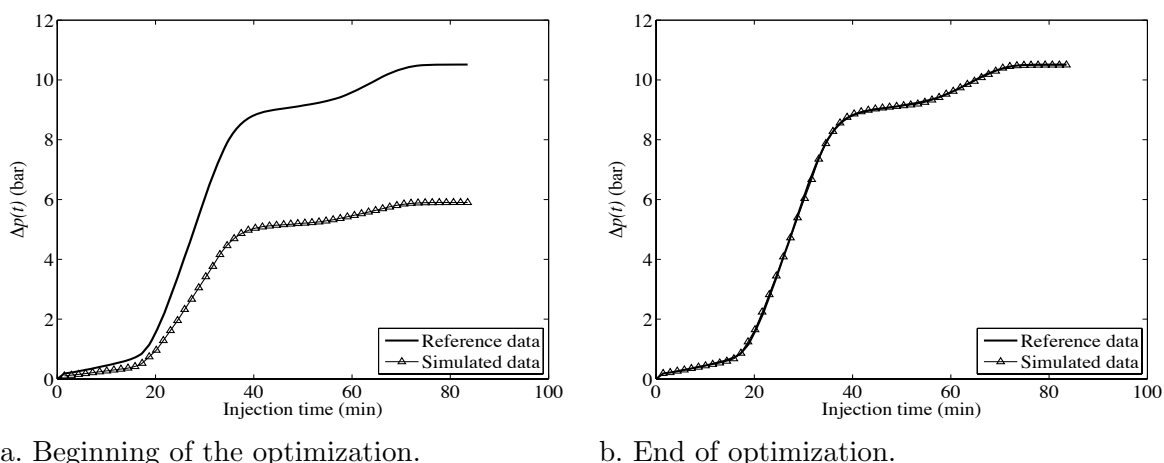


Figure 7.10: Comparison of the reference pressure drop data with the simulated ones for the numerical Model-4 before and after the primary optimization process.

The evolution of the parameters are very similar to that of Model-3. The variations in variance are less erratic than for Model-3, but they do not follow any general trend (see Table 7.4). The objective function is reduced to more than 99% of its original value.

## History matching of concentration data

Remember that the porosity and permeability fields of Model-4 are manually correlated using a  $\log(k) - \phi$  relation (see chapter 6, section 6.1.1). The reference concentration data are

Table 7.4: The comparison of the  $\sigma^2$  and the average permeability for the reference and the calibrate permeabilities for Model-4. Permeability fields are calibrated only to pressure data. Notice that  $\bar{k}$  is calculated from the harmonic-arithmetic-arithmetic average of 3D permeability data in  $XYZ$  directions.

		$\sigma_{\log_{10}(k)}^2$ (ref)	$\sigma_{\log_{10}(k)}^2$ (optim)	% error $_{\sigma^2}$	$\bar{k}_{ref}$ (mD)		$\bar{k}_{optim}$ (mD)		% error $_{\bar{k}}$	
Model-4	Block1-4	0.1818	0.2092	15	70	14.3	66.35	15.62	5.2	9.2
	Block2-4	0.08336	0.3082	270	4.5		5.04		12	
	Block3-4	0.1448	0.1953	35	106		168.69		59	
	Block4-4	0.1548	0.1738	12	29		27.27		6	

extracted from a  $20 \times 90 \times 90$  fine model while the simulated concentrations are extracted from a  $20 \times 30 \times 30$  coarse model. Therefore, the reference concentration maps must be upscaled to be compared to the simulated ones. We use Equation 7.4 to upscale the Model-4 reference concentration maps.

$$\bar{S} = \frac{\sum_{i=1}^n \sum_{j=1}^n S_{i,j} \phi_{i,j}}{\sum_{i=1}^n \sum_{j=1}^n \phi_{i,j}} \quad (7.4)$$

In this equation,  $S$  is the concentration,  $\phi$  is the porosity and  $i$  and  $j$  are the grid cell indices in  $Y$  and  $Z$  directions, respectively. The upscaling ratio is assumed to be  $n : 1$ . A concentration map at  $PVI = 0.22$  is extracted for the model obtained at the end of our primary optimization process. It is compared to the upscaled reference one in Figure 7.11. As expected, there is a big difference between the reference data and the concentrations simulated for the optimal model.

In the following step, we restart the optimization process from the previous optimal model and constrain it to concentration data on top of pressure drop. Just as for Model-3, we only focus on the first block of Model-4 and fix the other parameters to their optimal values determined at the end of our primary optimization process. Thus, we end up with 7 unknown parameters.

**First**, we perform a sensitivity analysis on parameter  $A$ . To do so, we fix  $A$  and start the gradual optimization with only 6 inversion parameters. After about 200 simulations, the objective function reduces to 60% of its initial value and reaches a plateau. However, the pressure match seems to degrade (Figure 7.12(a)). In other words, to keep the pressure data matched, we have to consider  $A$  as an inversion parameter. Moreover, if we do not tune  $A$  during the gradual optimization, we cannot come to any conclusion about the existence of a correlation between porosity and permeability.

**Second**, we add coefficient  $A$  to the inversion parameter list and restart the optimization from the best model identified at the **First** step. After more than 130 simulations, the objective function shows another 10% reduction. parameter  $A$  slightly influences the matching



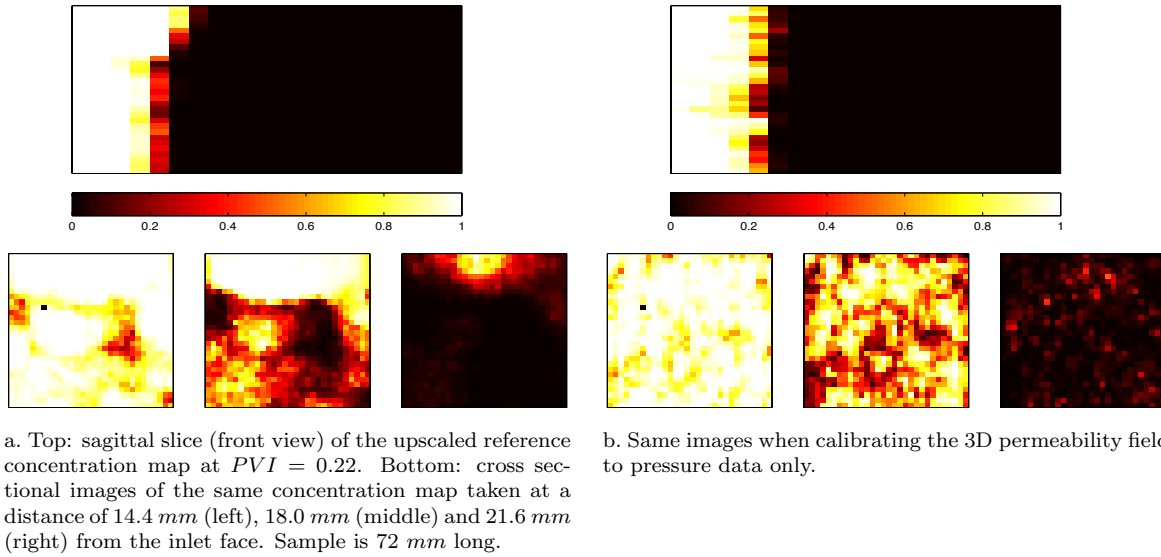


Figure 7.11: Comparison of the Model-4 reference concentration map with the optimized one when calibrating the 3D permeability field to pressure data only. The color bars show the injected fluid concentrations.

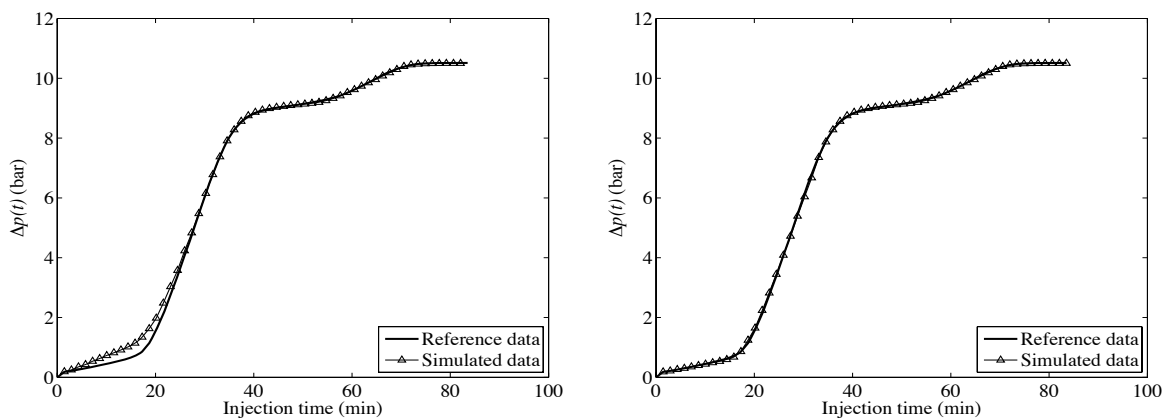


Figure 7.12: Comparison of the reference pressure drop data with the simulated ones for the numerical Model-4 when performing gradual optimization. (a) shows that the pressure match degrades without considering  $A$  as an inversion parameter.

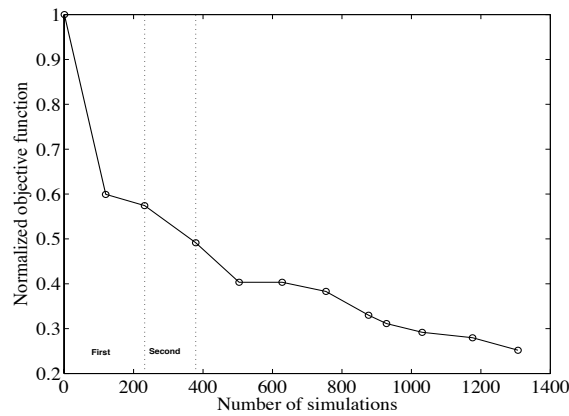


Figure 7.13: Evolution of the objective function against the number of simulations for the numerical Model-4. A gradual deformation based optimization process is used to calibrate the permeability field to both pressure and concentration data.

process.

The optimization process is continued to further improve the matching process. Overall, more than 1300 simulations are performed and the objective function is reduced to 25% of its initial value. Its evolution is shown in Figure 7.13.

The reduction of the objective function is mostly related to the concentration term. Again, the pressure match does not change during the optimization process. Figure 7.14 shows the evolution of the parameters during optimization. Parameter  $A$  increases while the mean of  $b(\mathbf{x})$  decreases. The variance of  $b(\mathbf{x})$  shows a sudden drop at the beginning and stays stable until the end of the optimization. However, there is still 26% difference between the reference and the optimal variance. The maximum values of  $L_x$ ,  $L_y$  and  $L_z$  are selected to be equal to the model size in  $X$ ,  $Y$  and  $Z$  directions, respectively. Figure 7.14(d) shows that the correlation length  $L_z$  has reached its upper limit after 80 simulations. This behavior may be observed for other parameters as well. That is why we check the evolution of the parameters time by time and change their upper or lower limits if necessary.

After the first drop, the objective function reduces slowly. The reference data are finely gridded and this can slow down the optimization process while getting closer to the actual response. We compare the optimized parameters with the reference ones for the first block. The results are reported in Table 7.5. For parameters  $A$ ,  $m$  and correlation lengths  $L_x$  and  $L_y$ , there is a good agreement between the optimal and the reference values. The optimal  $\sigma_{b(\mathbf{x})}^2$  and  $L_z$  are far from their reference values. Their variations do not follow a logical trend. Figure 7.15 compares the reference concentration map with the optimal one. The methodology is successful in reproducing the reference data with a high degree of acceptance.

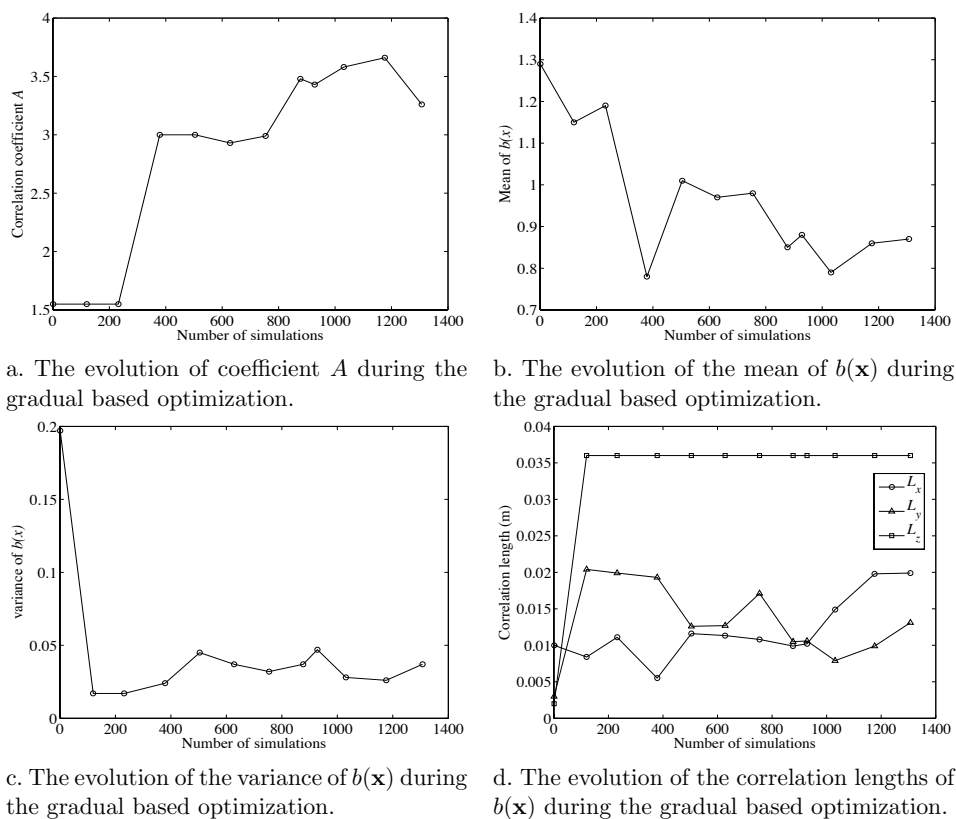
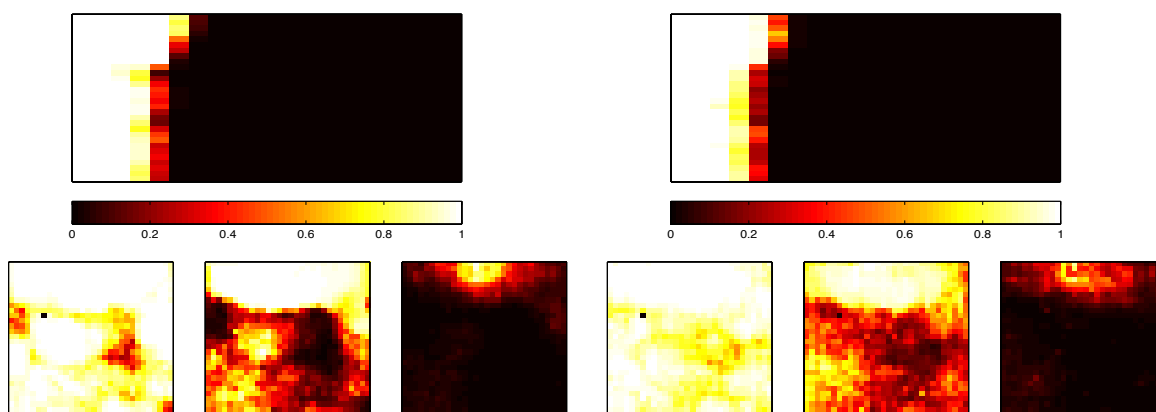


Figure 7.14: The evolution of different parameters for the numerical Model-4 (block1-4) during the gradual deformation based optimization process.

Table 7.5: Comparison of the parameters for the reference and the calibrate permeability field of Model-4 (block1-4). The permeability field is calibrated to both pressure and concentration data.

		Reference	Optimized	% error
Block1-4	$A$	3.28	3.26	0.6
	$m_b$	1.203	0.87	28
	$\sigma_{b(\mathbf{x})}^2$	0.1	0.037	63
	$L_x$	0.0144	0.0199	38
	$L_y$	0.02	0.0131	34
	$L_z$	0.02	0.036	80
	$\sigma_{\log_{10}(k)}^2$	0.1818	0.1352	26
	$k$	70	51.82	26



a. Top: sagittal slice (front view) of the reference concentration map at  $PVI = 0.22$ . Bottom: cross sectional images of the same concentration map taken at a distance of  $14.4\text{ mm}$  (left),  $18.0\text{ mm}$  (middle) and  $21.6\text{ mm}$  (right) from the inlet face. Sample is  $72\text{ mm}$  long.

b. Same images when calibrating the 3D permeability field to both pressure and concentration data.

Figure 7.15: Comparison of the Model-4 reference concentration map with the optimized one when calibrating the three-dimensional permeability field to both pressure and concentration data. The color bars show the injected fluid concentrations.

### 7.3 Experimental validation

The proposed methodology is also applied to two sets of experimental data. The first set of data is obtained during the viscous miscible flooding of composite 2. The second one is collected for sandstone SG20. To be able to use experimental data for validation purposes, the following criteria must be fulfilled:

- The collected data should be as noise free as possible.
- Pressure drop data, a 3D porosity map and at least one concentration map should be available.
- Core sample must be characterized by small scale heterogeneities. A liner pressure drop against time is not useful, because it is an indication of homogeneity along the flow direction axis. Similarly, a concentration map without evident heterogeneities does not contain any useful information and cannot improve the calibration process.

In the following subsections, we discuss the above criteria for the two selected samples. Then, our matching process is applied to integrate both pressure and concentration data in our models.

### 7.3.1 Composite 2

The available static and dynamic data of composite 2 are shown and discussed in previous chapters. We already discussed the problem of noise in both pressure and concentration data. Some data post processing were required to remove part of the noise. We consider the remaining of the noise as measurement errors and go on with calibration. The sample is made of four small plugs with different absolute permeabilities and thus, the pressure drop against time is not linear. They are used as the reference data inside our simple optimization technique. What about the reference concentration maps? Some of them are illustrated in Figures 6.15. At first glance, we observe that there is no clear heterogeneity inside concentration maps for second and forth plugs. The front is straight and stable like a piston. The situation is a bit different for the third plug. As mentioned in section 6.2.1, this plug is probably not clean. Some glycerin is evidenced in this third plug while the displacement front is still inside the first or second plug. Additionally, it has a low porosity compare to the other plugs and thus, get saturated very fast. Under these circumstances, the concentration data of the first plug are the only ones that can be integrated in our optimization process.

#### History matching of pressure data

The unknown parameters are coefficient  $A$  as well as and the mean  $m$  and variance  $\sigma^2$  of  $b(\mathbf{x})$ . Composite 2 is a stack of four small plugs perpendicular to flow axis. We assume that the correlation lengths of  $b(\mathbf{x})$  are similar to those of the 3D CT porosity map and construct a permeability field for each plug. Having three unknown parameters for each permeability zone, we get 12 inversion parameters for the entire model.

The composite 2 numerical model consists of  $20 \times 329 \times 329$  grid cells. We upscale the model during the optimization loops. The upscaled model consists of  $20 \times 29 \times 29$  grid cells, the upscaling ratio being 11 : 1 for cells along axes  $Y$  and  $Z$ . As a result, the CPU time reduces from around 600 *min* to around 5.8 *min* for a single flow simulation.

A simple optimization is first performed and the parameters are sequentially perturbed until the numerically simulated  $\Delta p(t)$  duplicates as well as possible the reference inlet-outlet pressure drop. The optimization stops after 9 iterations (42 simulations). The final pressure match is shown in Figure 7.16(a). Clearly, the optimization is not capable of reproducing the reference pressure drop data especially during the first 36 *min* of injection. We restart the simple optimization process from the already determined optimal point. No considerable change is observed. After performing several tests, the origin of this problem was found to be the permeability variations inside the second plug. This plug has the same origin as the low permeability limestone “Lavoux”. In chapter 4, we showed that this limestone sample is composed of two different regions with two different permeability values. Here, we assume that the second plug of composite 2 is also composed of two permeability zones. Thus, we divide the grid cells representing this plug into two zones perpendicular to the flow axis. In such condition, the number of total permeability zones equals 5, resulting into 15 unknown

parameters (three parameters per zone). The simple optimization is repeated with the new model. The results show that after 9 iterations (39 simulations), the observed  $\Delta p(t)$  curve is perfectly reproduced (Figure 7.16(b)).

The evolution of the inversion parameters for both cases is shown in Figure 7.17. Except for the second plug, the initial parameter values are the same for both cases. Obviously, the variations in parameters  $A$  and  $\mu$  are very close for the two cases. As already noticed for the numerical models, the variance does not follow a general trend. The objective function is reduced to 1% of its original value for the second case.

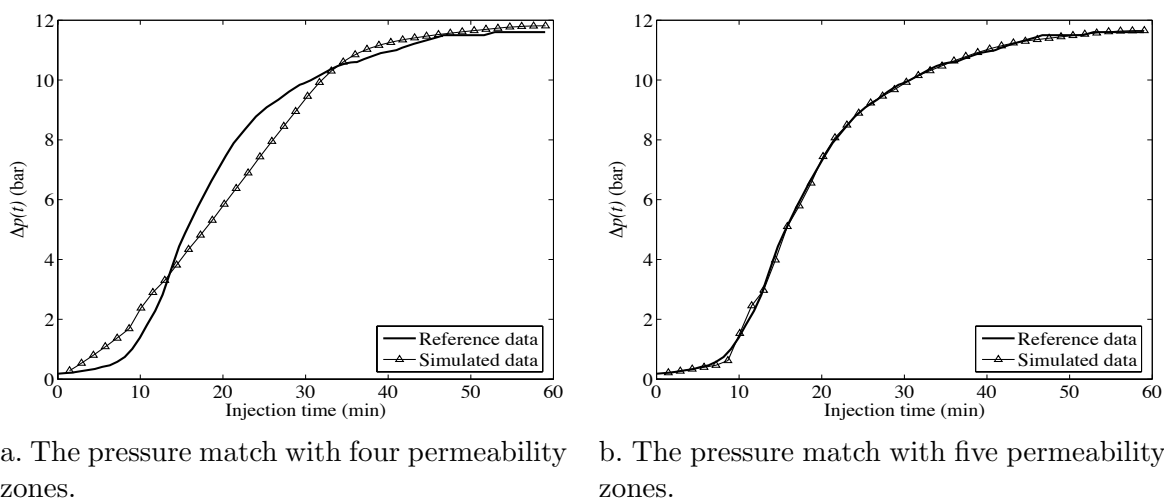


Figure 7.16: Comparison of the reference pressure drop data with the simulated ones for composite 2. (a) is the result of simple optimization when considering four permeability zones and 12 inversion parameters. (b) is the result of simple optimization when considering five permeability zones and 15 inversion parameters.

### History matching of concentration data

As discussed earlier, only the first plug of composite 2 exhibits small scale heterogeneities, which take the form of millimetric beddings. The other plugs look more and less homogeneous. Let us compare two concentration maps simulated for the optimal model derived at the end of our simple optimization to the corresponding observed data. One of them is extracted from the first plug (at  $PVI = 0.02$ ) and the other one from the second plug (at  $PVI = 0.46$ ). They are illustrated in Figure 7.18. As we can see, there are not much differences between the observed laboratory data and the simulated ones at  $PVI = 0.46$ . This means that continuing the optimization with the gradual deformation technique will not bring any significant improvement in the model predictions for this part of the sample. However, the simple optimization has not reproduced the observed data at  $PVI = 0.02$ . Therefore, adding this concentration map to the objective function may improve the model

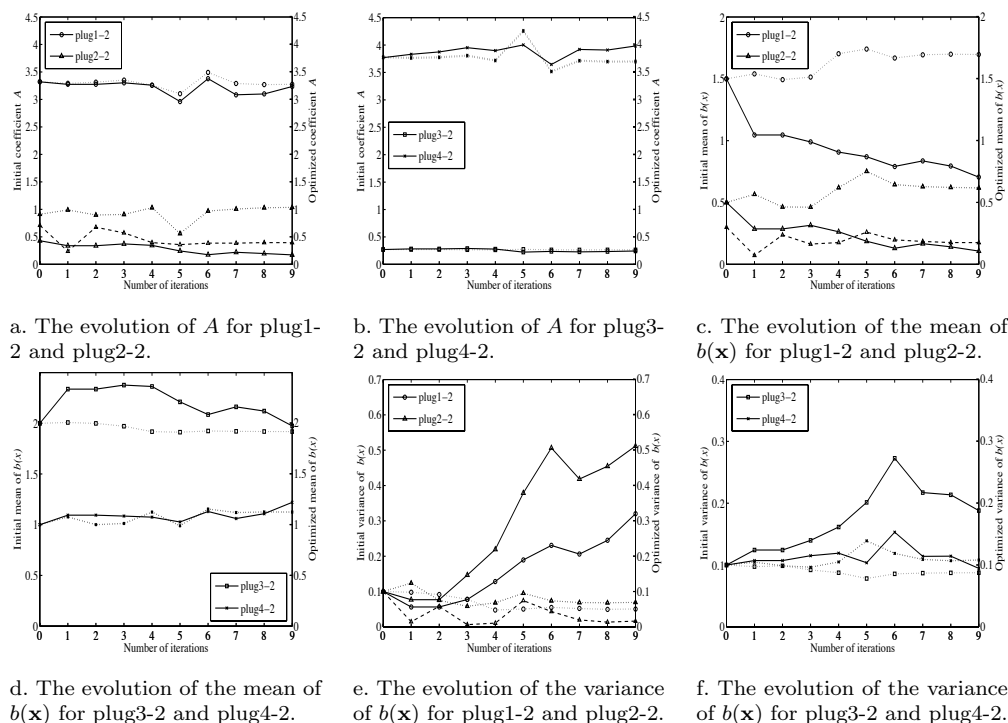
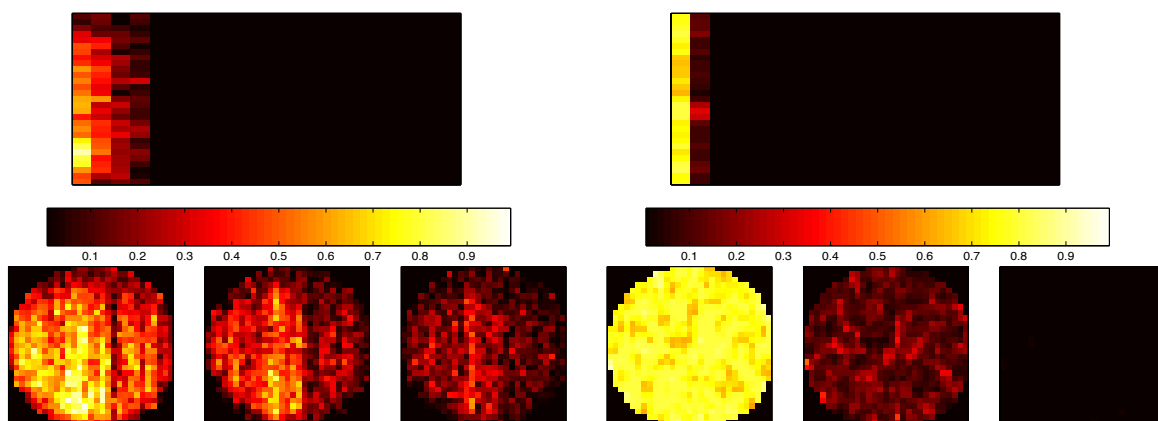


Figure 7.17: The evolution of different parameters for composite 2 during two cases of simple optimization process. In the first case (solid line), only four permeability zones are considered. In the second case (dotted line), a new permeability zone is added to plug2-2. Notice that the dashed and dotted lines are used to separate the two permeability zones of plug2-2.

predictions in this part of the sample.

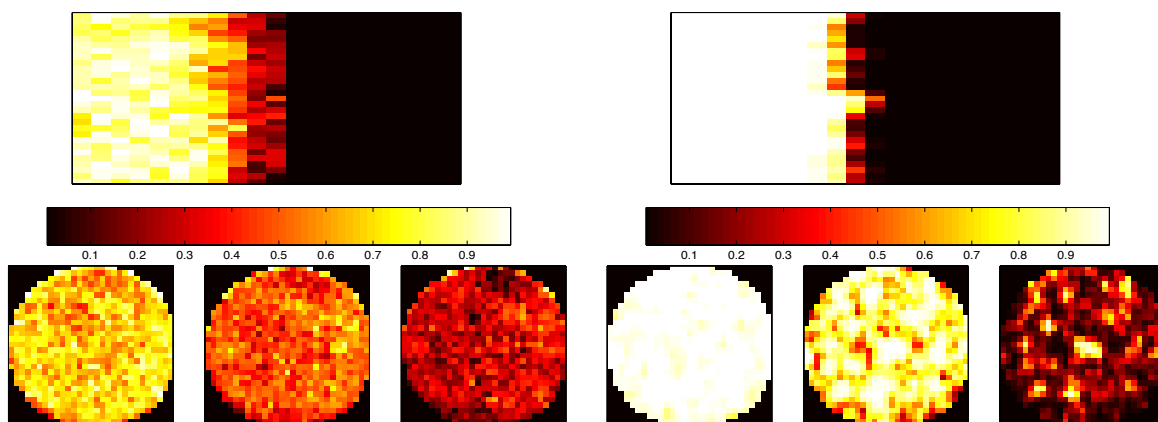
Starting from the permeability field obtained at the end of the primary optimization process, gradual optimizations are now performed to better constrain the permeability map of the first plug. The parameters related to the other plugs are fixed to their optimal values identified from our primary optimization. Thus, we handle only 7 inversion parameters. The optimization turns out to be more difficult. After 101 simulations, the objective function shows a 23% decrease and reaches a plateau. Repeating the optimization with another 100 simulations does not change the objective function value. At this point, the number of deformation parameters is increased to 3. After 110 additional simulations, the objective function shows another 14% decrease. 150 other simulations are run resulting in another 7% decrease of the objective function. The final results indicate that with 550 simulations, the objective function reduces to 56% of its initial value (Figure 7.19). The following remarks can be pointed out.

- The noise in the reference concentration data impediments the optimization process.
- The objective function reduces rapidly at the beginning of the optimization. Its reduc-



a. Top: sagittal slice (front view) of the reference concentration map at  $PVI = 0.02$ . Bottom: cross sectional images of the same concentration map taken at a distance of  $3.6\text{ mm}$  (left),  $7.2\text{ mm}$  (middle) and  $10.8\text{ mm}$  (right) from the inlet face. Sample is  $72\text{ mm}$  long.

b. Same images when calibrating the 3D permeability field to only the pressure data.



c. Top: sagittal slice (front view) of the reference concentration map at  $PVI = 0.46$ . Bottom: cross sectional images of the same concentration map taken at a distance of  $28.8\text{ mm}$  (left),  $32.4\text{ mm}$  (middle) and  $36.0\text{ mm}$  (right) from the inlet face. Sample is  $72\text{ mm}$  long.

d. Same images when calibrating the 3D permeability field to the pressure data only.

Figure 7.18: Comparison of the composite 2 reference concentration maps with the optimized ones when calibrating the three-dimensional permeability field to the pressure data only. The color bars show the injected fluid concentrations.



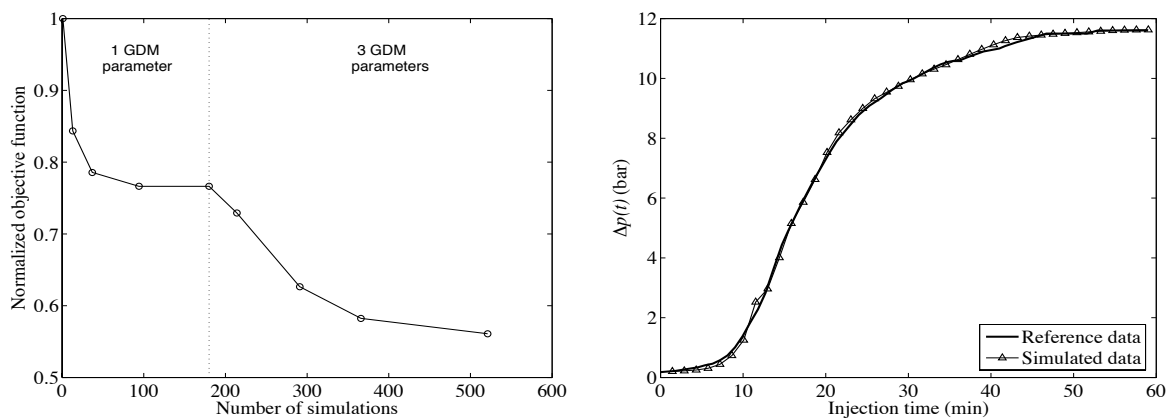


Figure 7.19: Left: evolution of the objective function against the number of simulations when gradually deforming the permeability field of the first plug of composite 2. The permeability field is calibrated to both pressure and concentration data. Right: comparison of the reference pressure drop data with the simulated ones after performing the optimization.

tion becomes more and more difficult afterwards.

- Increasing the number of deformation parameters helps to further decrease the objective function. The reducing rate of the objective function decreases as the number of simulations increases.
- The reduction of the objective function is mostly related to the concentration term. The pressure match remains unchanged because its objective function term is already very small.

The evolution of the inversion parameters is shown in Figure 7.20. Parameter  $A$  increases while the mean of  $b(\mathbf{x})$  decreases: there is a good correlation between porosity and permeability data. The variance of  $b(\mathbf{x})$ ,  $L_y$  and  $L_z$  are increased while  $L_x$  remains close to its initial value. We conclude that transverse heterogeneities in this plug are much stronger than longitudinal ones. The concentration maps are compared in Figure 7.21. The simulated concentration distribution is now much closer to the glycerin distribution. Last, parameter  $A$  and the correlation lengths of  $b(\mathbf{x})$  are the most influential parameters during this gradual deformation based optimization process.

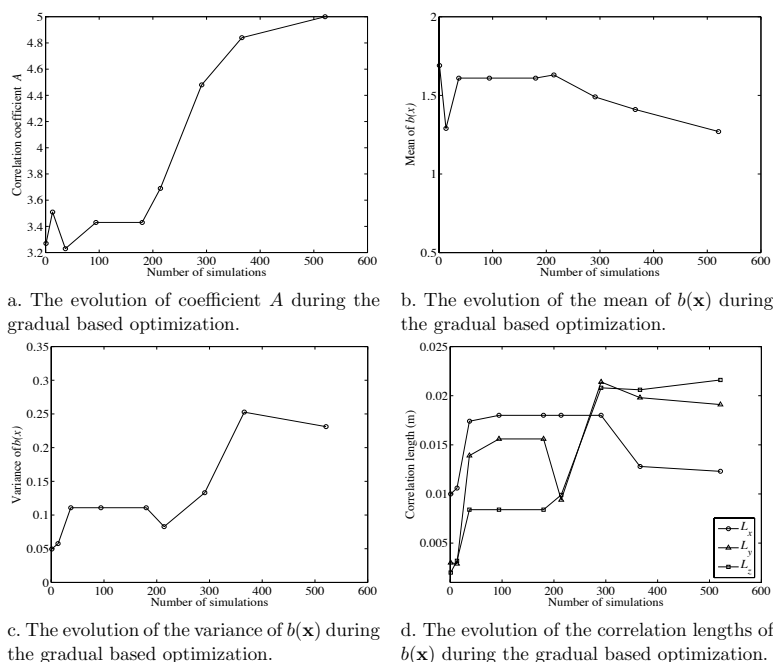
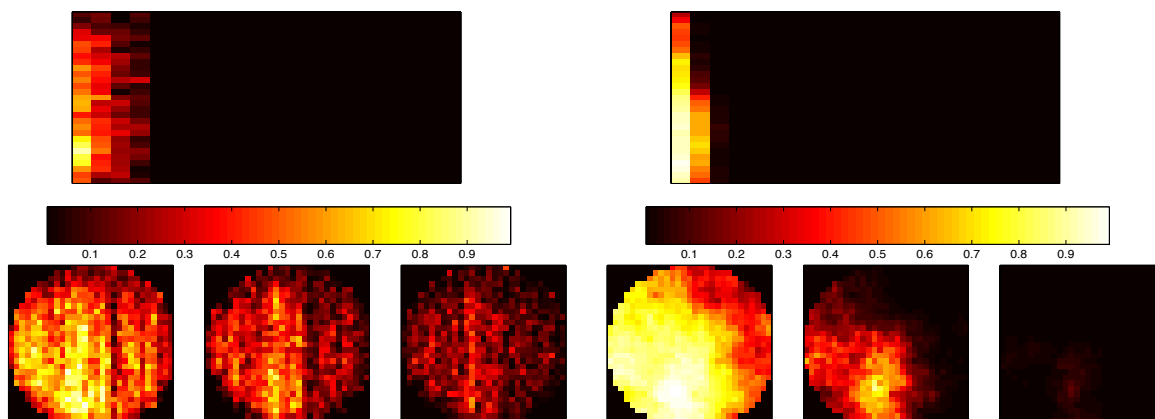


Figure 7.20: Evolution of the different parameters for the first plug of composite 2 during the gradual deformation based optimization process.



a. Top: sagittal slice (front view) of the reference concentration map at  $PVI = 0.02$ . Bottom: cross sectional images of the same concentration map taken at a distance of  $3.6\text{ mm}$  (left),  $7.2\text{ mm}$  (middle) and  $10.8\text{ mm}$  (right) from the inlet face. Sample is  $72\text{ mm}$  long.

b. Same images when calibrating the 3D permeability field to both pressure and concentration data.

Figure 7.21: Comparison of composite 2 reference concentration map with the optimized one when calibrating the three-dimensional permeability field (for the first plug) to both pressure and concentration data. The color bars show the injected fluid concentrations.

### 7.3.2 Sandstone SG20

As mentioned in chapter 6, two viscous miscible flooding (normal and inverse) are performed for this sample. The data collected during both displacements are noisy. We only use those parts of the data, which we believe to be more reliable. That is why the numerical model representing this core sample, with  $25 \times 334 \times 334$  grid cells, is divided into two parts. A numerical model with  $18 \times 334 \times 334$  cells is used to calibrate the permeability field to the data collected during the normal injection. The second numerical model, which consists of  $7 \times 334 \times 33$  cells is used to history match the data collected during the inverse injection. The permeability models are first calibrated to pressure data only. These models are then further constrained to both pressure and concentration data. During the optimization process, the first model is upscaled to  $18 \times 30 \times 30$  and the second model is upscaled to  $7 \times 30 \times 30$  grid cells. The upscaling ratio for both models is 11 : 1 for the grid cells along axes  $Y$  and  $Z$ .

#### History matching of pressure data

##### Normal injection:

From the measured  $\Delta p(t)$  evolution, one can recognize four different zones or layers perpendicular to the flow axis (Figure 7.22, left). It is a difficult task to accurately identify the boundaries of these layers. We made our decision based on the pressure variations observed during the experiments we performed on two composite samples. Without considering four different layers, it would be extremely difficult to obtain an acceptable  $\Delta p(t)$  match between simulated and observed data. To calibrate the permeability field to  $\Delta p(t)$ , we consider three unknown parameters per layer ( $A$ ,  $m$  and  $\sigma^2$ ), that is 12 parameters for the entire model. After 34 simulations, a satisfactory match is obtained (Figure 7.22, right). The objective function is reduced to more than 5% of its initial value. The evolution of the inversion parameters is similar to what was pointed out for composite 2.

##### Inverse injection:

We only consider the data related to the first 14 *min* of the injection. The remaining pressure drop data are very noisy and non reliable. From the measured  $\Delta p(t)$  evolution, we recognize three different zones or layers perpendicular to the flow axis (Figure 7.23, left). As for the normal injection, we consider three unknown parameters per layer, that is 9 parameters for the entire model. After 34 simulations, the optimization is stopped. The pressure match is not as good as the one obtained for the normal injection. Performing additional iterations did not significantly improve the matching. The result is reported in Figure 7.23 (right). The simulated pressure drop significantly changes when the displacement front enters the second zone. This indicates a sharp permeability contrast between these two zones. The objective function is reduced to more than 5% of its initial value. Notice that the evolution of the inversion parameters is similar to what was observed for the other experiments.

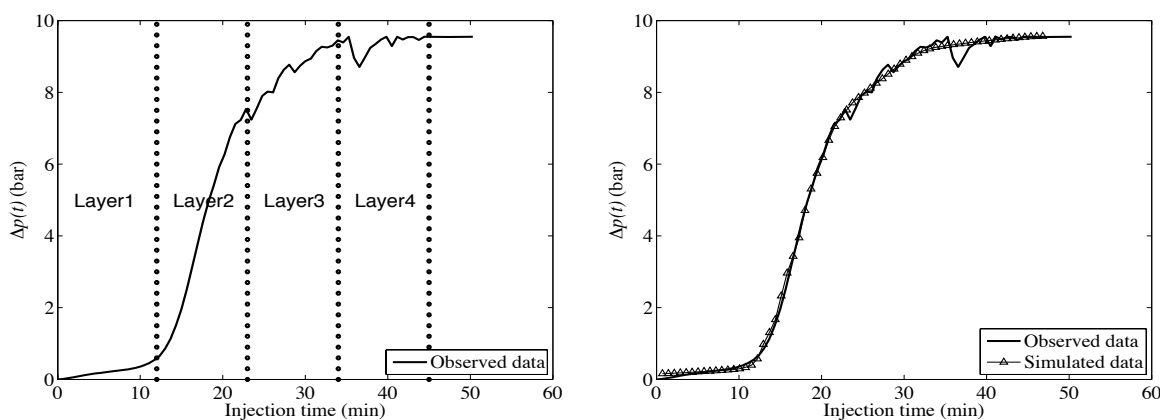


Figure 7.22: Left: sandstone sample pressure drop curve when performing normal injection. The vertical dotted lines show the boundary of selected layers perpendicular to flow axis. Right: comparison of the observed pressure drop data with the simulated ones after the simple optimization.

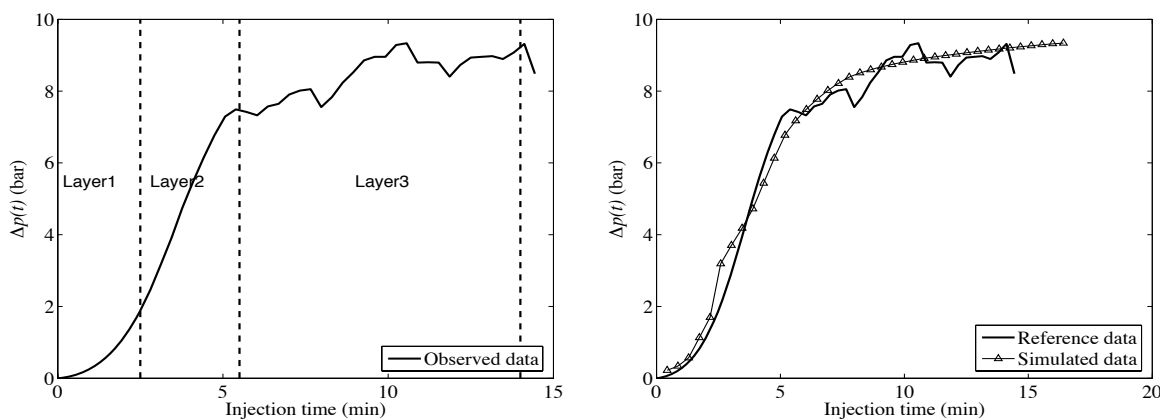


Figure 7.23: Left: sandstone sample pressure drop curve when performing inverse injection. The vertical dashed lines show the boundary of selected layers perpendicular to flow axis. Right: comparison of the observed pressure drop data with the simulated ones after the simple optimization.

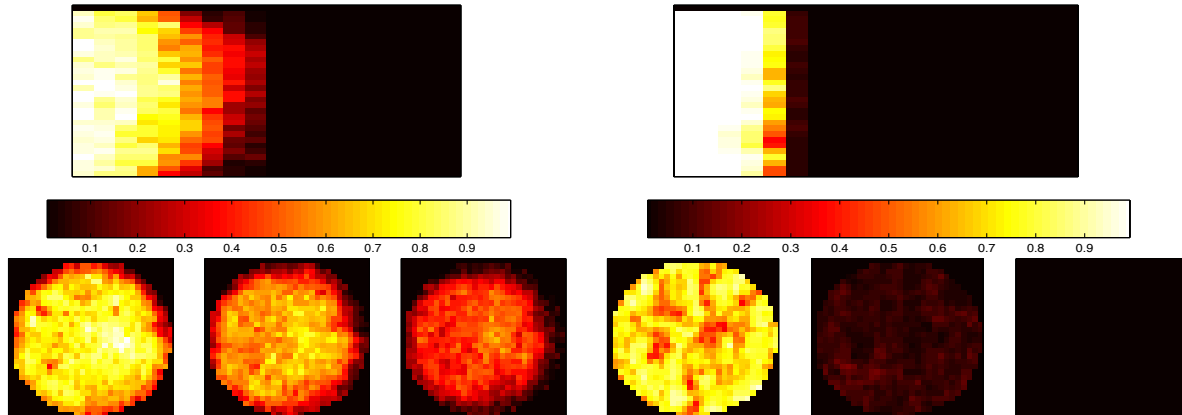
## History matching of concentration data

### Normal injection:

Figure 7.24 compares the concentration maps simulated for  $PVI = 0.25$  and  $PVI = 0.47$  with the observed X-ray CT images. The simulated data are derived from the model constrained to pressure data only. There are very important differences.

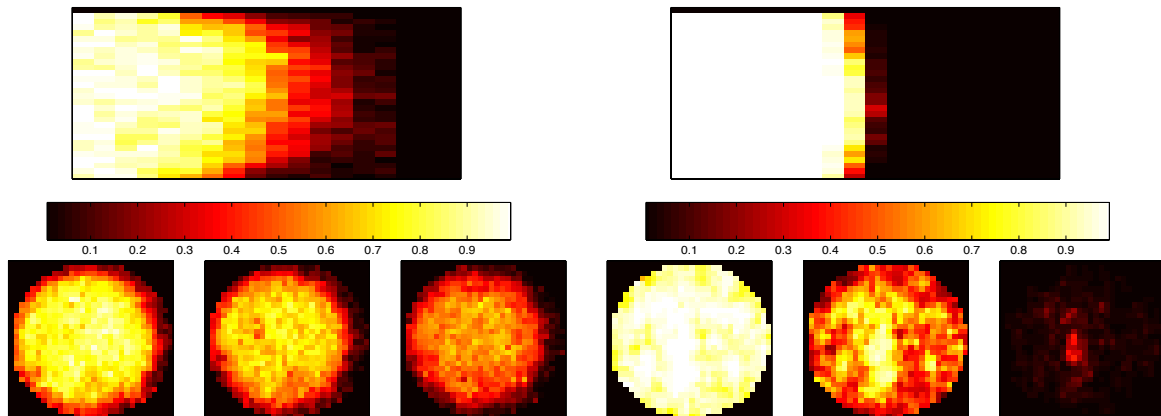
We refine the 3D permeability map using the measured concentration data. As mentioned in the sections above, we can use several concentration maps to obtain a detailed 3D permeability field. Here, we only use two X-ray CT concentration maps (*i.e.*, 14 unknown parameters for the first two layers). The parameters related to the other layers, are fixed to the optimal

values derived from the simple optimization. The permeability field constrained to  $\Delta p(t)$  data only is considered as the starting guess of this new optimization process.



a. Top: sagittal slice (front view) of the reference concentration map at  $PVI = 0.25$ . Bottom: cross sectional images of the same concentration map taken at a distance of  $19.2\text{ mm}$  (left),  $22.4\text{ mm}$  (middle) and  $25.6\text{ mm}$  (right) from the inlet face. Core sample is  $76\text{ mm}$  long.

b. Top: Same images after calibrating 3D permeability field to  $\Delta p(t)$  data.



c. Top: sagittal slice (front view) of the reference concentration map at  $PVI = 0.47$ . Bottom: cross sectional images of the same concentration map taken at a distance of  $25.6\text{ mm}$  (left),  $28.8\text{ mm}$  (middle) and  $32.0\text{ mm}$  (right) from the inlet face. Core sample is  $76\text{ mm}$  long.

d. Top: Same images after calibrating 3D permeability field to  $\Delta p(t)$  data.

Figure 7.24: Comparison of the reference concentration maps with the simulated ones at  $PVI = 0.25$  and  $PVI = 0.47$  for the sample SG20. The displacement is performed from left to right (normal injection). The permeability field is calibrated to  $\Delta p(t)$  data only. The color bars show the injected fluid concentrations.

The following points can be emphasized.

1. As noticed for composite 2, the optimization is slow. The noise intrinsic to concentration data reduces the optimisation efficiency.
2. After 256 simulations, the objective function reduces to only 84% of its initial value. Repeating the optimization with 181 additional simulations does not change the objective function value: it reaches a plateau.
3. The number of deformation parameters is changed to 3 for each zone. The optimization process is repeated. After 392 other simulations, the objective function shows another 6% decrease. This indicates that the gradual deformation method can slightly refine the matching process.
4. The reduction of the objective function is mostly related to concentration data. The pressure term in the objective function remains near zero.
5. Coefficient  $A$  reduces to near zero for both concentration maps. This indicates that there is no correlation between porosity and permeability. The small coefficient  $A$  obtained for the first permeability zone results in a minor reduction of the slope of pressure curve (see Figure 7.25). Remember that we have defined a maximum error of 0.63 *bar* for pressure match (see chapter 5, section 5.1). Reducing this value may slightly improve the pressure match. However, a small error value will put a huge weight on pressure data and degrade the concentration match. This is also valid for the concentration term.

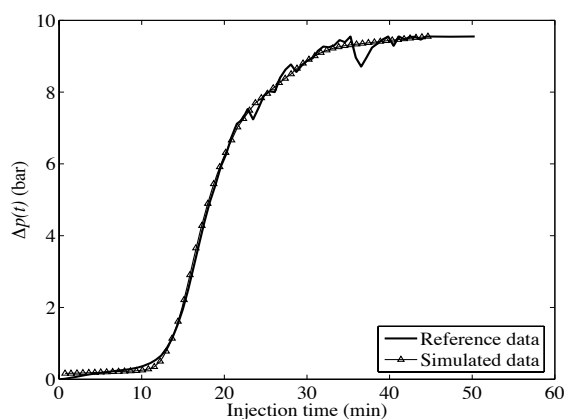
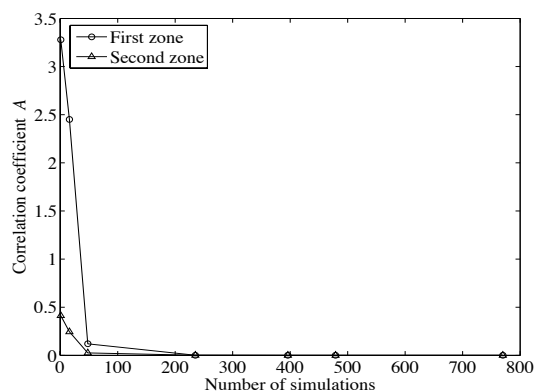


Figure 7.25: Comparison of the reference pressure drop data with the simulated ones for sample SG20 after performing gradual deformation based optimization. The displacement is performed from left to right (normal injection).

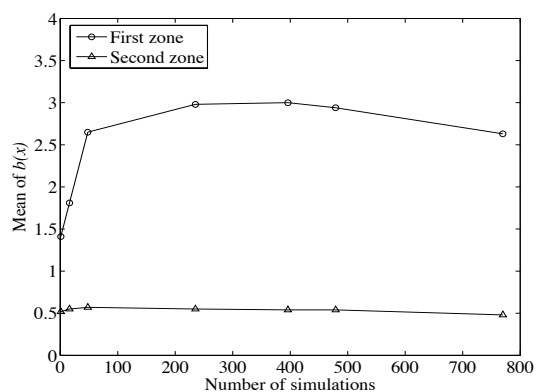
6. The results indicate that the correlation lengths of  $b(\mathbf{x})$  are the most influential parameters during optimization.

The evolution of the unknown parameters of the two permeability zones is shown in Figure 7.26. Parameter  $A$  reduces to zero for both zones while the variations in the mean of  $b(\mathbf{x})$  remain stable. The variance of  $b(\mathbf{x})$  reaches its lower bound in the first zone, but monotonically increases in the second one. The variations in the correlation lengths of  $b(\mathbf{x})$  are very similar for both zones. They indicate that transverse heterogeneities are much stronger than longitudinal ones in this part of the sample.

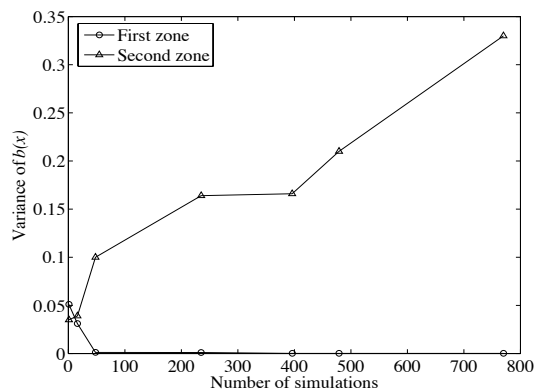
The final concentration maps are shown in Figure 7.27. The comparison of simulated concentration values with X-ray CT concentration data proves that a perfect match is far to be achieved. However, integrating the measured concentration data in the matching contributes to improve the characterization of the permeability field.



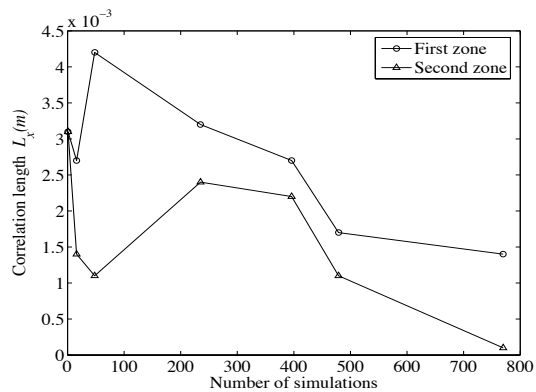
a. The evolution of coefficient  $A$  during the gradual based optimization.



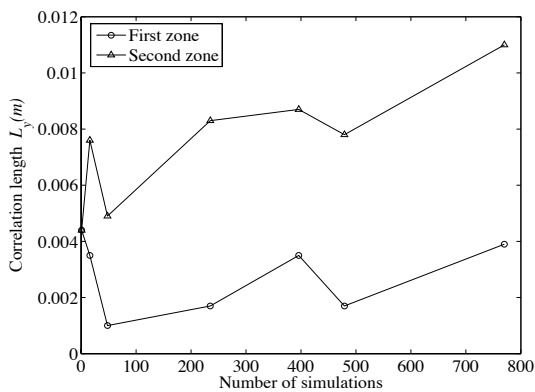
b. The evolution of the mean of  $b(\mathbf{x})$  during the gradual based optimization.



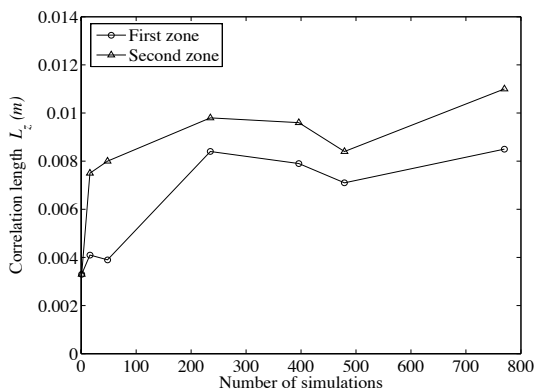
c. The evolution of the variance of  $b(\mathbf{x})$  during the gradual based optimization.



d. The evolution of  $L_x$  during the gradual based optimization.



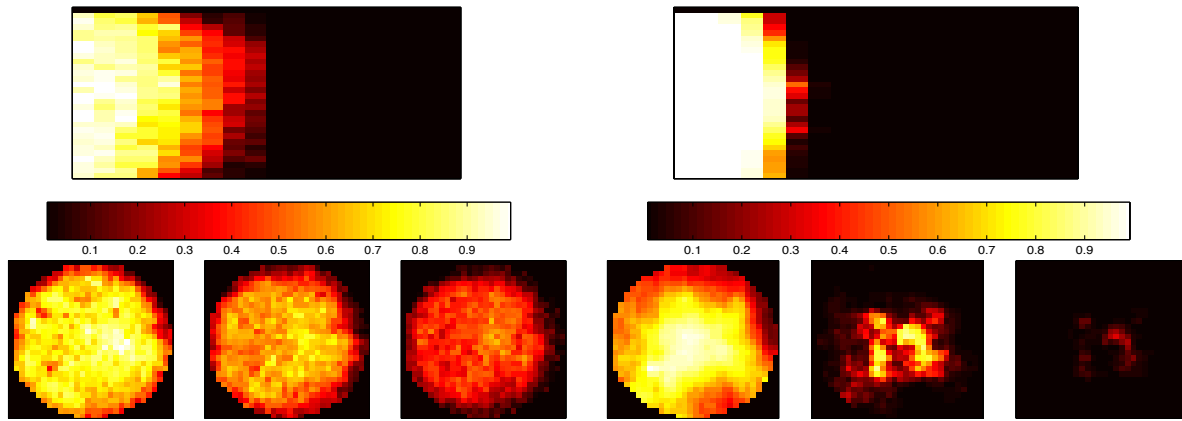
e. The evolution of  $L_y$  during the gradual based optimization.



f. The evolution of  $L_z$  during the gradual based optimization.

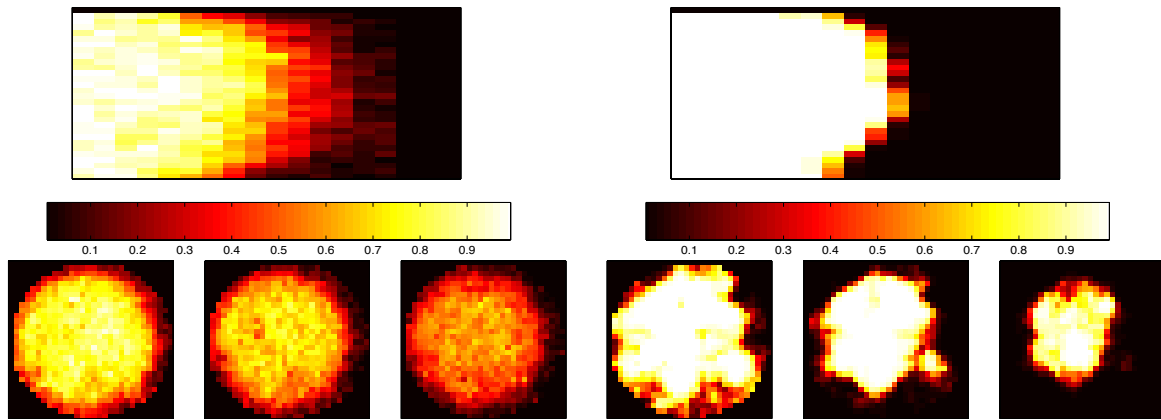
Figure 7.26: The evolution of different inversion parameters for the sample SG20 during the gradual deformation based optimization process. The displacement is performed from left to right (normal injection).





a. Top: sagittal slice (front view) of the reference concentration map at  $PVI = 0.25$ . Bottom: cross sectional images of the same concentration map taken at a distance of  $19.2\text{ mm}$  (left),  $22.4\text{ mm}$  (middle) and  $25.6\text{ mm}$  (right) from the inlet face. Core sample is  $76\text{ mm}$  long.

b. Top: Same images after calibrating 3D permeability field to both  $\Delta p(t)$  and concentration data.



c. Top: sagittal slice (front view) of the reference concentration map at  $PVI = 0.47$ . Bottom: cross sectional images of the same concentration map taken at a distance of  $25.6\text{ mm}$  (left),  $28.8\text{ mm}$  (middle) and  $32.0\text{ mm}$  (right) from the inlet face. Core sample is  $76\text{ mm}$  long.

d. Top: Same images after calibrating 3D permeability field to both  $\Delta p(t)$  and concentration data.

Figure 7.27: Comparison of the reference concentration maps with the simulated ones at  $PVI = 0.25$  and  $PVI = 0.47$  for the sample SG20. The displacement is performed from left to right (normal injection). The permeability field is calibrated to both  $\Delta p(t)$  and concentration data. The color bars show the injected fluid concentrations.

### Inverse injection, the GDM method:

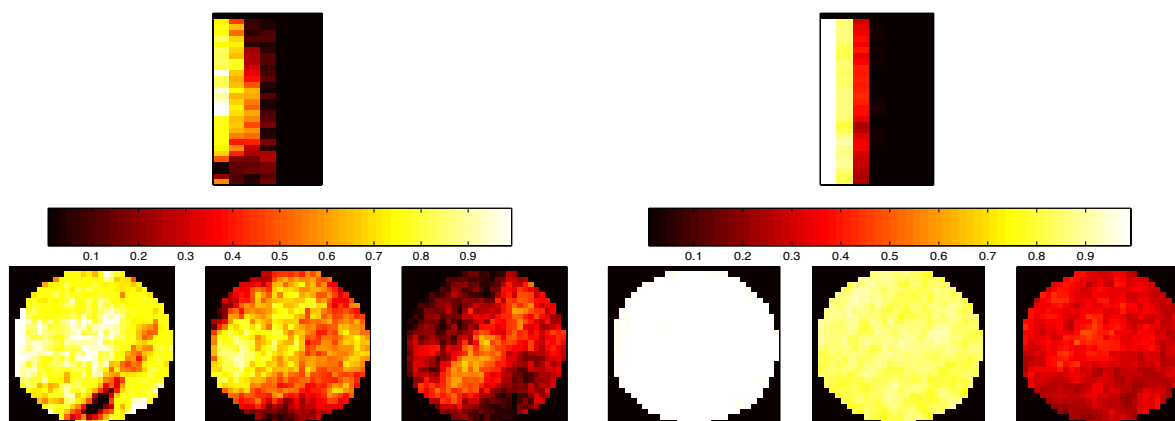
As shown in Figure 6.21, there is a piece of non permeable, but porous material at the inlet face of the sample SG20 when performing the inverse injection. It is non permeable because it corresponds to a zero glycerin concentration during displacement. Figure 7.28(a) shows a concentration map obtained at  $PVI = 0.06$ . We use this concentration map as the reference in our optimization process. The displacement front is located inside the first permeability zone. Thus, we have 7 unknown parameters. The parameters related to the other zones are fixed to the optimal values identified by the primary optimization. The permeability field calibrated to the  $\Delta p(t)$  data only is considered as our new starting point.

**First**, after 146 simulations, the objective function shows only 6% decrease. 101 additional simulations are run, but they do not lead to any improvement in the matching.

**Second**, the number of deformation parameters is increased to 3. Again, the objective function value shows no reduction after 135 simulations.

**Third**, the number of optimization parameters is increased to 6. After more than 750 simulations, the objective function shows another 6% decrease.

In total, more than 1050 simulations are performed and the objective function is reduced to only 88% of its initial value. Note that this reduction is mostly related to the concentration term. The pressure match does not change during the optimization process (see Figure 7.30). Coefficient  $A$  shows a sudden decrease at the beginning of the optimization (Figure 7.29). Then, it increases very slowly. Its variations are consistent with the variations in the

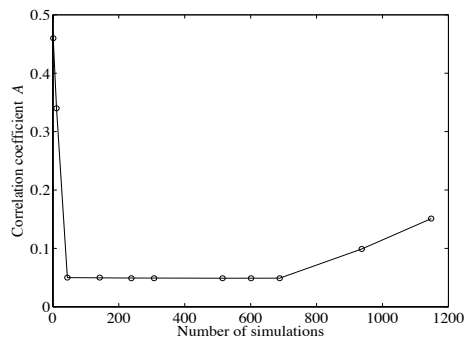


a. Top: sagittal slice (front view) of the reference concentration map at  $PVI = 0.06$ . Bottom: cross sectional images of the same concentration map taken at a distance of 3.2 mm (left), 6.4 mm (middle) and 9.6 mm (right) from the inlet face. Core sample is 76 mm long.

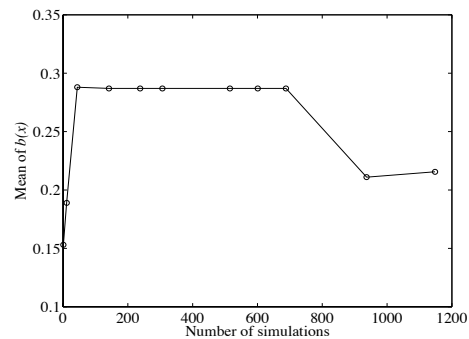
b. Top: Same images after calibrating 3D permeability field to  $\Delta p(t)$  data only.

Figure 7.28: Comparison of the reference concentration map with the simulated one at  $PVI = 0.06$  for the sample SG20. The displacement is performed from right to left (inverse injection). The permeability field is calibrated to  $\Delta p(t)$  data only. The color bars show the injected fluid concentrations.

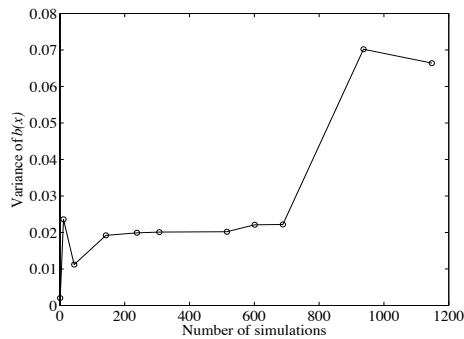
mean of  $b(\mathbf{x})$ . The small optimal value for the parameter  $A$  may be interpreted as a weak correlation between porosity and permeability. The variance of  $b(\mathbf{x})$  remains stable during 600 simulations and increases afterwards.  $L_x$  does not change, but both  $L_y$  and  $L_z$  increase until the end of optimization: transverse heterogeneities are stronger than longitudinal ones. The optimal concentration map is compared to the reference one in Figure 7.31. With the gradual deformation method, the optimization is not capable of reproducing the non permeable zone. However, it is successful in reproducing the general distribution of the reference concentration map. Again, correlation lengths of  $b(\mathbf{x})$  are the most influential parameters during the matching process.



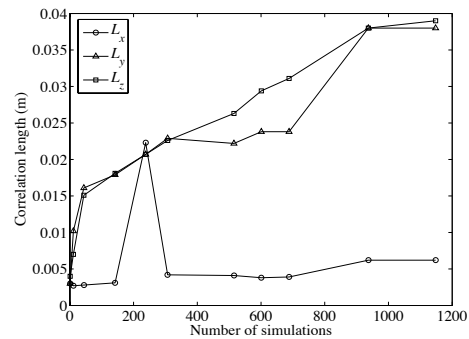
a. The evolution of coefficient  $A$  during the gradual based optimization.



b. The evolution of the mean of  $b(\mathbf{x})$  during the gradual based optimization.



c. The evolution of the variance of  $b(\mathbf{x})$  during the gradual based optimization.



d. The evolution of the correlation lengths of  $b(\mathbf{x})$  during the gradual based optimization.

Figure 7.29: The evolution of different parameters for the first zone in sample SG20 during the gradual deformation based optimization process. The displacement is performed from right to left (inverse injection).

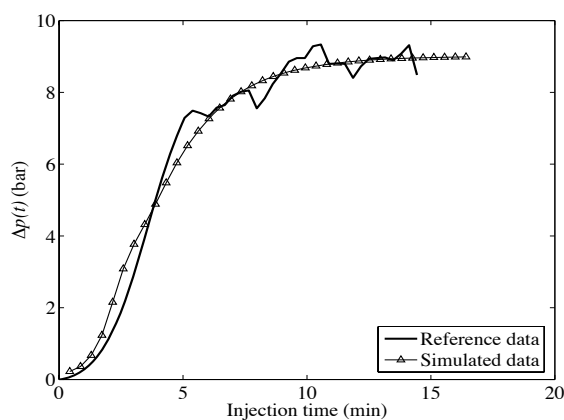
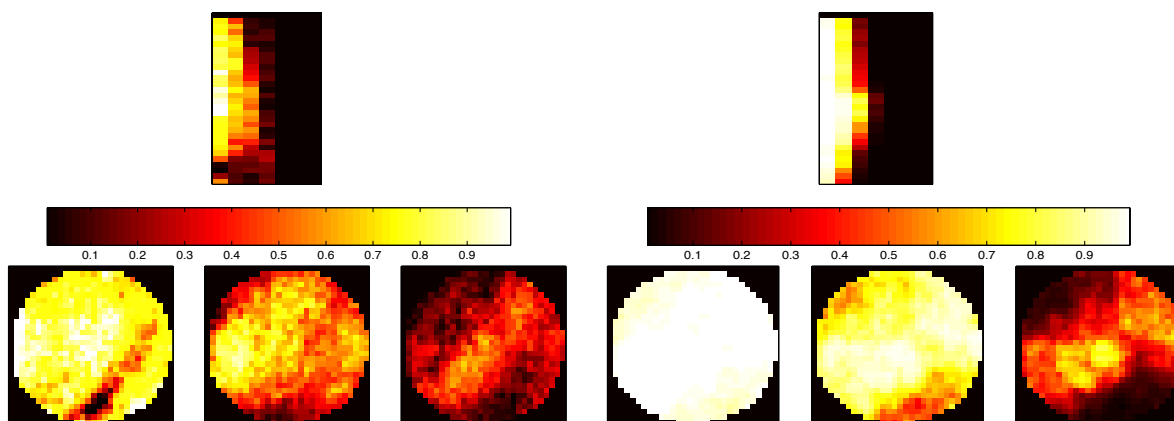


Figure 7.30: Comparison of the reference pressure drop with the simulated pressure drop for sample SG20 after performing gradual deformation based optimization. The displacement is performed from right to left (inverse injection).



a. Top: sagittal slice (front view) of the reference concentration map at  $PVI = 0.06$ . Bottom: cross sectional images of the same concentration map taken at a distance of 3.2 mm (left), 6.4 mm (middle) and 9.6 mm (right) from the inlet face. Core sample is 76 mm long.

b. Top: Same images after calibrating 3D permeability field to both  $\Delta p(t)$  and concentration data.

Figure 7.31: Comparison of the reference concentration map with the simulated one at  $PVI = 0.06$  for the sample SG20 (inverse injection). The permeability field is calibrated to both  $\Delta p(t)$  and concentration data using a gradual deformation based optimization. The color bars show the injected fluid concentrations.

### Inverse injection, the GDM plus the pilot point method:

As the gradual optimization technique is not successful in reproducing the non permeable zone, we decide to introduce two pilot points,  $x_1$  and  $x_2$ , close to the non permeable zone and perform a new optimization considering both the gradual deformation parameter and the pilot points. Conditioning realization  $b(\mathbf{x})$  to the two pilot points, we try to examine their

effects on the matching process. The two pilot points are located inside the first CT slice. The distance between them is about one correlation length ( $L_y$ , correlation estimated for the porosity data). The initial values of these two points are chosen so that their neighboring cells exhibit near zero permeability values. With the two pilot points, the number of inversion parameters for the first permeability zone is increased to 9.

The permeability field calibrated to the  $\Delta p(t)$  data only is considered as our starting point. Note that in this new optimization process, both the gradual deformation and the pilot point techniques are used together to reduce the objective function. After 300 simulations, the objective function reduces to 84% of its initial value. The convergence seems much faster than the one observed when only gradual deformation is considered. Then 260 other simulations are run, but the objective function remains unchanged.

Except for parameter  $A$  and the mean of  $b(\mathbf{x})$ , the behavior of the other inversion parameters is very similar what was observed in the previous section, when dealing only with GDM. The variance of  $b(\mathbf{x})$ ,  $L_y$  and  $L_z$  increase when  $L_x$  remains stable (see Figure 7.34). For coefficient  $A$ , a sudden decrease is observed after 114 simulations, which results in a 8% decrease of the objective function. This decrease is consistent with the increase in the mean of  $b(\mathbf{x})$ . After another 50 simulations, a sudden increase in  $A$  and decrease in the mean of  $b(\mathbf{x})$  is observed. Here, the objective function value shows a 2% additional decrease. Parameters  $A$  and  $m$  vary inversely again and stay stable until the end of optimization. The optimized value of the mean of  $b(\mathbf{x})$  is very close to the one obtained in the previous gradual optimization, but parameter  $A$  shows much smaller optimal value: permeability and porosity are not correlated in this part of the sample.

The evolution of the pilot points is very interesting. Figure 7.32 compares the concentration map (at  $PVI = 0.06$ ) simulated for the initial pilot point values with the reference data.

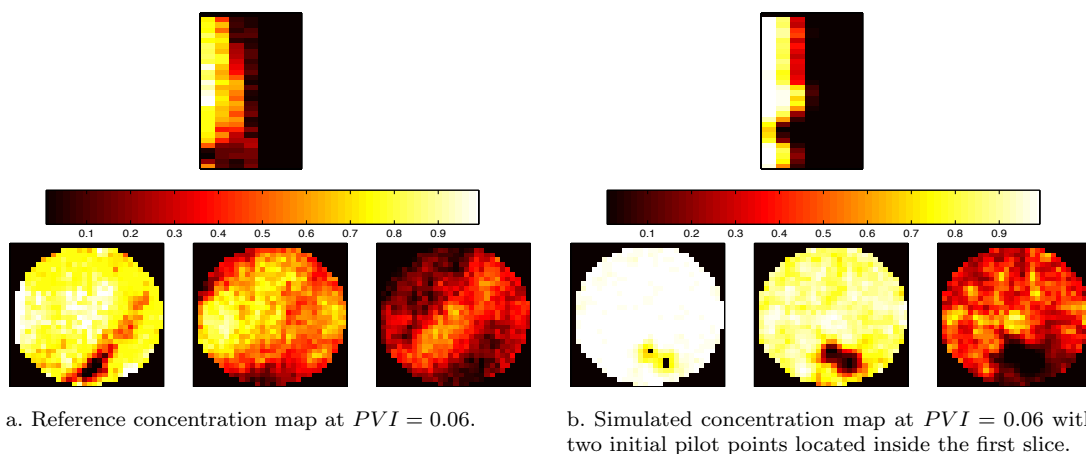


Figure 7.32: Comparison of the reference concentration map with the one simulated for the initial pilot point values located inside the first slice of SG20 numerical model. The color bars show the injected fluid concentrations.

Obviously, a non permeable zone is created around the pilot points. The zero permeability grid cells force the injected fluid to create a conic zone inside the grid. This zone starts from the non permeable grid cells, develops progressively through the model and diminishes as the flow streams rejoin again. This physical phenomenon is not clearly observed in the reference concentration map. The development of this conic zone is limited to the first slice (*i.e.*,  $3.6\text{ mm}$ ) and disappears afterwards. The increasing trend of the pilot points values during this second optimization, indicates that the optimization process tends to neglect the non permeable zone which is a tiny part of the whole concentration map and find the best match for the remaining of the data.

The optimized concentration map is compared with the reference one in Figure 7.33. Except for the first slice, the optimization is successful in reproducing the distribution of the reference concentration data. The pilot points as well as the correlation lengths of  $b(\mathbf{x})$  are the most influential parameters during this matching process.

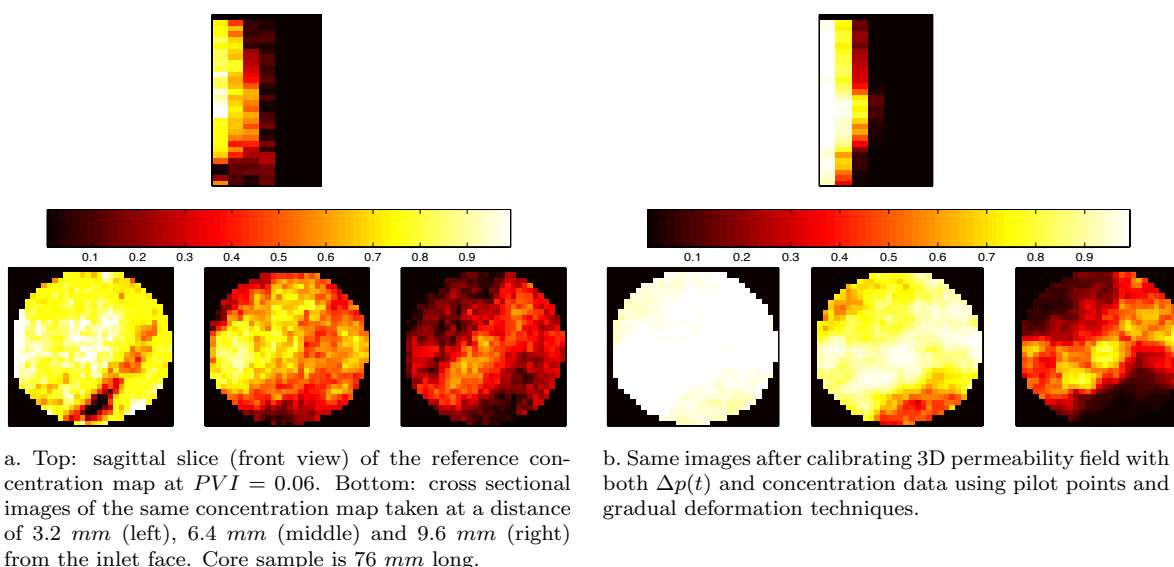
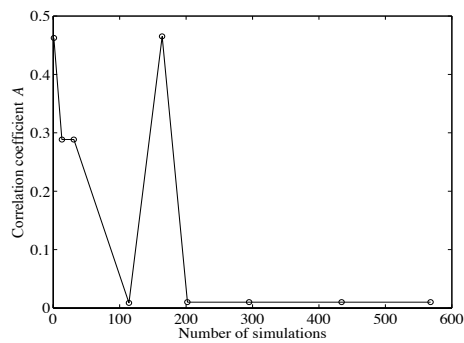
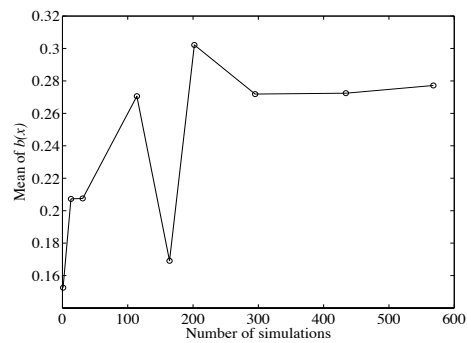


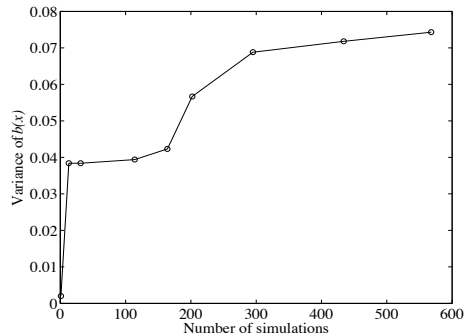
Figure 7.33: Comparison of the reference concentration map with the simulated one at  $PVI = 0.06$  for the sample SG20. The injection is performed from right to left (inverse injection). The permeability field is calibrated to both  $\Delta p(t)$  and concentration data using the pilot point and the gradual deformation methods. The color bars show the injected fluid concentrations.



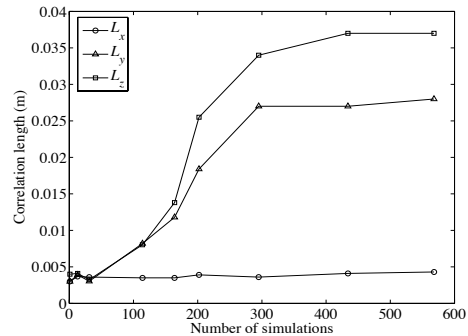
a. The evolution of coefficient  $A$  during the optimization.



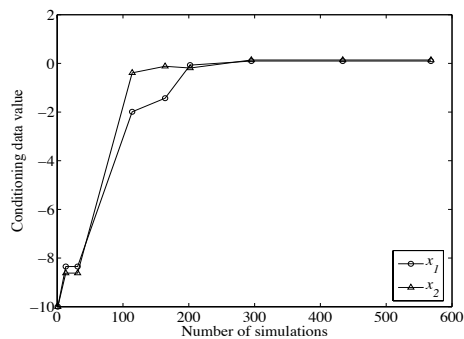
b. The evolution of the mean of  $b(\mathbf{x})$  during the optimization.



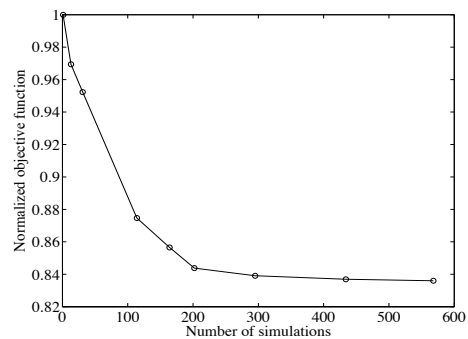
c. The evolution of the variance of  $b(\mathbf{x})$  during the optimization.



d. The evolution of the correlation lengths of  $b(\mathbf{x})$  during the optimization.



e. The evolution of two pilot points  $x_1$  and  $x_2$  during the optimization.



f. The evolution of the normalized objective function during the optimization.

Figure 7.34: The evolution of different parameters of the first zone for sample SG20 when defining two pilot points near non permeable zone. The optimization is performed using both pilot points and gradual deformation based optimization. The displacement is performed from right to left (inverse injection).

## 7.4 Concluding remarks

In this chapter, we applied our methodology to calibrate three-dimensional core scale permeability fields to both static and dynamic data. The permeability fields are modeled using a linear  $\log(k) - \phi$  relation and exhibit a spatial structure characterized by a nested combination of two individual variograms. The proposed methodology was applied to two sets of synthetic data and the data collected during the viscous miscible flooding of a composite sample and a sandstone sample.

For the numerical cases, the permeability field was preliminary calibrated to the inlet-outlet pressure drop data. The results showed a perfect match. However, the simulated concentration distributions were not similar to the reference data. To also constrain the permeability field to the concentration data, a gradual deformation based optimization process was used. The results showed about 70% decrease in the objective function for both models. It was shown that the  $\Delta p(t)$  was only a function of the average permeability and that a good concentration match could not be achieved without considering transverse permeability heterogeneities. Parameter  $A$  was shown to be a good indicator of porosity permeability correlation. The correlation lengths of  $b(\mathbf{x})$  were the most influential parameters during the matching of the concentration data.

For the experimental cases, the  $\Delta p(t)$  observed for the composite sample was perfectly matched with the simulated one after dividing the second plug into two permeability zones. The matching of the concentration data was more difficult. The objective functions of this sample decreased by 40% after performing more than 500 simulations and finally reached a plateau. A good correlation between porosity and permeability was observed.

For the sandstone sample, a good match was observed for pressure drop data. However, the objective function for concentration term reduced to only 80% of its initial value. Optimization was more difficult in this case because of the noise in the concentration data. The correlation between porosity and permeability was found to be very weak for this sample. Although not perfect, we showed that the method is still capable of reproducing the laboratory front shape and concentration distribution with a good degree of acceptance.



## Nomenclature

$A$	correlation coefficient	$m$	mean
$L_x$	correlation length along axis $X$	$\mathbf{x}$	location
$L_y$	correlation length along axis $Y$	$\Delta p(t)$	pressure drop as a function of time
$L_z$	correlation length along axis $Z$	$\Theta$	model parameter
$S$	concentration data	$\omega^S$	local weight assigned to concentration data
$\bar{S}$	upscaled concentration data	$\phi$	porosity
$XYZ$	Cartesian axes	$\mu$	viscosity
$b$	realization of a random function	$\mu_e$	effective viscosity
$k$	permeability	$\mu_m$	viscosity of the mixed zone
$\bar{k}$	upscaled permeability	$\omega$	mixing parameter
$k_r$	relative permeability	$\rho$	density
$m_i$	mass fraction of phase $i$	$\sigma^2$	variance

# Conclusions and Perspectives

In this work, we tried to quantify the heterogeneity of transport properties, mainly permeability, into core samples. The study was divided into three main parts. The objective of the first part was to select natural core samples, which exhibit longitudinal and transverse heterogeneities. For that purpose, we referred to classical selection procedures that are usually used to separate homogeneous core samples from heterogeneous ones. CT scanning were performed to investigate their homogeneity. Two-dimensional CT images provided information about the heterogeneity perpendicular to the flow axis. CT images were also used to calculate the average CT number per slice. Looking at these average values against location helped us to rapidly quantify longitudinal heterogeneities. Then, we created two artificially heterogeneous core samples by stacking together small homogeneous plugs. We also selected four core samples, which exhibit core scale heterogeneities. Four numerical models were also created with different types of heterogeneities for validation purposes.

In the second part of the study, we presented a new methodology to obtain the one-dimensional permeability profiles of the heterogeneous core samples. The leading idea was to inject a high viscosity glycerin into a core sample saturated with a low viscosity brine. The two fluids were miscible in all proportions. We assumed that the fluid displacement is piston-like due to the high viscosity ratio between the invading and the defending fluids. This assumption was validated by visualizing the front displacement from X-ray CT images. We investigated the evolution of the inlet-outlet pressure drop as a function of time until the breakthrough of glycerin. A continuous permeability profile was estimated along the flow direction from the pressure drop assuming that the core sample is a stack of infinitely thin cross sections perpendicular to the flow direction: a permeability value was determined for each cross section. The methodology was validated through numerical experiments. Flow simulations were performed for the two numerical models representing core samples. The models studied were sequences of blocks (similar to our composite samples) with given mean permeabilities. The transverse heterogeneities were negligible in both models. We simulated the pressure drop between the inlet and outlet faces considering both miscible and immiscible fluids. The interpretation procedure provided the expected permeability profile. The relative error between estimated and actual permeabilities was less than 13% for both models. We pointed out a smoothing effect in the case of miscible flow, which was due to

the mixing zone between the invading and defending fluids.

The methodology was also applied to laboratory experiments. The process worked well for low permeabilities. The relative error between estimated and measured absolute permeabilities was less than 5%. In the case of permeable samples (zones), as the pressure drop is inversely proportional to permeability, the estimated permeabilities were very noisy. The determination of the permeability profile was improved by performing an inverse injection. The results obtained for the heterogeneous cores were not as good as the one pointed out for numerical experiments and exhibited more than 40% error. However, we showed that the estimated permeabilities still follow the actual permeability variations (quantified from other measurements).

In the methodology that we developed for the one-dimensional core scale permeability characterization, we assumed that permeability is homogeneous per cross section, which means that heterogeneity is one-dimensional. This assumption does not hold when dealing with transverse heterogeneities such as small scale bedding. In the third part of the study, we focused on the development of a new procedure able to capture three-dimensional heterogeneities inside core samples. We selected samples with local heterogeneities. Their three-dimensional porosity maps were known: they were created for numerical models and were measured for natural samples. Inlet-outlet pressure drop was measured when performing viscous miscible flooding by displacing a low viscosity brine with a high viscosity glycerin. Concentration maps were obtained at successive times during the displacement. The 3D permeability fields were modelled using a relationship such as  $\log(k(\mathbf{x})) = A\phi(\mathbf{x}) + b(\mathbf{x})$  where  $A$  is a constant and  $b(\mathbf{x})$  is a realization of a random function characterized by a mean, a variance and a given variogram.

We developed an assisted history-matching process to model permeability heterogeneity inside the core samples while using three-dimensional porosity field as well as the measured pressure and concentration data. The unknown parameter were  $A$ , then mean and variance of  $b(\mathbf{x})$ , deformation parameter  $\theta$ , and correlation lengths of  $b(\mathbf{x})$ . A first guess was initially generated honoring the measured  $\Delta p(t)$  variations along the flow axis. This first guess was subsequently modified until the mismatch between measured pressure and concentration data and fluid flow simulated answers was minimized. We used a gradual deformation based optimization method to narrow the search space while preserving the overall spatial variability.

The proposed methodology was applied to two sets of numerical experiments and two other sets of laboratory experiments. The measured  $\Delta p(t)$  for all samples was perfectly matched with our simple optimization process. The objective function showed more than 95% decrease for all cases. Matching the concentration data was much more difficult due to the noise in X-ray CT acquisition. The reduction of the objective function was about 60% for the concentration term for the numerical experiments and 20% for the laboratory experiment. It was shown that the  $\Delta p(t)$  was only a function of the average permeability and that a good concentration match could not be achieved without considering transverse permeability het-

erogeneities. The parameter  $A$  was shown to be a good indicator of porosity-permeability correlation. The parameter  $A$  and the mean of  $b(\mathbf{x})$  were dependent parameters: an increase in the first one results in a decrease in the second one. Finally, we showed that the correlation lengths of  $b(\mathbf{x})$  are the most influential parameters when accounting for concentrations.

As in all practical studies, our modeling is based on assumptions and simplifications. Improving both theoretical and experimental conditions and assumptions may lead to a more realistic modeling and better results. Here, we discuss some of the possible future improvements.

- In our one-dimensional mapping technique, we assumed that the front is sharp and ignored the mixed zone between the invading and the defending phases. One possible improvement is to consider three zones inside the core sample: pure invading phase, the mixed zone and the pure defending phase. It would be interesting to develop a new formulation accounting for the pressure drop inside the mixed zone and its effect on the one-dimensional permeability estimation.
- Another possibility would be to perform immiscible flooding instead of miscible displacement. The flooding condition would be the same except that there is no mixed zone between the invading and the defending phases. The assumption of piston-like displacement can be verified more precisely.
- In order to improve the quality of the collected data especially during CT scan measurements, one can increase the duration of each intensity measurement, but decrease the number of slices along the flow axis. The optimization process can be done using two-dimensional concentration maps at a few locations along the sample. Our validation depends on the quality of the collected data. High quality and noise free data would be much more useful even if they are only available for some parts of the sample.
- In this work, we always assumed that the variogram of the permeability model is the same as the one estimated for the porosity data. Another idea is to change the variogram of permeability model and study its effect on the objective function evolution and the matching process.
- It would be interesting to test the power law relationship  $k = A(\phi - \phi_0)^\beta$  suggested by percolation theory when correlating permeability data with porosity. In this formulation,  $\phi_0$  is a minimum porosity at which a connected pathway through the sample will exist. Parameter  $A$  is a constant that determines the magnitude of  $k$ .  $\beta$  is an exponent related to pathway geometry. In this formulation, the parameters  $A$  and  $\beta$  are unknowns.  $\phi_0$  can be determined in laboratory.

- The permeability models in this work are upscaled using an arithmetic-arithmetic-harmonic average and a fixed upscaling ratio. Adequate study may be performed on the upscaling ratio and its effect on the final match. The evolution of inversion parameters should be studied with upscaling ratio. It would be also interesting to study the effect of upscaling on parameter  $\beta$  when using the power law  $k - \phi$  relationship suggested by percolation theory.
- The effect of miscibility on concentration distribution should be studied in details. In this work, we used an immiscible model and ignored the mixed zone when simulating our viscous miscible displacement. This assumption can be revised using for instance the Todd and Longstaff mixing coefficient.

# Bibliography

- [1] AZIZ, K., AND SETTARI, A. *Petroleum Reservoir Simulation*, second ed. Blitzprint Lt, Calgary, Alberta, 2002.
- [2] BAKKE, S., AND OREN, P. 3-D pore-scale modelling of sandstones and flow simulations in the pore networks. *SPE Journal* 2 (1997), 136–149.
- [3] BARAKA-LOKMANEA, S., MAINC, I., NGWENYAC, B., AND ELPHICK, S. Application of complementary methods for more robust characterization of sandstone cores. *Marine and Petroleum Geology*, DOI: 10.1016/j.marpetgeo.2007.11.003 (2007).
- [4] BATYCKY, R. *A Three-Dimensional Two-Phase Field Scale Streamline Simulator*. PhD thesis, Stanford University, 1997.
- [5] BEKRI, S., LAROCHE, C., AND VIZIKA, O. Pore-network models to calculate transport properties in homogeneous and heterogeneous porous media. *Computational Methods in Water Resources XIV, Delf, Netherlands* (2002).
- [6] BERNARD, S., DELAY, F., AND POREL, G. A new method of data inversion for the identification of fractal characteristics and homogenization scale from hydraulic pumping tests in fractured aquifers. *Journal of Hydrology* 328 (2006), 647–658.
- [7] BIJELJIC, B., AND BLUNT, M. Pore-scale modeling of transverse dispersion in porous media. *Water Resources Research* 43, W12S11 (2007).
- [8] BLUNT, M., AND KING, P. Relative permeabilities from 2-dimensional and 3-dimensional pore-scale network modeling. *Transport In Porous Media* 4, 6 (1991), 407–433.
- [9] BOURDET, D., WHITTLE, T., DOUGLAS, A., AND PIRARD, Y. A new set of type curves simplifies well test analysis. *World Oil* (1983), 95–106.
- [10] BUCKLEY, S., AND LEVERETT, M. Mechanism of Fluid Flow in Sands. *Trans. AIME* 146 (1942), 107–116.

- [11] CARDWELL, W., AND PARSONS, R. Average permeabilities of heterogenous oil sands. *Trans., AIME 160* (1945), 34.
- [12] DARCY, H. Les fontaines publiques de la ville de Dijon. *Victor Dalmont, Paris, France* (1856).
- [13] DAUBA, C., HAMON, G., QUINTARD, M., AND CHERBLANC, F. IDENTIFICATION OF PARALLEL HETEROGENEITIES WITH MISCIBLE DISPLACEMENT. *SCA-9933, Proceeding of the International Symposium of the Society of Core Analysts held in Golden, Colorado, USA, 1-4 August* (1999).
- [14] DE MARSILY, G. *De l'identification des systems hydrologiques*. PhD thesis, Universite Paris VI, 1978.
- [15] DELAY, F., POREL, G., AND BERNARD, S. Analytical 2D model to invert hydraulic pumping tests in fractured rocks with fractal behavior. *Geophysical Research Letters* 31, L16501 (2004).
- [16] DEZABALA, E., AND KAMATH, J. Laboratory Evaluation of Waterflood Behavior of Vugular Carbonates. *SPE 30780, 1995 SPE Annual Technical Conference and Exhibition held in Dallas, USA, 22-25 October* (1995).
- [17] DONG, H., TOUATI, M., AND BLUNT, M. Pore Network Modeling: Analysis of Pore Size Distribution of Arabian Core Samples. *SPE 105146, 15<sup>th</sup> SPE Middle East Oil & Gas Show and Conference held in Bahrain, Kingdom of Bahrain, 11-14 March* (2007).
- [18] DULLIEN, F. *Porous Media Fluid Transport and Pore Structure*. Academic Press, Inc., California, 1991.
- [19] FANCHI, J. *Principles of Applied Reservoir Simulation*, second ed. Gulf Professional Publishing, Houston, TX, 2001.
- [20] FEITOSA, G., CHU, L., THOMPSON, L., AND REYNOLDS, A. Determination of Permeability Distribution From Well-Tests Pressure Data. *SPE 26047, SPE Western Regional Meeting held in Anchorage, Alaska, 26-28 May* (1993), 607–615.
- [21] FINCHAM, A., AND GOUTH, F. IMPROVEMENTS OF COREFLOOD DESIGN AND INTERPRETATION USING A NEW SOFTWARE. *SCA2000-29, Proceeding of the International Symposium of the Society of Core Analysts held in Abu Dhabi, UAE, 18-22 October* (2000).
- [22] FOURAR, M. CHARACTERIZATION OF HETEROGENEITIES AT THE CORE SCALE USING THE EQUIVALENT STRATIFIED POROUS MEDIUM APPROACH. *SCA2006-49, Proceeding of the International Symposium of the Society of Core Analysts held in Trondheim, Norway, 12-16 September* (2006).

- [23] FOURAR, M., KONAN, G., FICHEN, C., ROSENBERG, E., EGERMANN, P., AND LENORMAND, R. TRACER TESTS FOR VARIOUS CARBONATE CORES USING X-RAY CT. *SCA2005-56, Proceeding of the International Symposium of the Society of Core Analysts held in Toronto, Canada, 21-25 August (2005)*.
- [24] GERVAIS, V., GAUTIER, Y., LE RAVALEC, M., AND ROGGERO, F. History Matching Using Local Gradual Deformation. *SPE 107173, 2007 SPE Europec/EAGE Annual Technical Conference and Exhibition held in London, United Kingdom, 11-14 June (2007)*.
- [25] HALDORSEN, H., AND LAKE, L. A New Approach to Shale Management in Field-Scale Models. *SPE Journal, Society of Petroleum Engineering 24*, 4 (August 1984), 447–457.
- [26] HAMON, G., AND ROY, C. INFLUENCE OF HETEROGENEITY, WETABILITY AND COREFLOOD DESIGN ON RELATIVE PERMEABILITY CURVES. *SCA2000-23, Proceeding of the International Symposium of the Society of Core Analysts held in Abu Dhabi, UAE, 18-22 October (2000)*.
- [27] HU, L. Gradual Deformation and Iterative Calibration of Gaussian-Related Stochastic Models. *Mathematical Geology 32*, 1 (2000), 87–108.
- [28] JOHNSON, E., BOSSLER, D., AND NEUMANN, V. Calculation of Relative Permeability from Displacement Experiments. *Trans, AIME 216* (1959), 370–372.
- [29] KACZMARYK, A., AND DELAY, F. Interference pumping tests in a fractured limestone (Poitiers–France): Inversion of data by means of dual-medium approaches. *Journal of Hydrology 337* (2007), 133–146.
- [30] KAMEDA, A. *PERMEABILITY EVOLUTION IN SANDSTONE: DIGITAL ROCK APPROACH*. PhD thesis, Stanford University, 2004.
- [31] KELKAR, M., AND PEREZ, G. *Applied Geostatistics for Reservoir Characterization*. Society of Petroleum Engineers, 2002.
- [32] KETCHAM, R., AND CARLSON, W. Acquisition, optimization and interpretation of X-ray computed tomographic imagery: Applications to the geosciences. *Computers and Geosciences 27* (2001), 381–400.
- [33] LAROCHE, C., AND VIZIKA, O. Two-phase flow properties prediction from small-scale data using pore-network modeling. *Transport in Porous Media*, 61 (2005), 77–91.
- [34] LE RAVALEC, M., NOETINGER, B., AND Y.HU, L. The FFT Moving average (FFT–MA) Generator: An Efficient Numerical Method for Generating and Conditioning Gaussian Simulations. *Mathematical Geology 32*, 6 (2000), 701–723.



- [35] LE RAVALEC-DUPIN, M. *Inverse Stochastic Modeling of Flow in Porous Media - application to reservoir characterization*, first ed. ISBN 2-7108-0864-1. Editions Technip, 2005.
- [36] LE RAVALEC-DUPIN, M., AND Y.HU, L. Combining the Pilot Point and Gradual Deformation Methods for Calibrating Permeability Models to Dynamic Data. *Oil & Gas Science and Technology* 62, 2 (2007), 169–180.
- [37] LOUIS, L., DAVID, C., METZA, V., ROBIONA, P., MENÉNDEZA, B., AND KISSELC, C. Microstructural control on the anisotropy of elastic and transport properties in undeformed sandstones. *International Journal of Rock Mechanics & Mining Sciences* 42 (2005), 911–923.
- [38] MATTHEWS, C., AND RUSSELL, D. Pressure Build-Up and Flow Tests in Wells. *SPE Monograph Series, AIME 1* (1967), 167.
- [39] MENÉNDEZ, B., DAVID, C., AND NISTA, A. Confocal scanning laser microscopy applied to the study of pore and crack networks in rocks. *Computers & Geosciences* 27 (2001), 1101–1109.
- [40] MEZGHANI, M., ARTUS, V., LANGLAIS, V., AND ROGGERO, F. *MONITOR REFERENCE MANUAL*. Institut Français du Pétrole, 1 et 4, avenue de Bois-Préau, 92852Rueil-Malmaison Cedex, France, June 2005.
- [41] MOCTEZUMA-BERTHIER, A., AND FLEURY, M. Permeability Mapping on Vuggy Core Sample Using Tracer Experiments and Streamline Simulations. *SPE 58992, Proceeding of 2000 SPE International Petroleum Conference and Exhibition held in Villahermosa, Mexico, 1-3 February* (2000).
- [42] NIELSEN, L. *Reservoir Characterisation by a Binary Level Set Method and Adaptive Multiscale Estimation*. PhD thesis, University of Bergen, 2006.
- [43] NORDHAUG, H., CELIA, M., AND DAHLE, H. A pore network model for calculation of interfacial velocities. *Advances in Water Resources* 26 (2003), 1061–1074.
- [44] NORDTVEDT, J., URKEDAL, H., KOLLTVEIT, E., PETERSEN, K., SYLTE, E., AND VALESTRAND, R. THE SIGNIFICANCE OF VIOLATED ASSUMPTIONS ON CORE ANALYSIS RESULTS. *SCA-9931, Proceeding of the International Symposium of the Society of Core Analysts held in Golden, Colorado, USA, 1-4 August* (1999).
- [45] OKABEA, H., AND BLUNT, M. Pore space reconstruction using multiple-point statistics. *Journal of Petroleum Science and Engineering* 46 (2005), 121–137.

- [46] OLIVIER, P., CANTEGREL, L., LAVEISSIERE, J., AND GUILLONNEAU, N. MULTIPHASE FLOW BEHAVIOUR IN VUGULAR CARBONATES USING X-RAY CT. *SCA2004-13, Proceeding of the International Symposium of the Society of Core Analysts held in Abu Dhabi, UAE, 5-9 October (2004)*.
- [47] POWELL, M. *A FORTRAN Subroutine for Solving Systems of Nonlinear Algebraic Equations*, p.rabinowitz ed. Gordon and Breach, London, 1970.
- [48] ROGGERO, F., DING, D., BERTHET, P., LERAT, O., CAP, J., AND SCHREIBER, P. Matching of Production History and 4D Seismic Data - Application to Girassol Field, Offshore Angola. *SPE 109929, 2007 SPE Annual Technical Conference and Exhibition held in Anaheim, California, USA, 11-14 November (2007)*.
- [49] ROGGERO, F., AND HU, L. Gradual Deformation of Continues Geostatistical Models for History Matching. *SPE 49004, 1998 SPE Annual Technical Conference and Exhibition held in New Orleans, USA, 27-30 September (1998)*.
- [50] SAHIMI, M. *Flow and Transport in Porous Media and Fractured Rock*. VCH, Germany, 1995.
- [51] SLIDER, H. *Worldwide practical petroleum reservoir engineering methods*. PennWell Publishing Company, 1983.
- [52] SOLTANI, A., LE RAVALEC, M., AND FOURAR, M. An experimental method for one dimensional permeability characterization of heterogeneous porous media at the core scale. *Transport In Porous Media*, DOI: 10.1007/s11242-008-9258-0 (2007).
- [53] SOLTANI, A., LE RAVALEC, M., AND FOURAR, M. Calibrating permeability heterogeneity at the core scale to static and dynamic data. *SPE 62976, Proceeding of the SPE Annual Technical Conference and Exhibition held in Denver, Colorado, USA, 21-24 September (2008)*.
- [54] SYLTE, A., MANNSETH, T., MYKKELTVEIT, J., AND NORDTVEDT, J. RELATIVE PERMEABILITY AND CAPILLARY PRESSURE: EFFECT OF ROCK HETEROGENEITY. *SCA-9808, Proceeding of the International Symposium of the Society of Core Analysts held in Hague, Netherlands, 14-16 September (1998)*.
- [55] TARANTOLA, A. *Inverse Problem Theory and Methods for Model Parameter Estimation*. SIAM, USA, 2005.
- [56] TARTAKOVSKY, D., MOULTON, J., AND ZOLTNIL, V. Kinematic Structure of Minipermeameter Flow. *Water Resources Research* 36, 9 (2000), 2433-2442.

- [57] TCHELEPI, H., ORR, F., RAKOTOMALALA, N., SALIN, D., AND WOUMÉNI, R. Dispersion, permeability heterogeneity, and viscous fingering: Acoustic experimental observations and particle-tracking simulations. *Phys. Fluids A* 5 (1993), 1558–1574.
- [58] TODD, M., AND LONGSTAFF, W. The Development, Testing, and Application Of a Numerical Simulator for Predicting Miscible Flood Performance. *Journal of Petroleum Technology* 24, 7 (1972), 874–882.
- [59] WATSON, A., KERIG, P., AND OTTER, R. A Test for Detecting Rock Property Nonuniformities in Core samples. *SPE Journal* 25, 6 (December 1985), 909–916.
- [60] WITHJACK, E. Computed Tomography for Rock-Property Determination and Fluid-Flow Visualization. *SPE 16951, Proceeding of the 1987 SPE Annual Technical Conference and Exhibition held in Dallas, USA, 27-30 September* (1987).
- [61] WITHJACK, E., ORSHAM, S., AND YANG, C. CT Determination of Heterogeneities and Miscible Displacement Characteristics. *SPE Formation Evaluation* 6, 4 (1991), 447–452.
- [62] XU, B., KAMATH, J., AND YORTSOS, Y. Use of Pore-Network Models to Simulate Laboratory Corefloods in a Heterogeneous Carbonate Sample. *Journal of Petroleum Science and Engineering* 20 (1998), 109–115.
- [63] ZHAN, L., AND YORTSOS, Y. Identification of permeability field of a porous medium from the injection of a passive tracer. *Physical Review* 62, 1 (2000), 863–879.
- [64] ZHU, W., DAVID, C., AND WONG, T. Network modelling of permeability evolution during cementation and hot isostatic pressing. *JOURNAL OF GEOPHYSICAL RESEARCH* 100, B8 (1995), 451–464.
- [65] ZWEERS, A., SCHERPENISSE, W., WIT, K., AND MASS, J. RELATIVE PERMEABILITY MEASUREMENTS ON HETEROGENEOUS SAMPLES, A PRAGMATIC APPROACH. *SCA-9909, Proceeding of the International Symposium of the Society of Core Analysts held in Golden, Colorado, USA, 1-4 August* (1999).

AUTORISATION DE SOUTENANCE DE THESE  
DU DOCTORAT DE L'INSTITUT NATIONAL  
POLYTECHNIQUE DE LORRAINE

o0o

VU LES RAPPORTS ETABLIS PAR :

**Monsieur Frédéric DELAY, Professeur, Université de Poitiers, Poitiers**

**Monsieur Christian DAVID, Professeur, Université de Cergy-Pontoise, Cergy-Pontoise**

Le Président de l'Institut National Polytechnique de Lorraine, autorise :

**Monsieur SOLTANI Amir**

à soutenir devant un jury de l'INSTITUT NATIONAL POLYTECHNIQUE DE LORRAINE,  
une thèse intitulée :

**"Caractérisation 3D de l'hétérogénéité de la perméabilité à l'échelle de l'échantillon"**

NANCY BRABOIS  
2, AVENUE DE LA  
FORET-DE-HAYE  
BOITE POSTALE 3  
F - 54501  
VANDŒUVRE CEDEX

en vue de l'obtention du titre de :

DOCTEUR DE L'INSTITUT NATIONAL POLYTECHNIQUE DE LORRAINE

Spécialité : « **Mécanique et Energétique** »

Fait à Vandoeuvre, le 07 octobre 2008

Le Président de l'I.N.P.L.,

F. LAURENT



# INSTITUT NATIONAL POLYTECHNIQUE DE LORRAINE

## ADMISSION AU GRADE DE DOCTEUR



Les membres du Jury soussignés, désignés par le Président de l'Institut National Polytechnique de Lorraine,  
Vu la loi 84-52 du 26 janvier 1984 sur l'Enseignement Supérieur  
Vu le décret 84-573 du 5 juillet 1984 relatif aux diplômes nationaux de l'Enseignement Supérieur  
Vu le décret 84-723 du 17 juillet 1984 fixant la classification d'Etablissements Publics à caractères scientifique,  
culturel et professionnel  
Vu l'arrêté interministériel du 30 mars 1992 relatif aux Etudes de 3<sup>ème</sup> cycle  
Vu le MASTER en : Reservoir Geoscience and Engineering, reservoir engineering major  
obtenu en : 2005

ou

Vu la dérogation d'inscription accordée par le Président de l'INPL le :  
Vu l'autorisation d'inscription à la préparation du Doctorat délivrée par le Président de l'Institut National  
Polytechnique de Lorraine en date du : 02 décembre 2005  
Vu l'autorisation de soutenance accordée par le Président de l'INPL le : 07 octobre 2008

Suite à la soutenance par l'intéressé(e) de la thèse ou des travaux intitulés :

« **Caractérisation 3D de l'hétérogénéité de la perméabilité à l'échelle de l'échantillon** »

prononcent l'admission de Monsieur **SOLTANI Amir**

né(e) à : **Golpayegan (IRAN)**

le : **08 janvier 1980**

au grade de **DOCTEUR DE L'INSTITUT NATIONAL POLYTECHNIQUE DE LORRAINE**

Spécialité : **Mécanique et énergétique**

Autre(s) Etablissement(s) dans le(s)quel(s) ont été préparés la thèse ou les travaux :

Fait le, 21 octobre 2008

Les membres du Jury (1) :

**M. Frédéric DELAY (Rap)**  
Professeur  
Université de Poitiers  
Poitiers

(signature)

**M. Christian DAVID (Rap)**  
Professeur  
Université de Cergy-Pontoise  
Cergy-Pontoise

(signature)

**M. Mostafa FOURAR (Dir. de la thèse)**  
Professeur  
ENSAM  
Châlons-en-Champagne

(signature)

**Mme Mickaële LE RAVALEC-DUPIN**  
Ingénieur  
Institut Français du Pétrole  
Rueil-Malmaison

(signature)

**M. Didier LASSEUX**  
Professeur  
ENSAM  
Talence

(signature)

**M. Patrick EGERMANN**  
Ingénieur  
Gaz-de-France  
La Plaine Saint-Denis

(signature)